

Supplementary Information

Noncanonical Rh(0)/Rh(I) Catalysis Enables Redox-neutral Epoxy Depolymerisation in Water

Emil V. Schwibinger¹, Alexander Ahrens^{1*}, Gabriel M. F. Batista^{1*}, Niels Hildebrandt¹, José P. A. de Carvalho¹, Joseph E. McPeak², Anders B. Nielsen¹, Clemens Kaussler¹, Nino Wili¹, Niels C. Nielsen¹, Troels Skrydstrup^{1*}

Affiliations:

¹Department of Chemistry and Interdisciplinary Nanoscience Center (iNANO), Aarhus University, Aarhus C, Denmark.

²Novo Nordisk Foundation EPR Center, Department of Chemistry, University of Copenhagen, Copenhagen, Denmark.

*Corresponding author. Email: aahrens@inano.au.dk, gmbf@inano.au.dk, ts@chem.au.dk,

Contents

S1. Materials and Methods	3
S1.1 General Information.....	3
S1.2 Polymer and Composite samples.....	4
S2. Optimization	8
S2.1 Methodologies Reported for C–O Bond Scission Lignin.....	9
S2.2 Screening of Ligands	11
S2.3 Screening of Reaction Conditions	13
S2.4 Screening of Conditions on Airstone 760E/766H	14
S2.5 Deconstruction of other Commercial Wind Energy Epoxy Resins	16
S3. Mechanistic Investigation.....	18
S3.1 Deconstruction of Ketone based Model Substrates	18
S3.2 Kinetic Isotope Effect Studies	19
S3.3 Probing Mononuclear and Dinuclear Complexes.....	19
S3.4 Testing for Hydrogen Peroxide Formation.....	21
S3.5 Reduction of terpy-Rh(III) to terpy-Rh(I) via β hydride elimination	23
S3.6 C–O Bond Scission on α -Phenoxyketones by terpy-Rh(0)	24
S3.7 Room Temperature EPR Studies.....	26
S3.8 Low Temperature EPR Studies and Simulations.....	28
S4. Cyclovoltammetric Studies.....	34
S4.1 General Remarks	34
S4.2 General Method for Obtention of CV Data	34
S4.3 CV Studies using TBAF ₄ as Supporting Electrolyte	35
S4.4 CV Studies using TBAOH as Supporting Electrolyte.....	38
S5. Computational Studies.....	41

S5.1 Computational Methods.....	41
S5.2 Comment on chosen Level of Theory	41
S5.3 Precatalyst Equilibrium in Reaction Medium.....	44
S5.4 Calculated Precatalyst Activation Pathways	45
S5.5 Calculated C–O Bond Activation	49
S5.6 Proposed Catalytic Cycle.....	56
S5.7 Comment on the Computational Method and Calculated Energies.....	58
S5.8 Reported Data for Individual Species and Mechanisms.....	60
S6. Synthesis of Compounds	70
S6.1 Ligands	70
S6.2 Complexes	77
S6.3 Model Substrates	84
S7. Catalytic Deconstruction	85
S7.1 On Model Substrates.....	85
S7.2 On Commercial Epoxy Resins.....	87
S7.3 On Fiber Reinforced Epoxy Composites.....	87
S8. Spectra and Images	89
S8.1 NMR Spectra of Synthesized Compounds	89
S8.2 Microscopic Images of Recovered Fibers (SEM)	128
S8.3 X-Ray Micro Computed Tomography (μ -CT)	129

S1. Materials and Methods

S1.1 General Information

Unless otherwise stated, all reactions were set up and worked up in a glovebox under an atmosphere of argon. All chemicals were purchased from Sigma-Aldrich, Tokyo Chemical Industry (TCI) or Strem Chemicals and used as received. Rhodium precursors $\text{RhCl}_3 \cdot 3 \text{H}_2\text{O}$ and $[\text{Rh}(\text{COD})\text{Cl}]_2$ were donated by Heraeus Precious Metals GmbH & Co. KG and used as received. THF, toluene and MeCN were retrieved from a MBraun SP-800 purification system, degassed using argon and stored over 3 Å molecular sieves. The remaining solvents were purchased from Sigma-Aldrich, degassed using argon, stored over 3 Å molecular sieves and used without further purification.

Thin layer chromatography (TLC) was carried out on pre-coated aluminium sheets ALUGRAM® Xtra SIL G/UV254 purchased by Macherey-Nagel. Visualisation of the products was achieved by UV-light irradiation (366 nm) and / or staining with a potassium permanganate in water.

Flash column chromatography was carried out using Silica gel (0.040 – 0.063 mm/ 230 – 400 mesh) ASTM purchased from Macherey-Nagel. Automated flash column chromatography (AFCC) was carried out with Interchim PuriFlash XS520Plus with 30 µm prepacked columns. Celite®545, coarse, was used for filtration.

Gas chromatography - mass spectrometry (GC-MS) were measured with an Agilent 8890 gas chromatograph coupled with an Agilent 5977B mass selective detector.

High resolution mass spectrometry (HRMS): ESI(+) spectral analysis were measured with a Bruker Maxis Impact Spectrometer. MALDI spectral analysis were measured on a Bruker Autoflex maX MALDI-TOF MS spectrometer using a MTP 384 target plate polished steel BC.

NMR spectra: ^1H NMR, ^{13}C NMR and ^{31}P NMR spectra were recorded on a Bruker 400 MHz Ascend spectrometers. Chemical shifts were given as δ value (ppm) with reference to residual solvent signal of the deuterated solvent. The peak patterns are indicated as follows: s, singlet; d, doublet; t, triplet; m, multiplet; q, quartet. Multiplicities reported for ^{13}C NMR spectra were assigned using DEPT-90 and/or DEPT-135 spectra. The coupling constants, J , are reported in Hertz (Hz). The spectra were calibrated to the residual solvent signals ¹. NMR spectra were processed with MestReNova Version 14.2.1-27684.

X-ray micro-computed tomography (µ-CT) on carbon fibers was measured with an Xradia 620 Versa (ZEISS, Germany). Fiber organization and diameter were assessed by segmentation using Dragonfly Version 2021.3 (Object Research Systems Inc, Montreal, Canada).

Reaction set up: Catalytic deconstruction reactions were set up in an Argon charged glovebox using either 10 ml or 40 ml COtubes as reaction vessels sealed with PTFE/silicon seals purchased from SyTracks, or in autoclaves equipped with 30 mL PTFE inlays purchased from Parr Instrument Company. Autoclaves were pressurized using a 5000 Multi Reactor System (Parr®) using Argon (99.999% purity) or hydrogen (99.999% purity) from Air Liquide. The reactions were performed using a Teflon-coated stirring bar with dried and degassed solvents. Reactions were stirred in metal heating blocks at 800 rpm. **Warning: Glassware under pressure.**

- glass equipment should always be examined for damage to its surface, which may weaken its strength
- one must abide to all laboratory safety procedures and always work behind a shield when working with glass equipment under pressure
- COware is pressure tested to 224 psi but should under no circumstances be operated above 60 psi (5 bar)



Fig. S1. 10 ml COtube with screw cap, Teflon disc and septum.

S1.2 Polymer and Composite samples

Sources and specifications for the commercial epoxy samples, as well as references, are listed below. The stated BPA contents are approximated to the best of our knowledge, but do not present absolute values.

1) The infusion resin for wind systems **Airstone 760E/766H** was provided by Olin Corporation and has an estimated BPA content of 43 wt%. The resin was powdered using a Retsch cutting mill SM 200 with a 6 disc rotor (steel ST 52) with tungsten carbide cutting tips. For sieving, a bottom sieve (steel 1.0353, trapezoid holes 0.25 mm) was placed below the cutting mill. Further specifications and details to the material and its contents can be found in a previously published article ².

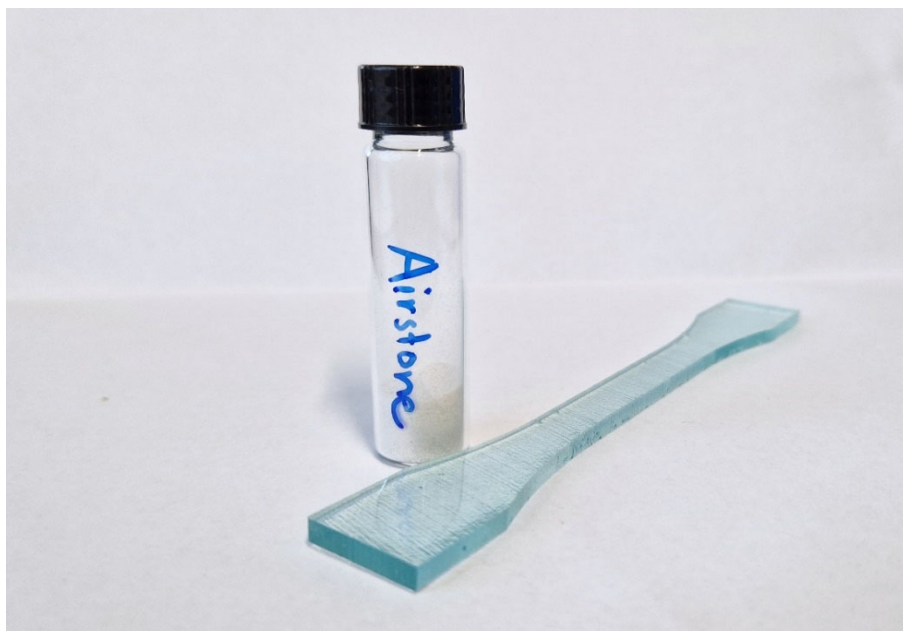


Fig. S2. Airstone infusion resin as a solid panel (right) and milled (left, in vial).

2) The “**Litestone**” resin for wind systems was provided by Olin Corporation and has an estimated BPA content of 33 wt%. Further specifications and details to the material and its contents can be found in a previously published article ².

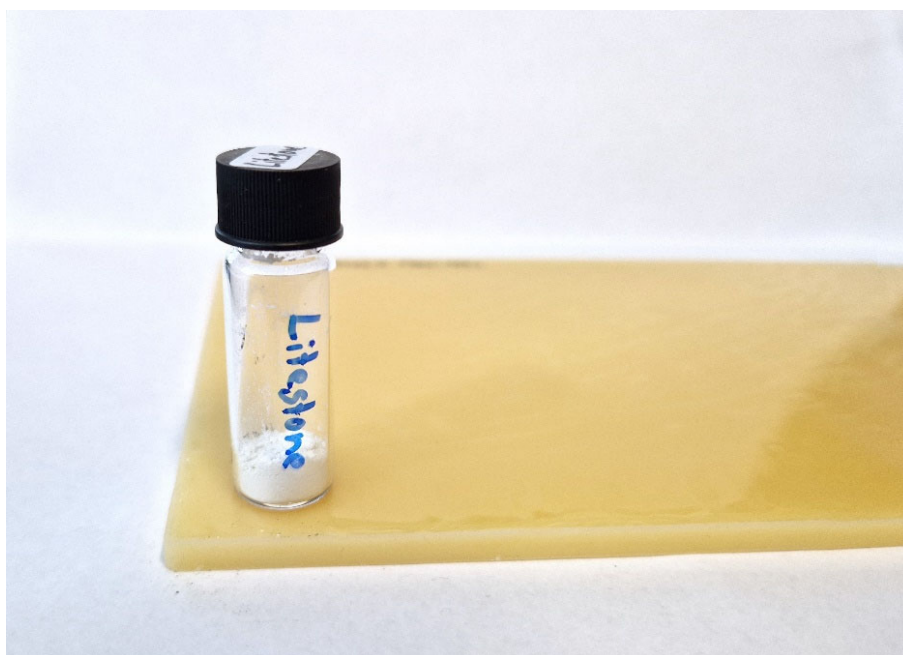


Fig. S3. Litestone infusion resin as a solid panel and milled (in vial).

3) The “**Recyclamine**” resin commercialized for wind systems was acquired from Aditya Birla Chemicals and prepared using a method published in a previous article ³. The BPA content is

unknown. In the previously published work, a maximum yield of 15 wt% BPA could be obtained through depolymerization.



Fig. S4. Recyclamine composite and the polymer powder after prior submerging in acetic acid (in vial).

4) A **product sample** of a **carbon fiber-based composite** was provided by Olin Corporation presenting as commercialized material. The composite was cut to size with a hacksaw and used without any other prior treatment.

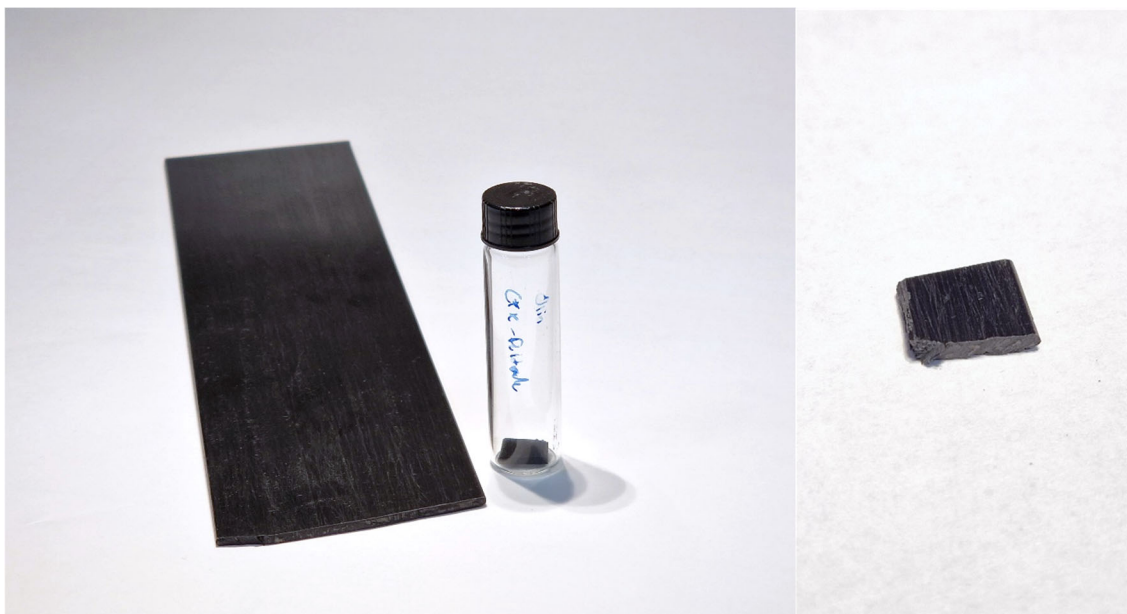


Fig. S5. A product sample of a carbon fiber-based pultrusion composite and a piece of it cut to size that was used in the deconstruction.

5) A **product sample** of a **carbon fiber-based composite** was provided by Vestas Wind Systems A/S presenting as commercialized material used in the core of wind turbine blades. The composite was cut to size with a hacksaw and used without any other prior treatment.

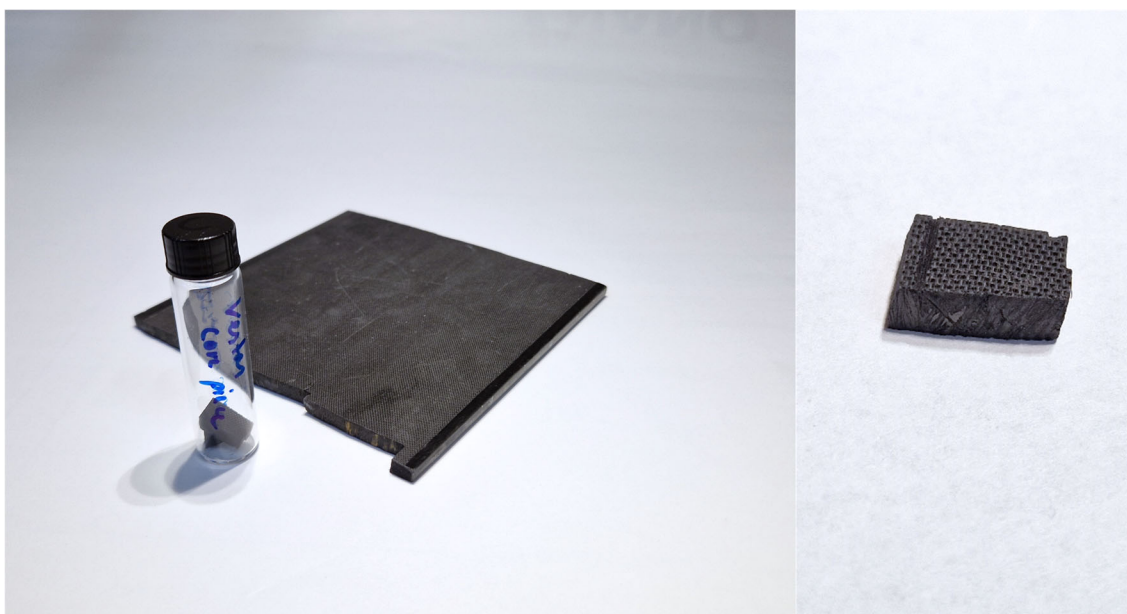


Fig. S6. A product sample of a carbon fiber-based pultrusion composite from the core of a wind turbine blade and a piece of it cut to size that was used in the deconstruction.

S2. Optimization

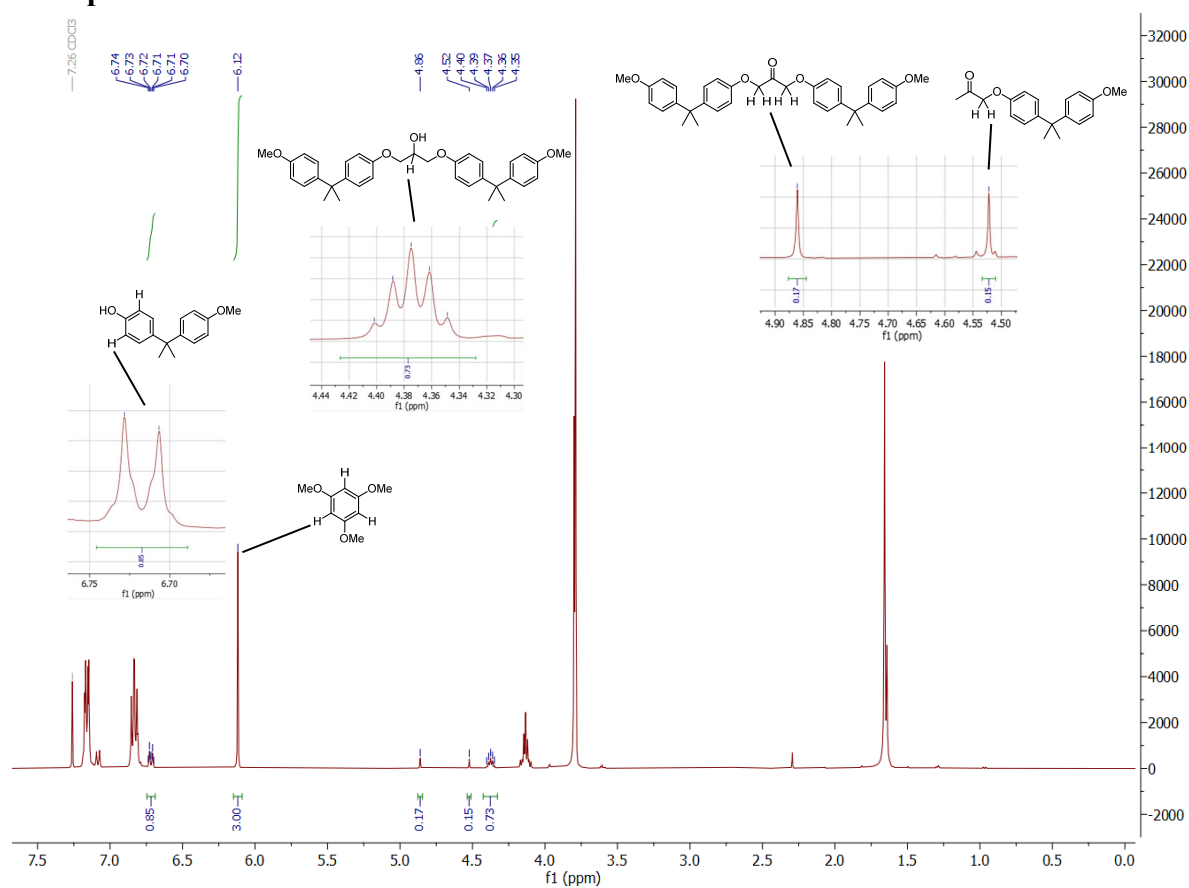


Fig. S7. ¹H NMR spectrum of catalytic deconstruction of model 1 using catalyst **2b**. Selected peaks of MeBPA, 1,3,5-trimethoxybenzene, model substrate and intermediate ketone products are highlighted.

S2.1 Methodologies Reported for C–O Bond Scission Lignin

Initially, methodologies for bond scissions in β -O-4 motif in lignin ^{4,5} were considered as an inspiration for C–O bond cleavage on epoxy models (**Fig. S8**). Here, mechanism of the cleavage is proposed to proceed *via* dehydrogenation of the alcohol with a subsequent activation of the C–O bond through a nucleophilic substitution type reaction of the rhodium hydride species ⁶.

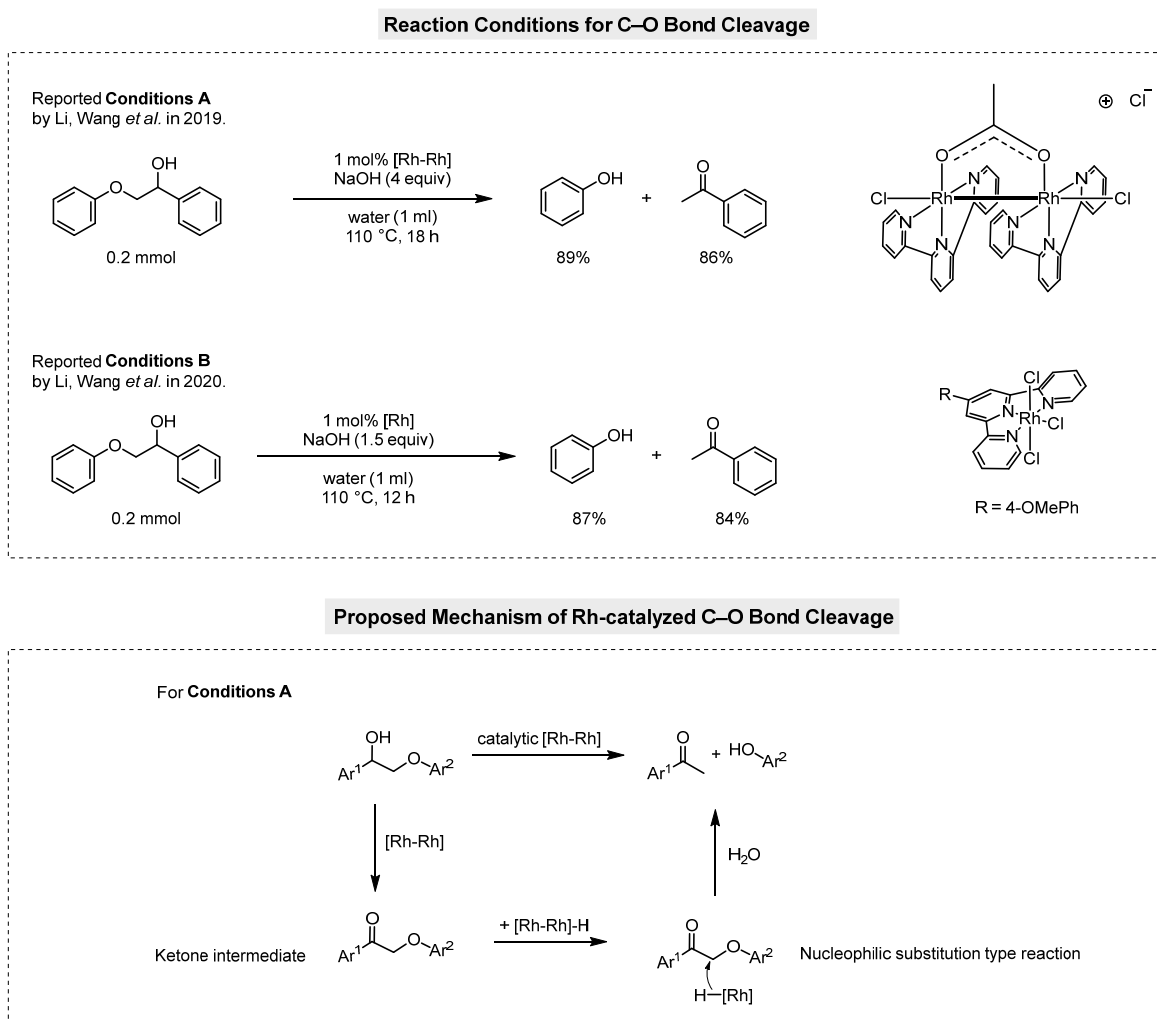


Fig. S8. Rhodium-catalyzed C–O bond cleavage reported for lignin model substrates and proposed mechanism.

S2.2 Screening of Ligands

Due to better tolerance towards lower temperatures, the mononuclear complexes from **Conditions B** were chosen for a ligand screening on epoxy model 1 and model 2. The screening was conducted with water as solvent at 140 °C, 3 mol% catalyst loading and a reaction time of 16 h.

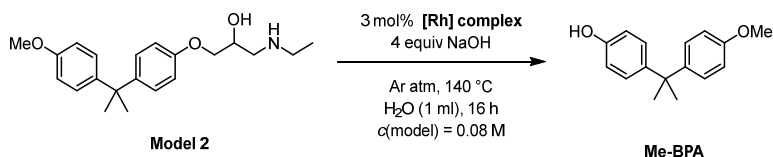
Table S2. Screening of a selection of terpyridine based ligands using model 1. Consumption and yields were determined by ¹H NMR spectroscopy with 1,3,5-trimethoxybenzene as internal standard.

Entry	Complex (Variation)	Consumption	MeBPA
1	2a	10%	6%
2	2b	27%	21%
3	2c	44%	26%
4	2d	>0%	Trace amounts
5	2e	>0%	Trace amounts
6	2f	0%	0%
7	2g	>0%	3%
8	2h	>0%	7%
9	2i	>0%	Trace amounts

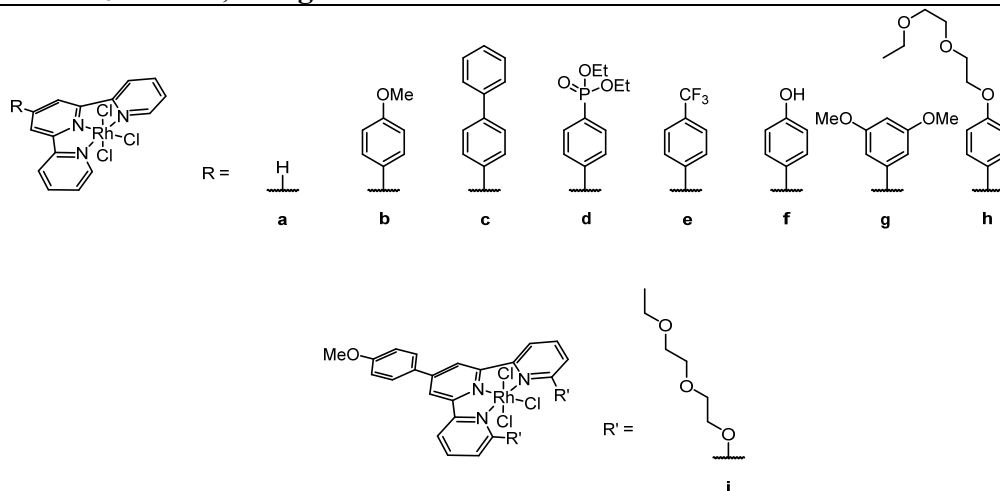
Using complex **2a** with the simple terpyridine ligand under standard conditions (entry 1) resulted in a low consumption of 10% and a corresponding MeBPA yield of 6%. Complexes **2b** and **2c** (entry 2 and 3) demonstrated improved activity, achieving yields of 21% and 26%, respectively, with a notably higher consumption of the starting material using **2c**. Complexes **2d** and **2e** (entries 4 and 5) showed minimal activity, with only trace amounts of MeBPA formed. Notably, complex **2f** (entry 6) was completely inactive, resulting in no consumption or product formation. Complex **2g** (entry 7) also exhibited limited reactivity, with only 3% MeBPA yield. Complex **2h** (entry 8)

performed slightly better, yielding 7% MeBPA. Complex **2i** (entry 9) resulted only in trace product formation.

Table S3. Screening of a selection of terpyridine based ligands using model 2. Consumption and yields were determined by ^1H NMR spectroscopy with 1,3,5-trimethoxybenzene as internal standard.



Entry	Complex (Variation)	Consumption	MeBPA
1	2a	Not determinable	46%
2	2b	>99%	>99%
3	2c	>99%	>99%
4	2d	Not determinable	61%
5	2e	48%	43%
6	2f	24%	24%
7	2g	70%	73%
8	2h	Not determinable	50%
9	2i	34%	20%
10	RhCl₃ · 3 H₂O, no ligand	Not determinable	17%



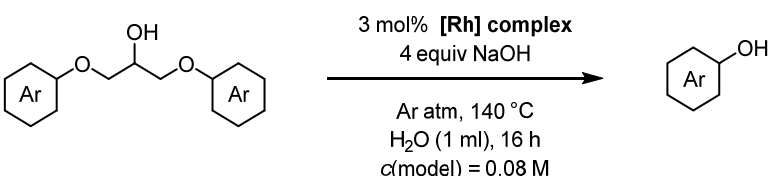
The average yields of the catalysis increased significantly using model 2 instead of model 1. One possible reason is that in this model substrate, one alcohol moiety corresponds to only one C–O bond scission, rather than two C–O bonds, as in model 1. However, we also observed that model 2 seemed to be better soluble in water, possibly because of the amine moiety, which could lead to a higher reaction surface and thus better yield. The simple terpyridine complex **2a** yielded a moderate 46% of MeBPA (entry 1). Yields improved drastically by employing catalyst **2b**, which entails an electron donating *para*-methoxy phenyl moiety, and **2c** under standard conditions (entries 2 and 3). In contrast, a catalyst with an electron-withdrawing ligand (**2e**) yielded only 43% of MeBPA (entry 5). Since most of the terpyridine-rhodium(III) trichloride complexes are also poorly water-soluble, we aimed at investigating the influence of the solubility of the complexes.

Therefore, we modified the terpyridine ligands to enhance solubility, e.g. through introducing phosphonates (**2d**), or hydroxy groups (**2f**). In the presence of 4 equiv of NaOH, the ligand of complex **2f** is likely to deprotonate and the complex dissolved quickly in the reaction mixture, however, the reaction resulted in poor results (entry 6). After a few hours of reaction time, the reaction mixture had a noticeably strong grey color, which could indicate the formation of nanoparticles, likely due to decomposition of the complex because of the strong electron-donating nature of the deprotonated ligand. Complex **2d** also showed increased solubility in water, but only provided modest yields (entry 4). The dimethoxyphenyl terpyridine complex **2g** showed good yields of 73% (entry 7). Introducing a polyether chain at the terminal phenyl substituent position for enhanced solubility did not result in enhanced yields (**2h**, entry 8), despite having similar electronic properties as the best performing complex **2b**. Employing complex **2i**, where the phenyl substituent on the outer terpyridine rings were replaced with polyether chains, also resulted in low yields of MeBPA (entry 10). Using **RhCl₃·3H₂O** without any ligand at standard conditions yielded only 17% (entry 11).

In the ligand screening, complexes **2b** and **2c** both gave quantitative yields under standard conditions. The ligand of complex **2b** can be synthesized in a simple one-pot procedure using 2-acetylpyridine and 4-anisaldehyde, which is cheap and readily available, and was thus found suitable as a standard catalyst for studies on polymer samples.

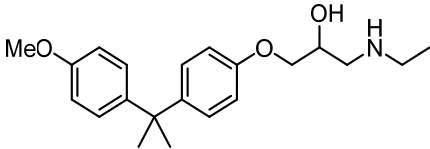
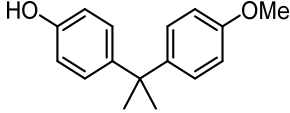
S2.3 Screening of Reaction Conditions

Table S4. Screening of varying reaction conditions using model 1 and model S. Consumption and yields were determined by ¹H NMR spectroscopy with 1,3,5-trimethoxybenzene as internal standard.

				
Model substrate Model 1: Ar = Me-BPA Model S: Ar = Ph		Phenol yield Model 1: Ar = Me-BPA Model S: Ar = Ph		
Entry	Model substrate	Complex (Variation)	Consumption	MeBPA
1	Model 1	1 (160 °C, 0.5 ml water)	72%	43%
2	Model 1	1 (160 °C, 1 equiv NaOH)	33%	19%
3	Model 1	1 (160 °C, 0.1 equiv NaOH)	Not determinable	6%
4	Model 1	2a (160 °C)	38%	25%
5	Model 1	2a (160 °C, under air)	49%	25%
6	Model 1	2b (10 equiv NaOH)	45%	20%
7	Model 1	2b (5 days)	78%	55%
8	Model 1	2b (6 mol%)	84%	56%
9	Model 1	2b (1 atm H ₂)	>0%	0%
10	Model S	2b	84%	55%

As shown in Table S1, the dinuclear rhodium complex **1** requires a temperature of 160 °C to operate efficiently. Using the dimer complex **1** on model 1 and reducing the solvent volume by half resulted in a decrease in yield, despite the higher base and catalyst concentration (entry 1). Reducing the base amount to 1 equivalent led to a drop in yield to 19%, and further reduction to 10 mol% resulted in only 6% yield (entries 2 and 3). At 160 °C, complex **2a** produced a 25% yield of MeBPA (entry 4). Interestingly, conducting the reaction under air did not reduce yield when using model 1 (entry 5). With the most effective catalyst from the ligand screening, **2b**, the yield did not improve when increasing NaOH from 4 to 10 equivalents, even though this was intended to explore base-mediated bond cleavage (entry 6). Stirring the reaction for 5 days resulted in a 78% conversion and a yield of 55% (entry 7). Doubling the catalyst loading to 6% did not double the yield but nearly tripled it (entry 8), suggesting a possible dinuclear reaction pathway, which is consistent with later mechanistic studies. Finally, conducting the catalysis under 1 atm of H₂ completely deactivated the reaction (entry 9). Since *in silico* studies were performed on model S in order to save on computational costs, we synthesized the substrate and reacted it with catalyst **2b** under standard conditions. The reaction reached 84% conversion and a 55% yield, outperforming model 1, most likely due to the better water-solubility of the substrate (entry 10).

Table S5. Screening of varying reaction conditions using model 2. Consumption and yields were determined by ¹H NMR spectroscopy with 1,3,5-trimethoxybenzene as internal standard.

		3 mol% [Rh] complex 4 equiv NaOH Ar atm, 140 °C H ₂ O (1 ml), 16 h c(model) = 0.08 M			
model 2				Me-BPA	
Entry	Complex (Variation)	Consumption	MeBPA		
1	1 (160 °C)	>99%	>99%		
2	1 (160 °C, under air)	76%	68%		
3	1	Not determinable	42%		
4	2b	>99%	>99%		
5	2b (120 °C)	63%	54%		
6	2b (120 °C, 48 h)	>99%	>99%		

Reacting model 2 with the dinuclear catalyst **1** at 160 °C (entry 10) resulted in excellent yields, with quantitative conversion and yield. Performing the same reaction under air (entry 11) led to a moderate reduction in efficiency, giving 68% MeBPA yield. Lowering the temperature to 140 °C with catalyst **1** (entry 12) caused a more pronounced drop, where yield decreased to 42%. For complex **2b**, which features a slightly electron donating ligand, quantitative yields were achieved at 140 °C (entry 4). Lowering the temperature to 120 °C was tolerated when increasing the reaction time (entries 3 and 4). This gave indications for reaction barriers and is discussed in **Chapter S5**.

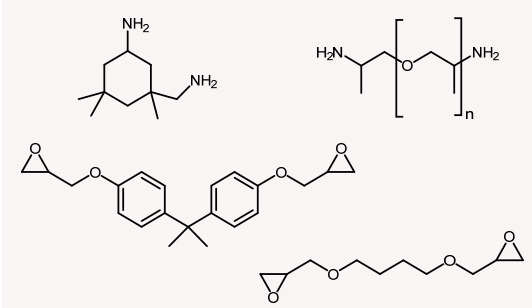
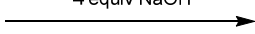
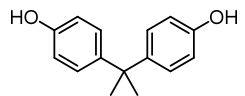
S2.4 Screening of Conditions on Airstone 760E/766H

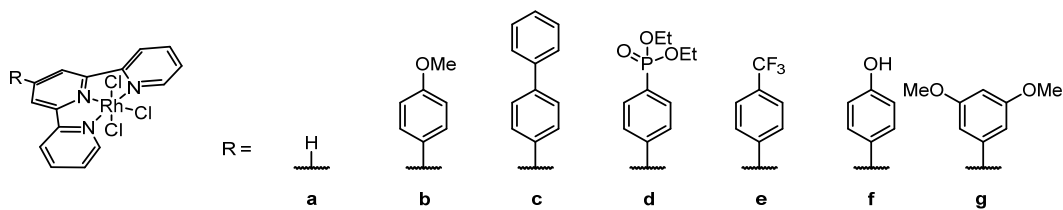
For the optimization on the polymer, 100 mg (approx. 43 mg BPA, 0.19 mmol, 1 equiv) of finely powdered epoxy resin and 3 mol% of Rh-terpyridine complex (5.6 μmol, 0.03 equiv) were given

into a 10 ml COtube (from SyTracks), or in a 45 mL high pressure autoclave using a 30 mL PTFE inlay purchased from Parr Instrument Company. In an Argon-charged glovebox, 30.2 mg of sodium hydroxide (0.75 mmol, 4 equiv) and 1.5 ml of water were added, and the reaction vessel sealed. Outside of the glovebox, the reaction mixture was stirred at 800 rpm in an aluminum block at 140 °C for 24 h. The reaction mixture was then allowed to cool to room temperature and 1.5 ml of 1M HCl was added. The water phase was extracted with ethyl acetate (4 × 8 mL). Celite was added and the solvent removed *in vacuo*. The resulting mixture was loaded onto a silica gel charged column. Automated flash column chromatography using a gradient from heptane to 1/4 heptane/ethyl acetate afforded bisphenol A.

Component specifications of Airstone 760E/766H and Limestone 3100E/3102H can be found in a previously published article ². The “Recyclamine” resin by Aditya Birla Chemicals was prepared after a procedure published in previous work ³.

Table S6. Optimizations on powdered Airstone 760E/766H.

<div style="text-align: center;"> <p>Airstone 760E/766H</p>  </div>			
<p>3 mol% [Rh] complex 4 equiv NaOH</p> <p>Ar atm, 140 °C 1.5 ml H₂O, 24 h</p> 			
 <p>BPA</p>			
Entry	Catalyst	Variations	Recovered BPA (yield)
1	None	T = 160 °C	0 mg (0 %)
2	1a	None	6.7 mg (16%)
3	1a	T = 160 °C	13.2 mg (31%)
4	2b	None	11.7 mg (27%)
5	2b	62 h	22.0 mg (51%)
6	2b	3 Equiv <i>i</i> PrOH	2.1 mg (5%)
7	2c	None	6.9 mg (16%)
8	2d	None	1.3 mg (3%)
9	2e	None	9.3 mg (22%)
10	2g	None	14.7 mg (34%)
11	2b	In autoclave, 2 ml water	20.2 mg (47%)
12	2b	In autoclave, 40 bar Ar, 2 ml water	27.7 mg (64%)
13	2b	In autoclave, 40 bar H ₂ , 2 ml water	Trace amounts
14	2b	In autoclave, 7 bar air pressure, 2 ml water	Trace amounts
15	2b	In autoclave, 2 ml water, 3.4 equiv NaOH (0.32 M)	14.8 mg (34%)
16	2b	In autoclave, 2 ml water, 5.35 equiv NaOH (0.5 M)	19.0 mg (44%)
17	2b	500 mg Airstone, in autoclave, 40 bar Ar, 7.5 ml water, 1 mol% 2b , 3 d	95.4 mg (44%)

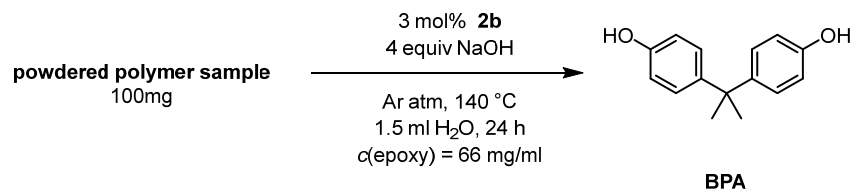


Without the catalyst, no BPA could be detected after the reaction (entry 1). Both the dinuclear rhodium catalyst **1a** and the mononuclear catalyst **2b** achieved satisfying yields (entries 2-4). However, as shown before on model substrates, the dinuclear catalyst needed a higher temperature than the mononuclear catalyst for a similar yield. Prolonging the reaction time to 62 h increased the yield significantly to 51% and proved that the catalyst is still active after 24 h (entry 5). When adding isopropanol, the yield decreased to only 5% (entry 6). Varying the ligand of the mononuclear catalyst afforded yields between 3-34% (entries 7-10). Even without additional pressure, yields could be improved using autoclaves equipped with PTFE inlays (entry 11). Due to the larger reactor size, an increased solvent amount of 2 ml had to be used in autoclaves. In the glass reaction vessels, we observed that when resin particles were washed up the vessel wall due to stirring, they tended to stick on the glass, thus preventing contact with the catalyst containing solution. We surmise that due to the lower polarity of the inlay material, this issue is resolved when using autoclaves. Charging the autoclaves with argon pressure could further improve the yield to 64% (entry 12). Employing hydrogen pressure, as well as pressured air, however, deactivated the reaction (entries 13 and 14). Decreasing the base concentration to the one used on model substrate (0.32 M), as well as increasing the concentration to 0.5 M, as used for Airstone in glass COtubes, did both lead to a slight decrease in yield (entries 15 and 16). Finally, the reaction was performed at 500 mg scale with a catalyst loading of 1 mol% **2b** and 7.5 ml of water as solvent. After three days of reaction time, 95.4 mg (44%) of BPA could be isolated (entry 17).

S2.5 Deconstruction of other Commercial Wind Energy Epoxy Resins

100 mg of finely powdered epoxy resin and 3 mol% of Rh-terpyridine complex **2b** were given into a 10 ml COtube (from SyTracks), or in a 45 mL high pressure autoclave using a 30 mL PTFE inlay purchased from Parr Instrument Company. In an Argon-charged glovebox, 4 equiv of sodium hydroxide and 1.5 ml of water were added, and the reaction vessel sealed. Outside of the glovebox, the reaction mixture was stirred at 800 rpm in an aluminum block at 140 °C for 24 h. The reaction mixture was then allowed to cool to room temperature and 1.5 ml of 1M HCl was added. The water phase was extracted with ethyl acetate (4 × 8 mL). Celite was added and the solvent removed *in vacuo*. The resulting mixture was loaded onto a silica gel charged column. Automated flash column chromatography using a gradient from heptane to 1/4 heptane/ethyl acetate afforded bisphenol A as a white, crystalline solid.

“Limestone” is an anhydride-cured resin for wind systems has an estimated BPA content of 33 wt%². The BPA content of the “Recylcamine” resin is unknown, however, due to the similar application, it was assumed to be similar to the one in Airstone, and thus estimated as 43 wt%.

Table S7. Deconstruction of other commercial wind energy epoxy resins.

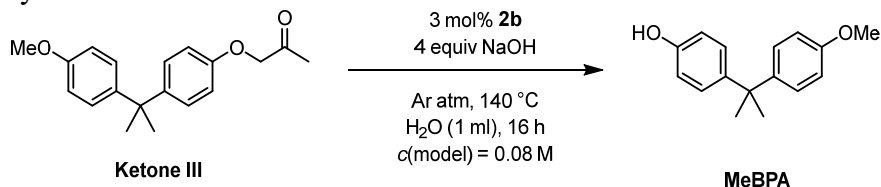
Entry	Resin	Variations	Recovered BPA (yield)
1	Litestone	No catalyst	0 mg (0%)
2	Litestone	None	22.9 mg (69%)
3	Litestone	In autoclave, 42 bar Argon pressure, 2 ml water	30.7 mg (93%)
4	Recyclamine	No catalyst	0 mg (0%)
5	Recyclamine	None	17.4 mg (17 wt%)
6	Recyclamine	In autoclave, 42 bar Argon pressure, 2 ml water	35.7 mg (36 wt%)

Exposing Litestone to the reaction conditions without adding the catalyst did not result in any BPA yield (entry 1). When adding 3 mol% of **2b** (with respect to the BPA content), 22.9 mg (69%) BPA could be isolated (entry 2). The yield could further be improved by performing the reaction in an autoclave under 42 bar of Argon pressure, yielding 30.7 mg (93%) of BPA. Without the catalyst, no BPA could be detected after the reaction of the Recyclamine resin (entry 6). Relative to the assumed BPA content of 43 wt%, 3 mol% of **2b** were added to yield 17.4 mg (17 wt%) of BPA (entry 5). Performing the reaction under Argon pressure resulted in improved yields of 35.7 mg (36 wt%) (entry 6). In our previously published work utilizing a base mediated cleavage in toluene at high temperatures, a maximum BPA yield of 15 wt% could be achieved ³.

S3. Mechanistic Investigation

S3.1 Deconstruction of Ketone based Model Substrates

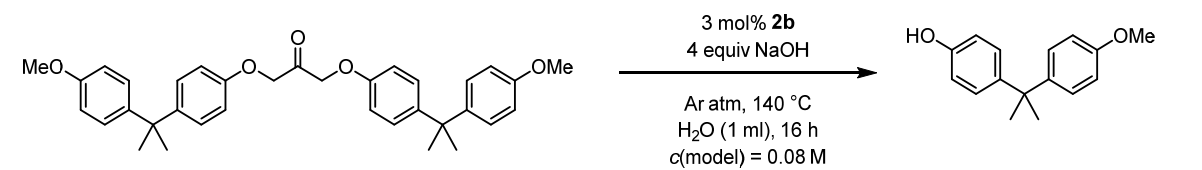
Table S8. Deconstruction of ketone III. Yields were determined by ^1H NMR spectroscopy with 1,3,5-trimethoxybenzene as internal standard.



Entry	Additive or variation	Yield MeBPA
1	No catalyst	0%
2	None	35%
3	160 °C	45%
4	1 equiv <i>i</i> PrOH	40%
5	3 equiv <i>i</i> PrOH	51%
6	3 equiv <i>i</i> PrOH, 1 equiv NaOAc	38%
7	1.5 mol% Dinuclear complex 2k instead of 2b	36%

Without any obvious hydrogen source, ketone III was expected to not be susceptible to catalytic C–O bond cleavage. Surprisingly, catalytic reactivity was observed when exposing ketone III to the standard catalytic conditions at both 160 °C and 140 °C. In contrast to the deconstruction to model 2, no sudden color change of the reaction mixture could be observed during the first minutes of the reaction. Only after approximately 2 h reaction time the mixture turned dark. In contrast to the catalysis on model 1, isopropanol does not hinder the reaction but increases the yield of MeBPA. (entries 4-6). Dinuclear complex **2k** resulted in similar yields compared to **2b** (entry 7). We surmise that through the dehydrogenation of isopropanol, the initial rhodium(III) complex can be reduced to a species that eventually enters the catalytic cycle. However, since the reaction also works without isopropanol, we presume that there must be pathways for an auto-reduction of the rhodium complexes which do not involve an alcohol.

Table S9. Deconstruction of Ketone **I**. Yields were determined by ^1H NMR spectroscopy with 1,3,5-trimethoxybenzene as internal standard.

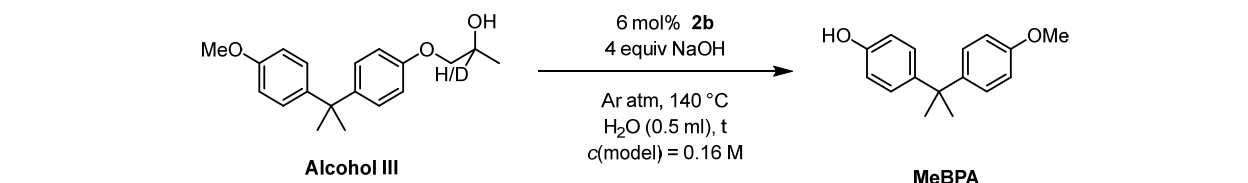
		
Entry	Additive or variation	Yield MeBPA
1	No catalyst	12%
2	None	63%
3	3 equiv <i>i</i> PrOH	67%

Reacting ketone **I** without addition of the catalyst resulted in a yield of 12% (entry 1). Employing standard catalytic conditions, the yield drastically improved to 63% (entry 2). Addition of 3 equiv isopropanol as an external hydrogen source could increase the yield to 67% (entry 3).

S3.2 Kinetic Isotope Effect Studies

Model substrate **alcohol III** was chosen to determine a kinetic isotope effect. The substrate is only susceptible to one dehydrogenation and one C–O bond cleavage.

Table S10. Kinetic isotope effect of the deconstruction of model **2**. Yields were determined by ^1H NMR spectroscopy with 1,3,5-trimethoxybenzene as internal standard.

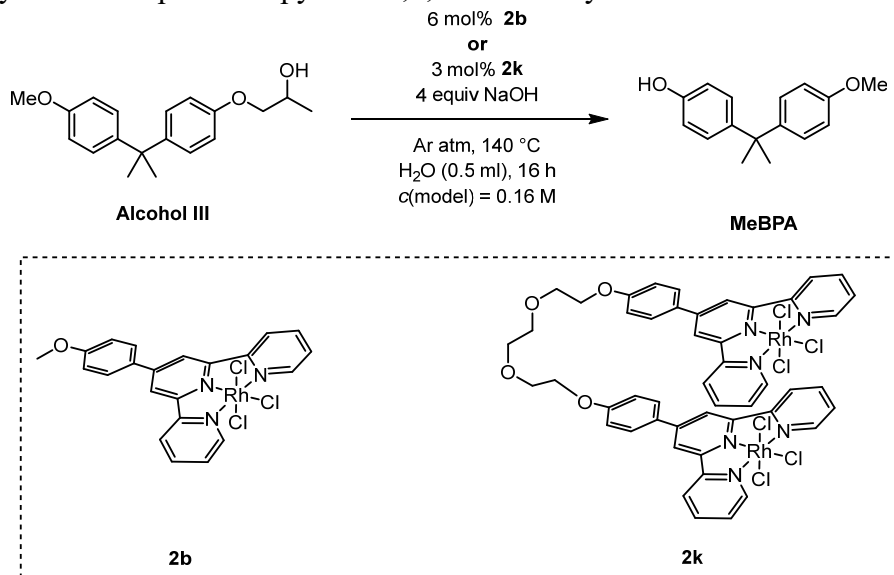
				
Entry	Time	Yield MeBPA Alcohol III	Yield MeBPA Alcohol III- <i>d</i>	KIE
1	1 h	13%	7%	1.8
2	2 h	20%	9%	2.2
3	3 h	24%	12%	2.0
4	6 h	33%	22%	1.5
5	16 h	37%	31%	1.2

S3.3 Probing Mononuclear and Dinuclear Complexes

The nearly threefold improvement by reaction yields of the deconstruction of model **1** using catalyst **2b** at 3 mol%, or 6 mol%, respectively (see **Table S3** entry 8), hinted towards a dinuclear reaction pathway with respect to the catalyst. To investigate, whether the mechanism proceeds via dinuclear transition states, or intermediates, rhodium bisterpyridine complex **2k** was synthesized. While having similar electronic properties as the benchmark catalyst **2b**, the polyether chain

connecting two terpyridines can keep two metal centers in proximity and possibly speed up initial rates of the reaction.

Table S11. Deconstruction of alcohol **III** with a mono- and bisterpyridine catalyst. Yields were determined by ^1H NMR spectroscopy with 1,3,5-trimethoxybenzene as internal standard.



Entry	Time	Yield MeBPA 2b	Yield MeBPA 2k
1	1 h	13%	17%
2	2 h	19%	25%
3	3 h	24%	31%
4	6 h	33%	46%

Complex **2b** was used at a double concentration of 6 mol% compared to complex **2k** (3 mol%) to obtain the same concentration of rhodium centers in the reaction mixture. Already after 1 h reaction time, a small difference in yield is noticeable (entry 1), and the difference continues to grow with increasing time (entries 2-4).

S3.4 Testing for Hydrogen Peroxide Formation

This subchapter only covers the qualitative detection of hydrogen peroxide under the catalytic conditions. Computational studies investigating peroxide formation can be found in chapter S5.4. Cyclovoltammetric investigations about C–O bond cleavage in ketone III without additional hydrogen source can be found in **Chapter S4.4**.

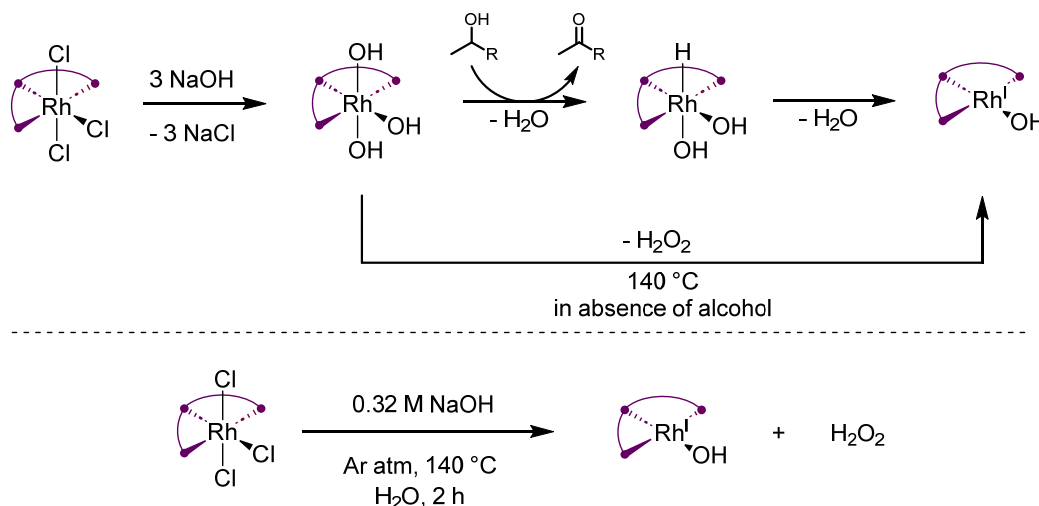


Fig. S9. Scheme of possible catalyst activation through peroxide elimination.

Because of the catalytic cleavage of ketone III, we surmised that the initial Rh^{III} -complex can be reduced without the presence of an alcohol source (**Fig. S9**). To probe the elimination of hydrogen peroxide, we used a **MQuant®** hydrogen peroxide test kit commercialized by Sigma Aldrich with a sensitivity of up to 0.5 mg/l (**Fig. S10**). We assumed high sensitivities to be necessary because of the low concentration of the catalyst, and the rapid decomposition of hydrogen peroxide to oxygen and water under reaction conditions. 1.32 mg rhodium complex **2b** was stirred at catalytic conditions (0.32 M NaOH in H_2O , 140°C , Ar atmosphere). After around 2 h, the solution started to turn from yellow to deep black. The reaction vessel was then opened (a: under air, b: in an argon filled glovebox) and neutralized using 4 M HCl to pH = 7. Pictures were taken immediately after the peroxide test was then held into the neutralized reaction mixture. As a third experiment, two peroxide tests were mounted in a two-chamber reactor with an integrated reflux condenser (c). The reaction was set up and sealed in an argon filled glovebox. In chamber A, **2b** was stirred under catalytic conditions. After 2 h, a blue color on the peroxide tests in both the connecting bridge (d) and in chamber B (e) was observed. Repeating the reaction without adding the rhodium catalyst did not result in a color change.

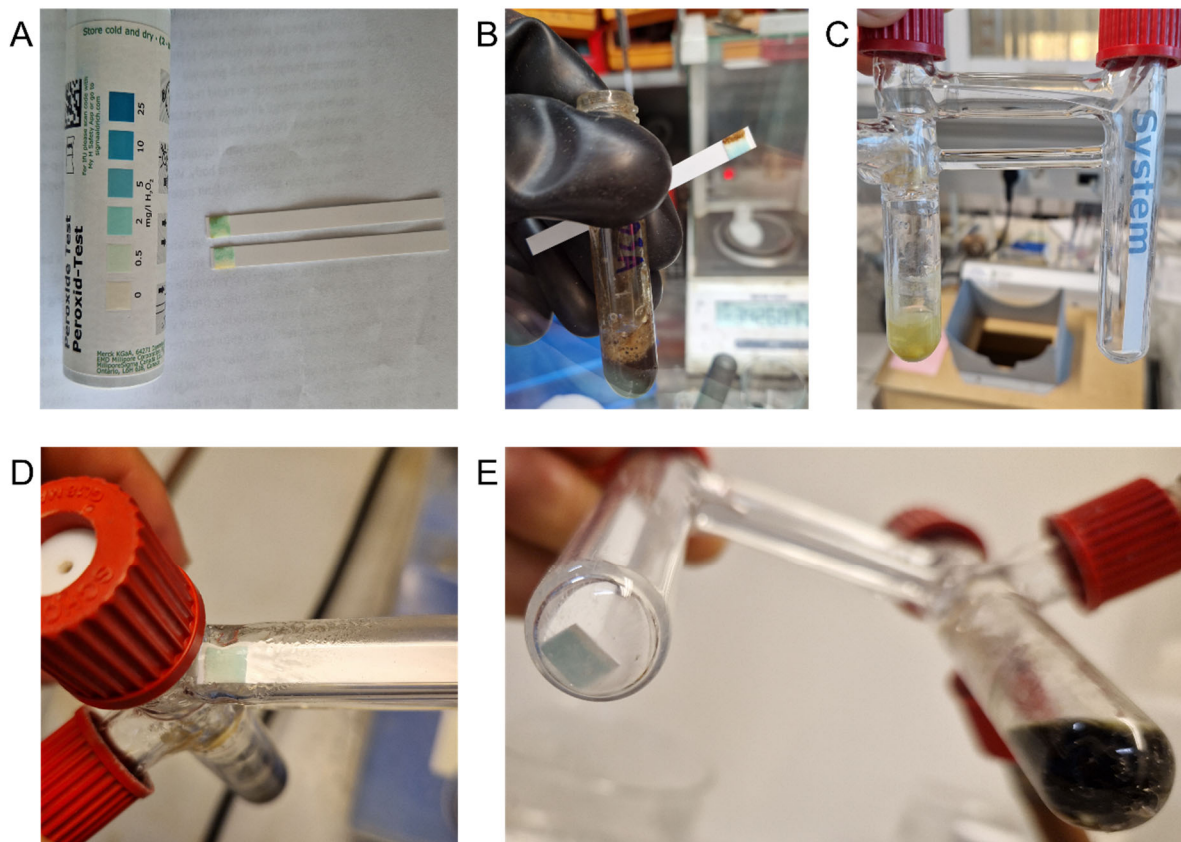


Fig. S10. (A) Hydrogen peroxide test taken from reaction opened under air. (B) Hydrogen peroxide test taken from reaction opened inside an argon charged glovebox. (C) Hydrogen peroxide test set-up in a two-chamber equipped with a refluxing system before the reaction. Catalyst **2b** is suspended in aqueous 0.32 M NaOH (left chamber) in an argon charged glovebox equipped with peroxide tests in bridge and right chamber. (D) Positive hydrogen peroxide test in connecting bridge. (E) Positive hydrogen peroxide test in second chamber.

S3.5 Reduction of terpy*-Rh(III) to terpy*-Rh(I) via β hydride elimination

In an argon-charged glovebox, in a J Young NMR tube, 6.10 mg (10.0 μmol , 1.0 equiv) of terpy*-Rh-Cl₃ was suspended in 0.5 ml of THF-*d*₈. 4.00 mg (25.0 μmol , 1.0 equiv) of potassium 2-phenylethanolate was added, the mixture shaken. ¹H NMR spectra were measured before and after addition of the alcoholate (**Fig. S11**).

Upon addition of the alcoholate, the greenish suspension turned deep blue to black in color and became a homogenous solution (as far as visible). After 5 min at room temperature, ¹H NMR spectroscopy revealed full conversion of the starting complex to terpy*-Rh-Cl as well as the formation of acetophenone.

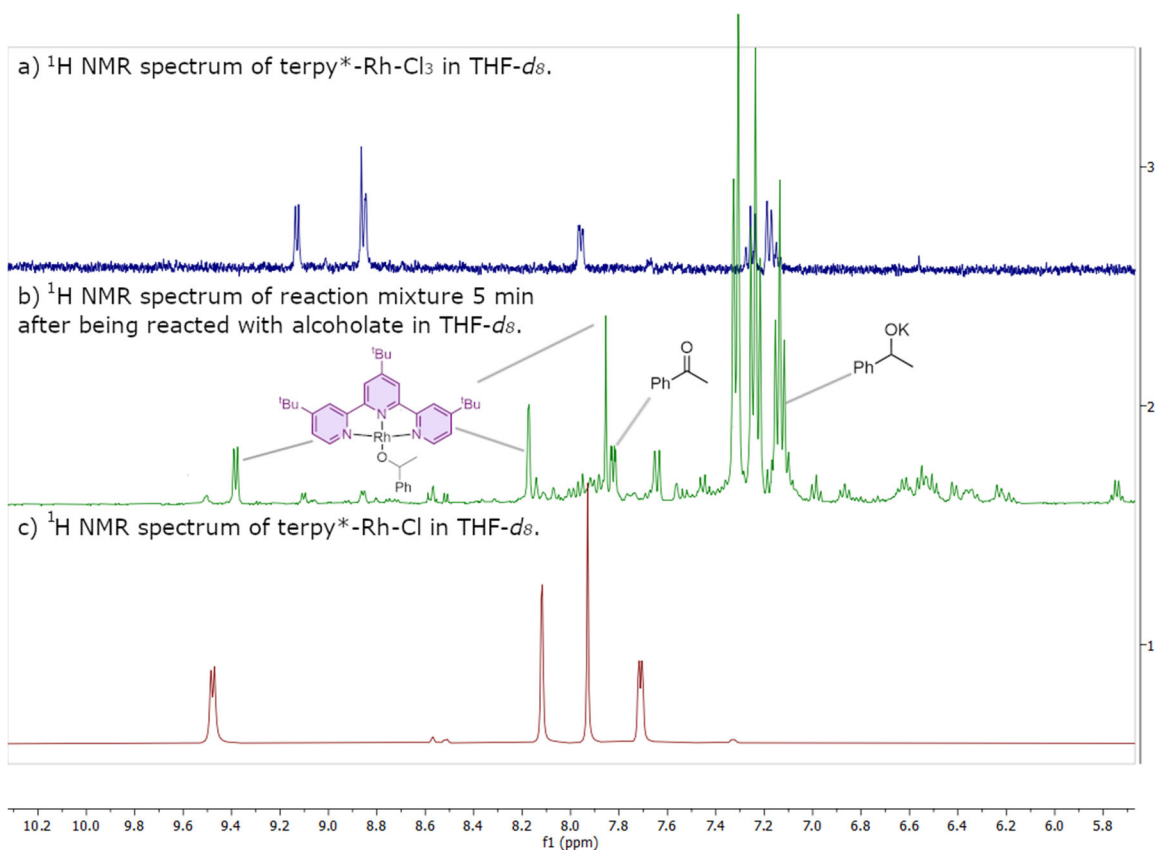


Fig. S11. ¹H NMR experiment on reduction of terpy*-Rh(III) to terpy*-Rh(I) in THF-*d*₈. (A) Reference spectrum of terpy*-Rh-Cl₃. (B) Reaction of terpy*-Rh-Cl₃ with alcoholate after 5 min at rt. (C) Reference spectrum of terpy*-Rh-Cl.

S3.6 C–O Bond Scission on α -Phenoxyketones by terpy-Rh(0)

In an argon-charged glovebox, in an 8 ml screw cap vial, 2.7 mg (5.0 μmol , 1.0 equiv) of terpy*-Rh-Cl was dissolved in 0.3 ml of THF- d_8 . 1.35 mg (10 μmol , 2.0 equiv) of KC_8 was added and the mixture stirred at room temperature for 15 min. Over the course of this time, the blue hue of the solution vanished. The mixture was filtered into a J Young NMR tube containing 1.49 mg (50.0 nmol, 1.0 equiv) of Ketone III over a plug of Celite (pipette), and the residue transferred using another 0.2 ml of THF- d_8 . The mixture was heated to 140 $^\circ\text{C}$ for 1 h, while being monitored using ^1H NMR spectroscopy (**Fig. S12**).

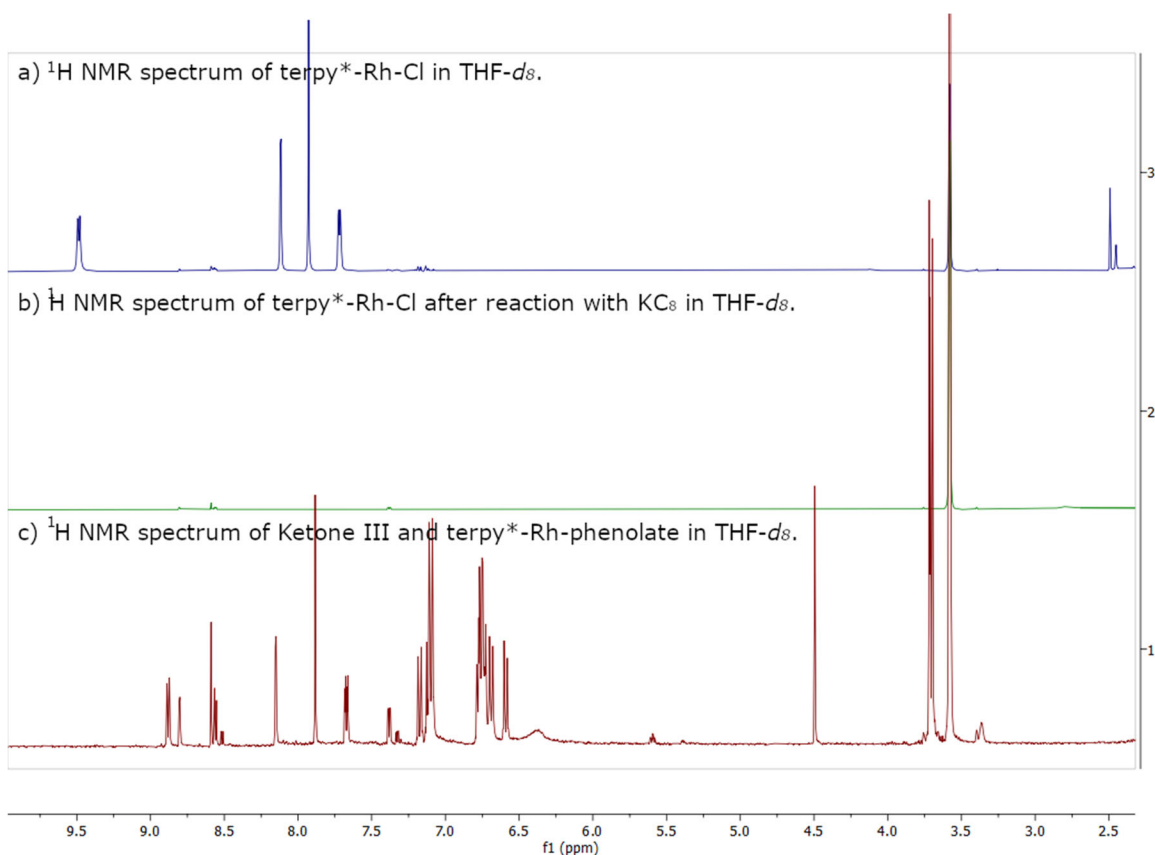
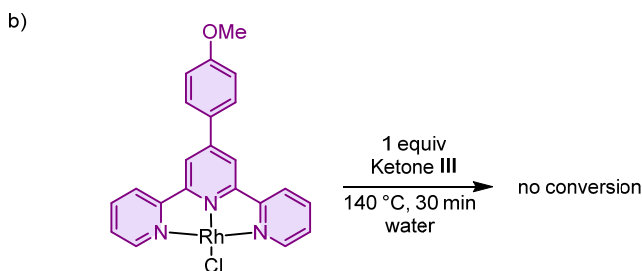
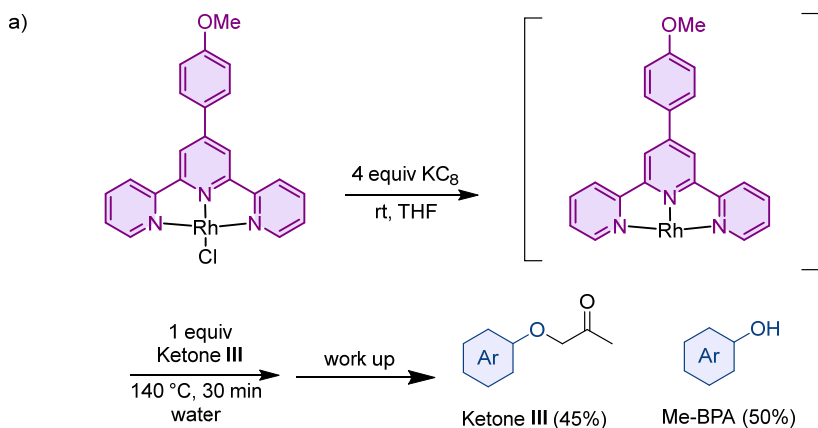


Fig. S12. ^1H NMR experiment on reaction of terpy*-Rh(0) with Ketone III in THF- d_8 . (A) Reference spectrum of terpy*-Rh-Cl. (B) Reference spectrum of terpy*-Rh-Cl reduced with KC_8 . (C) Mixture of Ketone III and terpy*-Rh-phenolate obtained after 1 h reaction time.

In an argon-charged glovebox, in an 8 ml screw cap vial, 7.64 mg (16.0 μmol , 1.0 equiv) of $\text{terpy}^{\text{OMe}}\text{-Rh-Cl}$ was dissolved in 0.3 ml of THF. 6.49 mg (48.0 μmol , 4.0 equiv) of KC_8 was added and the mixture stirred at room temperature for 15 min. Over the course of this time, the blue hue of the solution vanished. The mixture was filtered into a 10 ml pressure tube containing over a plug of Celite (pipette), and the residue transferred using another 0.2 ml of $\text{THF-}d_8$. The solvent was removed *in vacuo*, and then 4.78 mg (16.0 μmol , 1.0 equiv) of ketone III and 0.5 ml of water were added. The mixture was stirred for 30 min at 140 $^\circ\text{C}$. Then, the organic products were extracted with two times 0.3 ml of CDCl_3 , which was united, filtered through a MgSO_4 plug. ^1H NMR spectroscopy revealed approximately 45% of Ketone III remaining and 50% of MeBPA (Fig. S13 (A)).

A control experiments was conducted. 7.64 mg (16.0 μmol , 1.0 equiv) of $\text{terpy}^{\text{OMe}}\text{-Rh-Cl}$, 4.78 mg (16.0 μmol , 1.0 equiv) of ketone III and 0.5 ml of water were given into a 10 ml pressure vial. The mixture was stirred for 30 min at 140 $^\circ\text{C}$. Then, the organic products were extracted with two times 0.3 ml of CDCl_3 , which was united, filtered through a MgSO_4 plug. ^1H NMR spectroscopy revealed no conversion (Fig. S13 (B)).



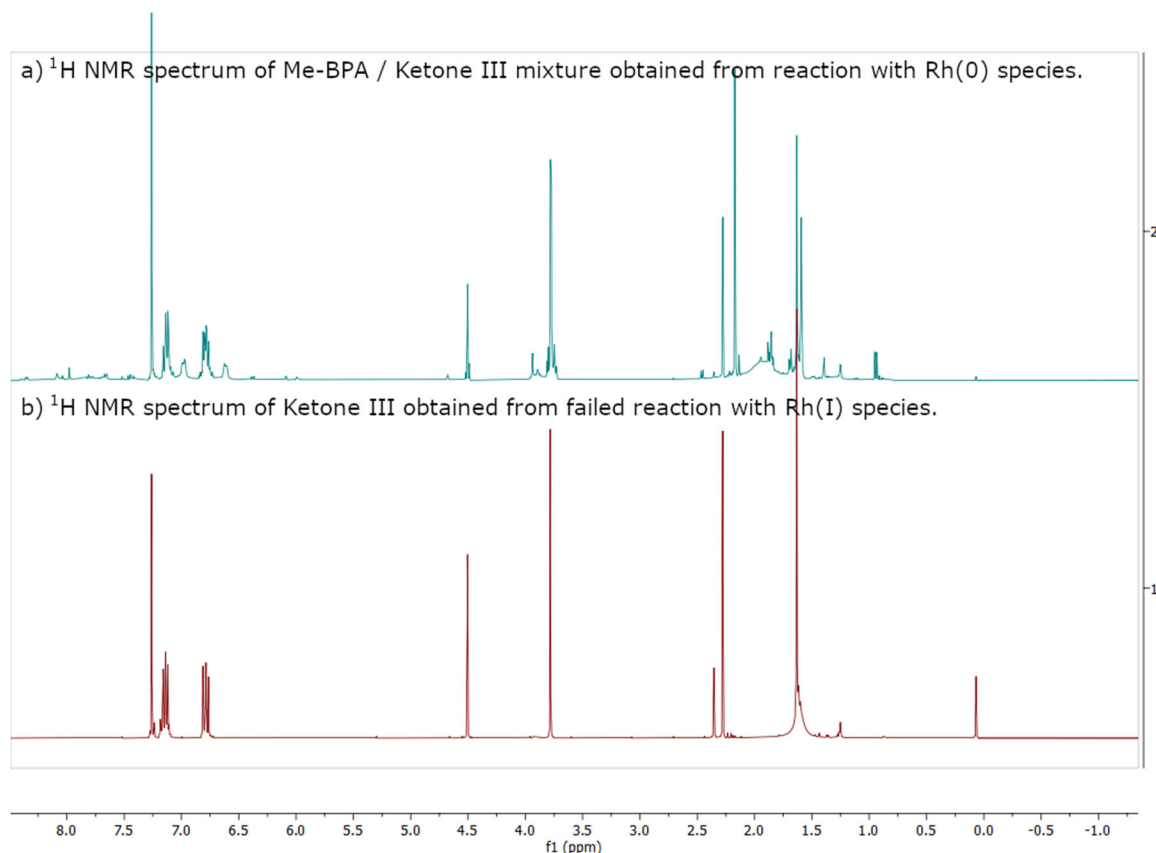


Fig. S13. ^1H NMR spectra after reacting $\text{terpy}^{\text{OMe}}\text{-Rh}$ with Ketone III in CDCl_3 . **(A)** Mixture obtained after reaction with Rh(0) species. **(B)** Recovered starting material obtained after attempted reaction with Rh(I) species.

S3.7 Room Temperature EPR Studies

terpy*-Rh-Cl

In an argon-charged glovebox, a J Young NMR tube was charged with 5.4 mg ($10.0\ \mu\text{mol}$, 1 equiv) of $\text{terpy}^*\text{-Rh-Cl}$ and 1.92 mg ($12.0\ \mu\text{mol}$, 1.2 equiv) of potassium 2-phenylethanolate. Then, 0.4 ml of $\text{THF-}d_8$ were added and within seconds, the dark suspension formed a deep black solution. The tube was sealed and heated outside the glovebox for 30 minutes at $140\ ^\circ\text{C}$. In ^1H NMR, the peaks corresponding to the terpyridine protons had vanished, and the formation of acetophenone could be confirmed. Then, inside the glovebox, a glass capillary was filled with the reaction mixture and placed into another J Young NMR tube, which was sealed and used for the room temperature EPR measurements.

Fig. S14. Reaction conditions for the preparation of the room temperature EPR measurement sample using terpy*-Rh-Cl and THF.

terpy^{OMe}-Rh-Cl

In an argon-charged glovebox, a J Young NMR tube was charged with 5.49 mg (10.0 μmol , 1 equiv) of terpy^{OMe}-Rh-Cl and 1.60 mg (10.0 μmol , 1 equiv) of potassium 2-phenylethanolate. Then, 0.4 ml of DMSO-*d*₆ were added. The tube was sealed and heated outside the glovebox for 30 minutes at 140 °C. In ¹H NMR, the peaks corresponding to the terpyridine protons had vanished, and the formation of acetophenone could be confirmed. Then, inside the glovebox, a glass capillary was filled with the reaction mixture and placed into another J Young NMR tube, which was sealed and used for the room temperature EPR measurements.

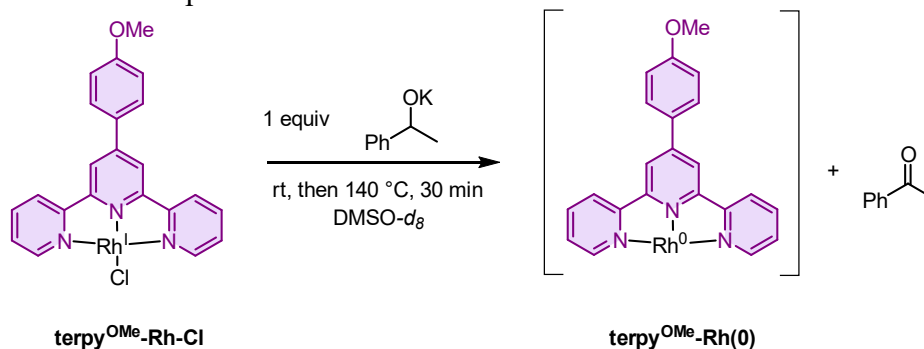


Fig. S15. Reaction conditions for the preparation of the room temperature EPR measurement sample using terpy^{OMe}-Rh-Cl and DMSO.

CW EPR spectra of terpy*-Rh in THF-*d*₈ and terpy^{OMe}-Rh in DMSO-*d*₆ were acquired at room temperature on a Magnettech MiniScope MS400 spectrometer. Spectra were acquired with a MW attenuation of 10 dB (0 dB corresponding to 100 mW of nominal power), a modulation amplitude of 2 G, and a modulation frequency of 100 kHz.

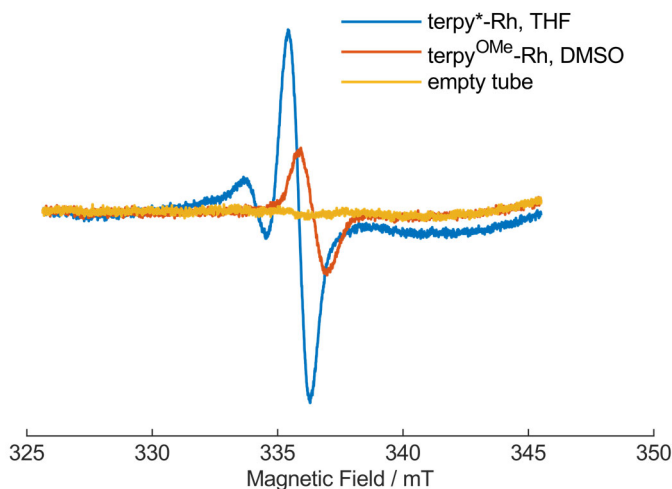


Fig. S16. Room temperature EPR sweep of reactions depicted in Fig. S14 and Fig. S15.

S3.8 Low Temperature EPR Studies and Simulations

Sample A:

In an argon-charged glovebox, a 10 ml COtube was charged with 4.32 mg (8.0 μmol , 1 equiv) of terpy*-Rh-Cl and 3.33 mg (20.8 μmol , 2.6 equiv) of potassium 2-phenylethanolate. Then, 0.4 ml of THF were added and within seconds, the dark suspension formed a deep black solution. The vessel was sealed and stirred outside the glovebox for 30 minutes at 140 °C. Then, inside the glovebox, 44 μl of toluene were added. The mixture was filtered through silica into a quartz tube, which was sealed under argon.

Sample B and C:

In an argon-charged glovebox, a 10 ml COtube was charged with 2.7 mg (5.0 μmol , 1 equiv) of terpy*-Rh-Cl and 2.7 mg (20.0 μmol , 4 equiv) of KC_8 . Then, 0.4 ml of THF were added, resulting in a black solution. The vessel was stirred inside the glovebox for 5 minutes at room temperature. Then, 44 μl of toluene were added. For sample C, 2.0 mg (17.0 μmol , 3.4 equiv) of acetophenone was added additionally. The mixture was filtered through silica into a quartz tube, which was sealed under argon.

CW EPR

Continuous wave EPR experiments were performed using a Bruker Elexsys E580 X-band Pulse EPR spectrometer and an MD-5 dielectric resonator. Samples were placed in 2 mm OD quartz EPR tubes and flame sealed. Experiments were performed under liquid He flow in an Oxford CF935 cryostat. All experiments were performed at 20 K using 100 kHz modulation with an amplitude of 2 G. The microwave power used was 9.5 microwatts resulting in a B1 field of approximately 12 milligauss. The spectra shown are the result of 8 magnetic field sweeps recorded using 10 ms conversion time for the lock in amplifier. The recorded spectra were normalized by dividing by the maximum intensity in each spectrum before plotting in Matlab (Mathworks).

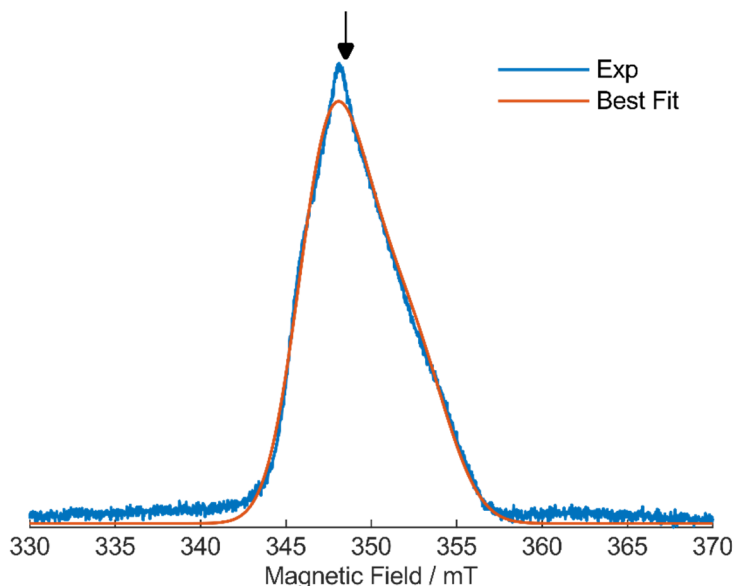


Fig. S17. Field sweep EPR spectrum of terpy*-Rh(0) recorded at 15 K. The black arrow indicates the magnetic field at which the Davies ENDOR was recorded.

PULSED EPR

Pulse EPR data were acquired at X-band frequencies on a homebuilt arbitrary waveform generator (AWG)-based pulse EPR spectrometer equipped with an MD-4 ENDOR resonator (Bruker BioSpin, Ettlingen, Germany) and a traveling wave tube amplifier with a nominal output power of 2 kW (Applied Systems Engineering, Fort Worth, US). The RF pulses were generated with a separate AWG (HDAWG, Zurich Instruments, Zurich, Switzerland) and amplified with a 250 W RF amplifier (NanoNord A/S, Aalborg, Denmark). The spectrometer is equipped with a helium flow cryostat to maintain a stable sample temperature of 15 K during the experiments.

Echo-detected field-swept spectra were recorded with $\pi/2$ and π pulses with a length of 16 ns and 32 ns, respectively, and an interpulse delay of 508 ns. The echo was integrated over a length of 478 ns around the maximum. A shot repetition time of 10 ms was used.

ENDOR spectra were acquired with the Davies ENDOR sequence, i.e. $\pi(\text{selective}) - \pi(\text{rf}) - \text{echo}$. The selective microwave pulse had a length of 200 ns, and the detection was done with $\pi/2$ and π pulses with a length of 16 ns and 32 ns, respectively, and an interpulse delay of 508 ns. The echo was integrated over a length of 478 ns around the maximum. Frequency-swept rf pulses with a linear sweep width of 0.5 MHz, a total length of 30 μs and a quarter-sine amplitude smoothing of 200 ns were used⁷. The center frequency of the rf chirp pulses were stepped with a step size of 0.05 MHz. A shot repetition time of 10 ms was used. The spectrum was recorded at 348.5 mT (marked in **Fig. S17**).

DFT EPR calculations

The calculation of the g-tensor, hyperfine couplings, and nuclear quadrupole couplings was carried out using ORCA 5.0.4⁸. A very tight SCF convergence criteria was considered (orca keyword *verytightscf*) as well as increased accuracy of numerical integration (orca keyword *defgrid3*). In particular, a strongly increased radial integration accuracy for the Rh atom was specified (orca keyword *SpecialGridIntAcc 12*). The resolution of the identity combined with the chain of spheres approximation were used (orca keyword *RIJCOSX*⁹⁻¹¹). Structural optimizations were performed at (U)M06-D3/def2-SVP level of theory. The EPR simulations were carried out at the DFT level of theory, using the B3LYP¹² and PBE0¹³, considering a relativistic ZORA Hamiltonian¹⁴, and with ZORA-TZVP basis-set for all atoms¹⁵. Auxiliary basis-sets were generated automatically (orca keyword *AutoAux*¹⁶). Picture change effects were also included.

The spin-orbit coupling operator was treated by the SOMF approximation, including one-electron terms, the Coulomb term computed semi-numerically, incorporating exchange via one-center exact integrals, the spin-other orbit interaction, and including local DFT correlation¹⁷.

The calculation of the A tensor included the isotropic, dipolar, and second-order contributions to the hyperfine coupling from the spin-orbit coupling for the Rh atom. For the remaining atoms, only the isotropic and dipolar terms were considered. The nuclear quadrupole couplings were calculated for the ¹⁷O and ¹⁴N isotopes of the nitrogen and oxygen atoms.

EPR Simulations

The field sweep EPR of terpy*-Rh(0) recorded at 15 K shown in **Fig. S17** was fit using the Levenberg–Marquardt algorithm implemented in Matlab toolbox (Mathworks) EasySpin¹⁸, using

the pepper module with microwave frequency set 9.75 GHz, matching the experimental conditions, and considering a simple single spin $S=1/2$ with an anisotropic g-tensor.

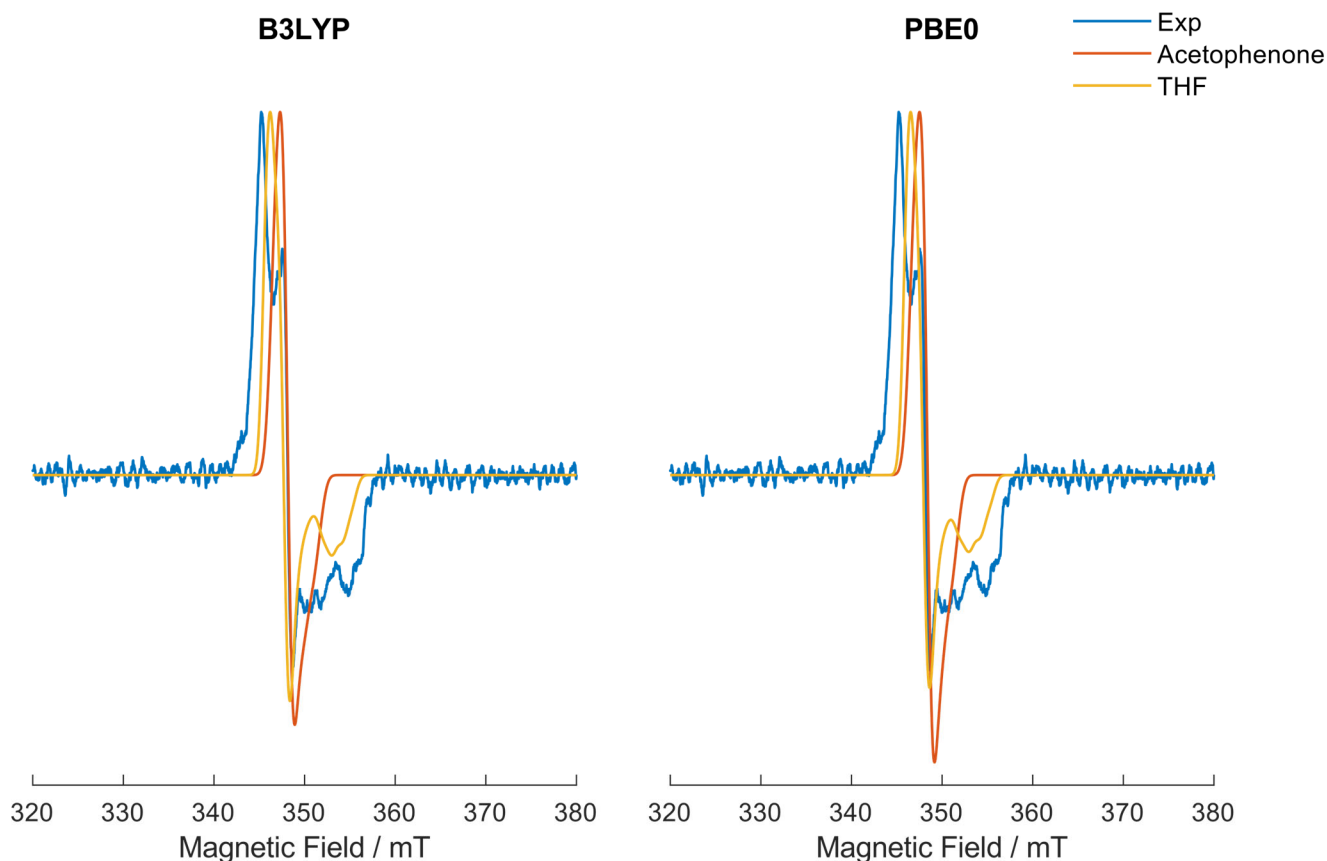


Fig. S18. Comparison of DFT based simulations of the first-harmonic EPR spectrum of the terpy*-Rh(0)-acetophenone and terpy*-Rh(0)-THF structural models, and the numerical derivative the field sweep EPR spectrum of terpy*-Rh(0) recorded at 15 K.

The DFT based simulations of the first-harmonic EPR spectrum shown in **Fig. S18** were calculated with EasySpin, using the pepper module with microwave frequency set 9.75 GHz, importing the EPR/NMR parameters from the ORCA output files. The simulations were carried out considering second-order perturbation theory, neglecting the nuclear Zeeman and nuclear quadrupole terms. The simulated spin systems included the hyperfine couplings of all nitrogen and rhodium atoms. All hydrogen atoms with a ^1H hyperfine coupling larger than 2.0 MHz were also included. In **Fig. S19** (shown below), the DFT based simulations are compared with the numerical derivative of the field sweep EPR spectrum shown in **Fig. S17**, computed using a Savitzky–Golay filter implemented in EasySpin.

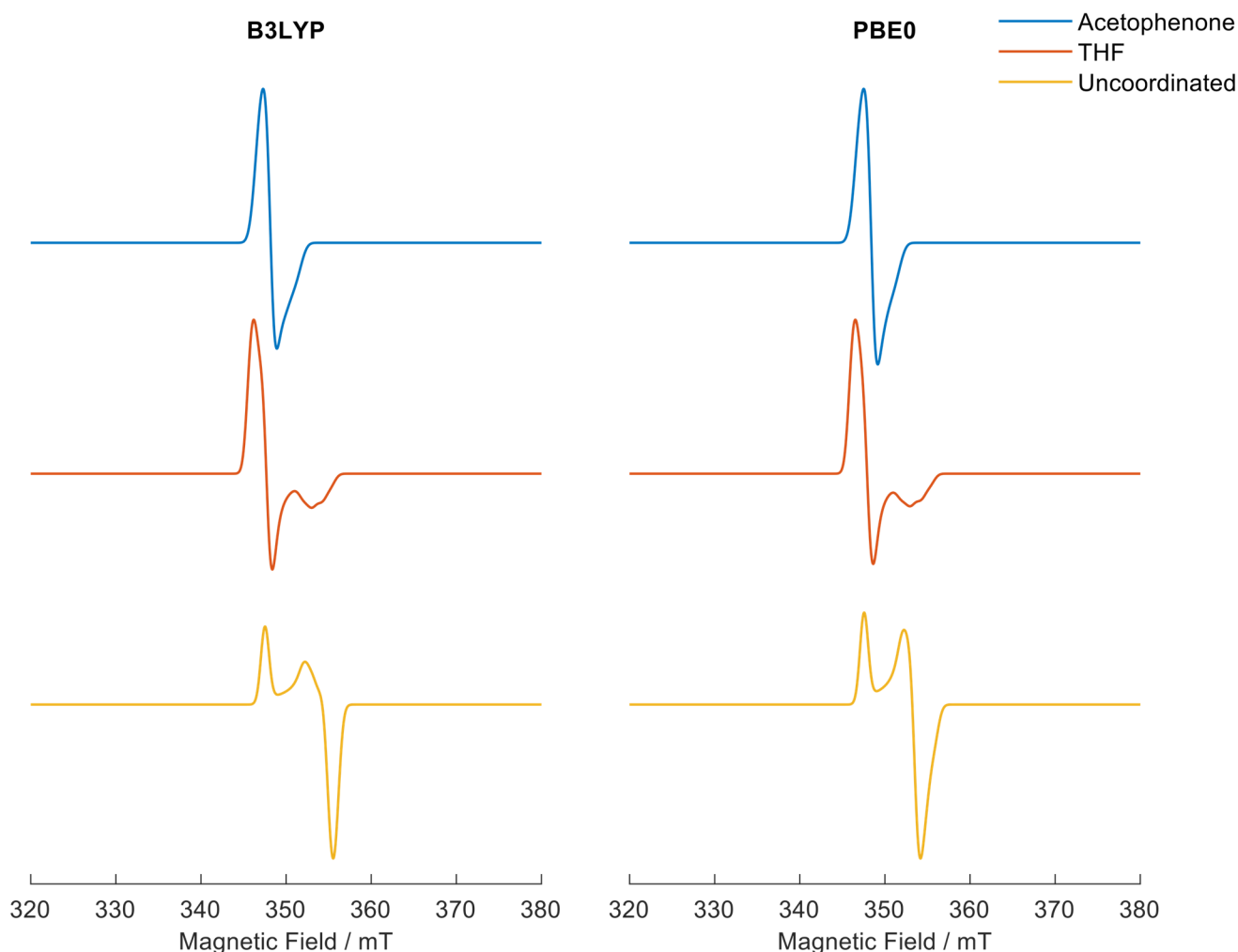


Fig. S19. DFT based simulations of the first-harmonic EPR spectrum of terpy*-Rh(0)-acetophenone and terpy*-Rh(0)-THF and terpy*-Rh(0) (uncoordinated).

The Davies ENDOR simulations shown in **Fig. S20** (shown below) were calculated in EasySpin, importing the EPR/NMR parameters from the ORCA output files, and using the salt module. They were calculated using two separate spin systems, one considering the nitrogen and rhodium atoms, calculated using matrix diagonalization, including the nuclear quadrupolar interaction, and one considering all hydrogen atoms with a ^1H hyperfine coupling larger than 2.0 MHz, calculated with second-order perturbation theory and convolved with a Gaussian function. The microwave frequency was set to be the maximum of the zeroth-harmonic of the simulated frequency sweep EPR spectrum for each spin system and the magnetic field was set to 348.5 mT, matching experimental conditions. The resulting simulated ENDOR spectra for the two spin systems were then added, after being scaled to match the peak intensities of the experimental data.

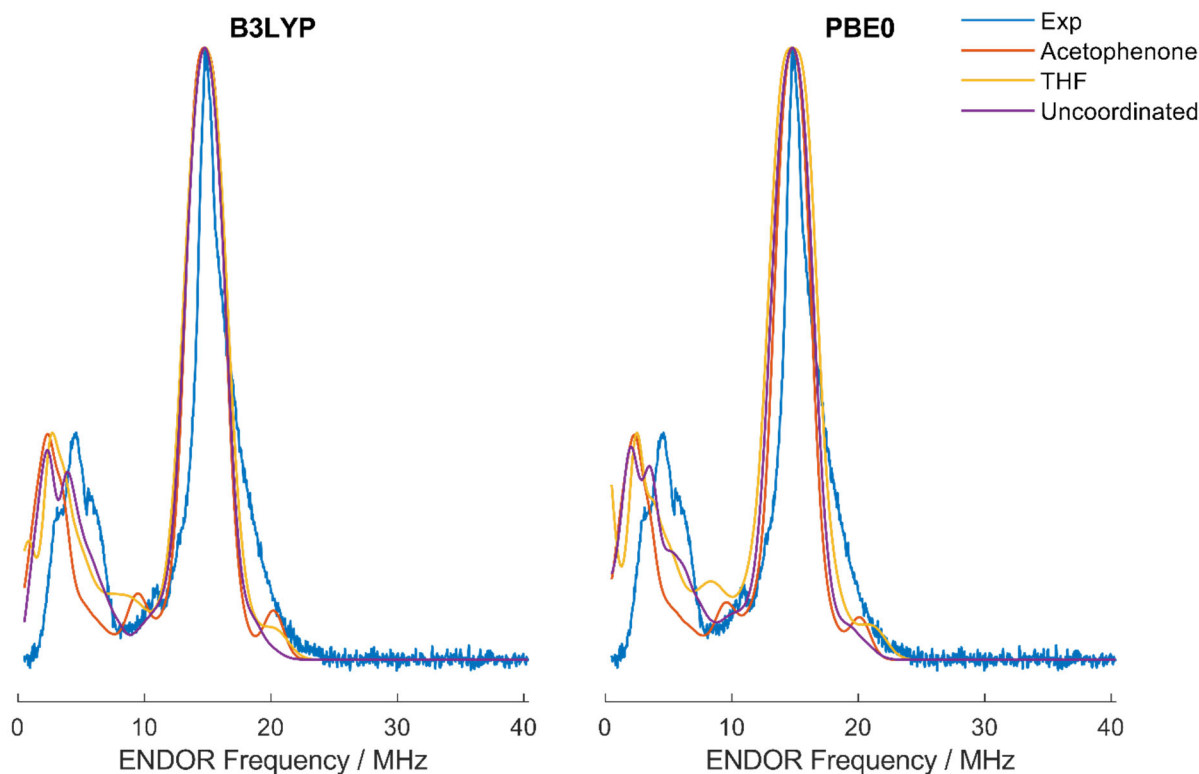


Fig. S20. Comparison of DFT based simulations of the ENDOR spectra of the terpy*-Rh(0) - acetophenone and terpy*-Rh(0)-THF structural models and the ENDOR spectrum of terpy*-Rh(0) recorded at 15 K.

Comment on the EPR Simulations

The experimental values for g_{iso} extracted from the field sweep EPR spectrum with a simple single $S=1/2$ model, are in reasonable agreement with the DFT calculations for the structural models of terpy*-Rh(0)-acetophenone and terpy*-Rh(0)-THF, c.f. **Table S12** and **Fig. S17**.

Table S12. Comparison of Experimental and DFT calculated g-tensor principal values.

		g_x	g_y	g_z	g_{iso}
Acetophenone	B3LYP	1.9873	2.0005	2.0080	1.9986
	PBE0	1.9875	1.9991	2.0072	1.9979
THF	B3LYP	1.9697	2.0031	2.0130	1.9953
	PBE0	1.9698	2.0018	2.0111	1.9942
Uncoordinated	B3LYP	1.9609	1.9671	2.0043	1.9774
	PBE0	1.9668	1.9689	2.0041	1.9799
Best Fit		1.9657 ± 0.0001	2.01 ± 0.02	2.01 ± 0.02	1.99 ± 0.01

In order to better assess the effect of fine structure in the field sweep EPR spectrum, the first-harmonic EPR spectrum was calculated via numerical differentiation. In **Fig. S18**, the experimental first-harmonic EPR spectrum was compared with the DFT based simulations of terpy*-Rh(0)-acetophenone and terpy*-Rh(0)-THF, where the hyperfine couplings are also

included. Even though the agreement between simulation and experiment, particularly for the terpy*-Rh(0)-THF complex, is reasonable, there are some discrepancies between simulation and experiment. These discrepancies can be attributed to shortcomings in the quantitative prediction of EPR parameters with DFT, particularly in the hyperfine coupling tensor^{19,20}. The simulations, including the simulations of uncoordinated terpy*-Rh(0), which expectedly matched the experimental spectra less well, are also shown in **Fig. S19**.

The ENDOR simulations shown in **Fig. S20** are also in reasonable agreement with experiments, where we observe ENDOR peaks in the 1-5 MHz region predominately due to ¹⁴N couplings, resulting from the ligating nitrogen atoms, and ¹H peaks around 15 MHz. In **Fig. S21**, the spin density plots for the terpy*-Rh(0)-acetophenone (left) and terpy*-Rh(0)-THF (right), calculated at the PBE0/ZORA-TZVP level of theory, are also shown, where significant density can be observed in the nitrogen atoms in the terpyridine ligand. This spin-density is manifested in the nitrogen hyperfine couplings that give rise to the ¹⁴N ENDOR peaks, observed in simulation and experimentally. The deviations between simulation and experiment are also attributed to the shortcoming of DFT, as well as difficulties in detecting ENDOR signals at lower RF frequencies due to limitations of our RF-amplifier.

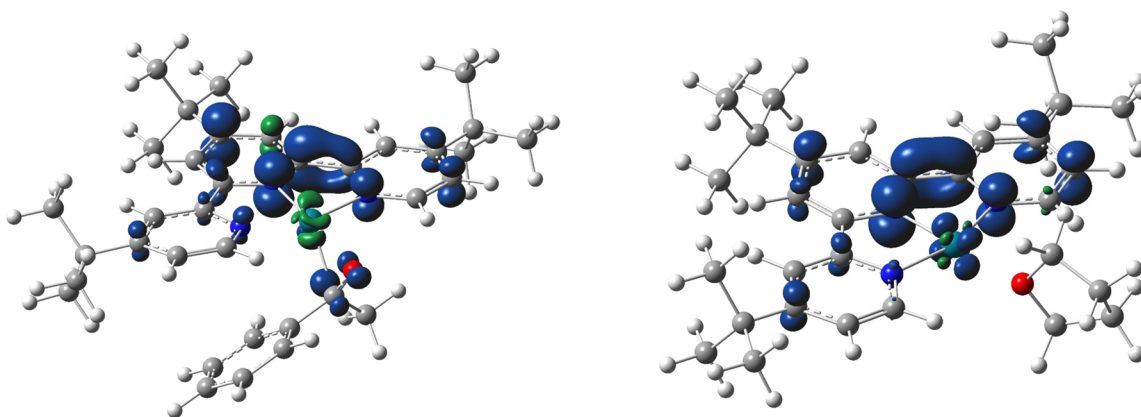


Fig. S21. Plots of the spin density of terpy*-Rh⁰-acetophenone (left) and terpy*-Rh⁰-THF (right). The spin density is plotted as the 0.04 e/Bohr³ isosurface calculated at the PBE0/ZORA-TZVP level of theory.

S4. Cyclovoltammetric Studies

S4.1 General Remarks

Due to the poor solubility of the $\text{terpy}^{\text{OMe}}\text{-Rh-Cl}_3$ precatalyst in water, obtention of cyclic voltammetry data using 0.1 M NaOH (in water) was not feasible. As an alternative DMSO was selected, due to its broader redox window ²¹ in tandem with a higher solubility of the $\text{terpy}^{\text{OMe}}\text{-Rh-Cl}_3$ precatalyst.

S4.2 General Method for Obtention of CV Data

Inside an argon-filled glovebox, a stock solution of the desired electrolyte in DMSO was prepared and sealed. Outside the glovebox, the solution was further degassed by bubbling argon for 10 minutes, after which an argon balloon was attached to maintain a positive pressure of inert gas. The solution was then transferred to a flame-dried, three-neck glassware setup (**Fig. S22**), under a continuous argon flow. Unless otherwise noted, a glassy carbon working electrode and a platinum wire counter electrode were used. A commercial leak-free Ag/AgCl reference electrode (LF-1.6-100, Leak-Free Reference Electrode 1.6 mm OD, 100 mm barrel from Innovative Instruments) was used without any modification. All reported Cyclic voltammetry data is plotted using the IUPAC convention ²².

To ensure the working electrode was clean, it was polished by performing 20 infinity loops on a microfiber cloth with an alumina slurry ²². Before reuse, the electrode was subsequently washed with water and acetone, dried with a paper towel, and rinsed with the electrolyte solution.

To maintain an inert atmosphere, the glassware was kept under constant argon pressure throughout the experiment using a needle connected to an argon line. After adding the substrate or catalyst for electrochemical analysis, the solution was stirred while being bubbled with argon for 5 minutes to further ensure an oxygen-free environment.



Fig. S22. Chosen equipment for the obtention of electrochemical data.

S4.3 CV Studies using TBAF₄ as Supporting Electrolyte

We started the electrochemical studies investigating the $\text{terpy}^{\text{OMe}}\text{-Rh(III)}$ precatalyst using TBABF_4 as the supporting electrolyte (Voltammogram S1). Based on previous studies on the electrochemical behavior of rhodium terpyridyl, bis-bipyridyl, and bis-terpyridyl, complexes²³⁻²⁸, the irreversible reduction peak observed at $E_{\text{pa}} = -0.87 \text{ V vs. Ag/AgCl}$ (**Fig. S23**) is attributed to the reduction of $\text{terpy}^{\text{OMe}}\text{-Rh(III)}$ to $\text{terpy}^{\text{OMe}}\text{-Rh(I)}$. When the first cycle is swept toward positive potentials, no oxidation peak is observed. However, after the reduction peak, a defined oxidation peak at $E_{\text{pa}} = -0.36 \text{ V vs. Ag/AgCl}$ and a less defined peak at $E_{\text{pa}} = 0.02 \text{ V vs. Ag/AgCl}$ are present, corresponding to the reoxidation of the $\text{terpy}^{\text{OMe}}\text{-Rh(I)}$ along with the re-coordination of two ligands, likely solvent molecules and/or chloride ion.

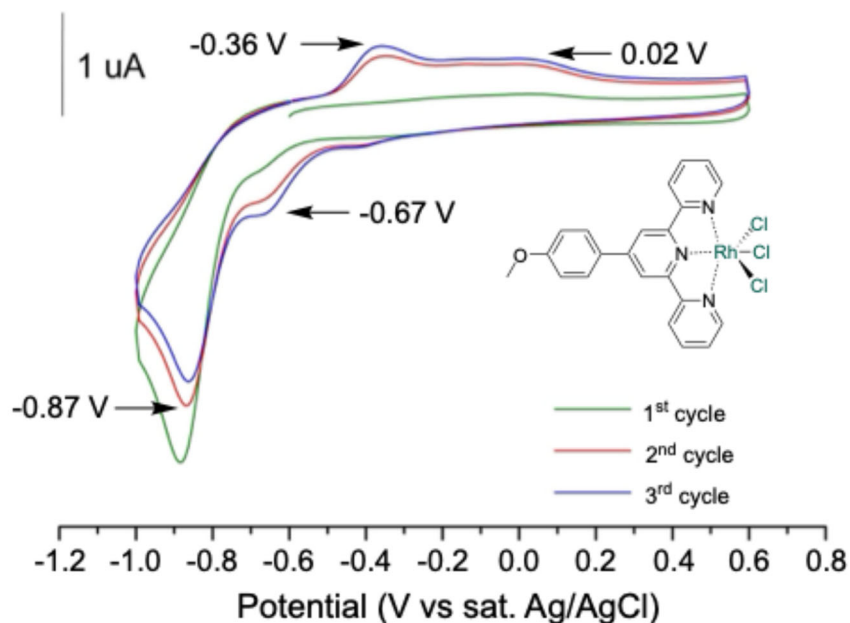


Fig. S23. Cyclic voltammogram of terpy^{OMe}-Rh-Cl₃ precatalyst (0.9 mM) with a glassy carbon electrode ($\varnothing = 1$ mm, 0.1 M TBABF₄ in DMSO, $\nu = 50$ mV s⁻¹).

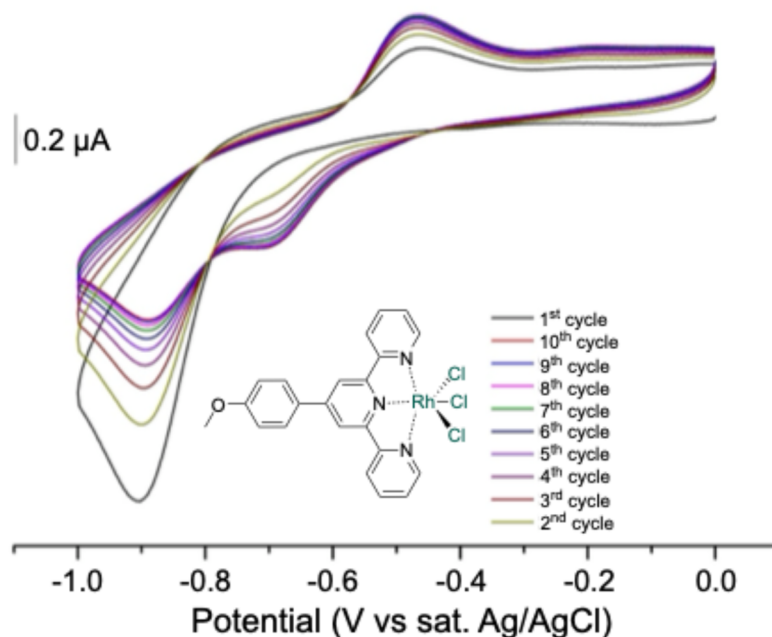


Fig. S24. Cyclic voltammogram of terpy^{OMe}-Rh-Cl₃ precatalyst (0.9 mM) with a glassy carbon electrode ($\varnothing = 1$ mm, 0.1 M TBABF₄ in DMSO, $\nu = 100$ mV s⁻¹).

This is further supported by the presence of an additional reduction peak at $E_{pa} = -0.67$ V vs. Ag/AgCl, which becomes more defined with increased cycles (**Fig. S24**). At a low scan rate (5 mVs⁻¹), this reduction peak is not observed, suggesting that under these conditions, the re-coordination of a chloride ion for the formation of the terpy^{OMe}-Rh-Cl₃ precatalyst is favored.

Conversely, when the scan rate is increased the reduction process at $E_{pa} = -0.67$ V vs. Ag/AgCl and the oxidation process at $E_{pa} = 0.02$ V vs. Ag/AgCl become more defined.

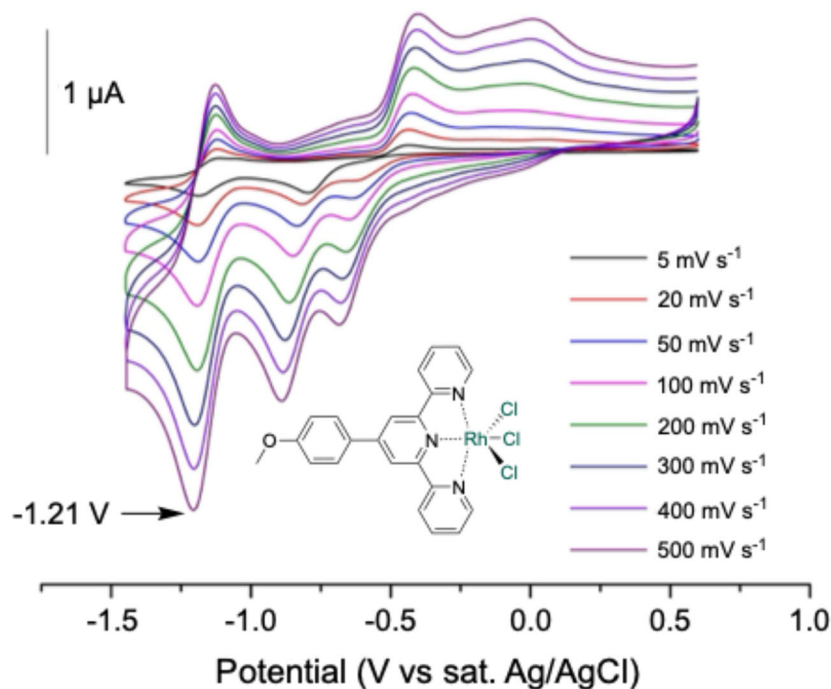


Fig. S25. Cyclic voltammogram of $\text{terpy}^{\text{OMe}}\text{-Rh-Cl}_3$ precatalyst (0.9 mM) with a glassy carbon electrode ($\varnothing = 1$ mm, 0.1 M TBABF₄ in DMSO).

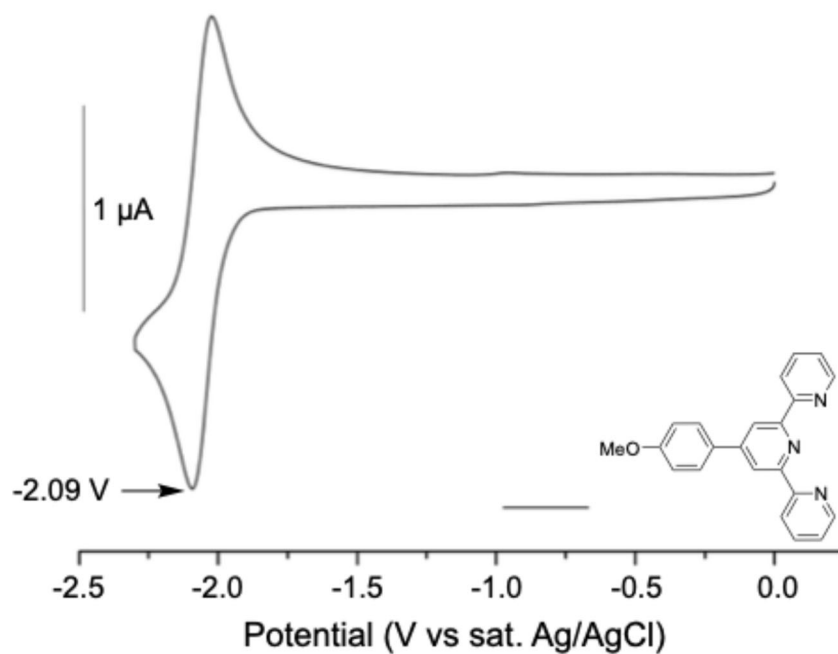


Fig. S26. Cyclic voltammogram of $\text{terpy}^{\text{OMe}}$ ligand (1 mM) with a glassy carbon electrode ($\varnothing = 1$ mm, 0.1 M TBABF₄ in DMSO, $\nu = 100$ mV s⁻¹).

Additionally, a reversible reduction peak at $E_{pa} = -1.21$ V vs. Ag/AgCl is observed (**Fig. S25**), which has previously been linked to the terpyridyl ligand²⁸. To further investigate this, a cyclic voltammogram of the terpyridyl^{OMe} ligand was recorded using the same electrolyte and solvent (**Fig. S26**). A reversible redox process is observed at $E_{pa} = -2.09$ V vs. Ag/AgCl, suggesting that the reversible process observed in **Fig. S25** corresponds to the reduction of the terpy^{OMe}-Rh(I) complex and is not related to the free terpyridine ligand.

For ketone 3, a distinct irreversible reduction is seen at $E_{pa} = -2.66$ V vs. Ag/AgCl, which occurs at a more negative potential than the redox processes for the terpy^{OMe}-Rh-Cl₃ precatalyst (**Fig. S27**).

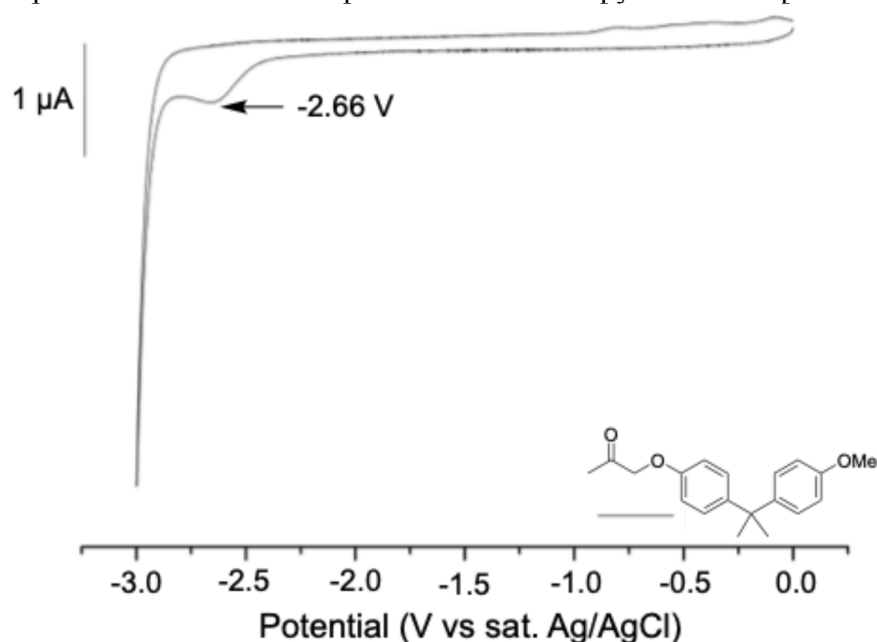


Fig. S27. Cyclic voltammogram of Ketone 3 (1 mM) with a glassy carbon electrode ($\varnothing = 1$ mm, 0.1 M TBABF₄ in DMSO, $\nu = 100$ mV s⁻¹).

S4.4 CV Studies using TBAOH as Supporting Electrolyte

Trying to emulate the reaction conditions, new cyclic voltammetry studies were performed using tetrabutylammonium hydroxide (TBAOH) as the electrolyte. In this case a 1 M solution of TBAOH in methanol was dissolved in DMSO to provide a stock solution of 0.1 M TBAOH in DMSO:MeOH 9:1.

Upon addition of the yellow terpy^{OMe}-Rh-Cl₃ precatalyst into the solution, it changed in color to a brownish yellow. Even in the first cycle, two oxidation processes at $E_{pa} = -1.44$ and $E_{pa} = -1.13$ V vs. Ag/AgCl are present, suggesting the formation of a terpy^{OMe}-Rh(I) species (**Fig. S28**). Interestingly, due to the high concentration of hydroxide ions in the medium, no additional reduction peak, which would indicate recomplexation with different ligands, is observed. This suggests that the terpy^{OMe}-Rh-Cl₃ precatalyst has undergone ligand exchange to form Ac3. Analogous to previous studies and voltammograms in TBABF₄, these two reduction processes at $E_{pa} = -1.23$ and $E_{pa} = -1.53$ V vs. Ag/AgCl are attributed to the formation of a low-valent terpy^{OMe}-Rh(0) species. Notably, when the solution is heated to 120 °C for 5 minutes both redox processes are quenched (**Fig. S29**), which is accompanied by a drastic color change to a greenish black (**Fig. S30**).

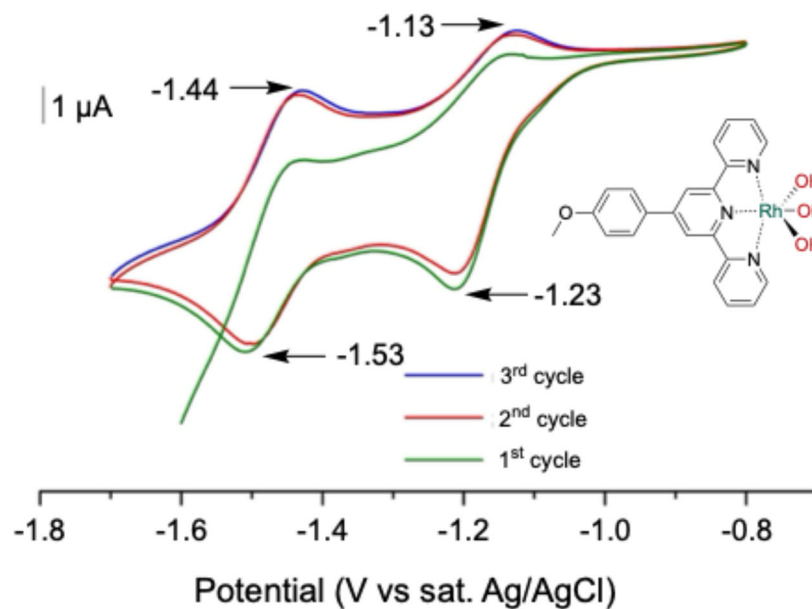


Fig. S28. Cyclic voltammogram of terpy^{OMe}-Rh-Cl₃ precatalyst (1.6 mM) with a glassy carbon electrode ($\varnothing = 3$ mm, 0.1 M TBAOH in 1:9 MeOH:DMSO, $\nu = 10$ mV s⁻¹)

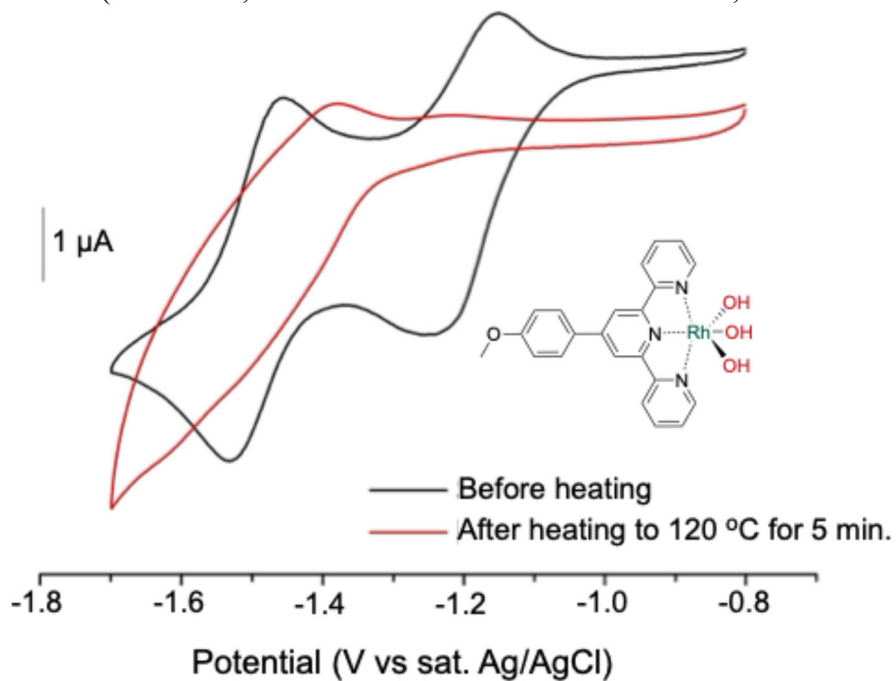


Fig. S29. Cyclic voltammogram of terpyOMe-Rh-Cl₃ precatalyst (1.6 mM) with a glassy carbon electrode ($\varnothing = 3$ mm, 0.1 M TBAOH in 1:9 MeOH:DMSO, $\nu = 50$ mV s⁻¹)

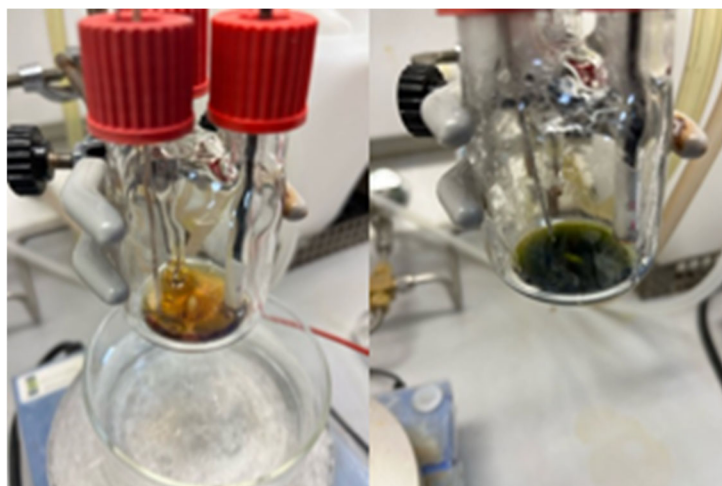


Fig. S30. Solution of terpyOMe-Rh-Cl₃ precatalyst (1.6 mM in 0.1 M TBAOH in 1:9 MeOH:DMSO) before and after heating to 120 °C for 5 minutes.

In the proposed mechanism, a Rh(0) complex dimer reacts with Ketone 3. In the electrochemical setup used here, this would suggest an electron reduction followed by a chemical reaction mechanism. To evaluate if this is a viable pathway, ketone 3 was titrated into a solution of terpy^{OMe}-Rh-Cl₃ precatalyst, and voltammograms were recorded (**Fig. S31**). As increasing equivalents of ketone 3 were added, the oxidation peaks are quenched, indicating that the low-valent Rh(0) complex, formed after the second reduction peak, reacts with ketone 3, leading to the formation of I12. Given that I12 is a Rh(I) complex, a decrease in the peak current of the first reduction, which corresponds to the Rh(III)→Rh(I) transition, is anticipated. This decrease is indeed observed, along with the emergence of a new reduction peak at $E_{Pa} = -1.45$ V vs. Ag/AgCl.

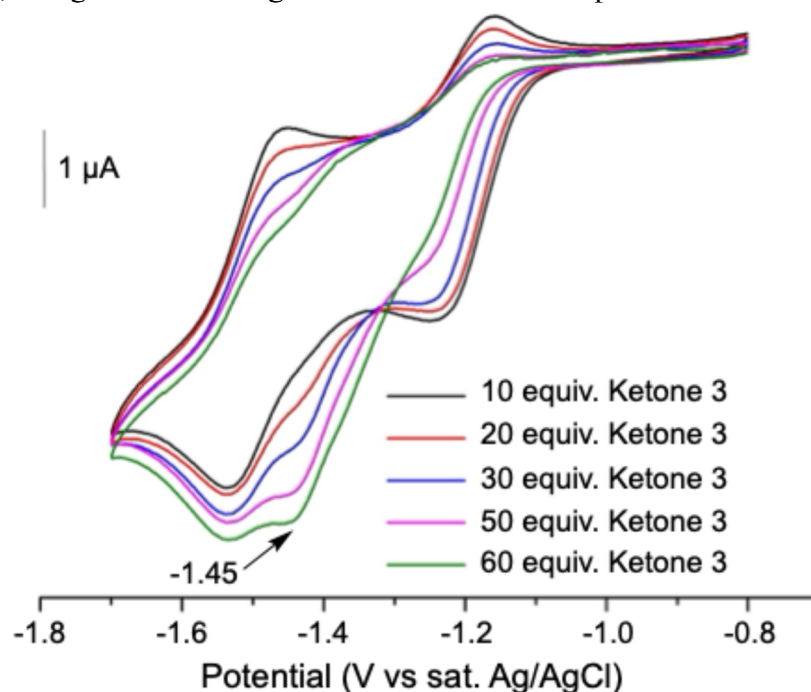


Fig. S31. Cyclic voltammogram of terpy^{OMe}-Rh-Cl₃ precatalyst (1 mM) in 0.1 M TBABF₄ (DMSO) measured at 5 mV s⁻¹ with varying equivalents of ketone 3.

S5. Computational Studies

S5.1 Computational Methods

Unless otherwise stated, all density functional theory (DFT) calculations presented in this paper were conducted using the Gaussian 16 software package at 413.15 K and 1 atm²⁹. Geometry optimizations for all molecules were carried out at the (U)M06-D3/def2-SVP level of theory, using an ultrafine integration grid and without imposing symmetry constraints³⁰⁻³². Energy refinement on the electronic energy was performed using single-point calculations at the (U)M06-D3/def2-TZVP level of theory, with the SMD solvation model for water³³.

To confirm the nature of stationary points as minima or saddle points, vibrational analyses were conducted at the same level of theory as the geometry optimizations. These analyses also provided Gibbs free energy and enthalpy corrections. Additionally, intrinsic reaction coordinate (IRC) calculations were performed to validate the identified transition states. Conformational analysis of relevant intermediates and transition states was carried out using the CREST program, with the best conformers subsequently optimized at the DFT level³⁴.

The Fractional occupation density (FOD) analysis and Electron Paramagnetic Resonance (EPR) simulations were performed using the Orca 5.0.4 software package^{8,35,36}. The FOD analysis was carried out using default settings, employing the TPSS/def2-TZVP level of theory with a smearing temperature of 5000 K, as outlined by Grimme³⁷. A detailed comment on the level of theory with a discussion on computational efficiency and accuracy of the selected method is depicted below.

S5.2 Comment on chosen Level of Theory

The studied system is highly complex, with the potential formation of rhodium aggregates, which exponentially increases the computational cost. The chosen level of theory was based on a previous study for the ruthenium-catalyzed C–O bond deconstruction in epoxy resins, which demonstrated a favorable balance between computational cost and accuracy³⁸. Additionally, the (U)M06/def2-TZVP, 6-311++G(d,p) level of theory was recently employed by Yang and coworkers to study the mechanism for the terpy-Rh-Cl₃ catalyzed lignin model depolymerization³⁹. To further validate the accuracy of the chosen level of theory for the system under investigation, reaction barriers presented in **Fig. S32** were compared to those obtained using the DLPNO-CCSD(T)/def2-TZVP(SMD for Water)/(U)M06-D3/def2-TZVP level of theory as a benchmark⁴⁰⁻⁴⁴. For these calculations, both the frequency analysis ((U)M06-D3/def2-TZVP) and energy refinement (DLPNO-CCSD(T)/def2-TZV (SMD for Water)) were performed using the Orca 5.0.4 software package.

The results show that the $\Delta G_{\text{exchange}}$ values correlate well with those obtained using the benchmark coupled-cluster methods, but at a significantly lower computational cost (**Fig. S32**). Increasing the level of theory for the geometry optimization results in only minor changes (a difference of 0.2 kcal mol⁻¹) while incurring a substantially higher computational expense. Based on these observations, the (U)M06-D3/def2-TZVP(SMD for water)/(U)M06-D3/def2-SVP level of theory was selected as an optimal compromise between computational efficiency and accuracy.

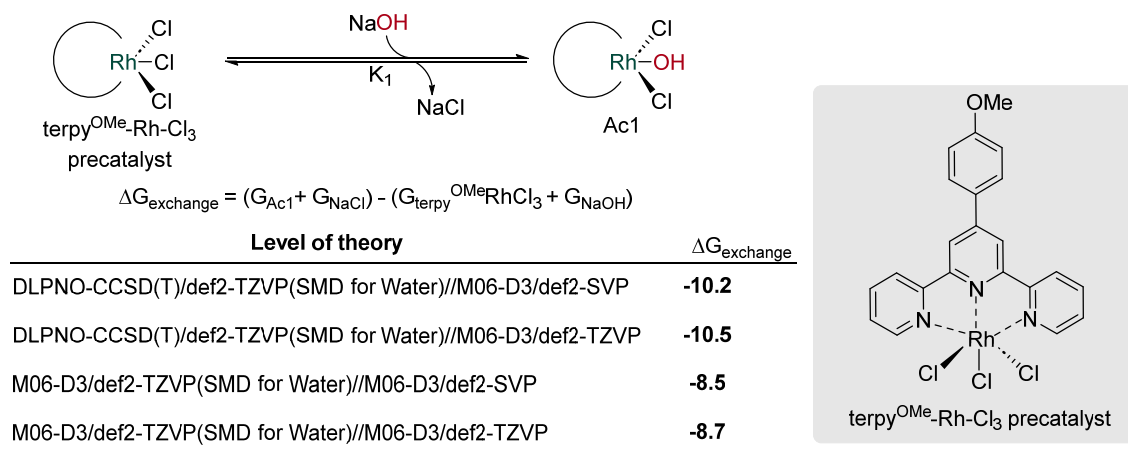


Fig. S32. Pre-equilibrium of the precatalyst.

To further assess the accuracy of the chosen level of theory for a key step in the main mechanism, the barrier for β -hydride elimination from I4 was compared to the benchmark DLPNO-CCSD(T) method (**Fig. S33**). The selected level of theory strikes an optimal balance between computational efficiency and accuracy, with a deviation of only 1 kcal mol⁻¹ from the benchmark.

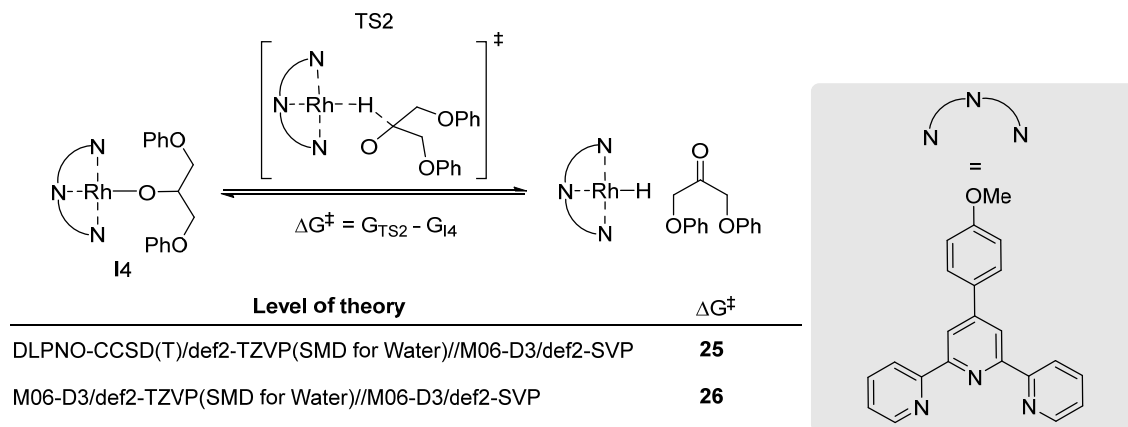
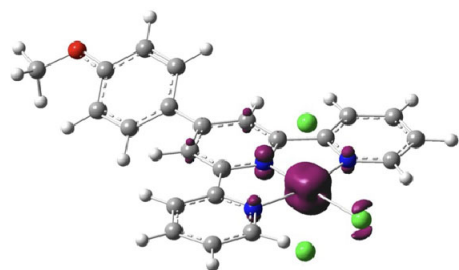


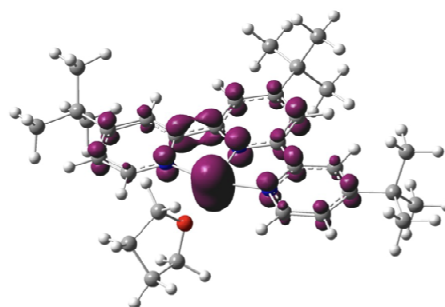
Fig. S33. Barriers for the β -hydride elimination from I4.

Complexes of late transition metals can exhibit strong multi-reference character, as, for example, described by Hartwig⁴⁵. To quantify and locate the static electron correlation in selected optimized structures, we performed Fractional Orbital Density (FOD) analysis, as described by Grimme^{6,37}.

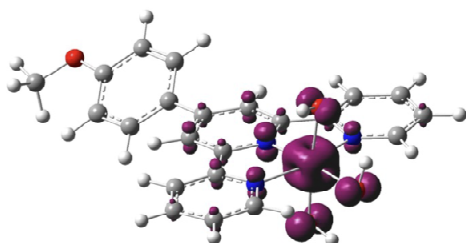
Our FOD analysis of various complexes potentially involved in the catalytic cycle revealed a significant degree of multi-reference character (**Fig. S34**). This strong multi-reference nature can lead to variations in computed energies depending on the choice of functional, potentially affecting reaction energetics and barrier heights. To minimize errors and establish a consistent trend across the proposed catalytic cycle, we computed the barriers for all steps using a range of functionals. A detailed discussion of these results is presented in **Chapter S5.7**.



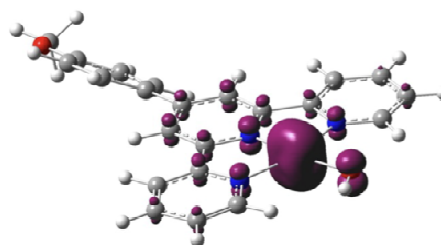
OMe(tpy)₃Rh(III)Cl₃
N_FOD = 0.97



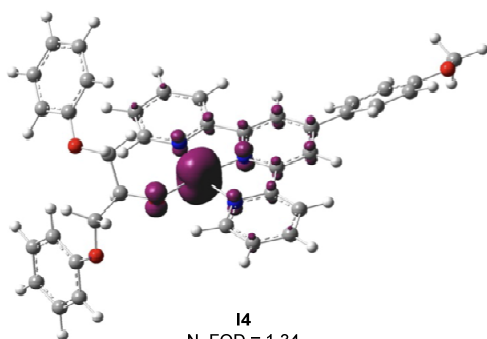
tBu(tpy)₃Rh(0)THF
N_FOD = 1.56



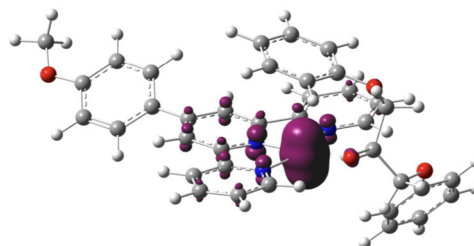
Ac₃
N_FOD = 1.22



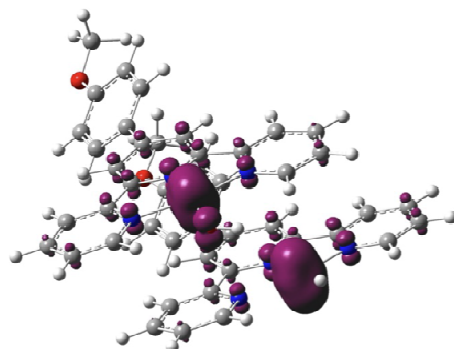
Ac₆
N_FOD = 1.28



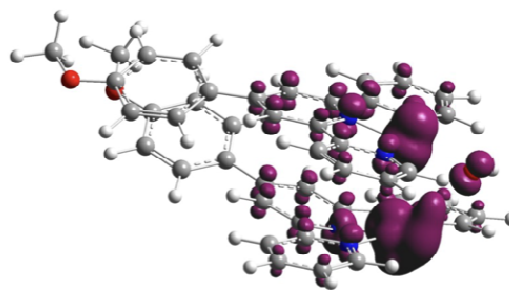
I₄
N_FOD = 1.34



TS₂
N_FOD = 1.41



I₇
N_FOD = 2.59



TS₃
N_FOD = 3.13

Fig. S34. Fractional occupancy density analysis for a selection of complexes presented in the study. The FOD is plotted as the 0.005 e/Bohr³ isosurface.

S5.3 Precatalyst Equilibrium in Reaction Medium

The $\text{terpy}^{\text{OMe}}\text{-Rh-Cl}_3$ precatalyst can undergo ligand exchange, replacing chloride to hydroxy ligands. Given the high temperatures and high concentration of hydroxide ions in the reaction medium, it is expected that the system will rapidly equilibrate to the lowest energy complex. To investigate this equilibrium, we computed the Gibbs free energy ($\Delta G_{\text{exchange}}$) for different plausible complexes (**Fig. S35**). The $\text{terpy}^{\text{OMe}}\text{-Rh-Cl}_3$ precatalyst is initially ligated to three chloride atoms, which can be exchanged due to the high hydroxide concentration, leading to the formation of various rhodium-hydroxide complexes (**Fig. S35**). To determine which complex is most likely to be present under the reaction conditions, we analyzed the thermodynamic equilibrium of these species, correlating the computed thermodynamic parameters with their respective equilibrium constants.

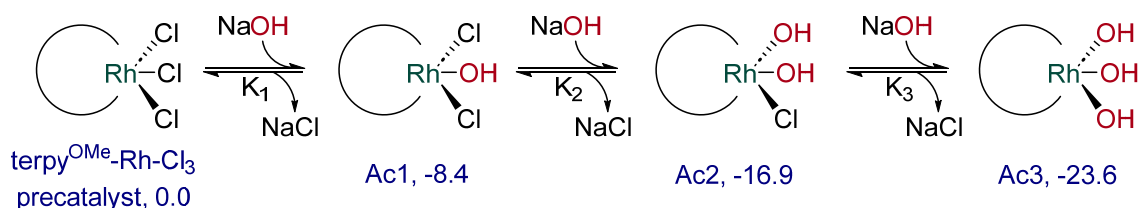


Fig. S35. Possible equilibrium of the precatalyst in the basic medium. Barriers calculated at the (U)M06-D3/Def2TZVP// (U)M06-D3/Def2SVP level of theory with SMD for water. All presented barriers are in kcal mol^{-1} .

The general equation correlating Gibbs free energy with the equilibrium constant was applied (**Equation S1**).

$$\Delta G = -RT \ln K$$

Equation S1. Correlation of Gibbs free energy and equilibrium constant.

Using the computed Gibbs free energy barriers, it was possible to calculate the equilibrium constants for each set of reactions (**Table S13**).

Table S13. Computed $\Delta G_{\text{exchange}}$ and equilibrium constants for the precatalyst equilibrium. Barriers calculated at the (U)M06-D3/Def2TZVP// (U)M06-D3/Def2SVP level of theory with SMD for water.

Reaction	$\Delta G_{\text{exchange}}$ (kcal mol^{-1})	Equilibrium constant	K Value
$\text{terpy}^{\text{OMe}}\text{-Rh-Cl}_3$ to Ac1	-8.4	K_1	27757.5
Ac1 to Ac2	-8.6	K_2	35414.0
Ac2 to Ac3	-6.6	K_3	3099.0

Using the computed equilibrium constants, the partial concentration of each complex in the medium at equilibrium can be determined using the equilibrium constant formula for each reaction. Due to the high concentration of hydroxide relative to chlorides in the medium, the reaction favors the formation of Ac3. This suggests that, at thermodynamic equilibrium, the $\text{terpy}^{\text{OMe}}\text{-Rh-Cl}_3$ precatalyst is converted to Ac3. This was taken into account for the individual analysis of the subsequent critical steps.

S5.4 Calculated Precatalyst Activation Pathways

Ogo *et al.*⁴⁶ previously reported that the reaction of a terpy-Rh(I) acetonitrile complex with triflic acid in acetonitrile leads to the formation of a terpy-Rh(III)-hydride complex, which subsequently eliminates H₂, forming a terpy-Rh(II) dimer. In our system, the only available hydride source is via oxidation of the alcohol present in the epoxy motif. However, the observed color change upon heating the complex with base in water, in the absence of model compound, suggests that an alternative mechanism may be operative under our reaction conditions.

Ogo *et al.* also reported that terpy-Rh complexes stirred in water at pH 7 do not produce hydrogen peroxide, but are capable of activating oxygen^{46,47}. Despite this, we investigated whether this pathway could be a feasible route for the reduction of Ac3 into Ac6 (**Fig. S36**). Several mechanisms were considered, including direct reductive elimination from Ac3, a pathway involving an additional hydroxide in the outside coordination sphere, and various bimolecular mechanisms. Considering that Ogo *et al.*⁴⁶ have previously reported that low-valent terpy-Rh(I) complexes can arrange in distances favorable for bimolecular mechanisms, we also examined elimination from Rh(II) dimers and Rh(I) dimers, but in all cases, the computed barriers were prohibitively high (ranging from 77 to 110 kcal mol⁻¹), and in many cases, no transition state could be located. Besides the high barriers, some of the molecular complexes before or after the transition state exhibited highly distorted and unphysical geometries. A summary of this data is presented in **Chapter S5.7**, and the corresponding structures are provided in the coordinates file.

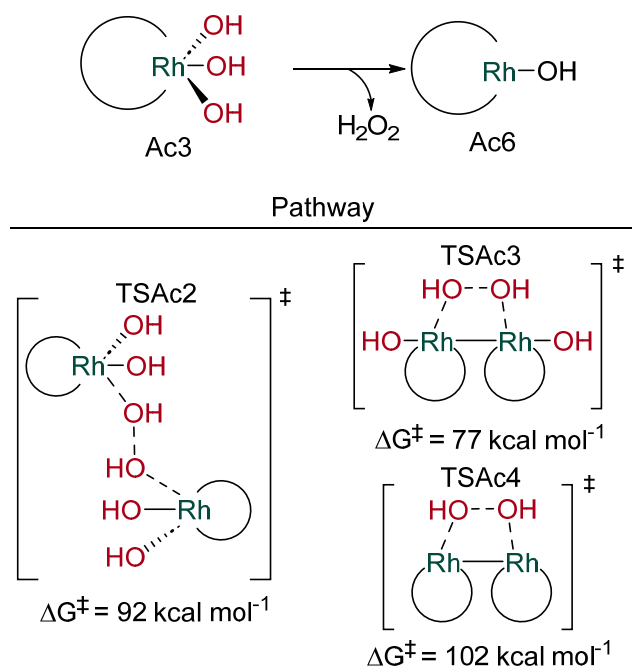


Fig. S36. Pre-activation from Ac3 into Ac6 via the elimination of hydrogen peroxide.

Next, we explored proposed water oxidation mechanisms, which have been studied in the context of terpy-Ru complexes (**Fig. S37**)⁴⁸⁻⁵¹. Two primary pathways have been proposed: (1) the water nucleophilic attack (WNA) cycle, in which a water molecule or hydroxide anion attacks a metal-oxo species, and (2) the interaction of two metal-oxo (I2M) species cycle. Both mechanisms

require the formation of a metal-oxo species, which, under our reaction conditions, could arise via deprotonation of a metal-hydroxo species, followed by ligand dissociation.

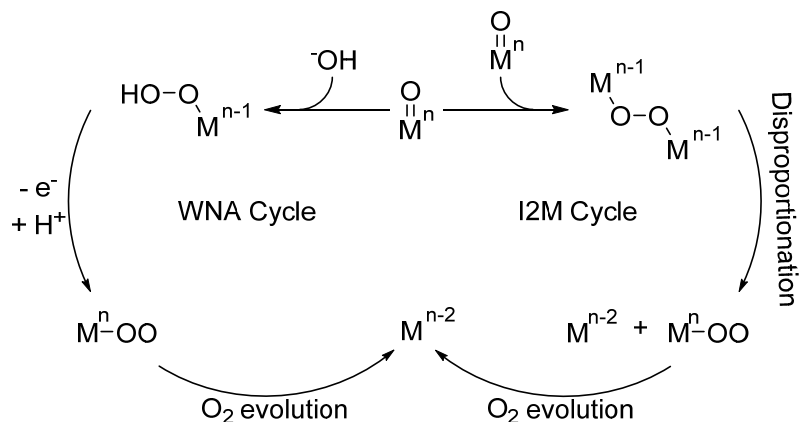


Fig. S37. Reaction scheme inspired by Shaffer *et al.*⁴⁹ of previously proposed mechanisms for water oxidation with a ruthenium catalyst⁴⁸⁻⁵¹.

Considering this, the formation of a terpy^{OMe}-Rh(III) oxide (Ac4) was evaluated (**Fig. S38**). Ac4 can form from Ac2 or Ac3 through deprotonation and ligand dissociation, occurring via either an inter- or intramolecular pathway. In the intramolecular pathway from Ac2 to Ac4 without additional base, the formation of HCl is highly thermodynamically unfavorable. However, in the intermolecular mechanism, where the HCl reacts with NaOH to form NaCl and H₂O, the formation of Ac4 becomes more favorable, although still requiring energy input. Similarly, the formation of Ac4 via Ac3 is energetically disfavored with an energy increase of 17.7 kcal mol⁻¹. Despite this, at the reaction temperatures, this transformation could be accessible, especially with the appropriate driving force.

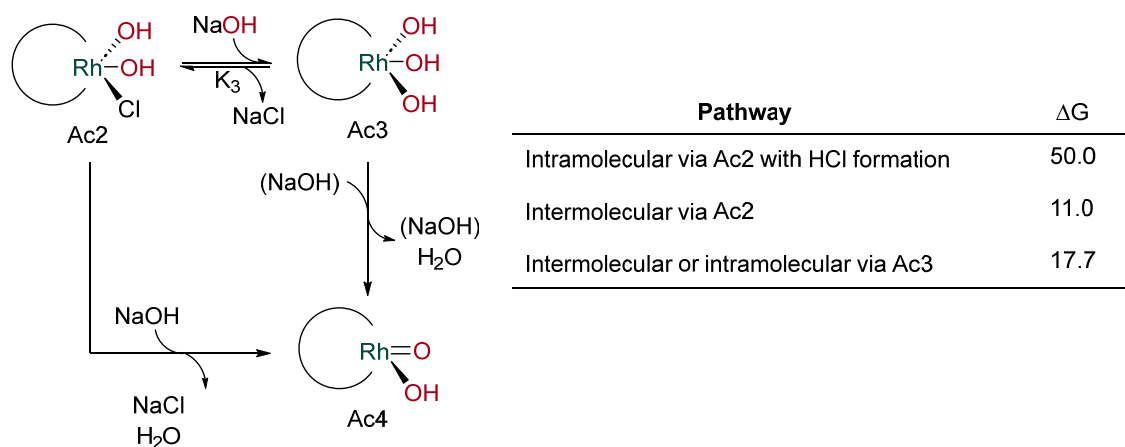


Fig. S38. Left: Formation of a rhodium oxide complex via Ac2 or Ac3. Right: Computed ΔG for different pathways. Barriers calculated at the (U)M06-D3/Def2TZVP//[(U)M06-D3/Def2SVP level of theory with SMD for water. All presented barriers are in kcal mol⁻¹.

Thus, possibilities for I2M and WNA mechanisms were computed (**Fig. S39**). Via deprotonation of Ac3 we can have the formation of two species, either Ac4 or Ac19. From Ac4 two mechanisms are possible, the direct attack of the hydroxy ligand into the metal-oxo (WNA) or the association

with a second Ac4 (I2M). The barrier for the WNA in this case was prohibitively high, but from rhodium peroxo complex Ac17 that arises from the interaction of two Ac4, disproportionation leads to Ac18 with a barrier of 30.8 kcal mol⁻¹ relative to Ac3. Elimination of oxygen from Ac18 occurs with a barrier of 36.7 kcal mol⁻¹ relative to Ac3 or 15.4 kcal mol⁻¹ relative to Ac18, and leads to formation of another Ac6 molecule. Another possibility that we considered is that Ac3 could be deprotonated to Ac19, where a subsequent hydroxide attack into the metal-oxo bond leads to Rh(I) complex Ac20, that upon dissociation of NaOOH leads to formation of Ac6.

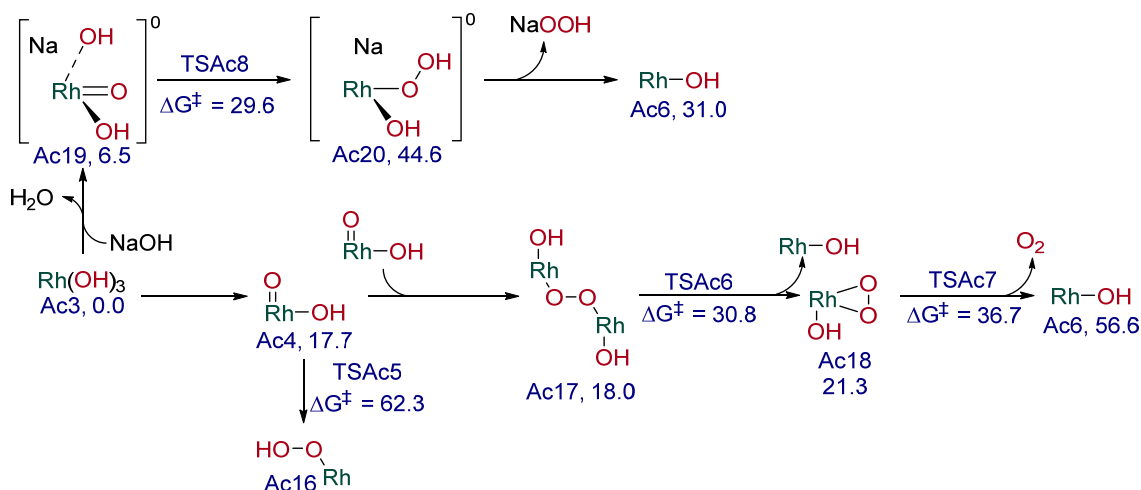


Fig. S39: Computed barriers for water oxidation starting from Ac3. Barriers calculated at the (U)M06-D3/Def2TZVP//((U)M06-D3/Def2SVP level of theory with SMD for water. All presented barriers are in kcal mol⁻¹.

In the absence of primary or secondary alcohols, the WNA or I2M mechanisms described above are the most likely pathways, among those studied. The activation pathways in the presence of alcohols (as the model compounds) were also examined (**Fig. S40**). Starting from Ac3, the first step involves ligand exchange with the secondary alcohol, forming Ac21. Given the high reaction temperature, this step is expected to be thermodynamically driven, with the primary kinetic limitation arising from the heterogeneous insoluble nature of epoxy resins/composites, rather than from a significant ligand exchange barrier. Previous studies by Tang, Su *et al.*⁶ and Yang *et al.*³⁹ on a similar terpy-Rh(III) system for lignin deconstruction further support that this first ligand exchange should be facile under reaction conditions. In our system, this step was also found to be energetically favorable, leading to the formation of Ac21. Subsequently, a β -oxidation over a barrier of 17.8 kcal mol⁻¹ can yield Ketone S and rhodium hydride Ac23 (green pathway, following TSac10). Ac23 can undergo reductive elimination of water with a 31.5 kcal mol⁻¹ barrier, forming Ac24, which upon water dissociation yields Ac6. An alternative pathway involving metal-ligand cooperation for direct reduction via water elimination (blue pathway, following TSac9) was found to be too energetically demanding.

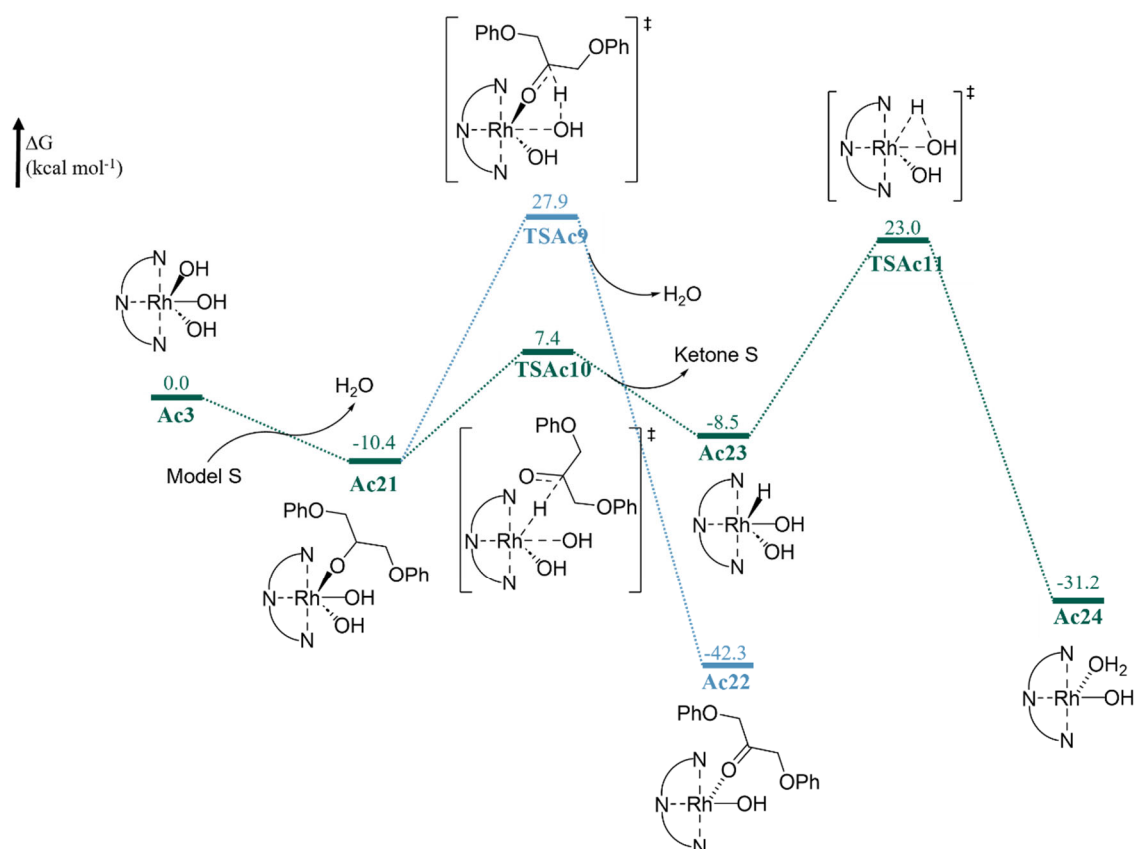


Fig. S40: Computed barriers for model S oxidation starting from Ac3. Barriers calculated at the (U)M06-D3/Def2TZVP// (U)M06-D3/Def2SVP level of theory with SMD for water. All presented barriers are in kcal mol⁻¹.

After the formation of terpy^{OMe}-Rh(I) hydroxo species Ac6, it can react with an alcohol, yielding a terpy^{OMe}-Rh(I) alkoxy complex, which can undergo β-hydride elimination to form a terpy^{OMe}-Rh(I) hydride species. The presence of two distinct terpy^{OMe}-Rh(I) species in solution, namely the hydride and hydroxy complexes, could facilitate bimetallic reductive eliminations. We computed the elimination of water, dihydrogen and hydrogen peroxide, with the associated barriers depicted in **Fig. S41**. While both water and dihydrogen elimination pathways are energetically feasible, H₂O₂ formation is prohibitively energy demanding. Although the barrier for H₂ elimination is lower, the limited availability of alcohol substrates as a hydride source, compared to the concentration of hydroxide, suggests that both pathways may occur under reaction conditions.

In addition to the attempts described above, the inclusion of an explicit water molecule was also explored to stabilize the H₂O₂ elimination transition states. However, no rational transition state could be identified. Despite several attempts to rationalize the experimentally observed peroxide formation mechanism (**Chapter S3.4**), no computed mechanism fully explains this observation.

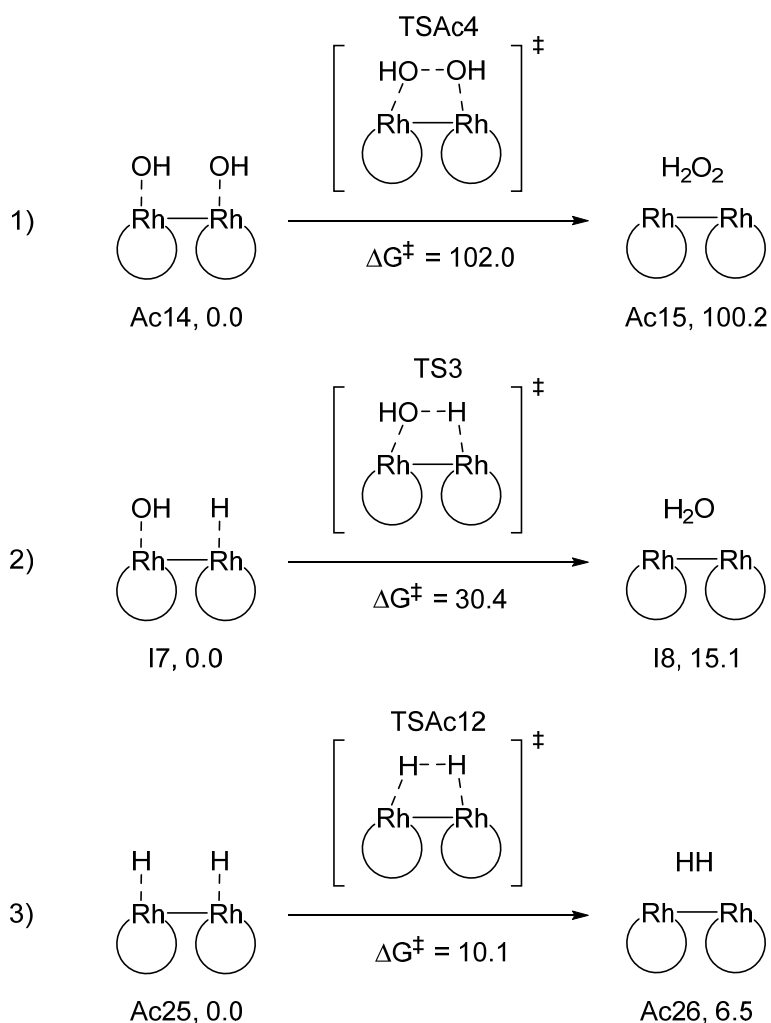


Fig. S41. Bimetallic reductive elimination of H₂O₂ (1), H₂O (2), and H₂ (3). Barriers calculated at the (U)M06-D3/Def2TZVP//((U)M06-D3/Def2SVP level of theory with SMD for water. All presented barriers are in kcal mol⁻¹.

S5.5 Calculated C–O Bond Activation

To gain further insight into the C–O bond activation method, the individual steps were examined separately to assess their thermodynamic feasibility. Based on reports by Wang *et al.*⁵, followed by mechanistic studies from Tang, Su *et al.*⁶ and Yang *et al.*³⁹, the attack of various rhodium species on the model compounds was computationally evaluated.

The addition of a water molecule near the leaving phenoxide was found to be preferential, leading to more stable structures. The initial calculations considered Ac3, but all computed barriers were too high considering the reaction conditions (**Fig. S42**). Next, Ac16, a terpy^{OMe}-Rh(III) hydride, was tested, but as in the previous case, the barriers remained unfeasible under the depicted reaction conditions (**Fig. S43**).

Similarly, when considering either terpy^{OMe}-Rh(I) species Ac6 (**Fig. S44**) or I6 (**Fig. S45**), the reaction remained unfeasible for all model compounds. This suggests that a different mechanism is likely responsible for the activation of stronger C–O bonds in epoxy composites.

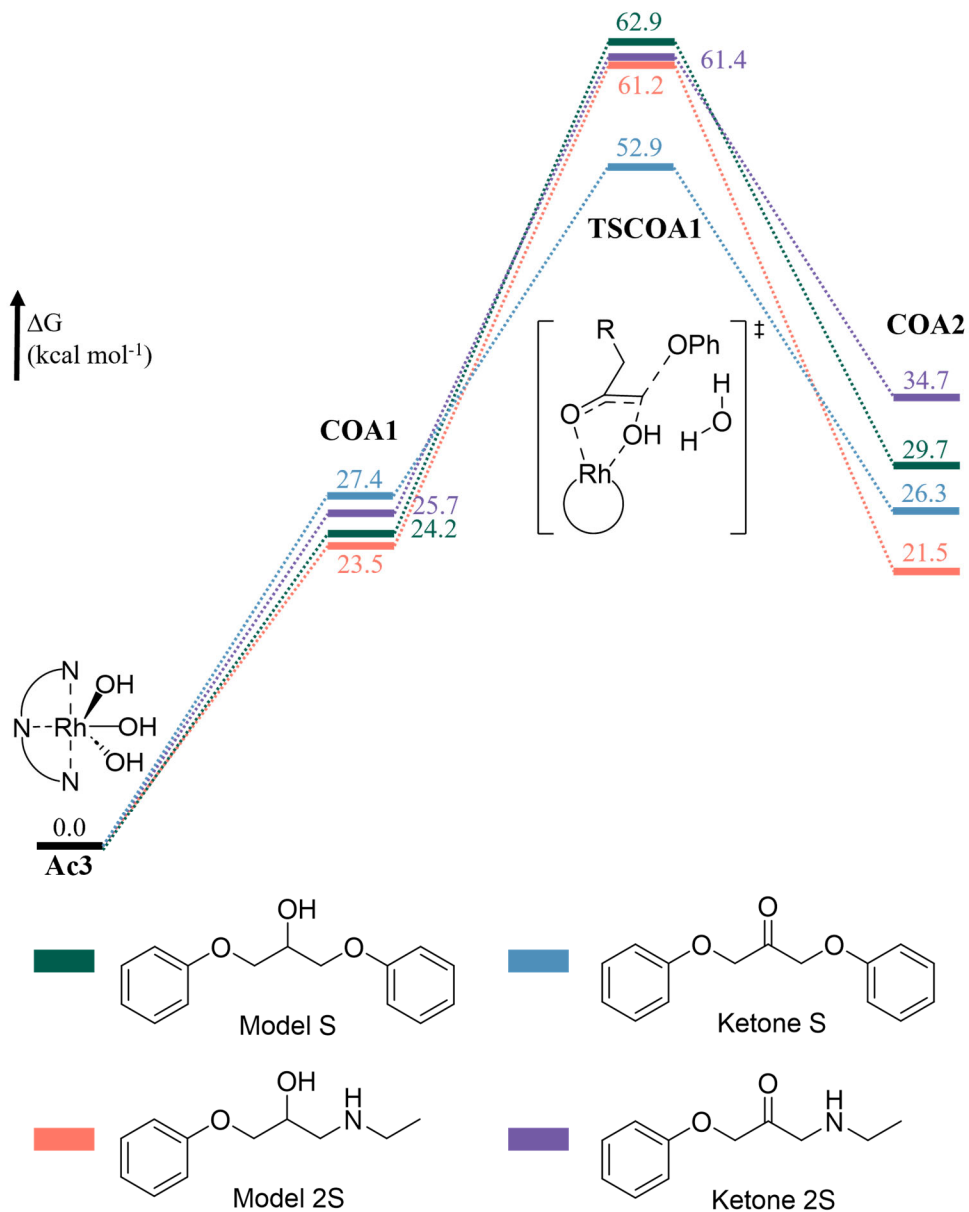


Fig. S42. Computed barriers for hydride attack from Ac3 into model compounds. Barriers calculated at the (U)M06-D3/Def2TZVP//(U)M06-D3/Def2SVP level of theory with SMD for water.

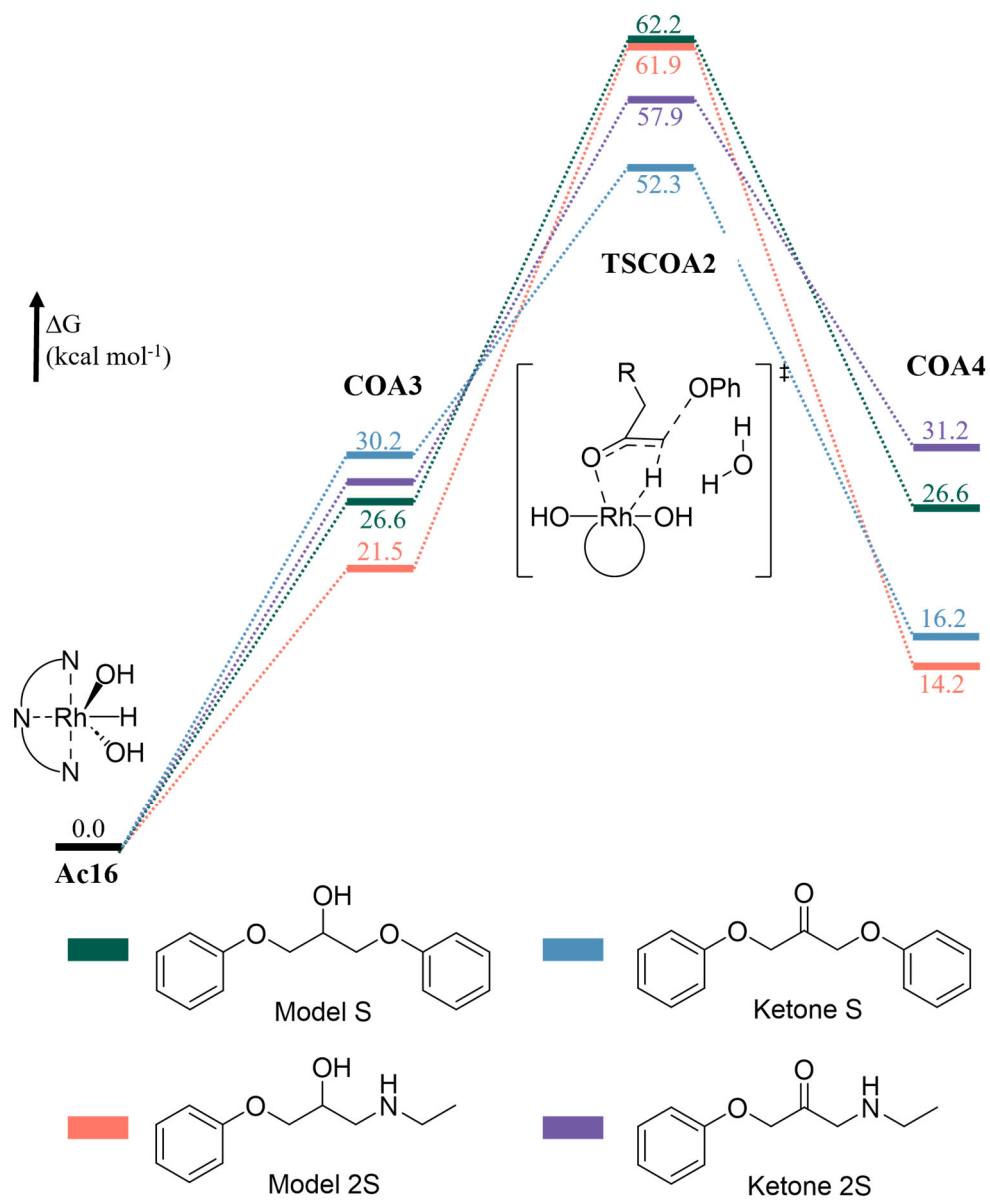


Fig. S43. Computed barriers for hydride attack from Ac16 into model compounds. Barriers calculated at the (U)M06-D3/Def2TZVP//((U)M06-D3/Def2SVP level of theory with SMD for water.

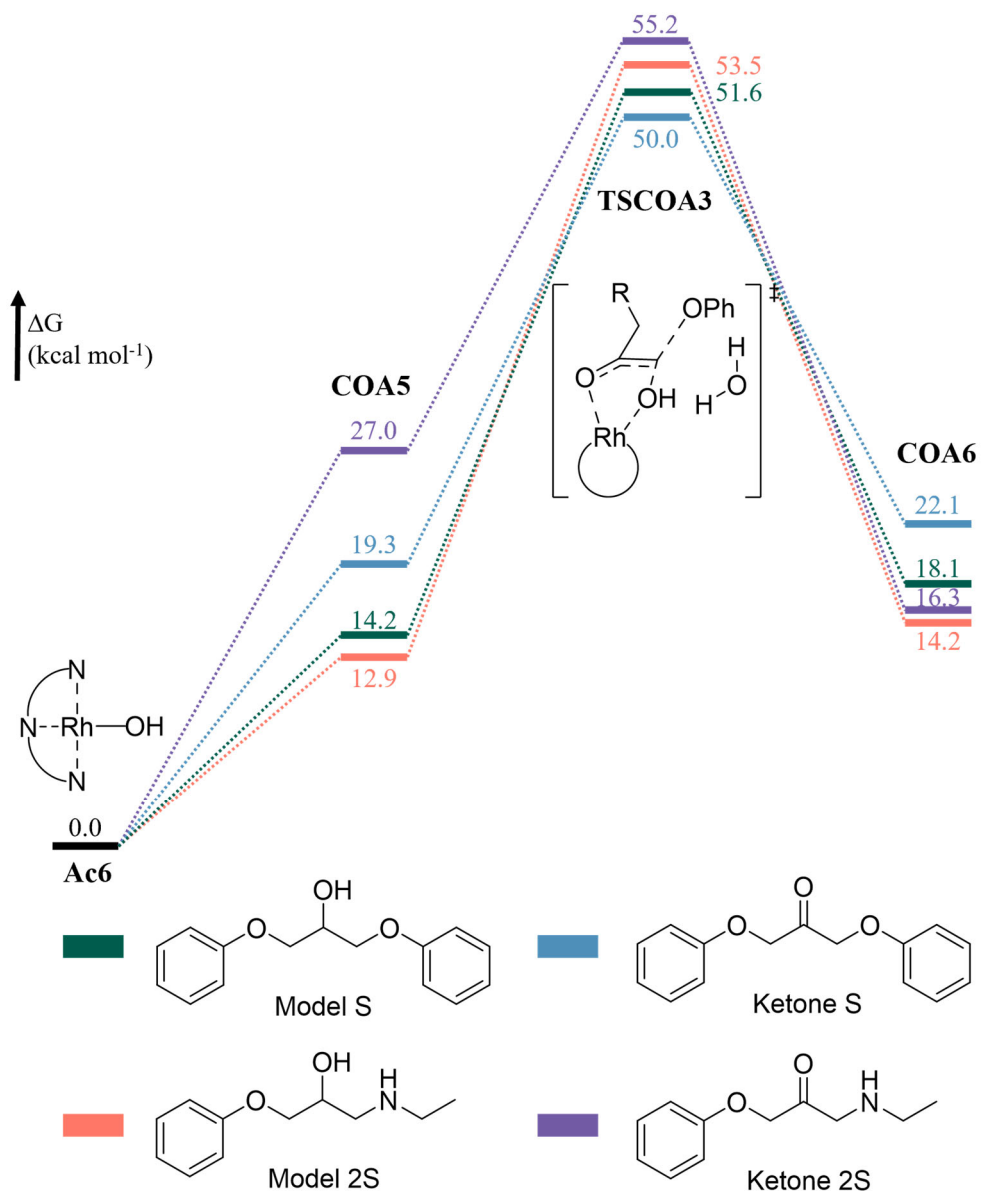


Fig. S44. Computed barriers for hydroxide attack from Ac6 into model compounds. Barriers calculated at the (U)M06-D3/Def2TZVP/(U)M06-D3/Def2SVP level of theory with SMD for water.

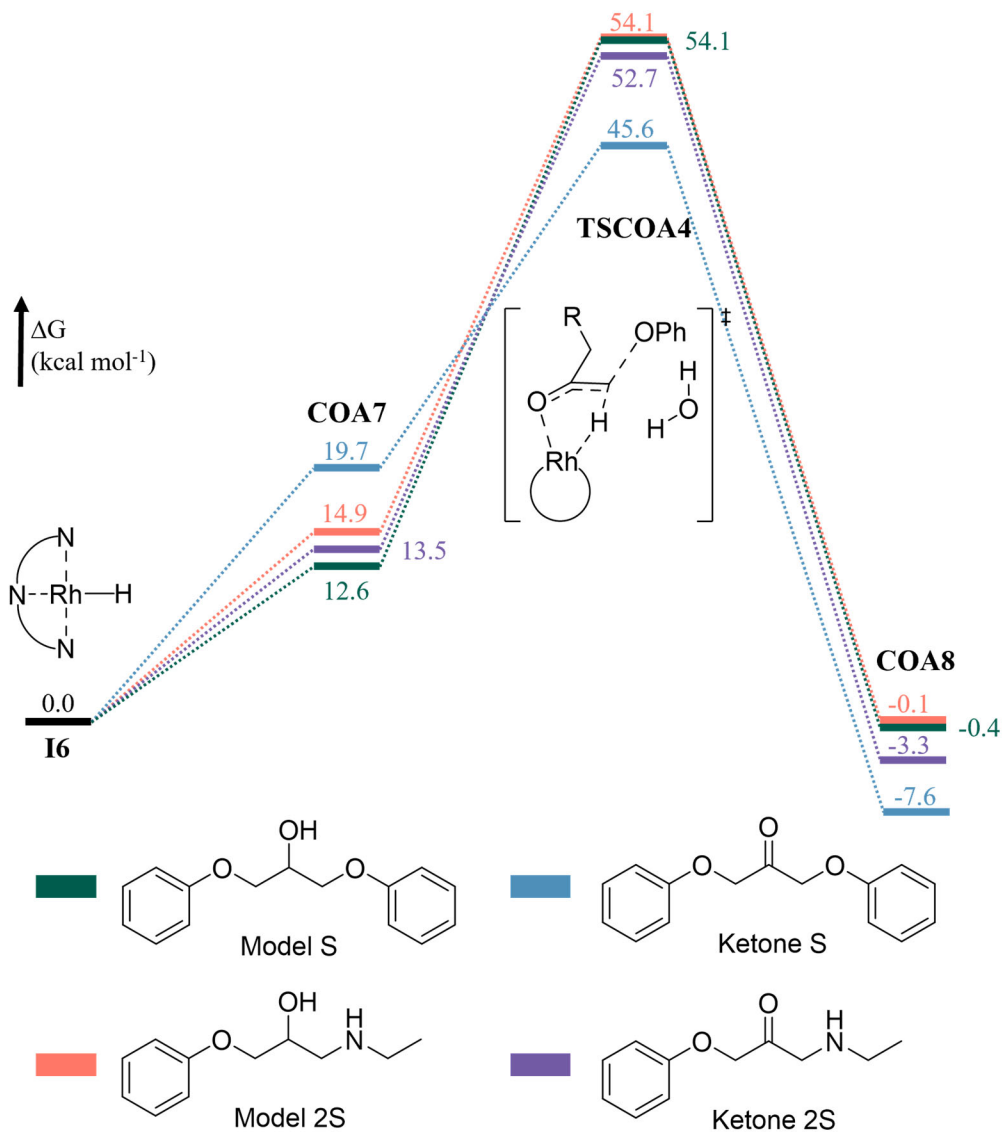


Fig. S45. Computed barriers for hydride attack from **I6** into model compounds. Barriers calculated at the (U)M06-D3/Def2TZVP//[(U)M06-D3/Def2SVP level of theory with SMD for water.

Next, the oxidative addition into the C–O bond with Rh(I) complexes was investigated (**Fig. S46**). Although modifications to the auxiliary ligand can reduce the reaction barrier, it remains 47.3 kcal mol⁻¹ for X = H₂O. Even the cationic $\text{terpy}^{\text{OMe}}\text{-Rh(I)}$ complex undergoes oxidative addition into the C–O bond with a significant barrier of 37.1 kcal mol⁻¹ (relative to **COA9**).

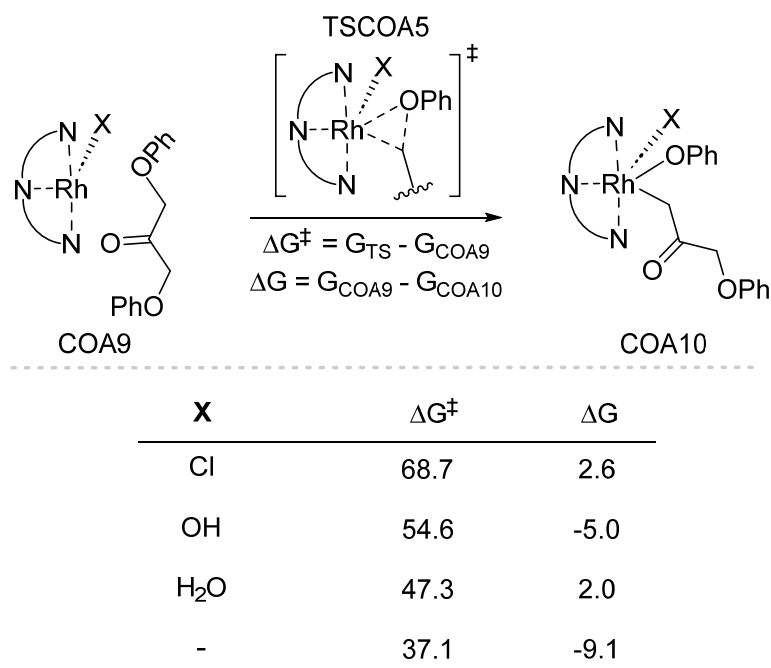


Fig. S46. Possibilities of C–O bond activation with a monomeric terpy^{OMe}-Rh(I) complex. Barriers calculated at the (U)M06-D3/Def2TZVP//((U)M06-D3/Def2SVP level of theory with SMD for water. All presented barriers are in kcal mol⁻¹.

As previously noted, Ogo *et al.*⁴⁶ reported that terpy-Rh complexes can form dimers, which may provide an optimal configuration for bimetallic reactions. Thus, a six-membered cyclic oxidative addition into the targeted C–O bond in ketone S was computed (**Fig. S47**). A plausible route for the formation of B1 is *via* the dimerization of two terpy^{OMe}-Rh(I)-OH complexes, yielding Ac14 ($\Delta G = -9.9$ kcal mol⁻¹), which can subsequently coordinate with Ketone S to afford complex B1. For the favorable six-membered concerted oxidative addition (TSB1) to occur, the geometry of the Rh(I) complex must be significantly perturbed. Due to the preference of the hydroxo ligand for square-planar geometry, the complexation of ketone S to form B1 is highly energetically disfavored ($\Delta G = 53.6$ kcal mol⁻¹). This results in an overall unfeasible activation barrier of 66.1 kcal mol⁻¹ for TSB1.

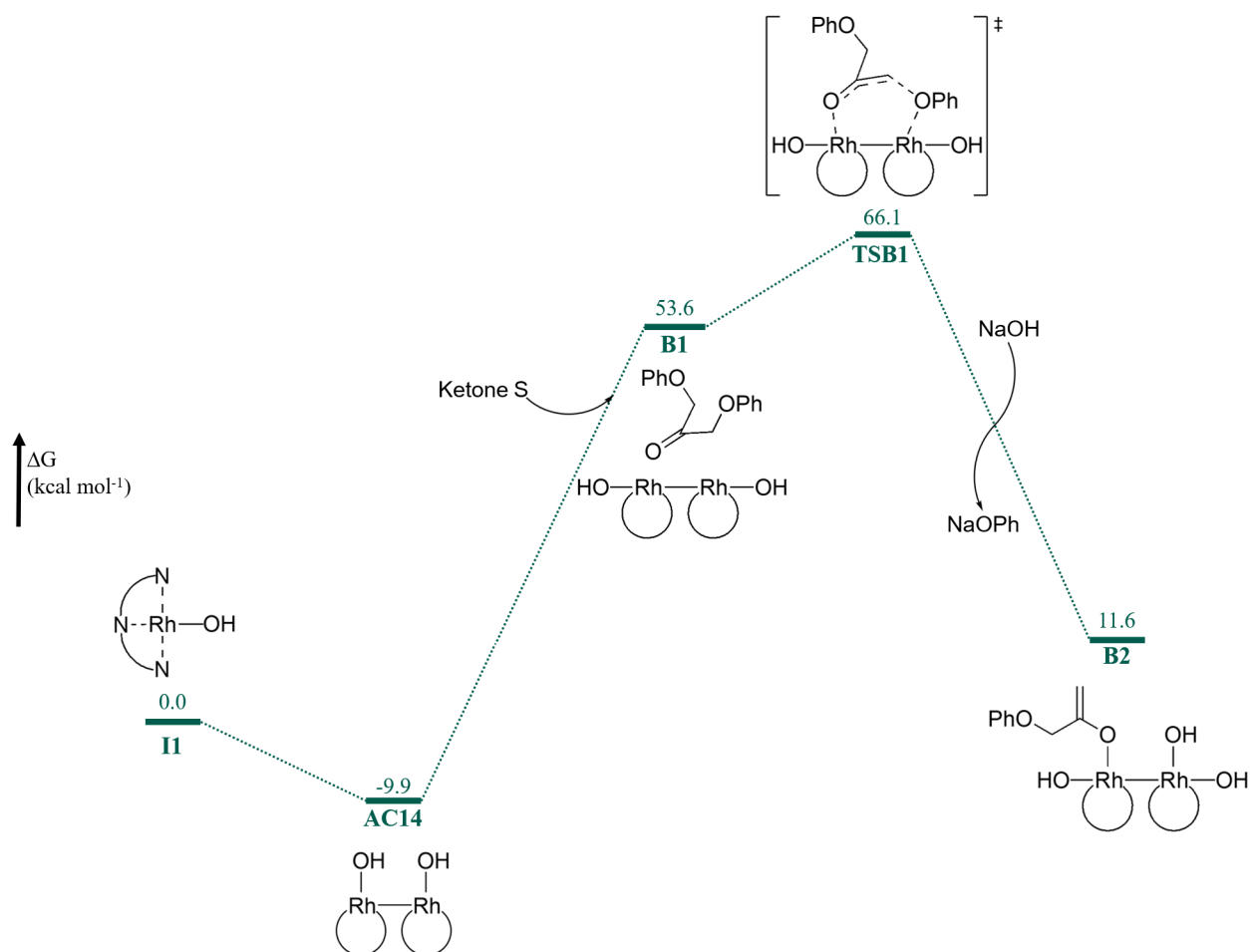


Fig. S47. Calculated C–O bond activation via terpy^{OMe}-Rh(I) dimer TSB1. Barriers calculated at the (U)M06-D3/Def2TZVP//((U)M06-D3/Def2SVP level of theory with SMD for water. All presented barriers are in kcal mol⁻¹.

The presence of two distinct terpy^{OMe}-Rh(I) species in solution, namely the hydride and hydroxy complexes, could enable a bimetallic reductive elimination of water or H₂, leading to the formation of a bimetallic terpy^{OMe}-Rh(0) complex (see **Fig. S42**). From this, two possible pathways emerge; In the first, I8 can dissociate to form a Rh(0)-H₂O monomer (COA11) and a Rh(0)-KetoneS monomer (COA12) (blue pathway - **Fig. S48**). However, this pathway is endergonic and, therefore, less favorable compared to the exergonic formation of I9, from which oxidative addition occurs readily, with a low barrier of only 14 kcal mol⁻¹ (relative to I9 - **Fig. S48**). When considering the ligand exchange from COA11 to form a second COA12, the dissociation of I8 into monomeric species is also not thermodynamically favorable, further supporting the bimetallic oxidative addition as the favored pathway. When comparing the barriers for monomeric and bimetallic oxidative addition (TSCOA6 vs TS4) the pathway going via the bimetallic complex (green pathway) is still more favorable, besides leading to a more stable product. Thus, according to the obtained results, the bimetallic pathway is both thermodynamically and kinetically more favorable.

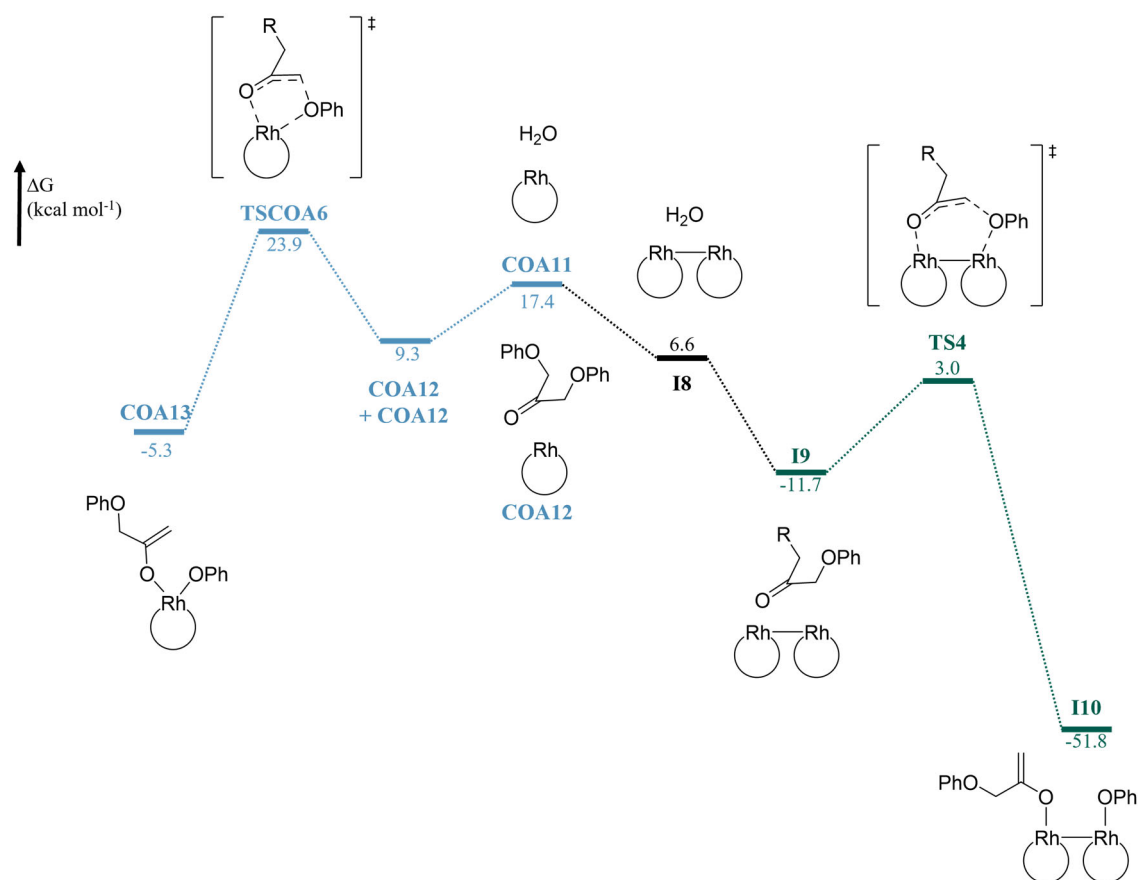


Fig. S48. Pathways for the C–O bond activation via $\text{terpy}^{\text{OMe}}\text{-Rh(0)}$ **I8**. Barriers calculated at the (U)M06-D3/Def2TZVP//((U)M06-D3/Def2SVP level of theory with SMD for water. All presented barriers are in kcal mol^{-1} .

S5.6 Proposed Catalytic Cycle

The previously discussed individual steps can be combined to form the most feasible cycle among those computed, as presented in **Fig. S49**. The cycle begins after the $\text{terpy}^{\text{OMe}}\text{-Rh-Cl}_3$ precatalyst activation step, generating **I1**.

First, **Ac6** undergoes ligand exchange, replacing the hydroxy ligand with an alkoxy group, leading to **I4**. This intermediate then undergoes β -hydride elimination, forming a $\text{terpy}^{\text{OMe}}\text{-Rh(I)}$ hydride (**I6**). **I6** can undergo reductive elimination of either H_2 or water (**Fig. S41**), which determines the rate determining step. If H_2 elimination occurs, β -hydride elimination is rate-determining, whereas if H_2O elimination occurs, the elimination step itself is rate-determining. Following elimination and ligand exchange (replacing water or dihydrogen with ketone **S**), complex **I9** is obtained. **I9** then undergoes a bimetallic six-membered cyclic oxidative addition (via **TS4**) into the C–O bond, forming a Rh(I) dimer (**I10**). This dimer can dissociate into monomeric **I12** and a $\text{terpy}^{\text{OMe}}\text{-Rh(I)}$ phenoxide complex. Due to the highly basic medium, the latter undergoes ligand exchange, regenerating **Ac6**. Finally, **I12** is protonated by water, forming another molecule of **Ac6**, thus completing the most feasible cycle among those computed.

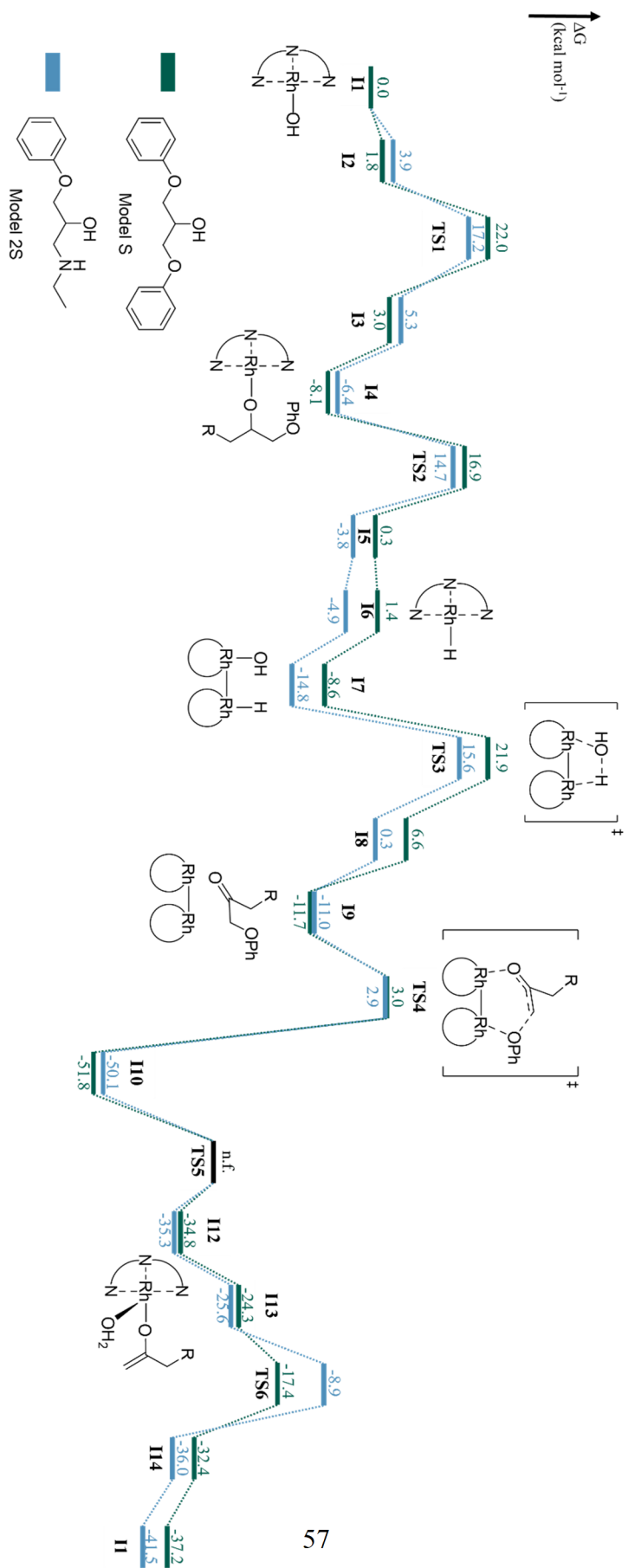


Fig. S49. Proposed catalytic cycle for the terpy^{OMe}-Rh catalyzed deconstruction of epoxy resins. Barriers calculated at the (U)M06-D3/Def2TZVP/(U)M06-D3/Def2SVP level of theory with SMD for water. All presented barriers are in kcal mol⁻¹.

S5.7 Comment on the Computational Method and Calculated Energies

As discussed in **Chapter S5.2**, some of the computed complexes exhibit a degree of multireference character. Grimme, Hansen *et al.* have previously reported that avoiding functionals with high degree of HF exchange can lead to more reliable results in such cases³⁷. To assess whether the observed trend in our catalytic cycle remains consistent regardless of the chosen functional, and to demonstrate that our findings are not heavily dependent on a specific functional, we computed the transition state barriers with energy refinement at different levels of theory (**Table S14**).

To assess the impact of functional choice on the conclusions drawn from the catalytic cycle, we kept the same optimized structures at the (U)M06-D3/def2-SVP level of theory, using an ultrafine integration grid and without imposing symmetry constraints³⁰⁻³². The electronic energy refinement was performed via single-point calculations, varying the functional while keeping the def2-TZVP(2) basis set and incorporating the SMD³³ solvation model for water. The selected functionals; TPSS⁵², M06L³², B3LYP^{12,53-55}, PBE^{56,57} and PBE0⁵⁸ were chosen due to their broad use in transition-metal systems and varying degrees of Hartree-Fock (HF) exchange^{38,45,59-62}. This approach enables us to evaluate whether the degree of multireference character significantly affects the computational results.

Although variations are observed between functionals, the overall trend remains consistent: either the reductive elimination or β -hydride elimination emerges as the rate-determining step across all studied functionals. Notably, the barrier for the key C–O bond activation step remains energetically accessible, regardless of the functional employed. Additionally, even the highest computed barrier falls within the expected range for such an intrinsically energy-demanding transformation (as discussed before, **Chapter S5.2**). Thus, we can conclude that the proposed catalytic cycle provides a reliable representation of the reaction mechanism, and this conclusion remains robust across different levels of theory.

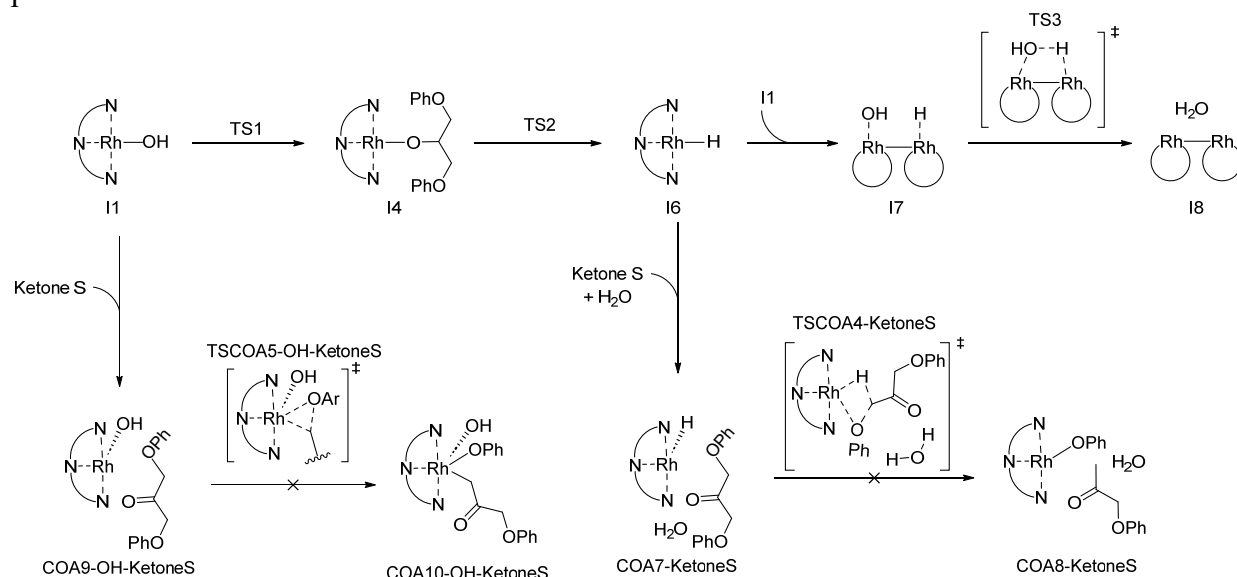
Table S14. Computed barriers computed with energy refinement using different functionals. All presented barriers are in kcal mol⁻¹.

Step	(U)M06-D3	(U)M06L-D3	(U)TPSS-D3	(U)PBE-D3	(U)PBE0-D3	(U)B3LYP-D3
I2→TS1	20	20	20	20	19	19
I4→TS2	25	27	27	28	31	28
I7→TS3	30	26	19	17	25	29
I9→TS4	15	10	7	7	14	10
I13→TS6	7	10	11	11	11	11

To further support the hypothesis that the proposed cycle is the most energetically favorable pathway, two other C–O bond activation mechanisms were computed using the same range of functionals (**Table S15**). From I1 complexation of ketone S leads to COA9-OH-KetoneS, however, the oxidative addition remains significantly higher in energy, compared to the barriers for TS1 and TS2 across all functionals (**Table S14** and **Table S15**). Following β -hydride elimination from I4, I6 is formed, which can subsequently undergo complexation with ketone S to generate COA7-KetoneS. In this case, the complexation of ketone S is endergonic, whereas the

formation of the I7 dimer is exergonic. Additionally, the barriers for TSCOA4-KetoneS are substantially higher than those for TS3. Notably, after water elimination, oxidative addition is an exergonic step with a low barrier (**Table S15**).

Table S15. Pathways from I6 computed with energy refinement using different functionals. All presented barriers are in kcal mol⁻¹.



Step	(U)M06-D3	(U)M06L-D3	(U)TPSS-D3	(U)PBE-D3	(U)PBE0-D3	(U)B3LYP-D3
I6→ COA7→ TSCOA4	45.7	42.5	37.3	37.7	42.7	44.6
I1→ COA9-OH→ TSCOA5-OH	57.3	48.0	45.6	48.11	54.2	58.8

S5.8 Reported Data for Individual Species and Mechanisms

Relevant computational data for the presented molecules:

Table S16. Energy of the reported species calculated at the (U)M06-D3/Def2TZVP// (U)M06-D3/Def2SVP level of theory with SMD for water.

Name	G kcal mol ⁻¹	H kcal mol ⁻¹	E _{electronic} kcal mol ⁻¹
terpy ^{OMe} -Rh-Cl ₃	-1618185.76141	-1618094.98161	-1618343.69312
Ac1	-1376959.75174	-1376869.15015	-1377125.73992
Ac2	-1135733.93646	-1135642.96214	-1135907.47661
Ac3	-894506.15969	-894415.78839	-894688.24513
Model S	-506033.49690	-505970.68164	-506165.17087
Ketone S	-505288.26020	-505225.83901	-505404.70914
Ketone 3S	-313219.49770	-313171.02646	-313289.67667
Model 2S	-397955.24826	-397896.52995	-398081.71901
Ketone 2S	-397216.28669	-397157.67694	-397326.78003
Ketone 4S	-205145.56300	-205102.70287	-205211.54212
NaOH	-149456.27922	-149432.11231	-149443.05591
NaCl	-390690.66426	-390666.90209	-390670.71353
Ac4	-846519.9858	-846434.2675	-846688.0529
Ac5	-846519.98584	-846434.26745	-846688.05293
Ac6	-799358.44594	-799276.05896	-799526.57453
O ₂	-94301.76662	-94281.50528	-94286.90303
H ₂ O	-47968.52046	-47948.22899	-47965.07109
NaOOH	-196604.48122	-196575.78879	-196590.48233
TSAc1	-942068.7796	-941974.1306	-942253.978
Ac8	-942068.2305	-941972.8386	-942254.3476
Ac9	-1789001.66574	-1788840.75152	-1789388.02753
TSAc2	-1788909.10610	-1788748.26028	-1789292.32223
Ac10	-1788967.36628	-1788809.21620	-1789356.62084
Ac11	-1789001.67672	-1788843.16395	-1789390.32951
TsAc2'	-1788891.27606	-1788731.45432	-1789274.29767
Ac12	-1788964.35898	-1788807.27189	-1789354.07790
B1	-1693866.69608	-1693718.01196	-1694242.11502
TSAc3	-1693787.23048	-1693635.50161	-1694157.56843
Ac13	-1693832.92491	-1693683.20278	-1694208.46734
Ac14	-1598726.76886	-1598584.61375	-1599087.08877
TSAc4	-1598624.76685	-1598482.93177	-1598983.35675

Ac15	-1598626.57355	-1598483.93841	-1598985.49037
TSAc5	-846475.36732	-846390.26263	-846642.58729
Ac17	-1693057.30171	-1692912.35737	-1693421.05844
TSAc6	-1693044.43307	-1692900.46637	-1693408.51484
Ac18	-893695.49946	-1692915.15872	-1693424.88575
TSAc7	-893680.10639	-893848.72756	-893848.72756
Ac19	-995987.40023	-995893.52058	-996160.11898
TSAc8	-894476.53183	-894384.34706	-894656.90106
Ac20	-995949.30809	-995852.93037	-996119.42585
Ac21	-1352581.57302	-1352454.21499	-1352904.26552
TSAc9	-1352543.30562	-1352413.33594	-1352859.18034
Ac22	-1304644.92950	-1304519.03355	-1304949.99176
TSAc10	-1352564.14264	-1352436.18472	-1352882.46021
Ac23	-847291.40578	-847204.21717	-847471.01699
TSAc11	-847259.92078	-847173.05094	-847438.12137
Ac24	-847314.08916	-847225.23516	-847494.74264
B1	-2103951.58354	-2103767.84526	-2104449.22743
TSB1	-2103939.03115	-2103756.45940	-2104436.67693
B2	-2103993.49207	-2103811.20269	-2104492.90488
Ac25	-1504277.41229	-1504141.04273	-1504631.78225
TSAc12	-1504267.33533	-1504132.94052	-1504621.77243
Ac26	-1504270.90135	-1504135.17122	-1504626.30794
COA1-ModelS	-1448484.01346	-1448346.24709	-1448833.92503
TSCOA1-ModelS	-1448445.34509	-1448309.06966	-1448795.55095
COA2-ModelS	-1448478.52873	-1448340.36641	-1448828.06694
COA1-KetoneS	-1447735.61096	-1447596.13591	-1448068.57125
TSCOA1-KetoneS	-1447710.08922	-1447572.59769	-1448043.70085
COA2-KetoneS	-1447736.67369	-1447597.71758	-1448069.97973
COA1-Model2S	-1340406.51054	-1340272.03604	-1340750.74700
TSCOA1-Model2S	-1340368.80827	-1340236.80800	-1340713.93327
COA2-Model2S	-1340408.51773	-1340275.41243	-1340753.55174
COA1-Ketone2S	-1339665.34840	-1339529.35283	-1339992.51121
TSCOA1-Ketone2S	-1339629.58943	-1339497.16622	-1339959.22522
COA2-Ketone2S	-1339656.30091	-1339525.39688	-1339988.41658
COA3-ModelS	-1401263.26109	-1401127.03022	-1401609.36311
TSCOA2-ModelS	-1401227.70575	-1401093.14591	-1401573.48084
COA4-ModelS	-1401263.28839	-1401127.03304	-1401609.36280
COA3-KetoneS	-1400514.47833	-1400376.37374	-1400843.66421

TSCOA2-KetoneS	-1400492.41587	-1400355.89885	-1400820.91526
COA4-KetoneS	-1400528.47321	-1400392.35403	-1400859.96138
COA3-Model2S	-1293190.15238	-1293057.97201	-1293530.73177
TSCOA2-Model2S	-1293149.76309	-1293020.10088	-1293491.03649
COA4-Model2S	-1293197.49118	-1293065.28634	-1293538.59704
TSCOA2-Ketone2S	-1292414.78508	-1292281.19284	-1292736.38761
COA4-Ketone2S	-1292441.46845	-1292311.64434	-1292769.83355
COA5-ModelS	-1353346.21842	-1353211.91585	-1353677.90739
TSCOA3-ModelS	-1353308.91153	-1353178.94750	-1353643.32825
COA6-ModelS	-1353342.33030	-1353209.85564	-1353676.00217
COA5-KetoneS	-1352595.94277	-1352462.13467	-1352911.92290
TSCOA3-KetoneS	-1352565.20926	-1352434.05110	-1352883.13214
COA6-KetoneS	-1352593.11136	-1352461.00630	-1352911.66048
COA5-Model2S	-1245269.31301	-1245140.29901	-1245596.64713
TSCOA3-Model2S	-1245228.73095	-1245103.11926	-1245557.56166
COA6-Model2S	-1245266.77458	-1245139.14987	-1245595.67934
COA5-Ketone2S	-1244516.22171	-1244388.14457	-1244829.25071
TSCOA3-Ketone2S	-1244488.04677	-1244362.97410	-1244802.70602
COA6-Ketone2S	-1244526.91337	-1244398.10142	-1244838.49096
COA7-ModelS	-1306123.20617	-1305991.75873	-1306451.68611
TSCOA4-ModelS	-1306081.65156	-1305951.43213	-1306409.76566
COA8-ModelS	-1306136.21243	-1306006.13984	-1306467.17099
COA7-KetoneS	-1305370.82646	-1305237.27438	-1305681.43519
TSCOA4-KetoneS	-1305344.90556	-1305214.21237	-1305656.97449
COA8-KetoneS	-1305398.13036	-1305264.88576	-1305710.50928
COA7-Model2S	-1198042.64426	-1197915.45503	-1198365.72770
TSCOA4-Model2S	-1198003.48299	-1197877.55316	-1198326.37755
COA8-Model2S	-1198057.66981	-1197930.32371	-1198381.78800
COA7-Ketone2S	-1197305.12576	-1197179.36346	-1197613.93796
TSCOA4-Ketone2S	-1197265.89508	-1197142.20668	-1197575.53308
COA8-Ketone2S	-1197321.86620	-1197194.36824	-1197630.45062
COA9-Cl	-1545881.23865	-1545754.21884	-1546177.36845
TSCOA5-Cl	-1545812.51077	-1545685.83672	-1546106.73548
COA10-Cl	-1545878.59737	-1545753.15008	-1546175.86985
COA9-OH	-1304644.03425	-1304518.59260	-1304949.78990
TSCOA5-OH	-1304589.41847	-1304464.28367	-1304893.48175
COA10-OH	-1304649.08317	-1304524.23389	-1304954.88589
COA9-H ₂ O	-1304941.29982	-1304815.11961	-1305255.62273

TSCOA5-H ₂ O	-1304894.03658	-1304764.49423	-1305202.30788
COA10-H ₂ O	-1304939.32408	-1304813.88118	-1305253.20334
COA9-cationic	-1256974.69236	-1256851.89438	-1257273.37295
TSCOA5-cationic	-1256937.55591	-1256816.51555	-1257235.70061
COA10-cationic	-1256983.76808	-1256862.18933	-1257282.66202
COA11	-799718.29184	-799632.88282	-799890.25257
COA12	-1257046.17823	-1256922.85879	-1257342.21390
TSCOA6	-1257031.52592	-1256908.08098	-1257325.79894
COA13	-1257060.75713	-1256938.02001	-1257357.16679
I2	-1305390.14210	-1305264.48272	-1305711.16106
TS1	-1305369.96973	-1305244.65171	-1305689.91943
I3	-1305388.93887	-1305261.67246	-1305708.26170
I4	-1257431.50477	-1257306.62913	-1257734.73348
TS2	-1257406.53014	-1257285.12019	-1257709.47773
I5	-1257423.09966	-1257301.17327	-1257726.27315
I6	-752133.78300	-752054.12689	-752298.86382
I7	-1551502.15950	-1551361.87560	-1551858.53683
TS3	-1551471.73598	-1551333.92004	-1551827.28187
I8	-1551487.01693	-1551346.17392	-1551844.16922
I9	-2008825.02163	-2008652.76660	-2009313.50277
TS4	-2008810.33028	-2008635.74221	-2009294.51870
I10	-2008865.12421	-2008688.85193	-2009349.44377
I11	-944241.09515	-944145.98309	-944452.41080
I12	-1064607.01910	-1064498.99372	-1064851.70896
I13	-1112565.11107	-1112449.35740	-1112820.77026
TS5	-1112558.18837	-1112449.54553	-1112818.09385
I14	-1112573.14037	-1112463.48538	-1112833.51083
I2-Model2S	-1197309.79793	-1197188.22420	-1197625.59296
TS1-Model2S	-1197296.53321	-1197176.43097	-1197611.92350
I3-Model2S	-1197308.40256	-1197180.89331	-1197617.43627
I4-Model2S	-1149351.63512	-1149233.90419	-1149652.50819
TS2-Model2S	-1149330.48856	-1149214.20590	-1149628.92881
I5-Model2S	-1149348.95105	-1149229.09541	-1149644.49602
I9-Model2S	-1900746.07421	-1900577.54842	-1901228.52194
TS4-Model2S	-1900732.14321	-1900562.39881	-1901211.56137
I10-Model2S	-1900785.25368	-1900612.71565	-1901263.87805
I12-Model2S	-956529.34432	-956426.76376	-956769.70757
I13-Model2S	-1004488.07590	-1004377.34913	-1004738.87071

TS5-Model2S	-1004471.42776	-1004366.41940	-1004725.18437
I14-Model2S	-1004498.49868	-1004390.33148	-1004751.44330
terpy*-Rh(0)	-830753.1800005	-830649.9788405	-831037.0246055
Acetophenone	-241383.36264125	-241342.52117625	-241438.43266875
THF	-145770.563969	-145738.1994015	-145817.1175665
terpy*-Rh(0)-THF	-976522.084232	-976403.113997	-976871.038237
terpy*-Rh(0)-Acetophenone	-1072139.134405	-1072015.71394	-1072500.280735

Table S17. Energy of the reported species calculated at the (U)M06L-D3/Def2TZVP//(U)M06-D3/Def2SVP level of theory with SMD for water.

Name	G kcal mol ⁻¹	H kcal mol ⁻¹	E _{electronic} kcal mol ⁻¹
I1	-799827.76907	-799745.38208	-799995.89765
Ketone S	-505561.47445	-505499.05326	-505677.92339
H2O	-47979.40789	-47959.11643	-47975.95853
I2	-1306125.92432	-1306000.26493	-1306446.94328
TS1	-1306106.35479	-1305981.03676	-1306426.30449
I4	-1258159.14310	-1258034.26747	-1258462.37181
TS2	-1258131.92002	-1258010.51006	-1258434.86761
I6	-752587.32174	-752507.66563	-752752.40256
I7	-1552419.45356	-1552279.16966	-1552775.83089
TS3	-1552393.87371	-1552256.05777	-1552749.41961
I9	-2010003.16411	-2009830.90908	-2010491.64525
TS4	-2009993.06619	-2009818.47812	-2010477.25460
I13	-1113200.05253	-1113084.29886	-1113455.71172
TS6	-1113190.38470	-1113081.74186	-1113450.29018
COA9-OH	-1305384.35385	-1305258.91221	-1305690.10950
TSCOA5-OH	-1305341.26330	-1305216.12851	-1305645.32658
COA7-KetoneS	-1306107.77664	-1305974.22456	-1306418.38538
TSCOA4-KetoneS	-1306085.73043	-1305955.03724	-1306397.79936

Table S18. Energy of the reported species calculated at the TPSS-D3/Def2TZVP//(U)M06-D3/Def2SVP level of theory with SMD for water.

Name	G kcal mol ⁻¹	H kcal mol ⁻¹	E _{electronic} kcal mol ⁻¹
I1	-800029.85739	-799947.47040	-800197.98597
Ketone S	-505729.88209	-505667.46090	-505846.33103
H2O	-47992.37644	-47972.08497	-47988.92707
I2	-1306498.01776	-1306372.35838	-1306819.03672
TS1	-1306477.76369	-1306352.44567	-1306797.71339
I4	-1258518.36087	-1258393.48524	-1258821.58958
TS2	-1258491.65943	-1258370.24948	-1258794.60702
I6	-752776.40933	-752696.75322	-752941.49014
I7	-1552808.48273	-1552668.19883	-1553164.86006
TS3	-1552789.27288	-1552651.45694	-1553144.81878
I9	-2010548.61899	-2010376.36396	-2011037.10013
TS4	-2010541.94552	-2010367.35745	-2011026.13394
I13	-1113506.45557	-1113390.70190	-1113762.11476
TS6	-1113495.22966	-1113386.58682	-1113755.13514
COA9-OH	-1305752.15677	-1305626.71512	-1306057.91242
TSCOA5-OH	-1305714.12161	-1305588.98681	-1306018.18489
COA7-KetoneS	-1306479.26925	-1306345.71717	-1306789.87799
TSCOA4-KetoneS	-1306461.33863	-1306330.64544	-1306773.40756

Table S19. Energy of the reported species calculated at the PBE-D3/Def2TZVP//(U)M06-D3/Def2SVP level of theory with SMD for water.

Name	G kcal mol ⁻¹	H kcal mol ⁻¹	E _{electronic} kcal mol ⁻¹
I1	-799039.76323	-798957.37624	-799207.89181
Ketone S	-505025.92460	-504963.50341	-505142.37354
H2O	-47937.56180	-47917.27033	-47934.11243
I2	-1304798.39736	-1304672.73798	-1305119.41632
TS1	-1304778.73051	-1304653.41249	-1305098.68021
I4	-1256873.88631	-1256749.01067	-1257177.11501
TS2	-1256846.09471	-1256724.68475	-1257149.04230
I6	-751836.05778	-751756.40168	-752001.13860
I7	-1550875.16075	-1550734.87685	-1551231.53808
TS3	-1550858.50364	-1550720.68770	-1551214.04953
I9	-2007966.11814	-2007827.09928	-2008454.59928
TS4	-2007959.22524	-2007815.91365	-2008443.41365
I13	-1112080.27251	-1111964.51884	-1112335.93170
TS6	-1112069.47323	-1111960.83039	-1112329.37871
COA9-OH	-1304058.04193	-1303932.60029	-1304363.79758
TSCOA5-OH	-1304017.57477	-1303892.43997	-1304321.63805
COA7-KetoneS	-1304780.25552	-1304646.70344	-1305090.86426
TSCOA4-KetoneS	-1304761.87492	-1304631.18173	-1305073.94385

Table S20. Energy of the reported species calculated at the PBE0-D3/Def2TZVP//(U)M06-D3/Def2SVP level of theory with SMD for water.

Name	G kcal mol ⁻¹	H kcal mol ⁻¹	E _{electronic} kcal mol ⁻¹
I1	-799045.02180	-798962.63482	-799213.15039
Ketone S	-505058.83585	-504996.41466	-505175.28479
H2O	-47938.32980	-47918.03833	-47934.88043
I2	-1304843.41070	-1304717.75132	-1305164.42966
TS1	-1304824.29655	-1304698.97852	-1305144.24625
I4	-1256917.39465	-1256792.51901	-1257220.62336
TS2	-1256886.80565	-1256765.39570	-1257189.75324
I6	-751845.82482	-751766.16871	-752010.90564
I7	-1550890.33935	-1550750.05545	-1551246.71668
TS3	-1550865.09935	-1550727.28341	-1551220.64525
I9	-2008012.04649	-2007839.79147	-2008500.52763
TS4	-2007997.59278	-2007823.00471	-2008481.78120
I13	-1112108.42925	-1111992.67558	-1112364.08844
TS6	-1112097.28309	-1111988.64025	-1112357.18857
COA9-OH	-1304096.23434	-1303970.79270	-1304401.98999
TSCOA5-OH	-1304045.02425	-1303919.88946	-1304349.08754
COA7-KetoneS	-1304822.24412	-1304688.69204	-1305132.85286
TSCOA4-KetoneS	-1304798.40646	-1304667.71327	-1305110.47539

Table S21. Energy of the reported species calculated at the B3LYP-D3/Def2TZVP//((U)M06-D3/Def2SVP level of theory with SMD for water.

Name	G kcal mol ⁻¹	H kcal mol ⁻¹	E _{electronic} kcal mol ⁻¹
I1	-799938.71546	-799856.32847	-800106.84404
Ketone S	-505656.69043	-505594.26924	-505773.13937
H2O	-47992.02774	-47971.73627	-47988.57837
I2	-1306338.06958	-1306212.41019	-1306659.08854
TS1	-1306318.65404	-1306193.33601	-1306638.60374
I4	-1258357.12004	-1258232.24441	-1258660.34875
TS2	-1258329.43412	-1258208.02416	-1258632.38170
I6	-752690.83251	-752611.17640	-752855.91332
I7	-1552632.32553	-1552492.04163	-1552988.70286
TS3	-1552603.61628	-1552465.80034	-1552959.16217
I9	-2010291.37844	-2010119.12341	-2010779.85958
TS4	-2010281.86240	-2010107.27433	-2010766.05081
I13	-1113374.52539	-1113258.77172	-1113630.18458
TS6	-1113363.85727	-1113255.21443	-1113623.76275
COA9-OH	-1305588.32191	-1305462.88027	-1305894.07756
TSCOA5-OH	-1305541.22697	-1305416.09217	-1305845.29025
COA7-KetoneS	-1306319.99620	-1306186.44412	-1306630.60493
TSCOA4-KetoneS	-1306296.82777	-1306166.13458	-1306608.89670

Table S22. Energy of the reported species calculated at the DLPNO-CCSD(T)/def2-TZVP//((U)M06-D3/Def2SVP level of theory with SMD for water.

Name	G kcal mol ⁻¹	H kcal mol ⁻¹	E _{electronic} kcal mol ⁻¹
NaOH	-149243.85051	-149230.89897	-149230.89897
NaCl	-390240.99737	-390221.04320	-390221.04320
terpy ^{OMe} -Rh-Cl ₃ precatalyst	-1616082.31903	-1616245.72343	-1616246.54446
Ac1	-1375095.35663	-1375267.59683	-1375267.59683
I4	-1255456.32486	-1255775.49259	-1255775.49259
TS2	-1255430.42913	-1255745.61158	-1255745.61158

Table S23. Energy of the reported species calculated at the DLPNO-CCSD(T)/def2-TZVP//((U)M06-D3/Def2TZVP level of theory with SMD for water.

Name	G kcal mol ⁻¹	H kcal mol ⁻¹	E _{electronic} kcal mol ⁻¹
NaOH	-149244.35902	-149231.46973	-149231.46973
NaCl	-390241.56686	-390221.50224	-390221.50224
terpy ^{OMe} -Rh-Cl ₃ precatalyst	-1616081.84565	-1616245.93118	-1616245.93118
Ac1	-1375095.17397	-1375267.25176	-1375267.25176

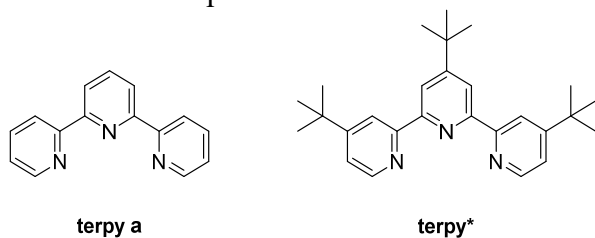
Table S24. Energy of the reported species calculated at the (U)M06-D3/Def2TZVP //((U)M06-D3/Def2TZVP level of theory with SMD for water.

Name	G kcal mol ⁻¹	H kcal mol ⁻¹	E _{electronic} kcal mol ⁻¹
NaOH	-149456.91299	-149432.81323	-149443.75244
NaCl	-390691.25888	-390667.42769	-390671.22469
terpy ^{OMe} -Rh-Cl ₃ precatalyst	-1618187.56629	-1618096.83167	-1618345.51432
Ac1	-1376961.96455	-1376871.41128	-1377128.02051

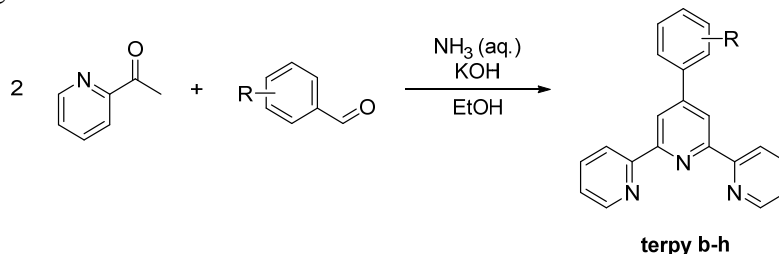
S6. Synthesis of Compounds

S6.1 Ligands

2,2':6',2''-Terpyridine **terpy a** and 3,3'',4'-tri-tert-butyl-2,2':6',2''-terpyridine **terpy*** were obtained commercially from Tokyo Chemical Industry Co., Ltd., and Sigma Aldrich, respectively, and used without further purification.



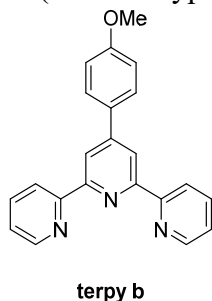
The 4'-aryl-2,2':6',2''-terpyridine ligands **terpy b-h** were synthesized in a modified procedure reported by Wang and Hanan⁶³.



General procedure for the ligands **terpy b-h**:

1.52 ml of *p*-Anisaldehyde (1.36 g, 10 mmol, 1 equiv) was added to a solution of 2.61 ml of 2-acetylpyridine (2.42 g, 20 mmol, 2 equiv) in EtOH (50 mL). Then, KOH (2.24 g, 20 mmol, 2 equiv) and aq NH₃ (34 mL, 25%, 25 mmol, 2.5 equiv) were added to the solution. The solution was stirred at rt for overnight. The precipitate was collected by filtration and washed with EtOH (3 × 10 mL). Recrystallisation from a CHCl₃ MeOH mixture afforded the crystalline solid (0.72 g, 2.1 mmol, 21%).

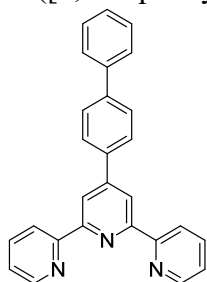
4'-(4-methoxyphenyl)-2,2':6',2''-terpyridine **terpy b**



The ligand was synthesized according to the general procedure and isolated in a yield of 21% (0.72 g, 2.1 mmol).

¹H NMR (CDCl₃, 400 MHz, 25 °C): δ = 8.74 – 8.72 (m, 2 H), 8.71 (s, 2 H), 8.68 – 8.66 (d, *J* = 8.0 Hz, 2 H), 7.90 – 7.85 (m, 4 H), 7.37 – 7.33 (ddd, *J* = 7.5, 4.8, 1.2 Hz, 2 H), 7.04 – 7.02 (m, 2 H), 3.89 (s, 3 H) ppm. The NMR spectra are in agreement with reported data⁶⁴.

4'-([1,1'-biphenyl]-4-yl)-2,2':6',2''-terpyridine **terpy c**

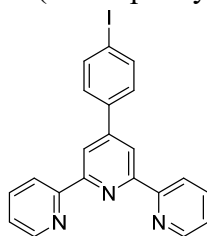


terpy c

The ligand was synthesized according to the general procedure using 4-phenylbenzaldehyde (0.61 g, 3.33 mmol, 1 equiv) and isolated in a yield of 22% (0.29 g, 0.74 mmol).

^1H NMR (CDCl_3 , 400 MHz, 25 °C): δ = 8.80 (s, 2 H), 8.76 – 8.74 (m, 2 H), 8.71 – 8.69 (dt, J = 8.0, 1.1 Hz, 2 H), 8.03 – 8.00 (m, 2 H), 7.92 – 7.87 (td, J = 7.7, 1.8 Hz, 2 H), 7.77 – 7.74 (m, 2 H), 7.70 – 7.67 (m, 2 H), 7.52 – 7.47 (m, 2 H), 7.41 – 7.36 (m, 3 H) ppm.

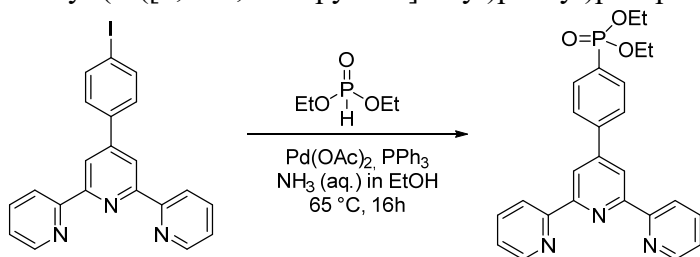
4'-(4-iodophenyl)-2,2':6',2''-terpyridine



The compound was synthesized according to the general procedure using 4-iodobenzaldehyde (1.45 g, 6.25 mmol, 1 equiv) and isolated in a yield of 41% (1.12 g, 2.58 mmol).

^1H NMR (CDCl_3 , 400 MHz, 25 °C): δ = 8.74 – 8.72 (m, 2 H), 8.70 (s, 2 H), 8.68 – 8.66 (d, J = 7.9 Hz, 2 H), 7.91 – 7.84 (m, 4 H), 7.68 – 7.61 (m, 2H), 7.36 (ddd, J = 7.5, 4.8, 1.2 Hz, 2H) ppm. The NMR spectra are in agreement with reported data ⁶⁵.

diethyl (4'-([2,2':6',2''-terpyridin]-4'-yl)phenyl)phosphonate **terpy d**

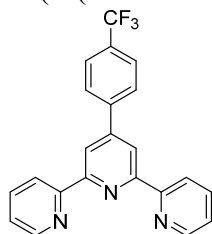


terpy d

The ligand was synthesized according to a modified procedure reported by Hampson *et al.* ⁶⁶. 0.90 ml of diethylphosphite (970 mg, 4 equiv, 7.02 mmol), 0.41 ml of triethylamine (298 mg, 2.94 mmol, 1.7 equiv), 39.7 mg of $\text{Pd}(\text{OAc})_2$ (0.17 mmol, 10 mol%) and 136 mg of PPh_3 (0.52 mmol, 0.3 equiv) were added to a suspension of 758 mg of 4'-(4-iodophenyl)-2,2':6',2''-terpyridine (1.74 mmol, 1 equiv) in ethanol under argon. The reaction mixture was refluxed at 75 °C under vigorous stirring for 24 h. The solution was filtered, and the solvent removed *in vacuo*. Column

chromatography over silica gel using a gradient of pentane 50% / ethyl acetate 50% to ethyl acetate 70% / methanol 30% afforded the product as a brown crystalline solid (480 mg, 1.08 mmol, 62%). ^1H NMR (CDCl_3 , 400 MHz, 25 °C): δ = 8.65 – 8.58 (m, 4H), 8.55 (dt, J = 8.0, 1.1 Hz, 2H), 7.93 – 7.81 (m, 4H), 7.76 (td, J = 7.7, 1.8 Hz, 2H), 7.24 (ddd, J = 7.5, 4.8, 1.2 Hz, 2H), 4.17 – 3.94 (m, 4H), 1.26 (t, J = 7.1 Hz, 7H) ppm; ^{31}P NMR (CDCl_3 , 162 MHz, 25 °C): δ = 18.3 ppm. The NMR spectra are in agreement with reported data ⁶⁶.

4'-(4-(trifluoromethyl)phenyl)-2,2':6',2''-terpyridine **terpy e**

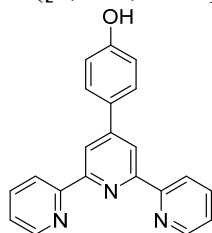


terpy e

The ligand was synthesized according to a modified version of the general procedure using 137 μl of 4-(trifluoromethyl)benzaldehyde (175 mg, 1.0 equiv, 1 mmol). Recrystallization from EtOH afforded the compound in a yield of 10% (38 mg, 0.46 mmol, 0.38 mmol).

^1H NMR (CDCl_3 , 400 MHz, 25 °C): δ = 8.76 – 8.71 (m, 4H), 8.68 (dt, J = 8.0, 1.1 Hz, 2H), 8.03 – 7.95 (m, 2H), 7.89 (td, J = 7.7, 1.8 Hz, 2H), 7.78 (s, 2H), 7.37 (ddd, J = 7.5, 4.8, 1.2 Hz, 2H) ppm. The NMR spectra are in agreement with reported data ⁵.

4-([2,2':6',2''-terpyridin]-4'-yl)phenol **terpy f**

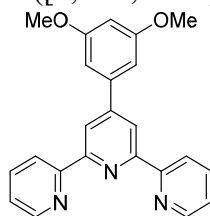


terpy f

The ligand was synthesized according to the general procedure using 4-hydroxybenzaldehyde (1.22 g, 10 mmol, 1 equiv) and isolated in a yield of 17% (560 mg, 1.72 mmol).

^1H NMR ($\text{DMSO}-d_6$, 400 MHz, 25 °C): δ = 8.76 – 8.75 (d, J = 4.7 Hz, 2 H), 8.67 – 8.65 (m, 4 H), 8.05 – 8.01 (t, J = 7.7 Hz, 2 H), 7.80 – 7.78 (d, J = 8.2 Hz, 2 H), 7.54 – 7.51 (m, 2 H), 6.98 – 6.96 (d, J = 8.2 Hz, 2 H), 3.89 (s, 3 H) ppm. The NMR spectra are in agreement with reported data ⁶⁷.

4-([2,2':6',2''-terpyridin]-4'-yl)phenol **terpy g**

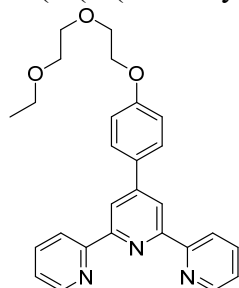


terpy f

The ligand was synthesized according to a modified version of the general procedure using 743 μ l of 3,5-dimethoxybenzaldehyde (831 mg, 1.0 equiv, 5.0 mmol). The crude precipitate was recrystallized using EtOH. Due to minor impurities, the compound was purified using automated flash chromatography with a gradient from heptane/ethyl acetate 1/1 to heptane/ethyl acetate/methanol 40/50/10 obtaining the product as a white crystalline solid with a yield of 3% (60 mg, 0.16 mmol).

^1H NMR (CDCl_3 , 400 MHz, 25 $^\circ\text{C}$): δ = 8.74 – 8.71 (m, 2H), 8.69 (s, 2H), 8.66 (d, J = 8.0 Hz, 2H), 7.87 (dt, J = 7.7, 1.8 Hz, 2H), 7.37 – 7.31 (m, 2H), 7.00 (d, J = 2.2 Hz, 2H), 6.56 (t, J = 2.3 Hz, 1H), 3.89 (s, 6H) ppm. The NMR spectra are in agreement with reported data ⁶⁸.

4'-(4-(2-(2-ethoxyethoxy)ethoxy)phenyl)-2,2':6',2''-terpyridine **terpy h**

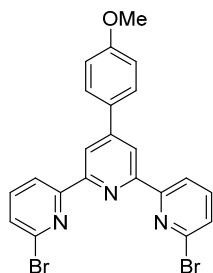


terpy h

The title compound was prepared according to a modified reported procedure ⁶⁹. 4'-(4-Iodophenyl)-2,2':6',2''-terpyridine (80.1 mg, 0.184 mmol, 1.0 equiv), CuCl_2 (1.6 mg, 0.0094 mmol, 5.0 mol%), and K_2CO_3 (76.3 mg, 0.552 mmol, 3.0 equiv) were added under ambient atmosphere in a CO-tube. In an argon charged glove box, 249.0 μ l carbitol (247 mg, 1.84 mmol, 10.0 equiv.) was added. The reaction was sealed and stirred at 130 $^\circ\text{C}$ overnight outside the glovebox. The mixture was left to cool to room temperature and brought to pH 7. The aqueous phase was extracted with DCM (3 x 15 ml) and the solvent of the combined organic phases was removed under *vacuo*. Automated flash column chromatography over basic alumina using a gradient of heptane to heptane/ethyl acetate 80/20 afforded the product as an off-white viscous oil with a yield of 58 % (47.3 mg, 0.107 mmol).

^1H NMR (CDCl_3 , 400 MHz, 25 $^\circ\text{C}$): δ = 8.73 – 8.68 (m, 4H), 8.65 (dt, J = 8.0, 1.1 Hz, 2H), 7.88 – 7.82 (m, 4H), 7.33 (ddd, J = 7.5, 4.8, 1.2 Hz, 2H), 7.06 – 7.00 (m, 2H), 4.22 – 4.17 (m, 2H), 3.89 (dd, J = 5.7, 4.1 Hz, 2H), 3.76 – 3.72 (m, 2H), 3.65 – 3.61 (m, 2H), 3.54 (q, J = 7.0 Hz, 2H), 1.22 (t, J = 7.0 Hz, 3H) ppm. ^{13}C NMR (CDCl_3 , 101 MHz, 25 $^\circ\text{C}$): δ = 159.8 (1C), 156.4 (2C), 155.9 (2C), 149.8 (1C), 149.2 (2C), 136.9 (2C), 130.9 (2C), 128.6 (1C), 123.9 (2C), 121.4 (2C), 118.4 (2C), 115.1 (2C), 71.1 (1C), 70.0 (1C), 69.7 (1C), 67.6 (1C), 66.8 (1C), 15.3 (1C) ppm. HRMS (ESI+) calculated for $\text{C}_{27}\text{H}_{28}\text{N}_3\text{O}_3$ $[\text{M}-\text{H}]^+$ 442.2125; found 442.2134.

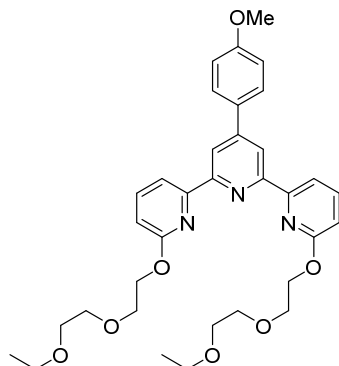
6,6''-Dibromo-4'-(4-methoxyphenyl)-2,2':6',2''-terpyridine



The compound was synthesized according to the general procedure using 304 μ l of 4-anisaldehyde (0.34 g, 2.5 mmol, 1 equiv) and 2-acetyl-6-bromopyridine (1.0 g, 5.0 mmol, 2 equiv) to obtain the product as an off-white crystalline solid in a yield of 33% (0.41 g, 0.83 mmol).

^1H NMR (CDCl_3 , 400 MHz, 25 $^\circ\text{C}$): δ = 8.64 (s, 2H), 8.56 (d, J = 7.7 Hz, 2H), 7.83 (d, J = 8.8 Hz, 2H), 7.71 (t, J = 7.8 Hz, 2H), 7.52 (d, J = 7.8 Hz, 2H), 7.05 (d, J = 8.9 Hz, 2H), 3.90 (s, 3H) ppm. The NMR spectra are in agreement with the reported data ⁷⁰.

6,6''-bis(2-(2-ethoxyethoxy)ethoxy)-4'-(4-methoxyphenyl)-2,2':6',2''-terpyridine **terpy i**



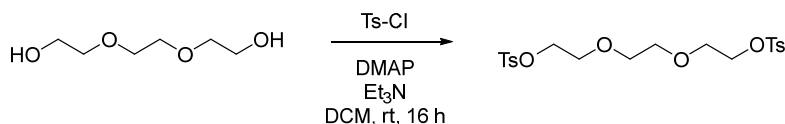
terpy i

The ligand was prepared according to a modified reported procedure ⁷¹. In an argon charged glovebox, NaOH (11.3 mg, 0.28 mmol, 2.8 equiv) was suspended in 205 μ l of carbitol (203 mg, 1.52 mmol, 15 equiv). Then, 6,6''-Dibromo-4'-(4-methoxyphenyl)-2,2':6',2''-terpyridine (50.2 mg, 0.1 mmol, 1 equiv) was added in portions outside the glovebox. The mixture was stirred overnight at 100 $^\circ\text{C}$ and then at 140 $^\circ\text{C}$ for 2 hours. The crude residue was purified using automated flash column chromatography with a gradient of heptane to heptane/ethyl acetate 80/20 to afford the product as a crystalline colorless solid with a yield of 66 % (40.1 mg, 0.066 mmol).

^1H NMR (CDCl_3 , 400 MHz, 25 $^\circ\text{C}$): δ = 8.54 (s, 2H), 8.24 (dd, J = 7.5, 0.8 Hz, 2H), 7.79 – 7.71 (m, 4H), 7.10 – 7.04 (m, 2H), 6.84 (dd, J = 8.2, 0.9 Hz, 2H), 4.69 – 4.64 (m, 4H), 3.98 – 3.93 (m, 4H), 3.89 (s, 3H), 3.77 – 3.73 (m, 4H), 3.65 – 3.61 (m, 4H), 3.53 (q, J = 7.0 Hz, 4H), 1.21 (t, J = 7.0 Hz, 6H) ppm. ^{13}C NMR (CDCl_3 , 101 MHz, 25 $^\circ\text{C}$): δ = 163.1 (2C), 160.5 (1C), 155.7 (2C), 153.7 (2C), 149.5 (1C), 139.4 (2C), 131.4 (2C), 128.5 (1C), 118.2 (2C), 114.6 (2C), 114.3 (2C), 111.5 (2C), 70.9 (2C), 70.0 (1C), 69.9 (1C), 66.8 (2C), 65.1 (2C), 55.5 (2C), 15.2 (2C) ppm. HRMS (ESI) calculated for $\text{C}_{34}\text{H}_{42}\text{N}_3\text{O}_7^+$ $[\text{M}-\text{H}]^+$ 604.3017; found 604.3044.

Preparation of terpy j for the dinuclear complex 2j

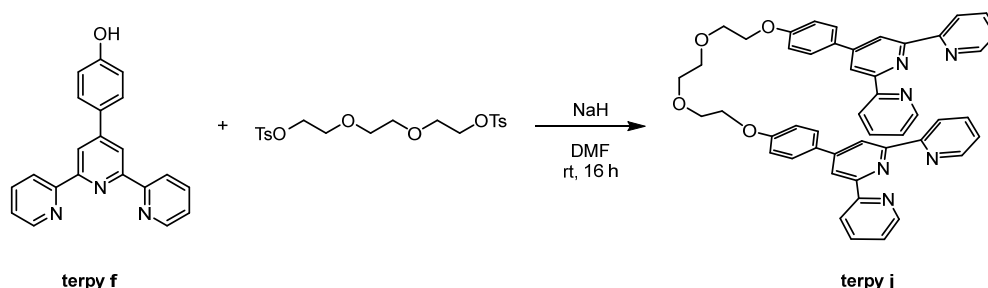
triethylene glycol di(*p*-toluenesulfonate)



The compound was synthesized after a modified procedure reported in literature ⁷². To a solution of 93.9 μ l of triethylene glycol (105 mg, 0.7 mmol, 1 equiv) in anhydrous DCM (5 ml) were added 294 mg of tosyl chloride (1.54 mmol, 2.2 equiv), 214 μ l of triethylamine (156 mg, 1.54 mmol, 2.2 equiv), and 8.55 mg of 4-dimethylaminopyridine (0.07 mmol, 10 mol%) in a 40 mL COtube. The reaction was stirred at room temperature overnight. After completion, 5 mL of water was added, and the mixture was extracted with DCM (3 x 10 mL). The combined organic phases were dried over anhydrous MgSO₄, concentrated under *vacuo* and washed with methanol (2 x 1 mL) to give the product as a white solid in a yield of 75% (240 mg, 0.52 mmol).

¹H NMR (CDCl₃, 400 MHz, 25 °C): δ = 7.79 (d, *J* = 8.3 Hz, 4H), 7.34 (d, *J* = 8.0 Hz, 4H), 4.20 – 4.08 (m, 4H), 3.73 – 3.62 (m, 4H), 3.53 (s, 4H), 2.45 (s, 6H) ppm. The NMR spectra are in agreement with the reported data ⁷³.

1,2-bis(2-(4-([2,2':6',2''-terpyridin]-4'-yl)phenoxy)ethoxy)ethane **terpy k**



To synthesize **terpy k**, 78.1 mg of **terpy f** (0.24 mmol, 2.4 equiv) were dissolved in 1 mL of anhydrous DMF in a 10 mL COtube inside an argon charged glovebox. To the solution was added 6.9 mg of 90% sodium hydride in mineral oil (0.26 mmol, 2.6 equiv) in portions under vigorous stirring. The reaction was stirred at room temperature for 30 minutes. Then, 45.9 mg of triethylene glycol di(*p*-toluenesulfonate) (0.1 mmol, 1 equiv) was added and the reaction was stirred at 80 °C overnight. After completion, the reaction was quenched with 5 ml water and 5 ml of 4 M NaOH were added. The resulting mixture was extracted with DCM (4 x 10 ml). The combined organic phases were dried over MgSO₄ and the solvent was removed under *vacuo*. Recrystallisation from ethanol afforded the product as an off-white solid in a yield of 59% (76.5 mg, 59.2 μ mol).

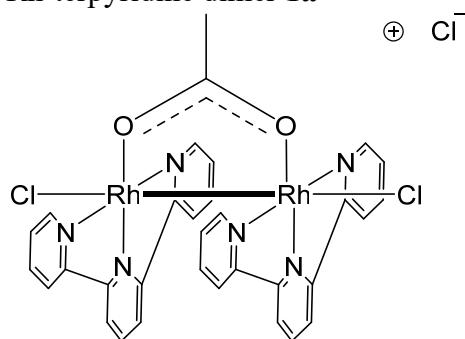
¹H NMR (CDCl₃, 400 MHz, 25 °C): δ = 8.74 – 8.68 (m, 4H), 8.60 (t, *J* = 3.6 Hz, 8H), 7.99 (t, *J* = 7.8 Hz, 4H), 7.81 (d, *J* = 8.3 Hz, 4H), 7.48 (t, *J* = 6.2 Hz, 4H), 7.12 (d, *J* = 8.3 Hz, 4H), 4.18 (s, 4H), 3.81 (d, *J* = 5.6 Hz, 4H), 3.67 (s, 4H) ppm. ¹³C NMR (CDCl₃, 101 MHz, 25 °C): δ = 159.7 (2C), 155.5 (4C), 155.1 (4C), 149.3 (4C), 148.9 (2C), 137.4 (4C), 129.7 (2C), 128.2 (4C), 124.5

(4C), 120.9 (4C), 117.3 (4C), 115.4 (4C), 70.1 (2C), 69.0 (2C), 67.4 (2C) ppm. HRMS (ESI+) calculated for $\text{C}_{48}\text{H}_{40}\text{N}_6\text{O}_4\text{Na}^+$ $[\text{M}+\text{Na}]^+$ 787.3003; found 787.3009.

S6.2 Complexes

Dinuclear rhodium(II) terpyridine

Rh-terpyridine dimer **1a**



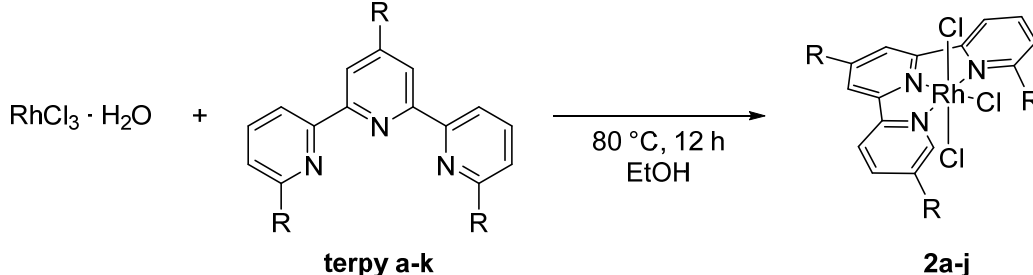
1a

The dinuclear rhodium(II) terpyridine complex **1a** was synthesized according to a modified procedure reported by Pruchnik *et al.*⁷⁴. 46.7 mg of 2,2':6',2''-terpyridine (0.2 mmol, 2 equiv) and NaCl (1.0 mmol, 10 equiv) were added to 44.2 mg Rh₂(OAc)₄ (0.1 mmol, 1 equiv) in 2.5 ml ethanol under argon atmosphere. The reaction mixture was refluxed over-night, however, formation of the product could only be observed when the reaction was refluxed under air. The product was then filtered off. Recrystallisation from water afforded the product as a red solid in a yield of 95% (76.4 mg, 0.1 mmol).

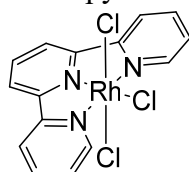
¹H NMR (D₂O, 400 MHz, 25 °C): δ = 8.28 (d, J = 5.5 Hz, 4H), 8.21 – 7.87 (m, 14H), 7.58 (ddd, J = 7.4, 5.4, 1.4 Hz, 4H), 2.86 (s, 3H) ppm. The NMR spectra are in agreement with reported data⁷⁴.

Rhodium(III) terpyridine complexes **2a-j**

General procedure: The rhodium(III) terpyridine complexes were synthesized according to a modified procedure reported by Paul *et al.*⁷⁵. 88.6 mg of 2,2':6',2''-terpyridine (0.38 mmol, 1 equiv) were added to 100 mg RhCl₃ · 3 H₂O (0.38 mmol, 1 equiv) in 15 ml ethanol. The reaction mixture was refluxed over-night, after which the precipitated product was filtered off. The crude product was washed with water, warm ethanol, and diethyl ether to afford the product as a yellow solid in a yield of 86% (145 mg, 0.33 mmol).



Rh-terpyridine monomer **2a**

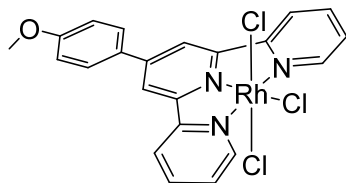


2a

Complex **2a** was synthesized according to the general procedure for the mononuclear Rh-terpyridines using 88.6 mg of **terpy a** (0.38 mmol, 1 equiv) and isolated in a yield of 86% (145 mg, 0.33 mmol).

^1H NMR (DMSO- d_6 , 400 MHz, 25 °C): δ = 9.27 (d, J = 5.5 Hz, 2H), 8.80 (dd, J = 15.5, 8.0 Hz, 4H), 8.55 (t, J = 8.1 Hz, 1H), 8.39 (t, J = 7.8 Hz, 2H), 7.96 (t, J = 6.6 Hz, 2H) ppm. The NMR spectra are in agreement with reported data ⁷⁵.

Rh-terpyridine monomer **2b**

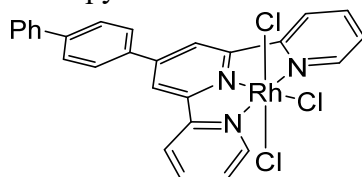


2b

Complex **2b** was synthesized according to the general procedure for the mononuclear Rh-terpyridines using 67.9 mg of **terpy b** (0.20 mmol, 1 equiv) and isolated in a yield of 92% (75.5 mg, 0.14 mmol).

^1H NMR (DMSO- d_6 , 400 MHz, 25 °C): δ = ^1H NMR (400 MHz, DMSO- d_6) δ 9.28 (dd, J = 5.5, 1.5 Hz, 2H), 9.12 (s, 2H), 8.97 (d, J = 8.0 Hz, 2H), 8.42 (td, J = 7.9, 1.6 Hz, 2H), 8.28 – 8.22 (m, 2H), 7.96 (ddd, J = 7.3, 5.6, 1.3 Hz, 2H), 7.29 – 7.22 (m, 2H), 3.91 (s, 3H) ppm. The NMR spectra are in agreement with reported data ⁵. Slowly diffusing ethanol into a DMSO solution of complex **2b** afforded red crystals suitable for X-ray diffraction.

Rh-terpyridine monomer **2c**



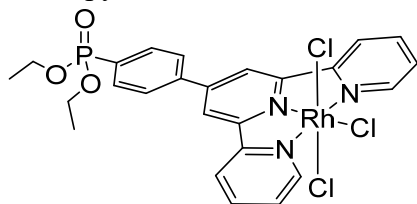
2c

Complex **2c** was synthesized according to the general procedure for the mononuclear Rh-terpyridines using 57.8 mg of **terpy c** (0.15 mmol, 1 equiv) and isolated in a yield of 89% (97.3mg, 0.13 mmol).

^1H NMR (DMSO- d_6 , 400 MHz, 25 °C): δ = 9.30 (d, J = 5.5 Hz, 2H), 9.24 (s, 2H), 9.01 (d, J = 8.1 Hz, 2H), 8.44 (td, J = 7.8, 1.6 Hz, 2H), 8.37 (d, J = 8.4 Hz, 2H), 8.06 – 7.94 (m, 4H), 7.90 – 7.84

(m, 2H), 7.55 (t, $J = 7.5$ Hz, 2H), 7.46 (t, $J = 7.4$ Hz, 1H) ppm; Due to poor solubility in various NMR solvents, a ^{13}C NMR spectrum could not be measured successfully. HRMS (ESI⁺): calculated $[\text{M}-\text{Cl}]^+ = [\text{C}_{25}\text{H}_{24}\text{Cl}_3\text{N}_3\text{O}_3\text{PRh}+\text{Na}]^+ 558.0006$; found 557.9989.

Rh-terpyridine monomer **2d**

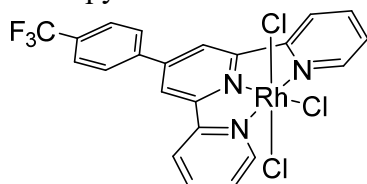


2d

Complex **2d** was synthesized according to the general procedure for the mononuclear Rh-terpyridines using 66.8 mg of **terpy d** (0.15 mmol, 1 equiv) and isolated in a yield of 84% (82.0 mg, 0.13 mmol).

^1H NMR (DMSO- d_6 , 400 MHz, 25 °C): $\delta = 9.32 - 9.26$ (m, 2H), 9.21 (s, 2H), 8.96 (d, $J = 8.0$ Hz, 2H), 8.44 (td, $J = 7.8, 1.5$ Hz, 2H), 8.37 (dd, $J = 8.3, 3.4$ Hz, 2H), 8.06 – 7.95 (m, 4H), 4.19 – 4.01 (m, 4H), 1.29 (t, $J = 7.0$ Hz, 6H) ppm; ^{13}C NMR (DMSO- d_6 , 101 MHz, 25 °C): $\delta = 157.3$ (2C), 155.5 (2C), 153.2 (2C), 150.6 (1C), 140.3 (2C), 139.2 (1C), 132.1 (d, $J = 10.0$ Hz, 2C), 130.8 (d, $J = 186.0$ Hz, 1C), 128.6 (2C), 128.5 (d, $J = 10.6$ Hz, 2C), 125.5 (2C), 122.6 (2C), 62.1 (d, $J = 5.5$ Hz, 2C), 16.3 (d, $J = 6.0$ Hz, 2C) ppm; ^{31}P NMR (DMSO- d_6 , 162 MHz, 25 °C): $\delta = 16.7$ ppm; HRMS (ESI⁺): calculated $[\text{M}+\text{Na}]^+ = [\text{C}_{25}\text{H}_{24}\text{Cl}_3\text{N}_3\text{O}_3\text{PRh}+\text{Na}]^+ 675.9568$; found 675.9559.

Rh-terpyridine monomer **2e**

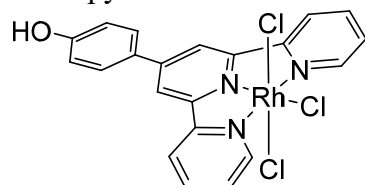


2e

Complex **2e** was synthesized according to the general procedure for the mononuclear Rh-terpyridine complexes using 18.9 mg of **terpy** (0.05 mmol, 1 equiv). As an additional purification step, the crude residue was washed with warm DCM to afford the product as a yellow solid with a yield of 86% (31 mg, 43 μmol).

^1H NMR (DMSO- d_6 , 400 MHz, 25 °C) δ 9.29 (d, $J = 5.4$ Hz, 2H), 9.24 (s, 2H), 8.97 (d, $J = 8.0$ Hz, 2H), 8.44 (m, 4H), 8.10 (d, $J = 8.2$ Hz, 2H), 7.99 (t, $J = 6.6$ Hz, 2H) ppm. The NMR spectra are in agreement with reported data ⁵.

Rh-terpyridine monomer **2f**

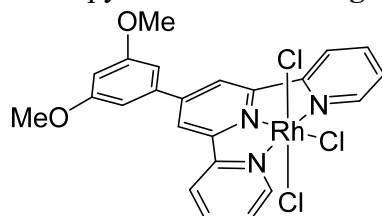


2f

Complex **2f** was synthesized according to the general procedure for the mononuclear Rh-terpyridine complexes using 48.8 mg of **terpy f** (0.15 mmol, 1 equiv). The crude product was additionally washed with 10 ml of water and 10 ml of hot ethanol and water. The yellow solid was then dissolved in warm dimethylformamide and crashed out with methanol to afford the product as an orange solid in a yield of 39% (31 mg, 0.06 mmol).

^1H NMR (DMSO- d_6 , 400 MHz, 25 °C): δ = 10.27 (s, 1H), 9.28 (dd, J = 5.6, 1.5 Hz, 2H), 9.06 (s, 2H), 8.94 (dd, J = 8.1, 1.4 Hz, 2H), 8.40 (td, J = 7.9, 1.6 Hz, 2H), 8.17 – 8.10 (m, 2H), 7.95 (ddd, J = 7.3, 5.5, 1.4 Hz, 2H), 7.07 – 7.01 (m, 2H) ppm, ^{13}C NMR (DMSO- d_6 , 101 MHz, 25 °C): δ = 160.5 (1C), 157.6 (2C), 155.1 (2C), 153.2 (2C), 151.6 (1C), 140.1 (2C), 129.8 (2C), 128.3 (2C), 125.7 (1C), 125.3 (2C), 120.7 (2C), 116.2 (2C) ppm; HRMS (ESI+) calculated $[\text{M}+\text{Na}]^+ = [\text{C}_{21}\text{H}_{15}\text{Cl}_3\text{N}_3\text{ORhNa}]^+ 555.9228$; found 555.9221.

Rh-terpyridine monomer **2g**

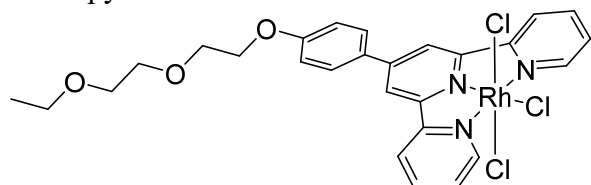


2g

Complex **2g** was synthesized according to the general procedure for the mononuclear Rh-terpyridine complexes using 18.5 mg of **terpy g** (0.05 mmol, 1 equiv). As an additional purification step, the crude residue was washed with warm DCM to afford the product as a yellow solid with a yield of 70% (20.3 mg, 35.1 μmol).

^1H NMR (DMSO- d_6 , 400 MHz, 25 °C) δ 9.29 (d, J = 5.4 Hz, 2H), 9.24 (s, 2H), 8.97 (d, J = 8.0 Hz, 2H), 8.44 (m, 4H), 8.10 (d, J = 8.2 Hz, 2H), 7.99 (t, J = 6.6 Hz, 2H) ppm. Due to poor solubility in various NMR solvents, a ^{13}C NMR spectrum could not be measured successfully. HRMS (ESI) calculated $[\text{M}-\text{Cl}]^+ = [\text{C}_{23}\text{H}_{19}\text{Cl}_2\text{N}_3\text{O}_2\text{Rh}]^+ 541.9904$; found: 541.9912.

Rh-terpyridine monomer **2h**

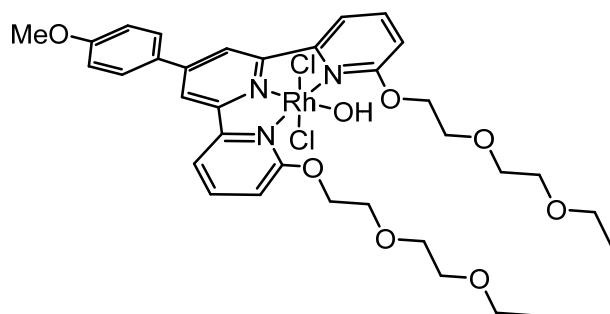


2h

Complex **2h** was synthesized according to the general procedure for the mononuclear Rh-terpyridine complexes using **terpy h** (25.6 mg, 58.0 μmol , 1.0 equiv.) and afforded the product as a brown solid with a yield of 89 % (33.5 mg, 51.2 μmol).

^1H NMR (DMSO- d_6 , 400 MHz, 25 $^\circ\text{C}$): δ = 9.32 – 9.26 (m, 2H), 9.14 (s, 2H), 8.98 (d, J = 8.1 Hz, 2H), 8.43 (td, J = 7.8, 1.6 Hz, 2H), 8.26 (d, J = 8.9 Hz, 2H), 8.01 – 7.93 (m, 3H), 7.30 – 7.26 (m, 2H), 4.30 – 4.26 (m, 2H), 3.84 – 3.81 (m, 2H), 3.65 – 3.61 (m, 2H), 3.55 – 3.52 (m, 2H), 3.46 (q, J = 7.0 Hz, 3H), 1.12 (t, J = 7.0 Hz, 3H) ppm. ^{13}C NMR (DMSO- d_6 , 101 MHz, 25 $^\circ\text{C}$): δ = 161.1 (1C), 157.6 (2C), 155.2 (2C), 153.2 (2C), 151.2 (1C), 140.2 (2C), 129.7 (2C), 128.3 (2C), 127.3 (2C), 125.4 (2C), 121.0 (2C), 115.3 (2C), 70.0 (1C), 69.3 (1C), 68.9 (1C), 67.6 (1C), 65.6 (1C), 15.2 (1C) ppm. HRMS (ESI) calculated $[\text{M}-\text{Cl}]^+ = [\text{C}_{27}\text{H}_{27}\text{Cl}_2\text{N}_3\text{O}_3\text{Rh}]^+$ 614.0484; found: 614.0481.

Rh-terpyridine monomer **2i**



2i

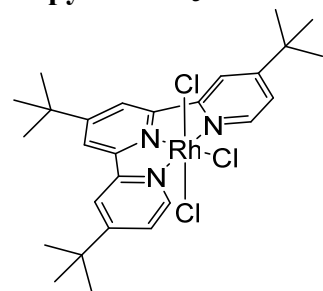
Complex **2i** was synthesized according to the general procedure for the mononuclear Rh-terpyridine complexes using **terpy i** (26.6 mg, 44.0 μmol , 1.0 equiv.) and afforded a brown solid with a yield of 58 % (20.7 mg, 25.5 μmol). As visible in ^1H NMR, the one chloride exchanges with hydroxide, presumably during the washing steps, to yield the mono-hydroxo di-chloride complex. Upon addition of small amounts of D_2O , the hydroxo signal at 6.43 ppm vanishes within minutes.

^1H NMR (DMSO- d_6 , 400 MHz, 25 $^\circ\text{C}$): δ = 9.09 (s, 2H), 8.70 (d, J = 7.7 Hz, 2H), 8.48 (t, J = 8.1 Hz, 2H), 8.29 (d, J = 8.7 Hz, 2H), 7.64 (d, J = 8.8 Hz, 2H), 7.25 (d, J = 8.8 Hz, 2H), 6.43 (s, 1H), 4.68 (m, 4H), 3.98 (s, 4H), 3.91 (s, 3H), 3.57 (t, J = 4.8 Hz, 4H), 3.44 (q, J = 7.0 Hz, 4H), 1.10 (t, J = 6.9 Hz, 6H) ppm. Due to poor solubility in various NMR solvents, a ^{13}C NMR spectrum could not be measured successfully. HRMS (ESI) calculated for $[\text{M}-\text{Cl}]^+ \text{C}_{34}\text{H}_{41}\text{Cl}_2\text{N}_3\text{O}_7\text{Rh}^+$ = 776.1377; found: 776.1384.

The chemical structure shows a macrocyclic ligand consisting of two 4-phenoxyethoxy chains connected by two 4-phenylene groups. This macrocycle is coordinated to two rhodium (Rh) centers. Each Rh center is also coordinated to a phenylpyridine ligand and a chloride ligand, forming a dimeric complex.

For complex **2j**, the general procedure for the mononuclear Rh-terpyridine complexes was modified due to the low solubility of the ligand. To 7.4 mg of RhCl₃ (0.028 mmol, 1.1 equiv) were added 19.4 mg of **terpy j** (0.025 mmol, 1 equiv) and ethanol (1 ml). The suspension was stirred at room temperature overnight and then refluxed for 3 h. The mixture was filtered and washed according to the general procedure to afford the product as a brown solid (12.3 mg, 0.025 mmol, 82%).

terpy*-Rh-Cl₃

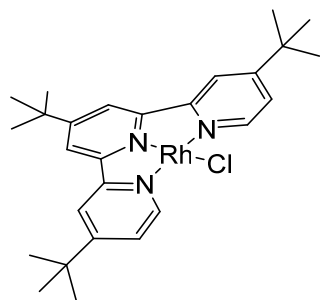


Complex **terpy*-Rh-Cl₃** was synthesized according to the general procedure for the mononuclear Rh-terpyridine complexes using 80.3 mg (200 μmol, 1 equiv) of **terpy*** (4,4',4''-tri-tert-butyl-2,2':6',2''-terpyridine) and 52.7 mg (200 μmol, 1.0 equiv) of mg RhCl₃ · 3 H₂O and afforded the product as a green-grey solid with a yield of 71% (87.0 mg, 142 μmol).

¹H NMR (DMSO-*d*₆, 400 MHz, 25 °C) δ = 9.13 (d, *J* = 5.5 Hz, 2H), 8.86 (d, *J* = 6.6 Hz, 4H), 7.96 (d, *J* = 6.1 Hz, 2H), 7.29 – 7.14 (m, 4H), 1.59 (s, 9H), 1.48 (s, 18H) ppm. Due to poor solubility in various NMR solvents, a ¹³C NMR spectrum could not be measured successfully. **HRMS** (ESI) calculated for [M-Cl]⁺ C₂₇H₃₅Cl₂N₃Rh⁺ = 574.1231; found: 574.1757.

Rhodium(I) terpyridine complexes

terpy*-Rh-Cl

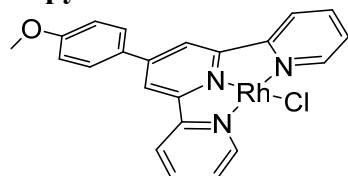


terpy*-Rh-Cl

Complex **terpy*-Rh-Cl** was synthesized according to a modified procedure reported by O'Reilly *et al.*⁷⁶. In an argon charged glovebox, 74.0 mg (0.150 mmol, 0.5 equiv) of [Rh(Cl)(COD)]₂ and 133.0 mg (0.330 mmol, 1.1 equiv) of **terpy*** were given into a 10 ml COtube and stirred in 1 ml of toluene for 1 h at room temperature. Then, 1 ml of pentane was added and the resulting deep blue suspension was stirred for 15 min, before letting the precipitate settle. The liquid phase was decanted and the solid residue washed with pentane. Drying the precipitate *in vacuo* afforded the product in a yield of 65% (106 mg, 0.196 mmol).

¹H NMR (THF-*d*₈, 400 MHz, 25 °C): δ = 9.48 (d, *J* = 6.0 Hz, 2H), 8.12 (d, *J* = 2.0 Hz, 2H), 7.93 (s, 2H), 7.71 (dd, *J* = 6.0, 2.1 Hz, 2H), 1.46 (s, 9H), 1.44 (s, 18H) ppm. The NMR spectra are in agreement with reported data⁷⁶.

terpy^{OMe}-Rh-Cl



Rh(I) terpy 2b*

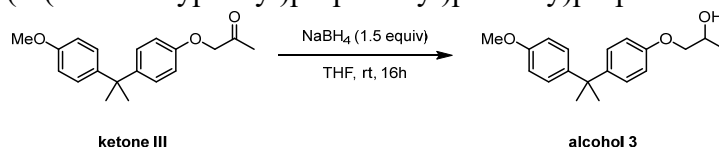
Complex **terpy^{OMe}-Rh-Cl** was synthesized according to a procedure adapted from Hartl *et al.*⁷⁷. In an argon-charged glovebox in an 8 ml screwcap vial 29.9 mg (88.0 μmol, 1.1 equiv) of **terpy b** and 19.7 mg (40.0 μmol, 0.5 equiv) of [COD-Rh-Cl]₂ were stirred in 1 ml of toluene for 4 h at room temperature. The resulting deep blue suspension was decanted and the solid residue washed with toluene. The solid residue was dried *in vacuo*, affording the product as a blue-black solid in a yield of 35% (13.2 mg, 27.6 μmol).

¹H NMR (400 MHz, DMSO-*d*₆): δ = 8.99 (s, 2H), 8.43 – 8.36 (m, 4H), 8.16 – 8.05 (m, 4H), 7.64 (s, 2H), 7.07 – 7.05 (m, 2H), 3.86 (s, 3H) ppm. Due to poor solubility in various NMR solvents, a ¹³C NMR spectrum could not be measured successfully.

S6.3 Model Substrates

Model substrates model 1, model 3, ketone 3 and model 4 were synthesized after procedure reported by Ahrens *et al.*². Model substrates model 2 and ketone I were synthesized after a procedure reported by Sun *et al.*³. Model substrate model S was synthesized after a procedure reported by Pan *et al.*⁷⁸. All analytical data were in agreement with reported data, respectively.

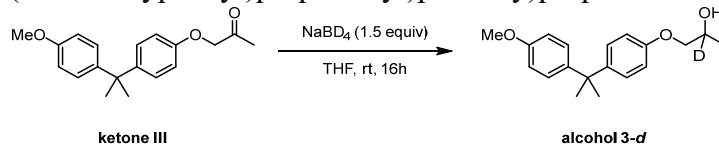
Alcohol 3 1,3-bis(4-(2-(4-methoxyphenyl)propan-2-yl)phenoxy)propan-2-one



To a solution of 179 mg of ketone III (0.60 mmol, 1 equiv) in THF (7 ml) was added 45.4 mg sodium borohydride (1.20 mmol, 2 equiv) under stirring. The reaction was stirred overnight at room temperature. After completion, the reaction mixture was filtered over a silica plug and the solvent was removed *in vacuo* to afford the product in a yield of 98% (177 mg, 0.59 mmol).

R_f (pentane/ethyl acetate 9/1, silica gel) = 0.13 ^1H NMR (CDCl_3 , 400 MHz, 25 °C): δ = 7.19 – 7.10 (m, 4H), 6.85 – 6.76 (m, 4H), 4.18 (ddt, J = 9.8, 6.6, 3.3 Hz, 1H), 3.92 (dd, J = 9.2, 3.1 Hz, 1H), 3.81 – 3.72 (m, 4H), 2.33 (d, J = 3.4 Hz, 1H), 1.64 (s, 6H), 1.27 (d, J = 6.4 Hz, 3H) ppm; ^{13}C NMR (CDCl_3 , 101 MHz, 25 °C): δ = 157.50 (1C), 156.48 (1C), 143.80 (1C), 143.17 (1C), 127.93 (2C), 127.83 (2C), 114.03 (2C), 113.38 (2C), 73.36 (1C), 66.43 (1C), 55.33 (1C), 41.82 (1C), 31.18 (2C), 18.84 (1C) ppm; HRMS (ESI⁺): calculated $[\text{M}+\text{H}]^+ = [\text{C}_{19}\text{H}_{24}\text{O}_3+\text{Na}]^+ 323.1617$; found 323.1617.

Alcohol 3-*d* 1-(4-(2-(4-methoxyphenyl)propan-2-yl)phenoxy)propan-2-*d*-2-ol



To a solution of 179 mg of ketone III (0.60 mmol, 1 equiv) in THF (7 ml) was added 50.2 mg sodium borodeuteride (1.20 mmol, 2 equiv) under stirring. The reaction was stirred overnight at room temperature. After completion, a saturated solution of ammonium chloride (10 ml) diluted in water (10 ml) was added. The mixture was extracted with ethyl acetate (3 x 20 ml) and the solvent was removed *in vacuo*. Column chromatography with a gradient of heptane/ethyl acetate 95:5 to 55:45 afforded the product in a yield of 95% (171 mg, 0.57 mmol).

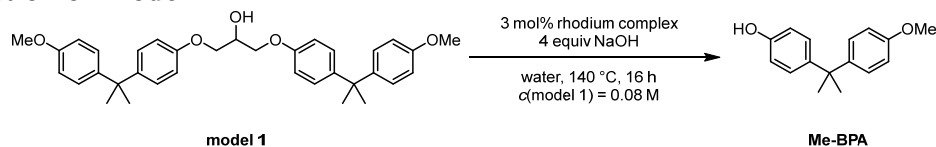
R_f (pentane/ethyl acetate 9/1, silica gel) = 0.13; ^1H NMR (CDCl_3 , 400 MHz, 25 °C) δ = 7.19 – 7.10 (m, 4H), 6.85 – 6.77 (m, 4H), 3.92 (d, J = 9.3 Hz, 1H), 3.79 (s, 4H), 2.35 (s, 1H), 1.64 (s, 6H), 1.27 (s, 3H) ppm; ^{13}C NMR (CDCl_3 , 101 MHz, 25 °C): δ = 157.49 (1C), 156.48 (1C), 143.79 (1C), 143.16 (1C), 127.92 (2C), 127.82 (2C), 114.02 (2C), 113.37 (2C), 73.26 (1C), 66.23 – 65.79 (t, J = 21.9 Hz, 1C), 55.32 (1C), 41.81 (1C), 31.17 (2C), 18.73 (1C) ppm. ^2H NMR (CHCl_3 , 400 MHz, 25 °C) δ = 4.18 (m, 1 H), HRMS (ESI⁺): calculated $[\text{M}+\text{H}]^+ = [\text{C}_{19}\text{H}_{23}\text{DO}_3+\text{Na}]^+ 324.1680$; found 324.1682.

S7. Catalytic Deconstruction

S7.1 On Model Substrates

General procedure 5.1: 1 equiv of model substrate is given into 10 ml COtube. In an Argon-charged glovebox, 3 mol% of rhodium complex, 4 equiv of NaOH and 1 ml water are added and the reaction vessel sealed. Outside of the glovebox, the reaction mixture is stirred at 800 rpm in an aluminum block at 140 °C for 16 h. The reaction mixture is then cooled to room temperature and the internal standard 1,3,5-trimethoxybenzene was added. The mixture is extracted with 4 x 8 ml ethyl acetate and the solvent is removed *in vacuo*. The yield is analyzed using ¹H NMR spectroscopy (see Chapter S2, Fig. S7) using the average of two entries.

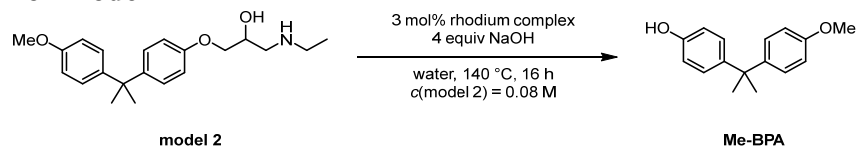
Deconstruction of Model 1



The reaction was carried out according to the general procedure 5.1. 43.3 mg (0.08 mmol, 1 equiv) of model 1, 1.31 mg (2.40 μmol , 3 mol%) of rhodium complex **2b**, 12.8 mg (0.32 mmol, 4 equiv) of sodium hydroxide and 1 ml of water were used. An average yield of 21% was determined using 1,3,5-trimethoxybenzene as internal standard.

¹H NMR (CDCl_3 , 400 MHz, 25 °C): $\delta = 7.16 - 7.14$ (m, 2H), 7.11 – 7.09 (m, 2H), 6.83 – 6.81 (m, 2H), 6.74 – 6.72 (m, 2H), 4.76 (s, 1H), 3.80 (s, 3H), 1.64 (s, 6H) ppm. The NMR spectra are in agreement with reported data ⁷⁹.

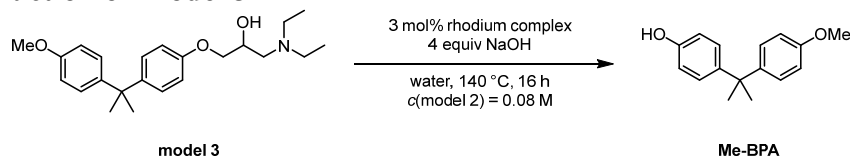
Deconstruction of Model 2



The reaction was carried out according to the general procedure 5.1. 27.5 mg (0.08 mmol, 1 equiv) of model 2, 1.31 mg (2.40 μmol , 3 mol%) of rhodium complex **2b**, 12.8 mg (0.32 mmol, 4 equiv) of sodium hydroxide and 1 ml of water were used. A quantitative yield (>99%) was determined using 1,3,5-trimethoxybenzene as internal standard.

¹H NMR (CDCl_3 , 400 MHz, 25 °C): $\delta = 7.16 - 7.14$ (m, 2H), 7.11 – 7.09 (m, 2H), 6.83 – 6.81 (m, 2H), 6.74 – 6.72 (m, 2H), 4.76 (s, 1H), 3.80 (s, 3H), 1.64 (s, 6H) ppm. The NMR spectra are in agreement with reported data ⁷⁹.

Deconstruction of Model 3

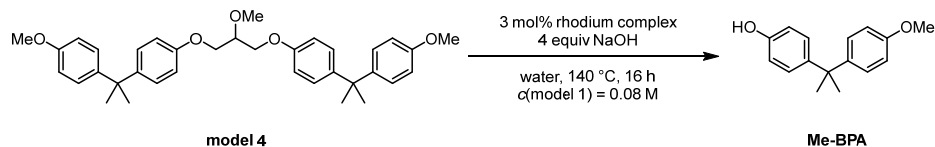


The reaction was carried out according to the general procedure 5.1. 29.7 mg (0.08 mmol, 1 equiv) of **model 3**, 1.31 mg (2.40 μmol , 3 mol%) of rhodium complex **2b**, 12.8 mg (0.32 mmol, 4 equiv)

of sodium hydroxide and 1 ml of water were used. An average yield of 60% was determined using 1,3,5-trimethoxybenzene as internal standard.

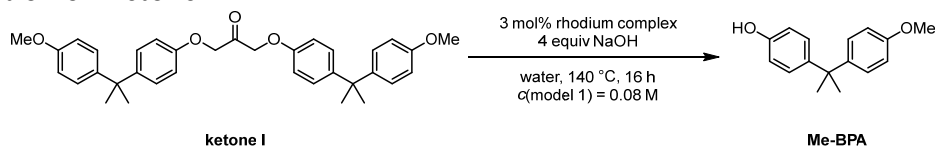
^1H NMR (CDCl_3 , 400 MHz, 25 °C): δ = 7.16 – 7.14 (m, 2H), 7.11 – 7.09 (m, 2H), 6.83 – 6.81 (m, 2H), 6.74 – 6.72 (m, 2H), 4.76 (s, 1H), 3.80 (s, 3H), 1.64 (s, 6H) ppm. The NMR spectra are in agreement with reported data ⁷⁹.

Deconstruction of Model 4



The reaction was carried out according to the general procedure 5.1. 44.4 mg (0.08 mmol, 1 equiv) of **model 4**, 1.31 mg (2.40 μmol , 3 mol%) of rhodium complex **2b**, 12.8 mg (0.32 mmol, 4 equiv) of sodium hydroxide and 1 ml of water were used. No consumption and a yield of 0% were determined using 1,3,5-trimethoxybenzene as internal standard.

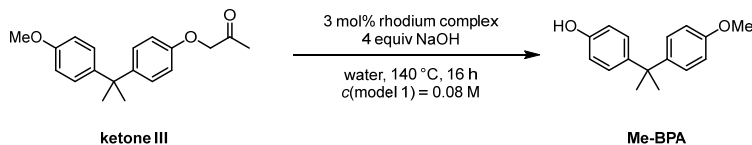
Deconstruction of Ketone I



The reaction was carried out according to the general procedure 5.1. 43.1 mg (0.08 mmol, 1 equiv) of Ketone I, 1.31 mg (2.40 μmol , 3 mol%) of rhodium complex **2b**, 12.8 mg (0.32 mmol, 4 equiv) of sodium hydroxide and 1 ml of water were used. An average yield of 65% was determined using 1,3,5-trimethoxybenzene as internal standard.

^1H NMR (CDCl_3 , 400 MHz, 25 °C): δ = 7.16 – 7.14 (m, 2H), 7.11 – 7.09 (m, 2H), 6.83 – 6.81 (m, 2H), 6.74 – 6.72 (m, 2H), 4.76 (s, 1H), 3.80 (s, 3H), 1.64 (s, 6H) ppm. The NMR spectra are in agreement with reported data ⁷⁹.

Deconstruction of Ketone III



The reaction was carried out according to the general procedure 5.1. 23.9 mg (0.08 mmol, 1 equiv) of Ketone III, 1.31 mg (2.40 μmol , 3 mol%) of rhodium complex **2b**, 12.8 mg (0.32 mmol, 4 equiv) of sodium hydroxide and 1 ml of water were used. An average yield of 35% was determined using 1,3,5-trimethoxybenzene as internal standard.

^1H NMR (CDCl_3 , 400 MHz, 25 °C): δ = 7.16 – 7.14 (m, 2H), 7.11 – 7.09 (m, 2H), 6.83 – 6.81 (m, 2H), 6.74 – 6.72 (m, 2H), 4.76 (s, 1H), 3.80 (s, 3H), 1.64 (s, 6H) ppm. The NMR spectra are in agreement with reported data ⁷⁹.

S7.2 On Commercial Epoxy Resins

General procedure 7.2: 100 mg of finely powdered epoxy resin and 3 mol% of Rh-terpyridine complex were given into a 10 ml COtube (from SyTracks), or in a 45 mL high pressure autoclave using a 30 mL PTFE inlay purchased from Parr Instrument Company. In an Argon-charged glovebox, 4 equiv of sodium hydroxide and 1.5 ml of water were added, and the reaction vessel sealed. When carried out in a high pressure autoclave, the vessel was optionally charged with 40 atm of argon. Outside of the glovebox, the reaction mixture was stirred at 800 rpm in an aluminum block at 140 °C for 24 h. The reaction mixture was then allowed to cool to room temperature and 1.5 ml of 1M HCl was added. The water phase was extracted with ethyl acetate (4 × 8 mL). Celite was added and the solvent removed *in vacuo*. The resulting mixture was loaded onto a silica gel charged column. Automated flash column chromatography using a gradient from heptane to 1/4 heptane/ethyl acetate afforded bisphenol A.

The deconstruction of **Airstone 760E/766H** (approx. BPA content 43 wt%) was carried out according to the **General procedure 7.2**. 100 mg of the powdered resin, 3.1 mg (5.7 μmol, 3 mol% with respect to BPA content) of rhodium complex **2b**, 30.2 mg (0.75 mmol, 4 equiv) of NaOH and 1.5 ml of water were used. Automated flash column chromatography using a gradient from heptane to 1/4 heptane/ethyl acetate afforded bisphenol A as a white, crystalline solid.

BPA: Yield of 64% (27.7 mg, 107 μmol); *R_f* (pentane/ethyl acetate 4/1, silica gel) = 0.21; ¹H NMR (CDCl₃, 400 MHz, 25 °C): δ = 7.11 – 7.07 (m, 4H), 6.76 – 6.70 (m, 4H), 4.57 (s, 2H), 1.62 (s, 6H) ppm. The NMR spectra are in agreement with reported data ⁸⁰.

S7.3 On Fiber Reinforced Epoxy Composites

General procedure 7.3: A composite piece, cut to size with a hacksaw, is placed in a 10 ml COtube (from SyTracks), or in a 45 mL high pressure autoclave using a 30 mL PTFE inlay purchased from Parr Instrument Company. For the composite, a maximum amount of 50 wt% is estimated to be epoxy resin, of which a maximum of 55 wt% is estimated to be bisphenol A. In an Argon-charged glovebox, 3 mol% of rhodium complex **2b** with respect to the maximal estimated bisphenol A content is added. Then, 4 equiv of sodium hydroxide and 2.5 ml of water are added and the reaction vessel is sealed. Outside of the glovebox, the reaction mixture is stirred at 50 rpm in an aluminum block at 140 °C for 4 days. The reaction mixture was then allowed to cool to room temperature and the reaction mixture was brought to pH = 8 using 1M HCl. The water phase was extracted with ethyl acetate (4 × 12 mL). The fibers are washed using water and acetone and then dried *in vacuo*. The extracted organic phase is transferred into a round bottom flask. Celite® is added and the solvent removed *in vacuo*. The resulting powder is loaded onto a silica gel charged column. Column chromatography using gradient of pentane to 1/4 pentane/ethyl acetate affords bisphenol A.

The deconstruction of a piece of a **carbon fiber-based wind turbine blade core piece** (see **Chapter 1.2, Fig. S6**) donated by **Vestas** was carried out according to the **General procedure 7.3**. A piece of the composite material (220 mg, maximal estimated bisphenol A content 60.5 mg, 265 μmol, 1 equiv), 4.4 mg (7.95 μmol, 3 mol%) of rhodium terpyridine **2b**, 42.4 mg (1.06 mmol, 4 equiv) of sodium hydroxide and 2 ml water were used. The reaction was left to stir for 4 days. The reaction was left to stir for 4 days and worked up according to the **General procedure 7.3**.

Carbon fibers were recovered, as well as a rest fraction in form of brown powder by evaporating the water phase. Column chromatography afforded BPA as colorless solid.

BPA: Yield of 10.3 wt% (22.6 mg, 99.0 μmol); R_f (pentane/ethyl acetate 4/1, silica gel) = 0.21; ^1H NMR (CDCl_3 , 400 MHz, 25 $^\circ\text{C}$): δ = 7.11 – 7.07 (m, 4H), 6.76 – 6.70 (m, 4H), 4.57 (s, 2H), 1.62 (s, 6H) ppm. The NMR spectra are in agreement with reported data ⁸⁰.

Carbon fibers: Yield of 73 wt% (160.1 mg).

Rest fraction: Yield of 18 wt% (40.1 mg). Due to evaporating the water phase, the rest fraction may contain salts from neutralizing the solution, which we assume to be the reason for formally exceeding 100 wt%.

The deconstruction of a piece of **commercial product sample of carbon-fiber based pultrusion composite** (see **Chapter 1.2, Fig. S5**) donated by **Olin** was carried out according to the **General procedure 7.3**. A piece of the composite material (158 mg, maximal estimated bisphenol A content 43.5 mg, 190 μmol , 1 equiv), 3.1 mg (5.7 μmol , 3 mol%) of rhodium terpyridine **2b**, 30.4 mg (0.76 mmol, 4 equiv) of sodium hydroxide and 1.5 ml water were used. The reaction was left to stir for 4 days and worked up according to the **General procedure 7.3**. Carbon fibers were recovered, as well as a rest fraction in form of brown powder by evaporating the water phase. Column chromatography afforded BPA as white, crystalline solid.

BPA: Yield of 13 wt% (20.6 mg, 90.2 μmol); R_f (pentane/ethyl acetate 4/1, silica gel) = 0.21; ^1H NMR (CDCl_3 , 400 MHz, 25 $^\circ\text{C}$): δ = 7.11 – 7.07 (m, 4H), 6.76 – 6.70 (m, 4H), 4.57 (s, 2H), 1.62 (s, 6H) ppm. The NMR spectra are in agreement with reported data ⁸⁰.

Carbon fibers: Yield of 56 wt% (89.0 mg).

Rest fraction: Yield of 25 wt% (39.4 mg).

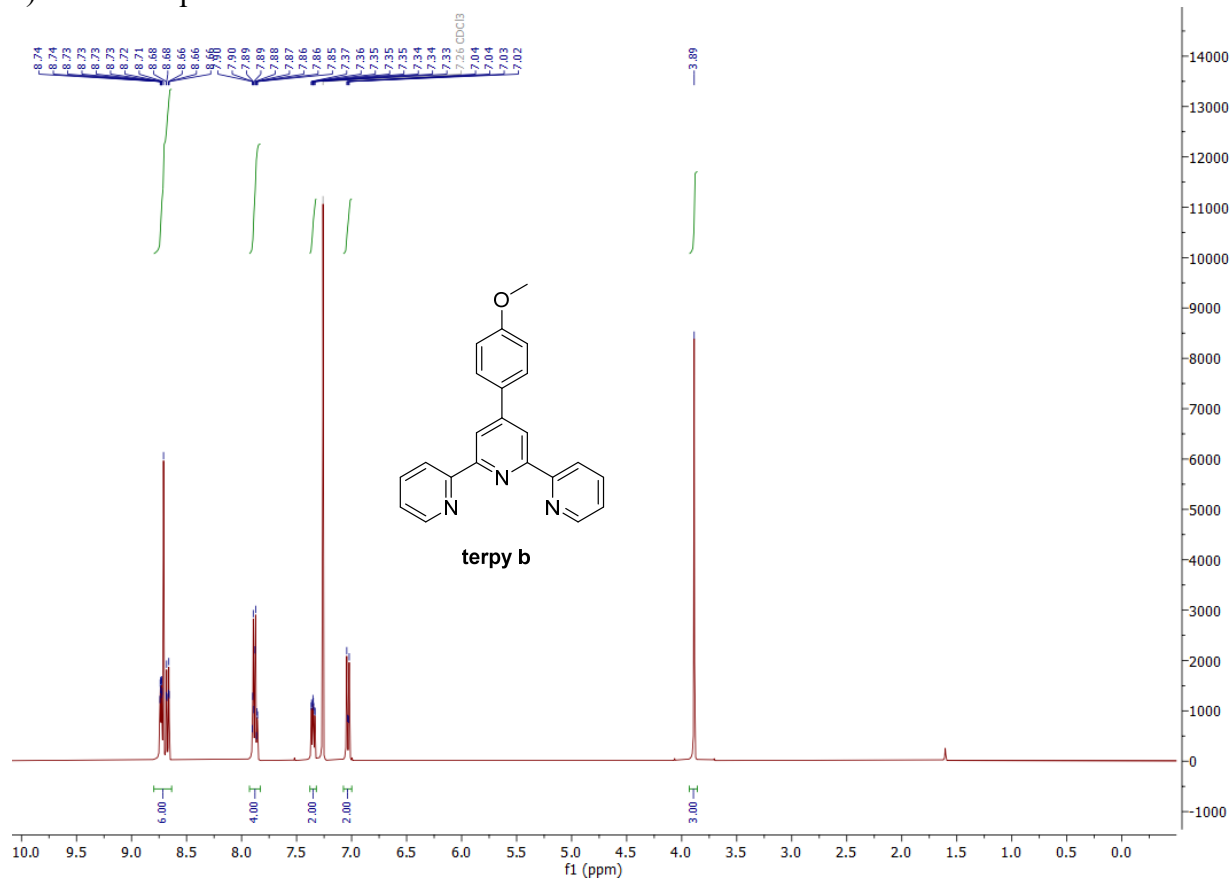
S8. Spectra and Images

S8.1 NMR Spectra of Synthesized Compounds

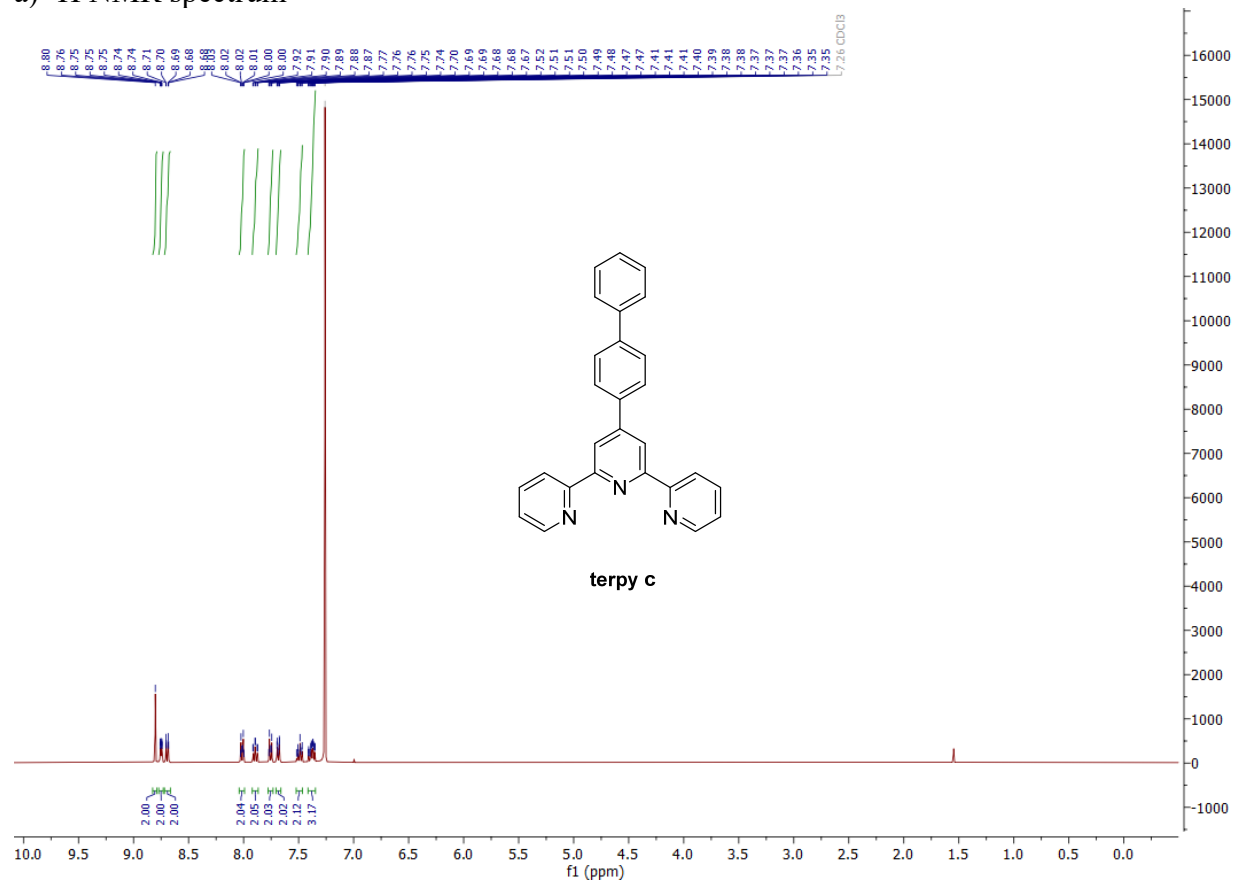
Synthesized terpyridine ligands:

4'-(4-Methoxyphenyl)-2,2':6',2''-terpyridine **terpy b**

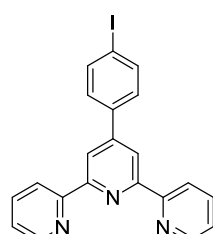
a) ^1H NMR spectrum



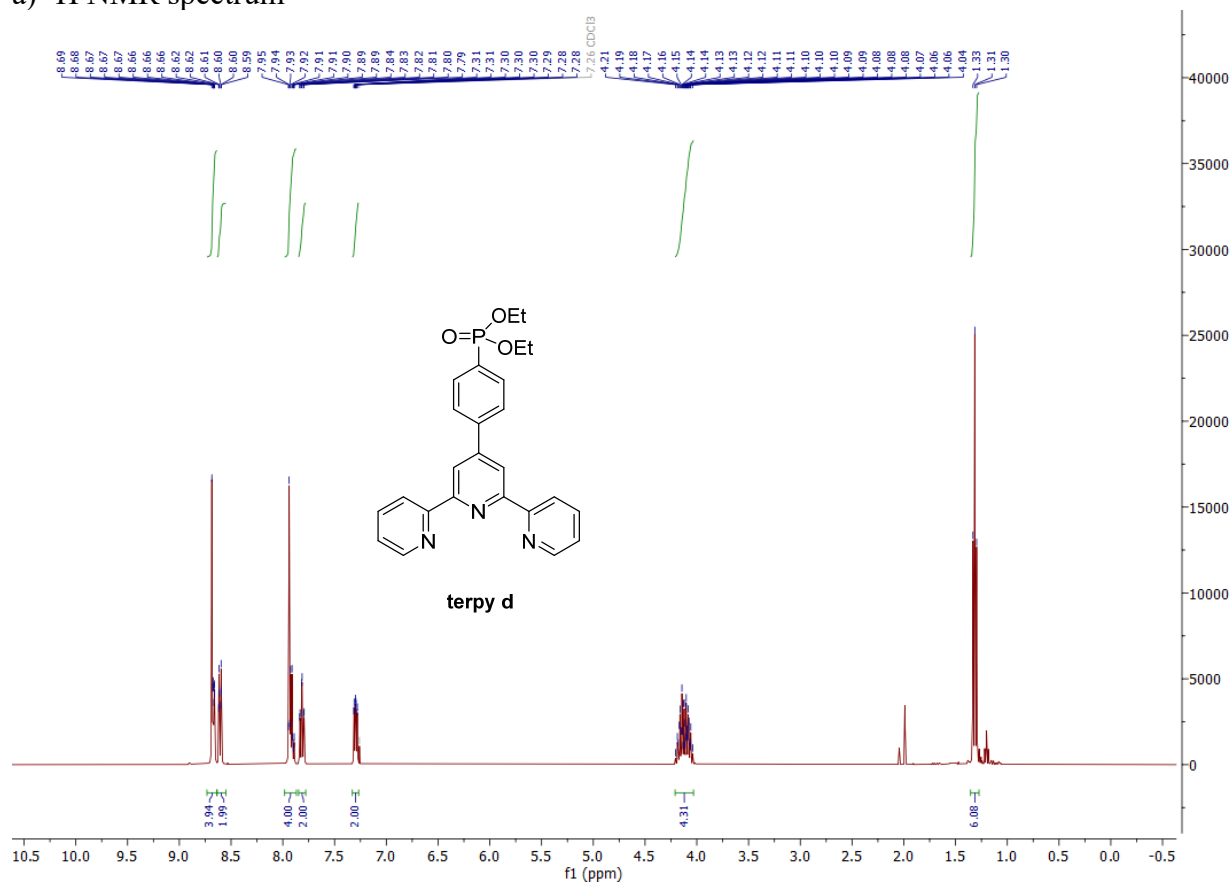
4'-([1,1'-Biphenyl]-4-yl)-2,2':6',2''-terpyridine **terpy c**
a) ^1H NMR spectrum



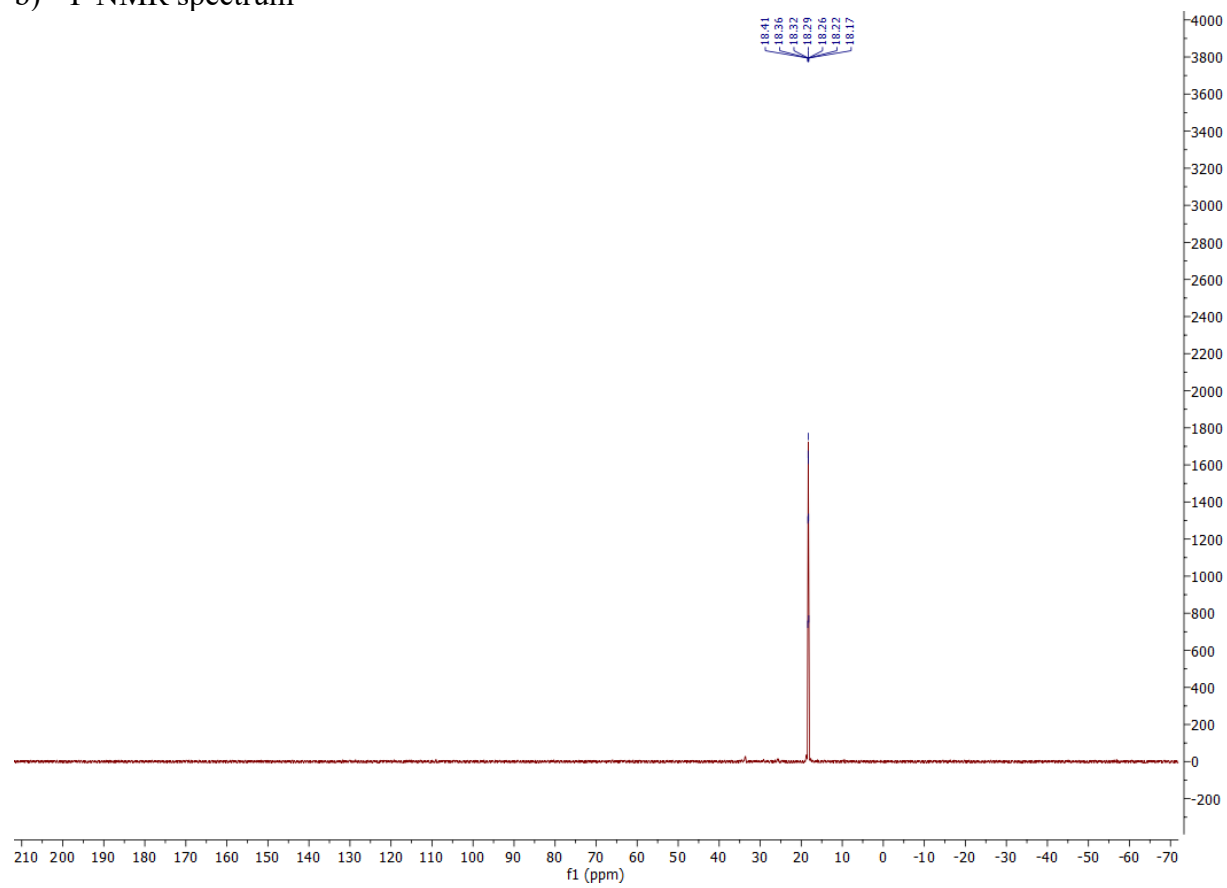
a) ^1H NMR spectrum



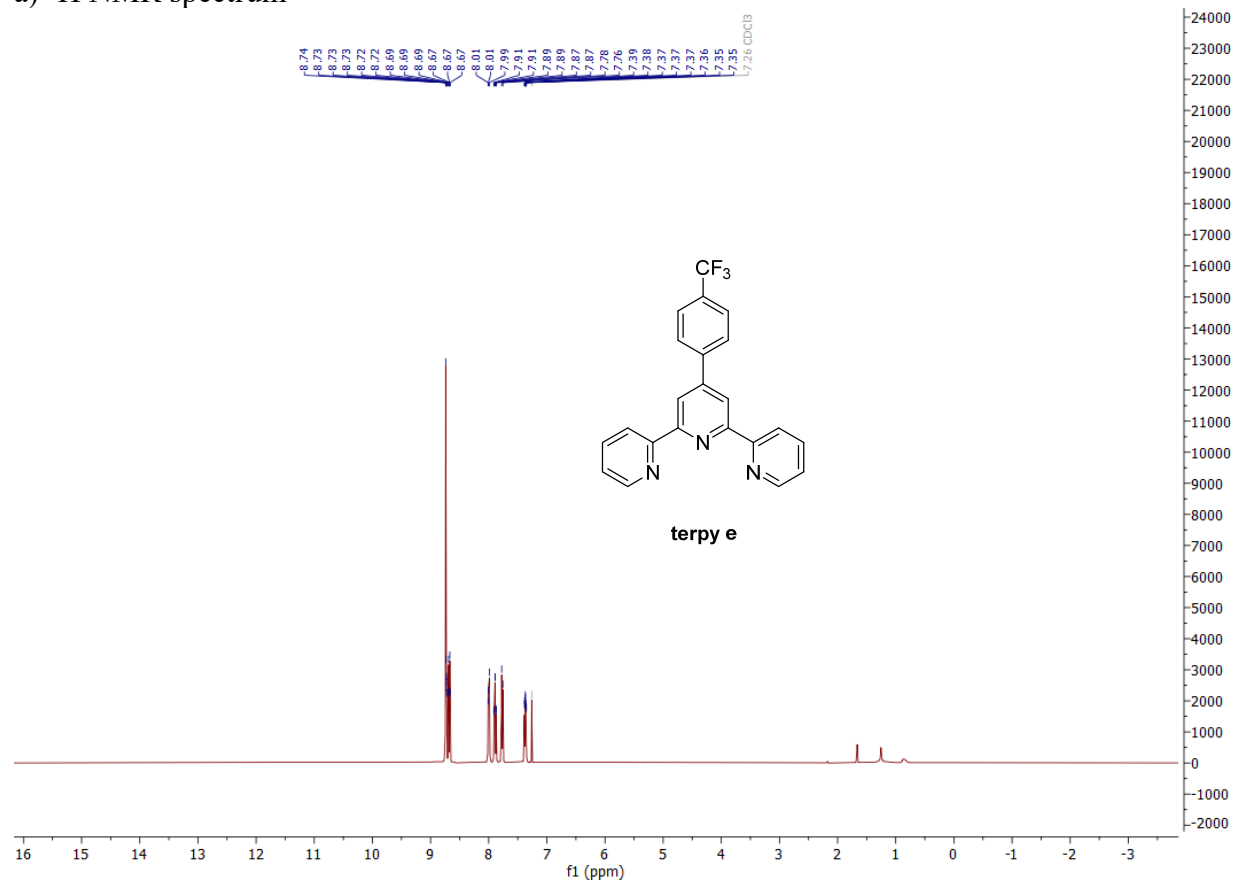
Diethyl (4-([2,2':6',2''-terpyridin]-4'-yl)phenyl)phosphonate **terpy d**
a) ^1H NMR spectrum



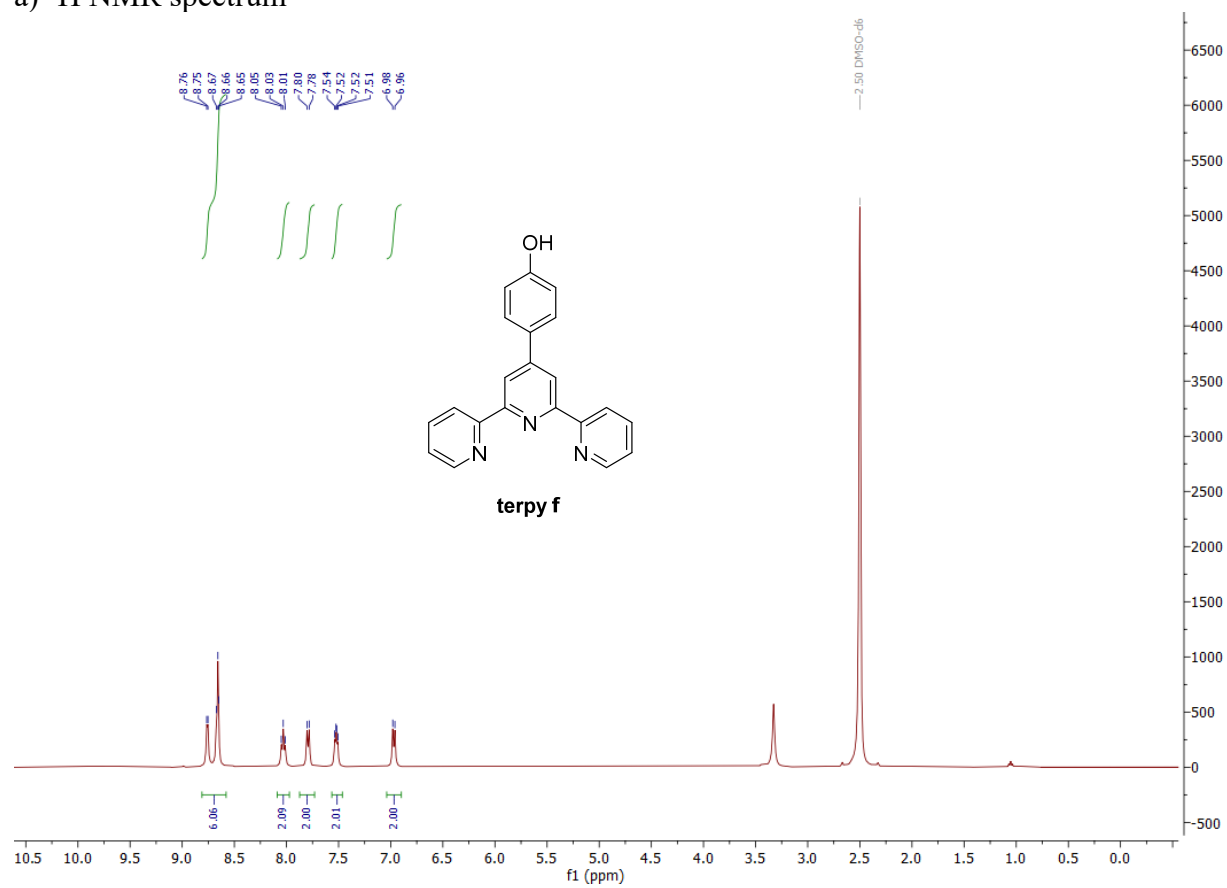
b) ^{31}P NMR spectrum



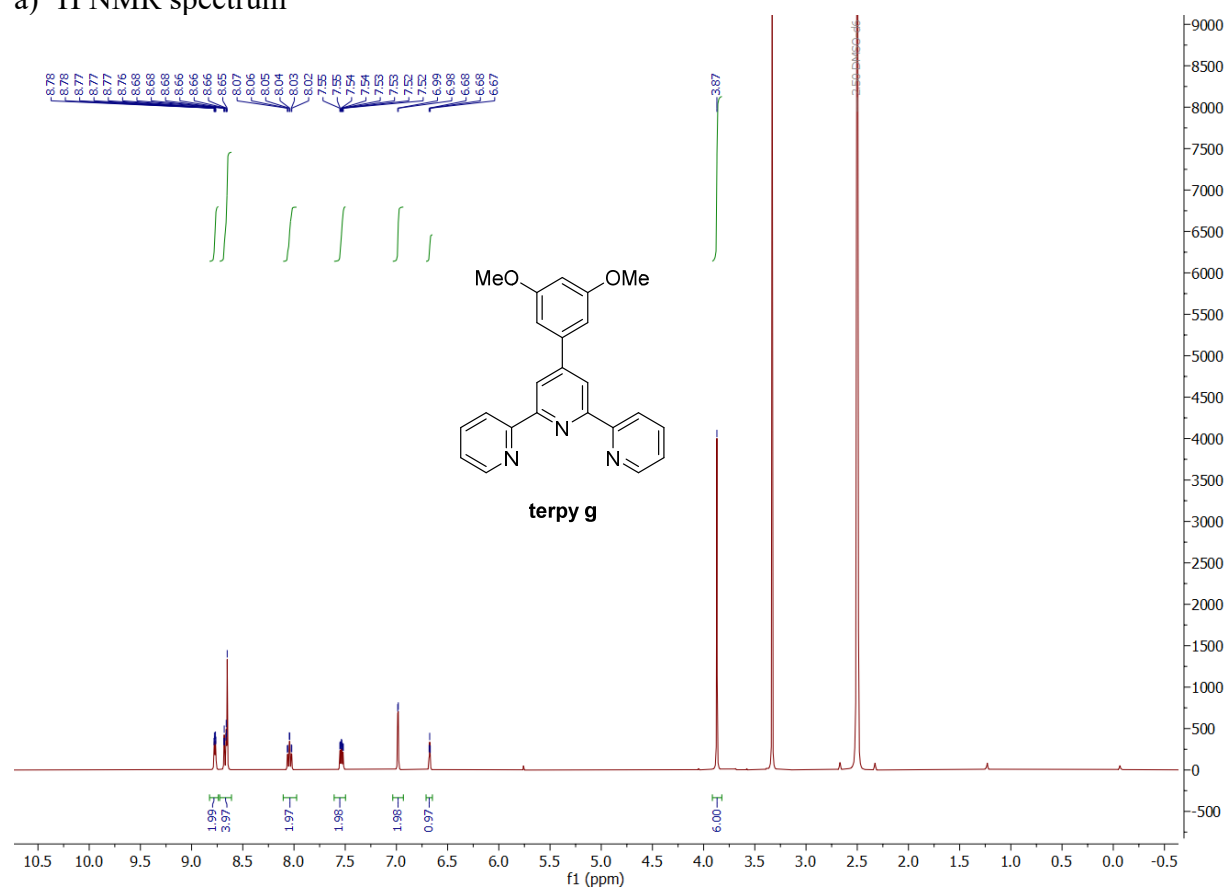
4'-(4-(Trifluoromethyl)phenyl)-2,2':6',2''-terpyridine **terpy e**
a) ^1H NMR spectrum



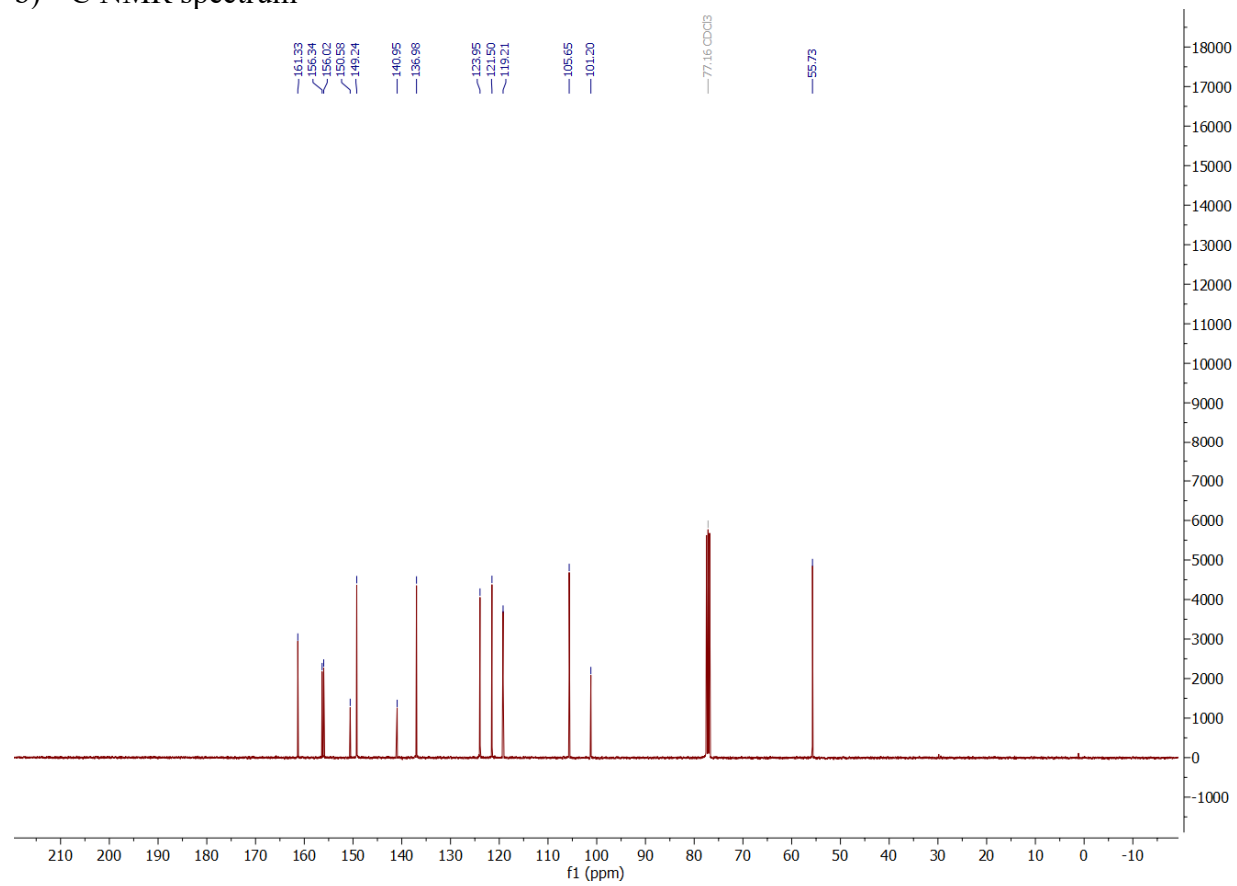
4-([2,2':6',2''-Terpyridin]-4'-yl)phenol **terpy f**
a) ^1H NMR spectrum



4'-(3,5-Dimethoxyphenyl)-2,2':6',2''-terpyridine **terpy g**
a) ^1H NMR spectrum

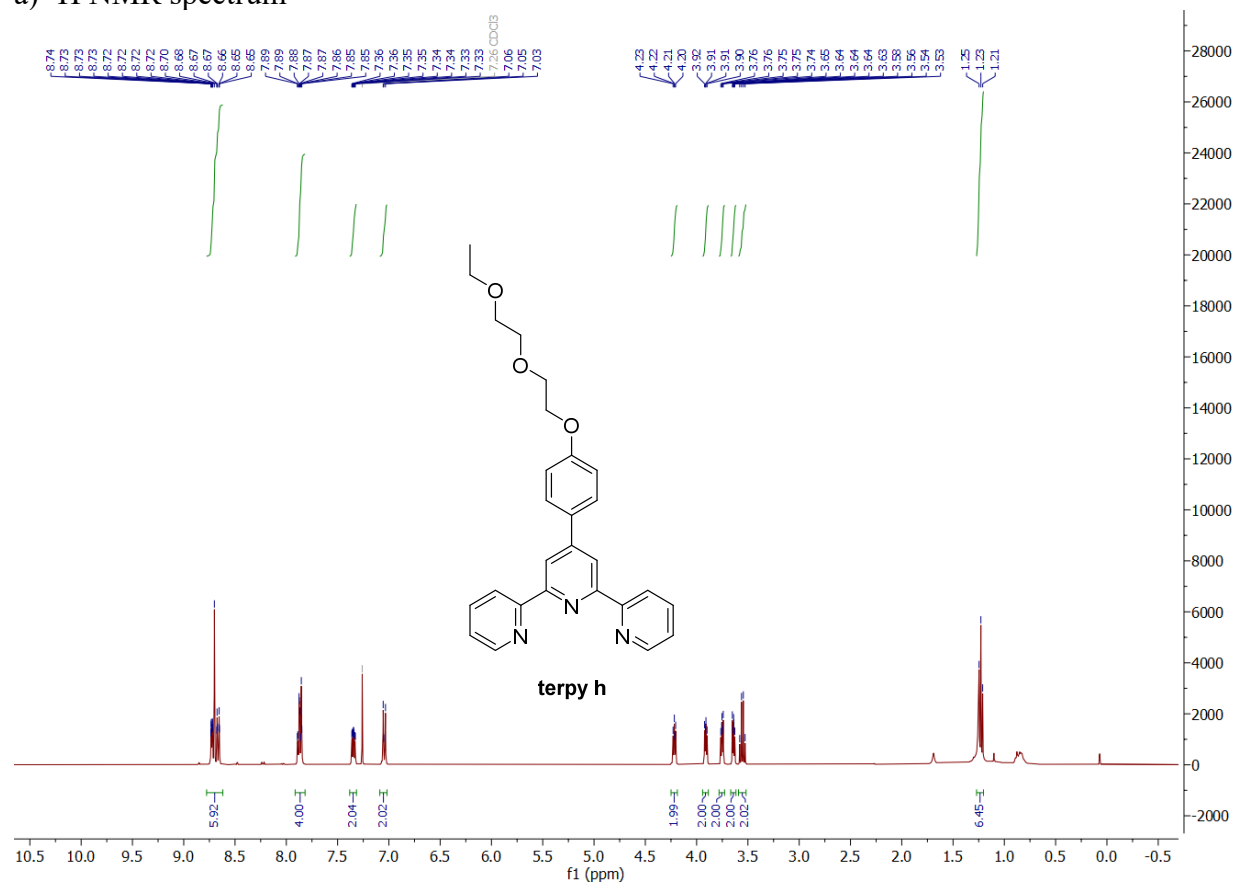


b) ^{13}C NMR spectrum

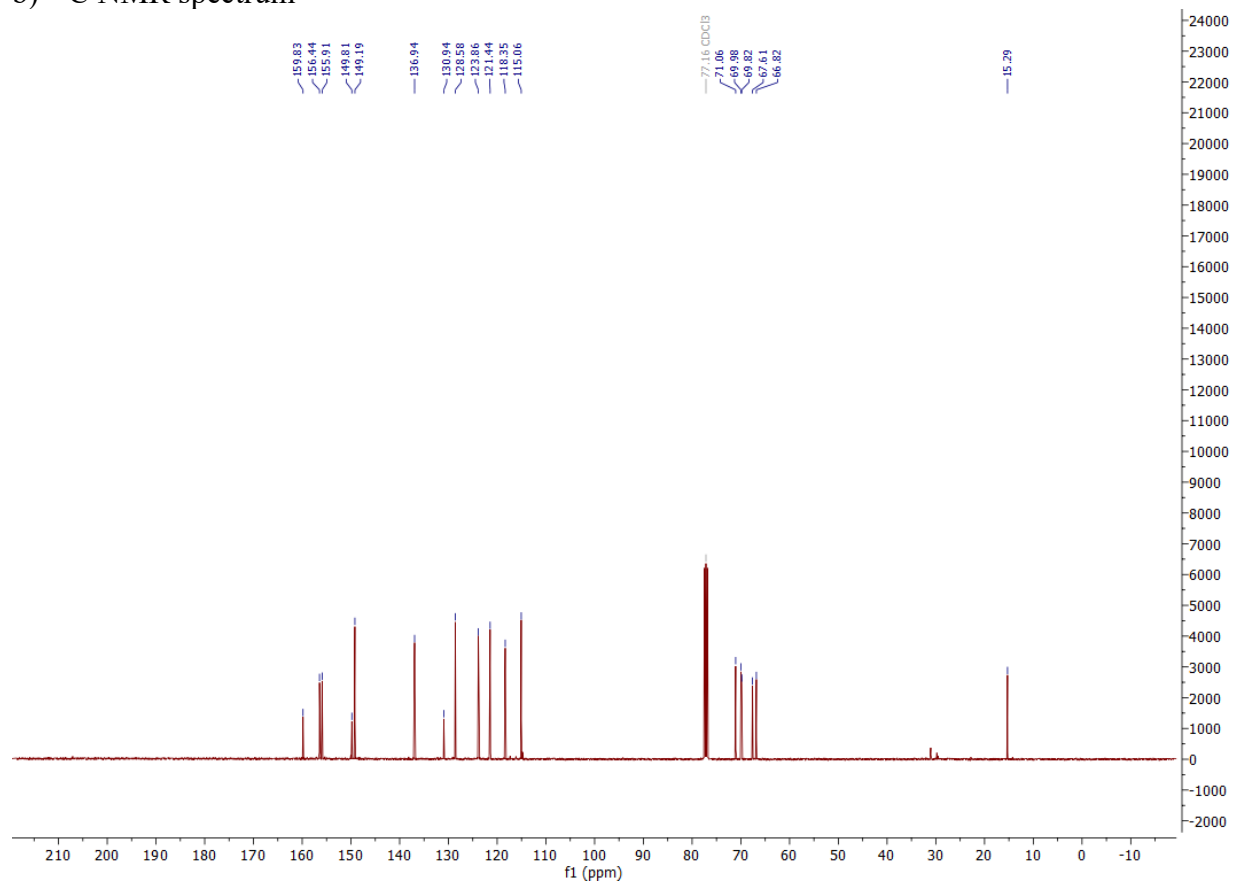


4'-(4-(2-(2-Ethoxyethoxy)ethoxy)phenyl)-2,2':6',2''-terpyridine **terpy h**

a) ^1H NMR spectrum

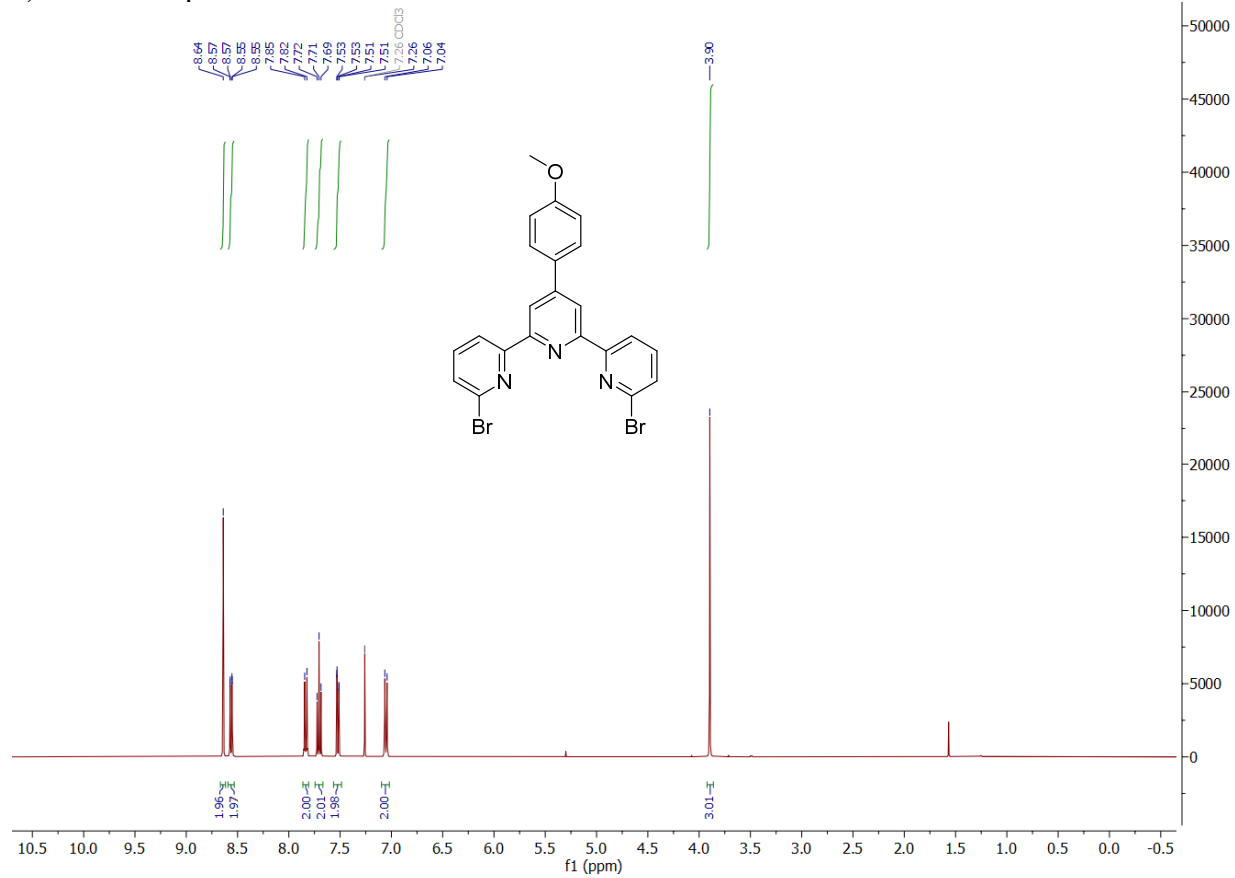


b) ^{13}C NMR spectrum

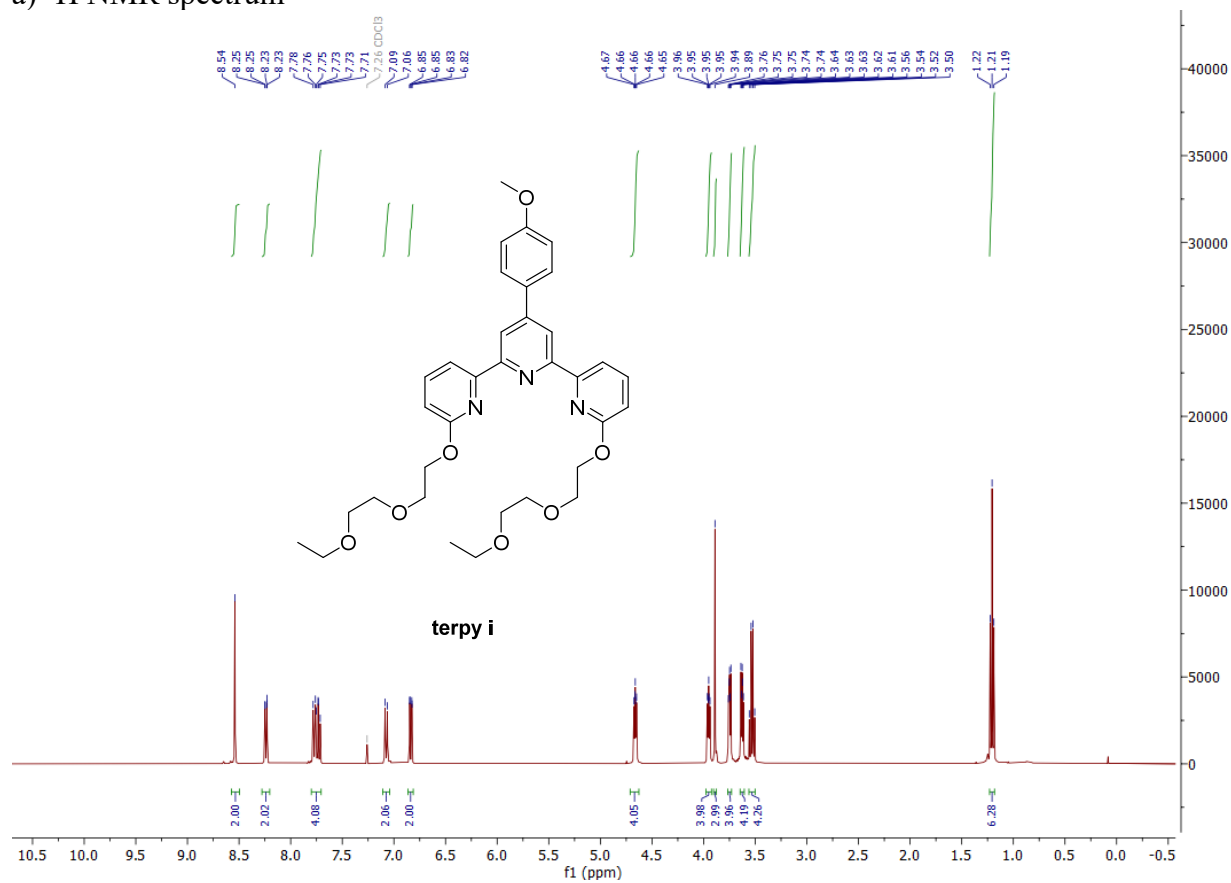


6,6''-Dibromo-4'-(4-methoxyphenyl)-2,2':6,2''-terpyridine

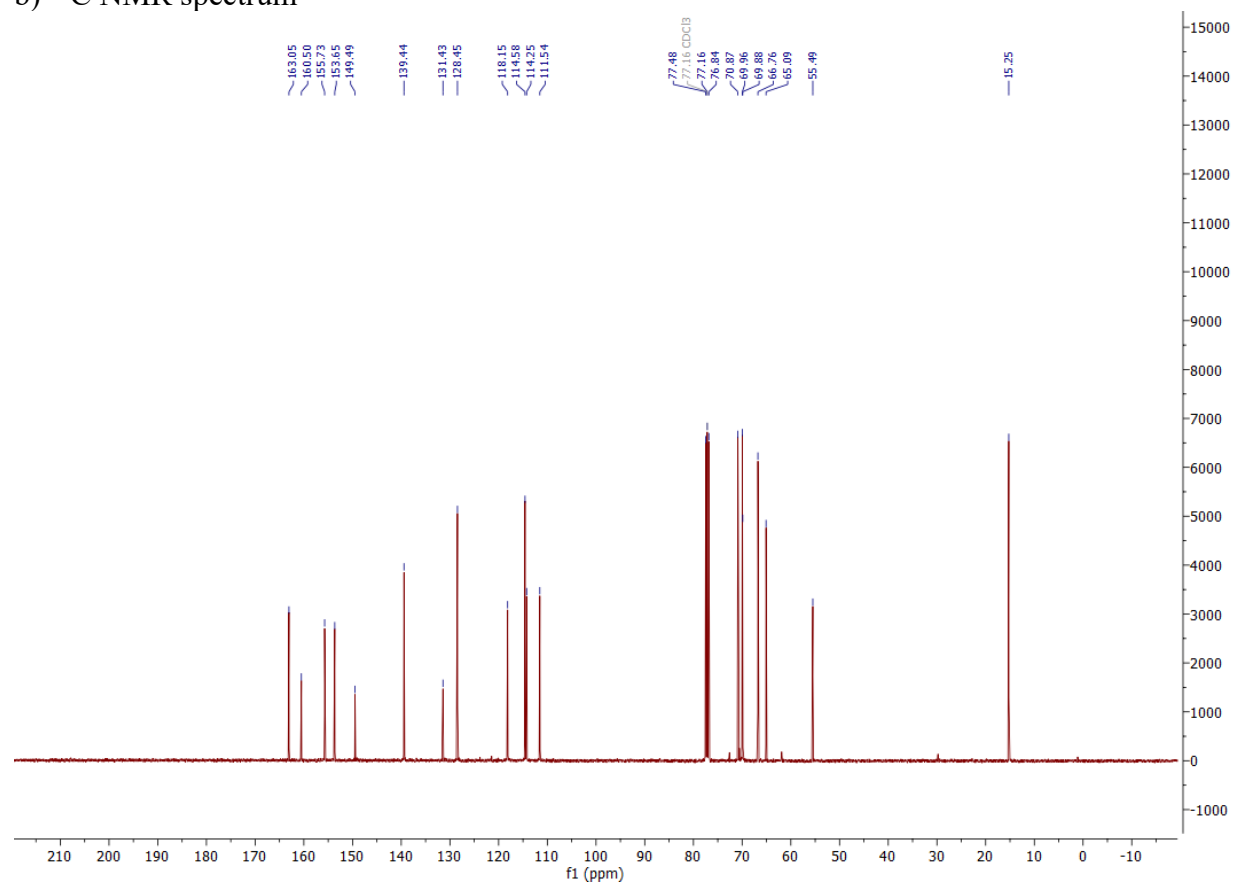
a) ¹H NMR spectrum



6,6''-Bis(2-(2-ethoxyethoxy)ethoxy)-4'-(4-methoxyphenyl)-2,2':6',2''-terpyridine **terpy i**
a) ^1H NMR spectrum

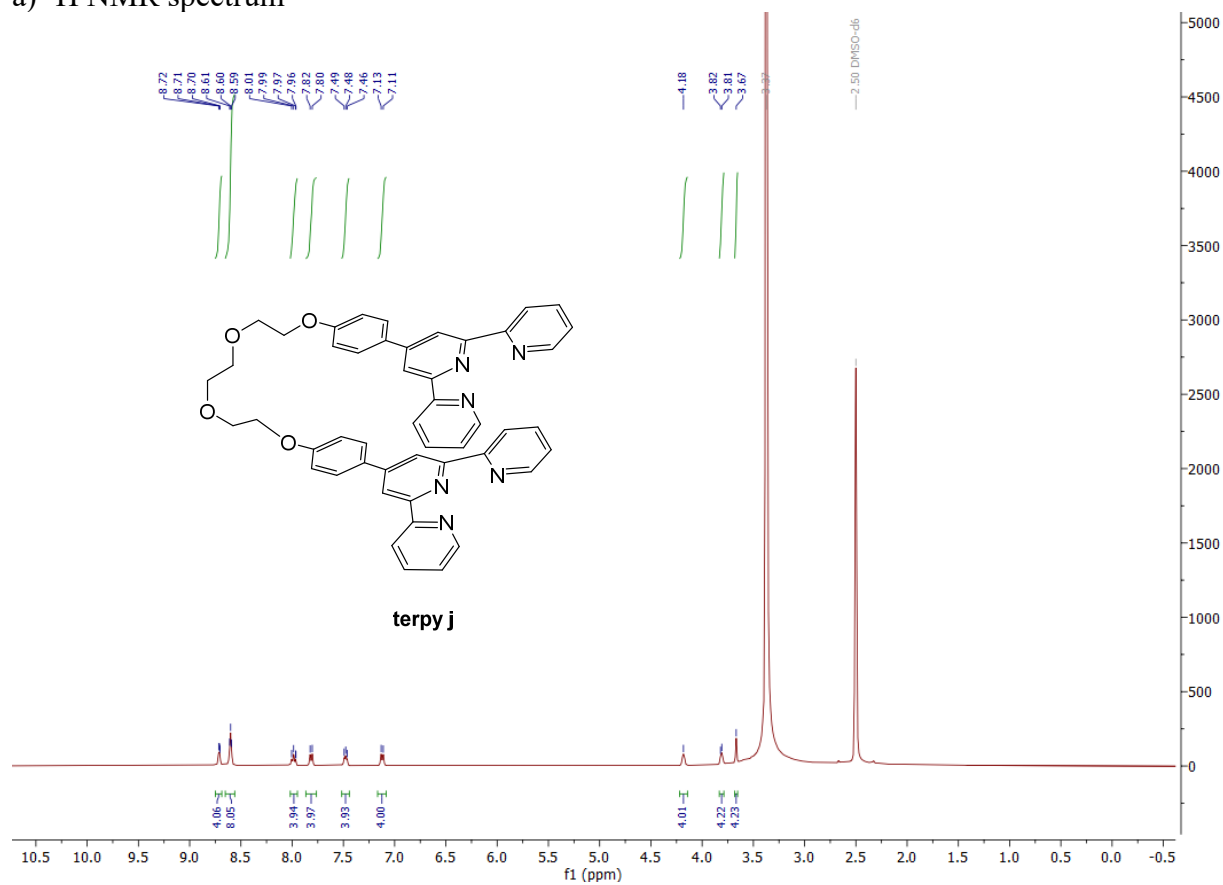


b) ^{13}C NMR spectrum

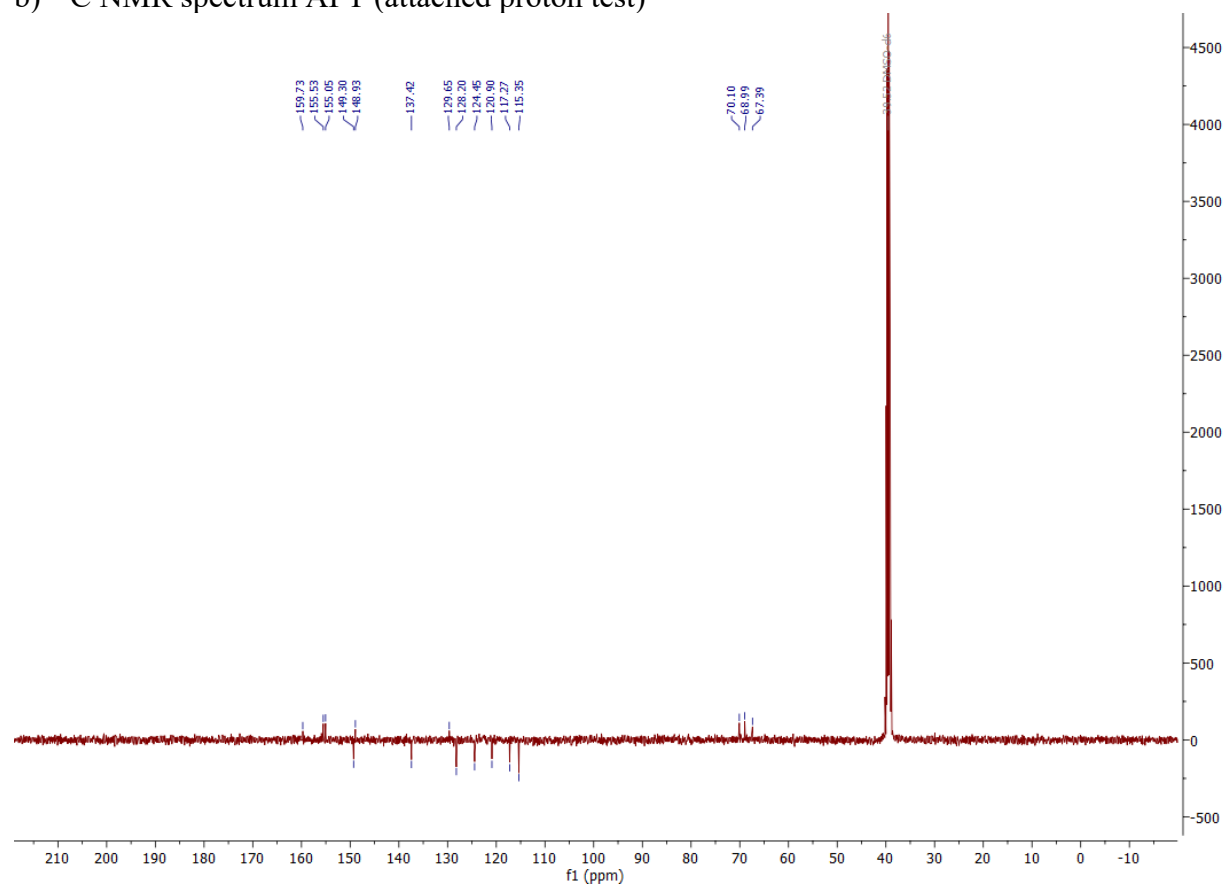


1,2-Bis(2-(4-([2,2':6',2''-terpyridin]-4'-yl)phenoxy)ethoxy)ethane **terpy j**

a) ^1H NMR spectrum



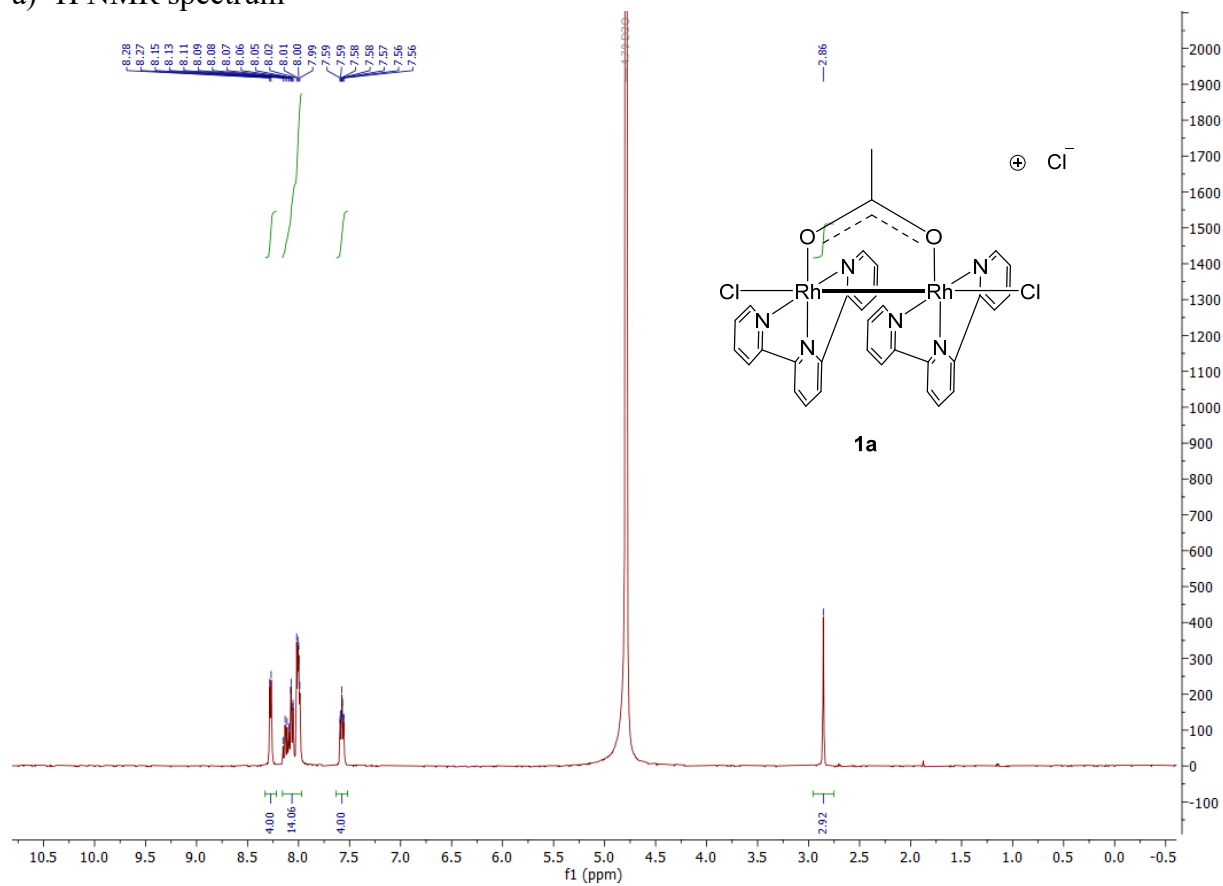
b) ^{13}C NMR spectrum APT (attached proton test)



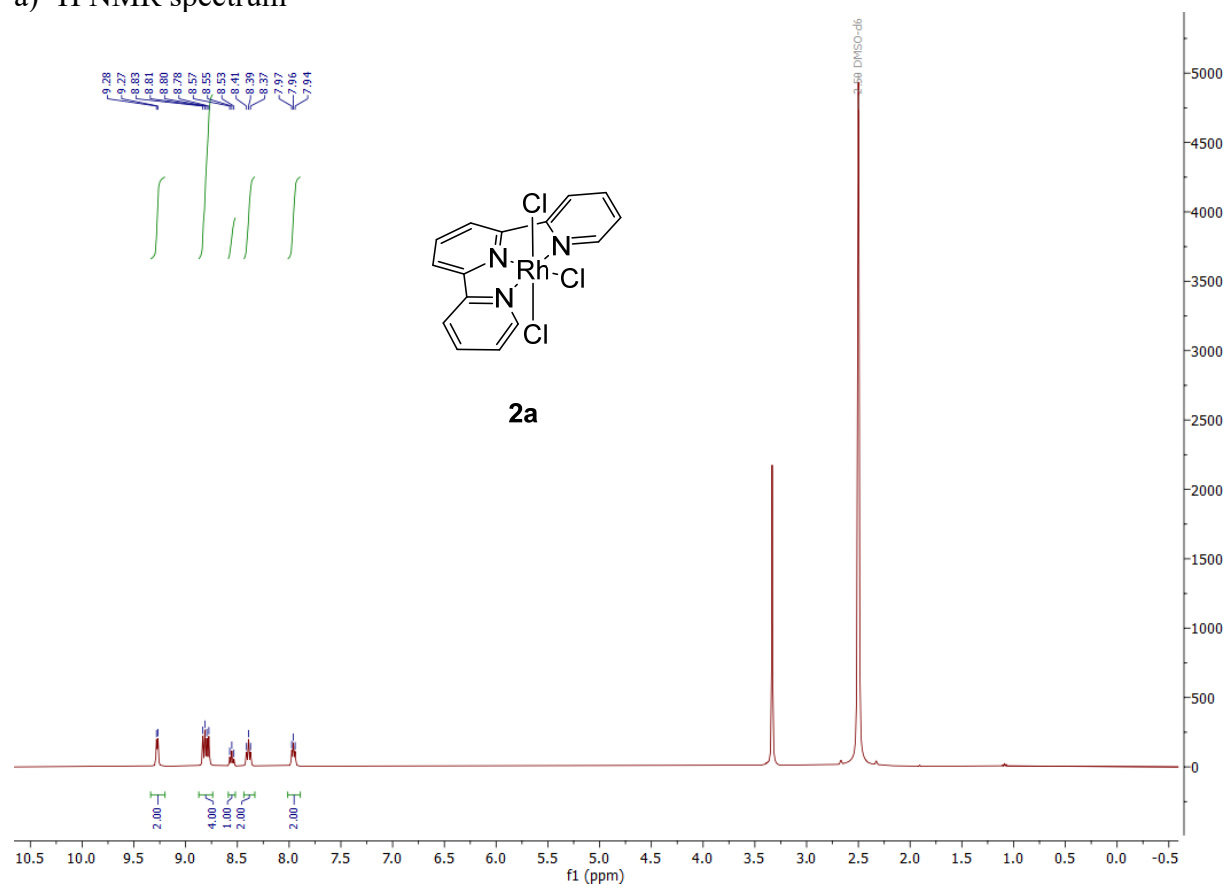
Synthesized rhodium terpyridine complexes

Rh-terpyridine dimer **1a**

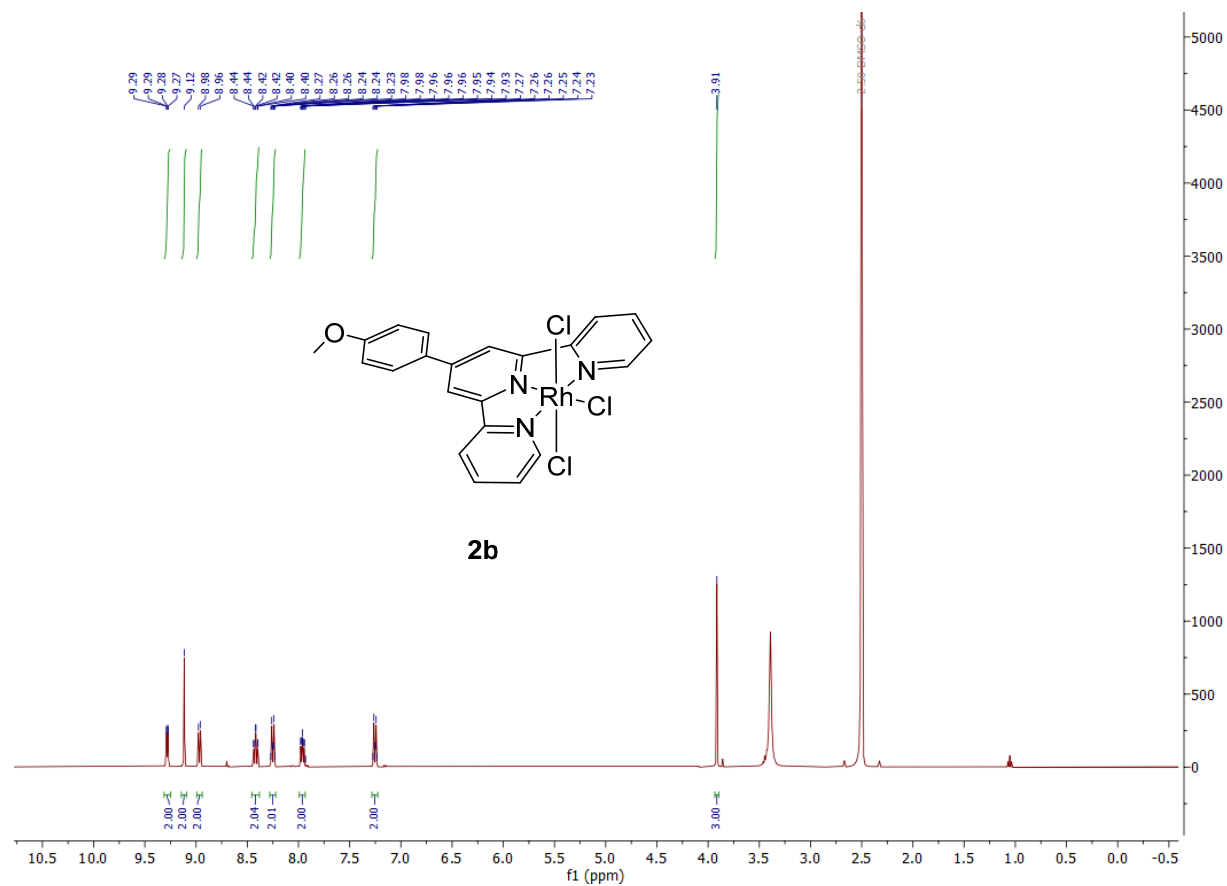
a) ^1H NMR spectrum



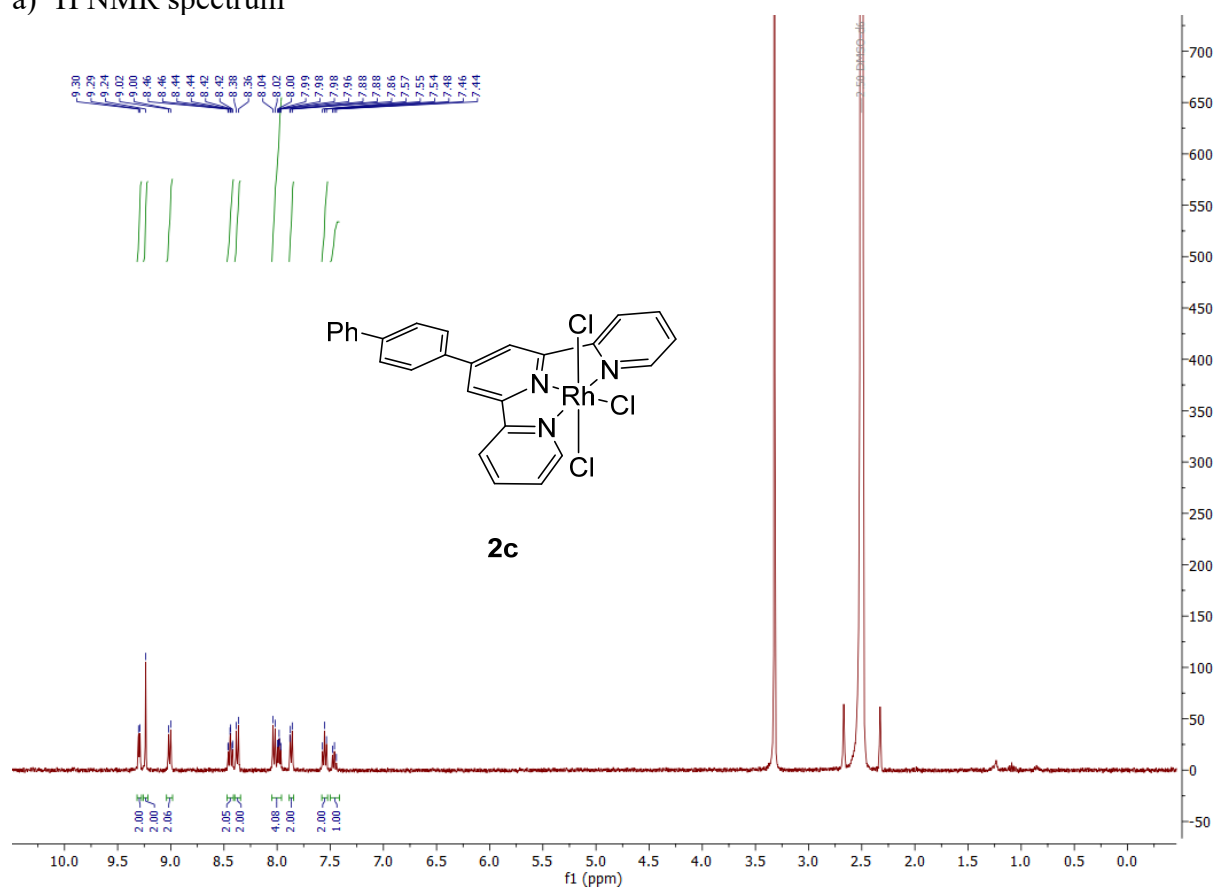
Rh-terpyridine **2a**
a) ^1H NMR spectrum



Rh-terpyridine **2b**
a) ^1H NMR spectrum

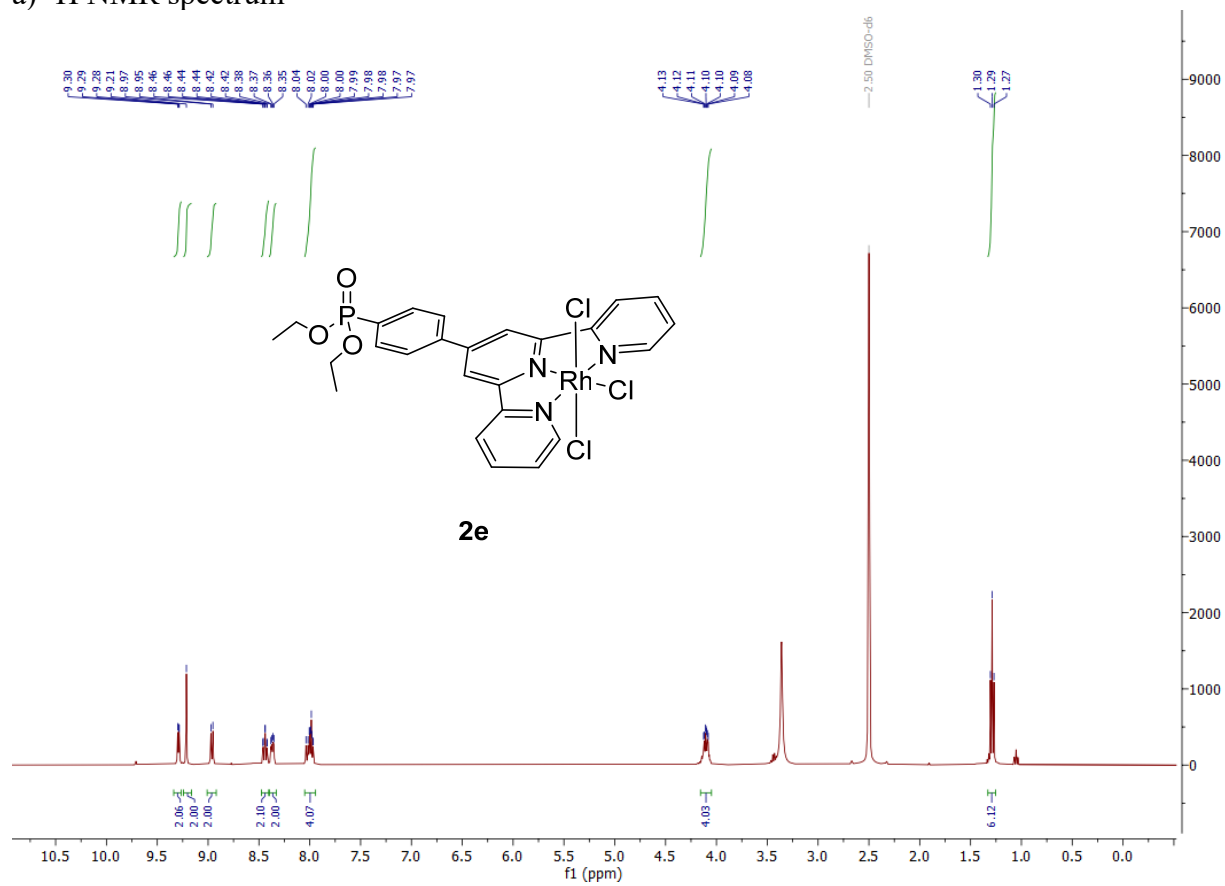


Rh-terpyridine **2c**
a) ^1H NMR spectrum

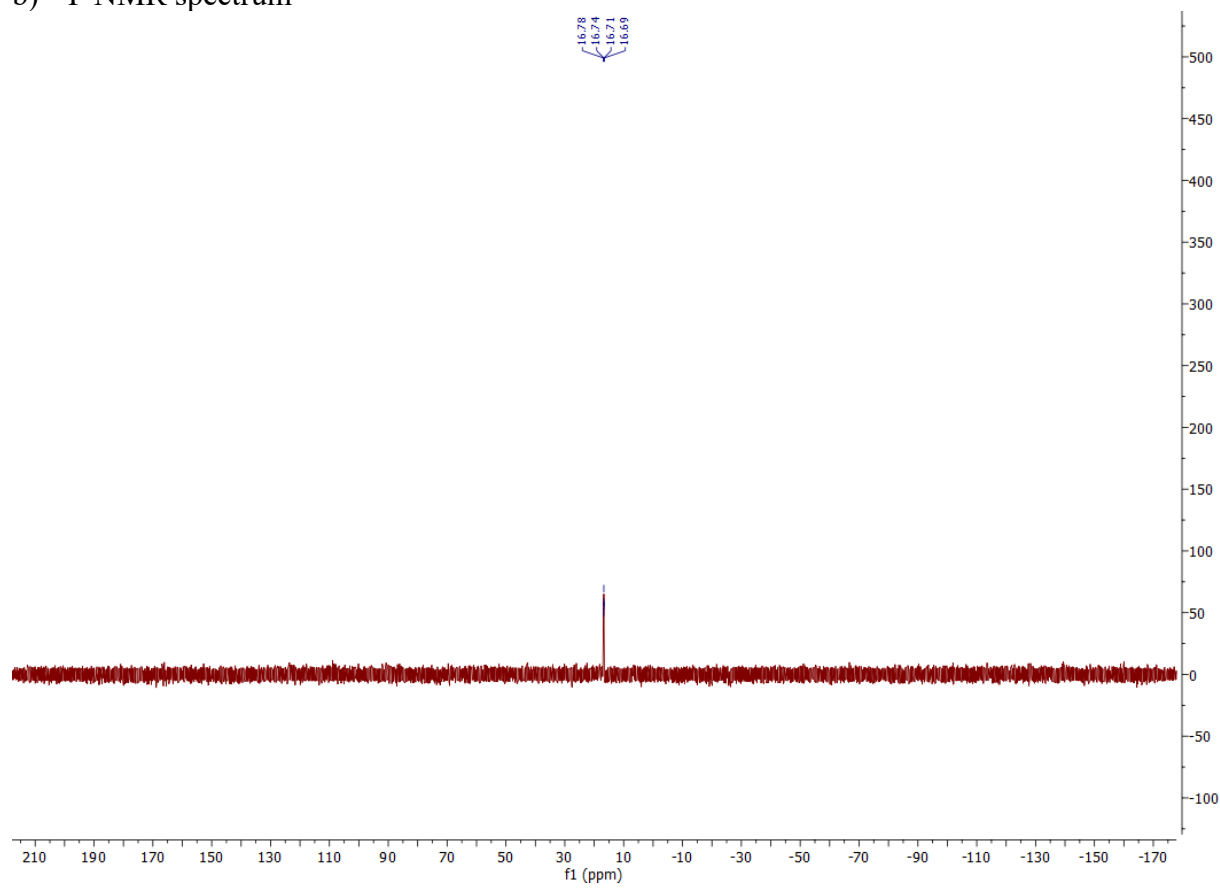


Rh-terpyridine **2d**

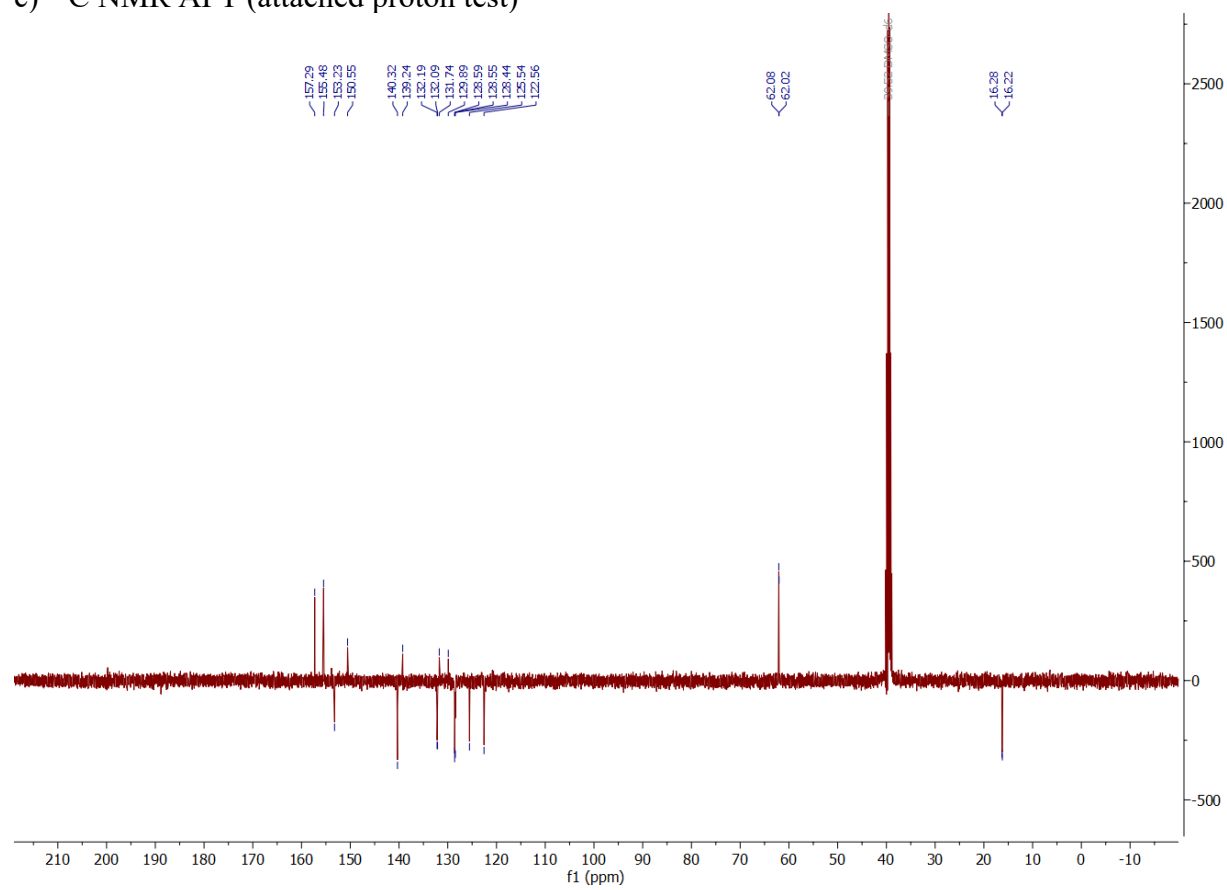
a) ^1H NMR spectrum



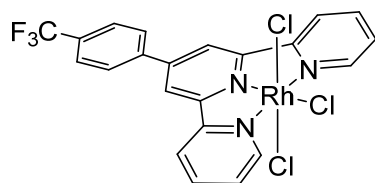
b) ^{31}P NMR spectrum



c) ^{13}C NMR APT (attached proton test)

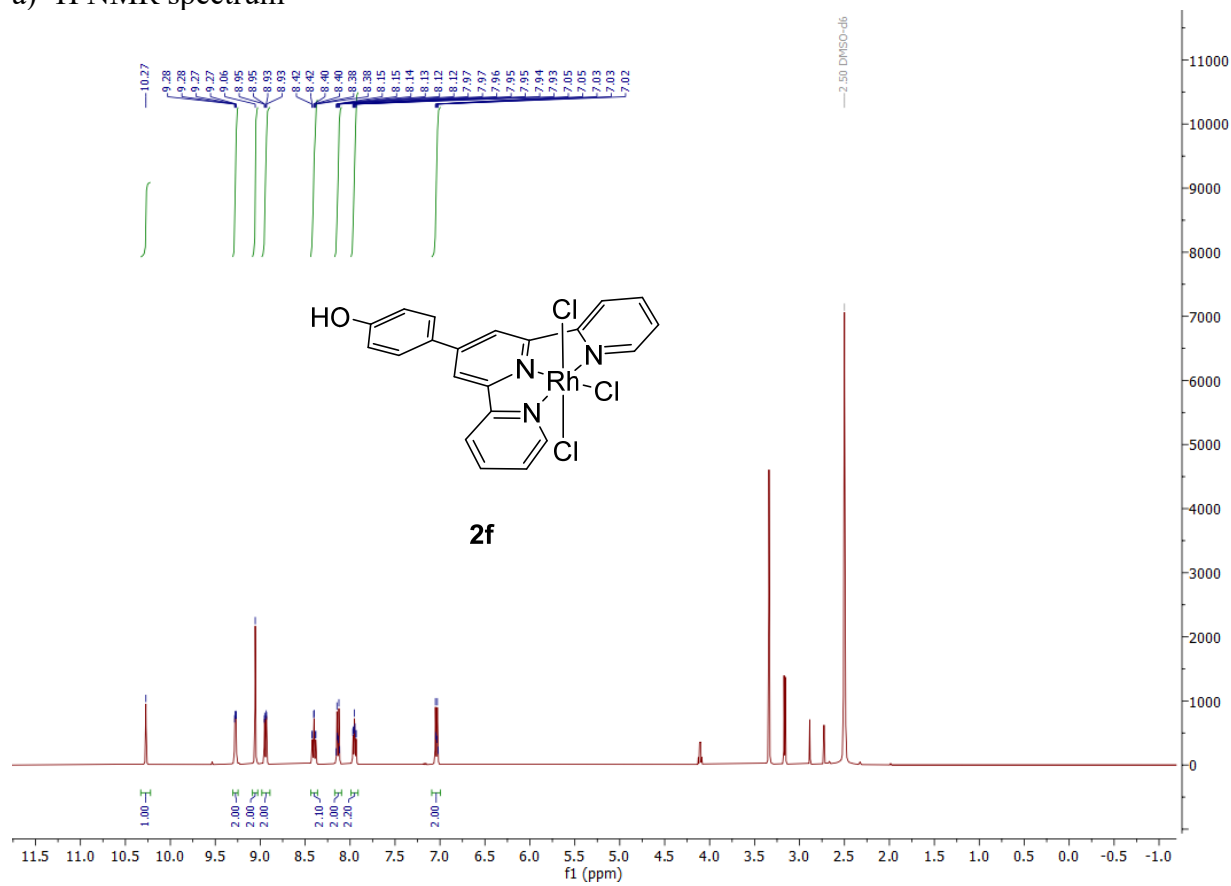


a) ^1H NMR spectrum

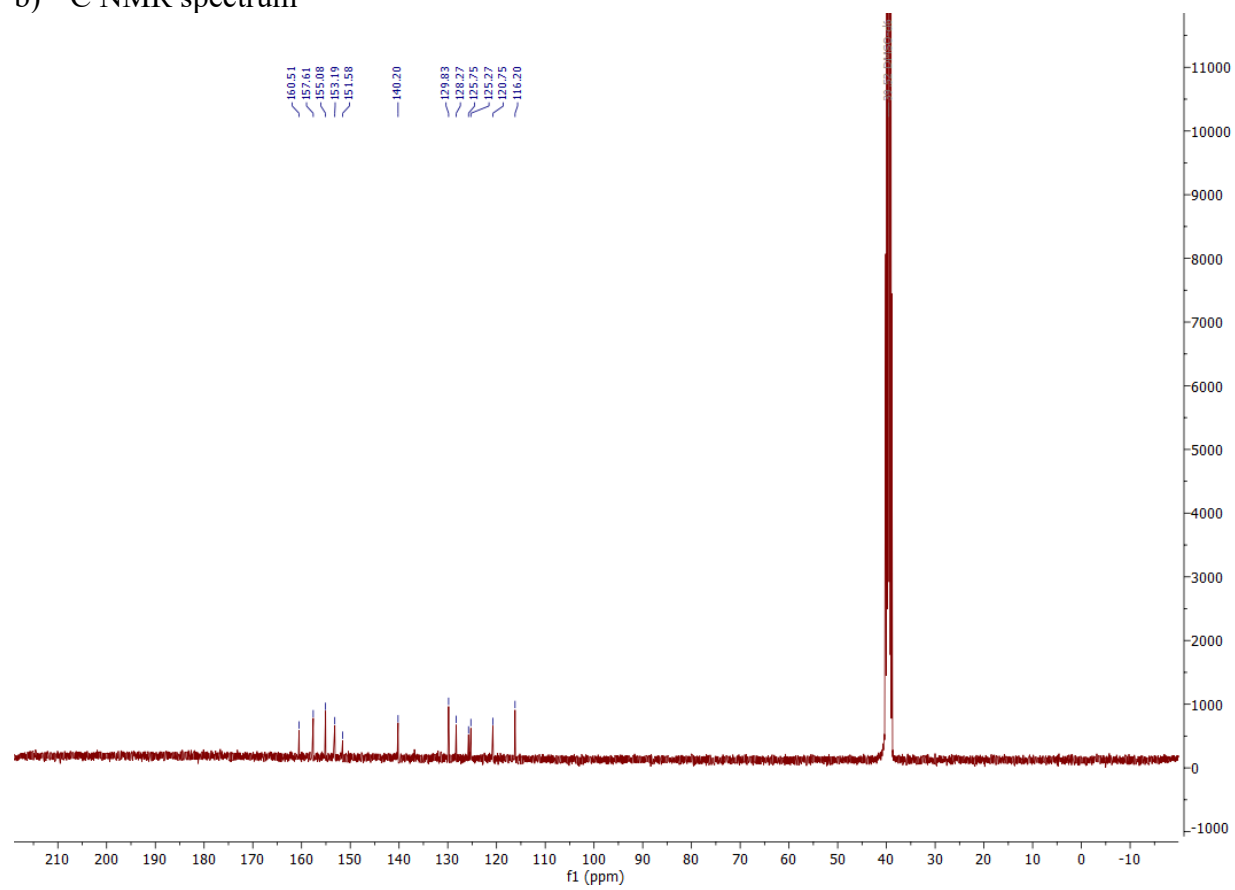


2e

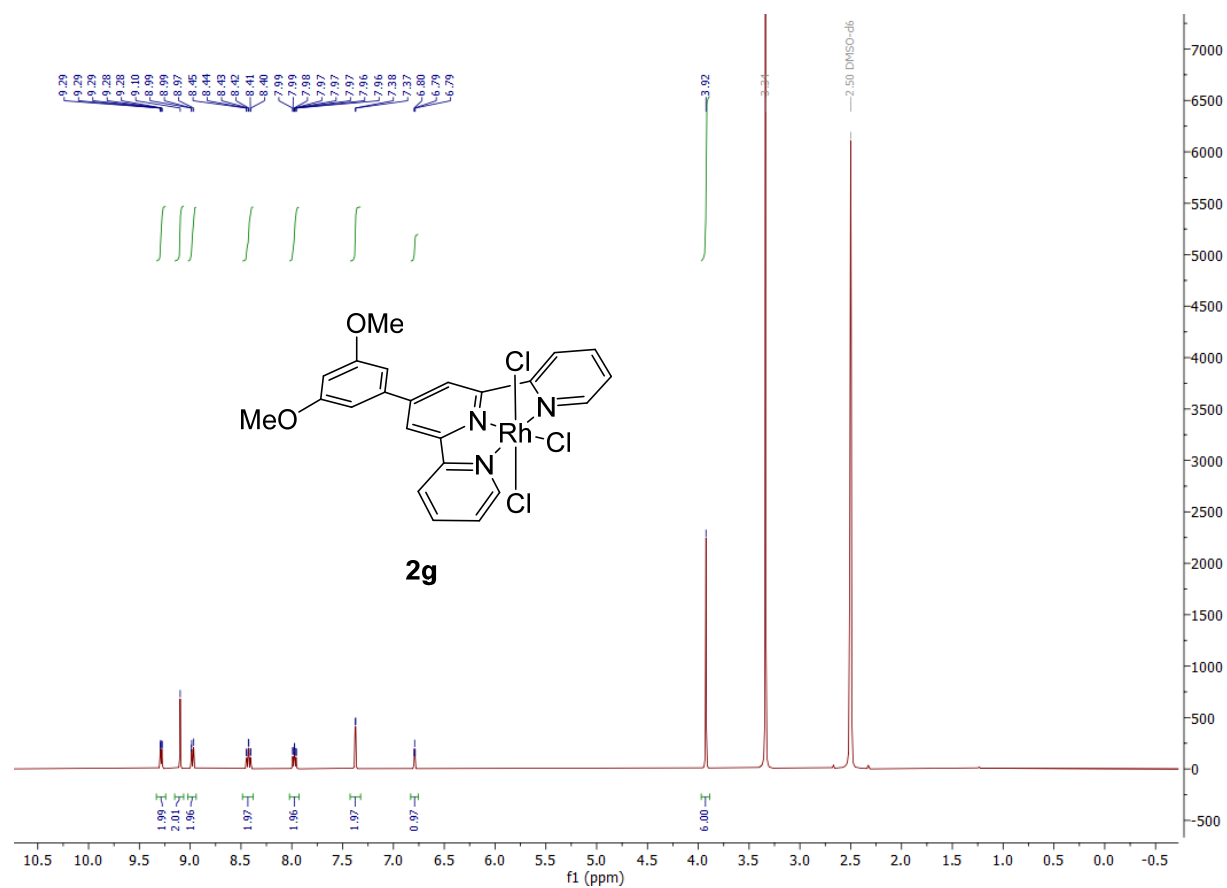
Rh-terpyridine **2f**
a) ^1H NMR spectrum



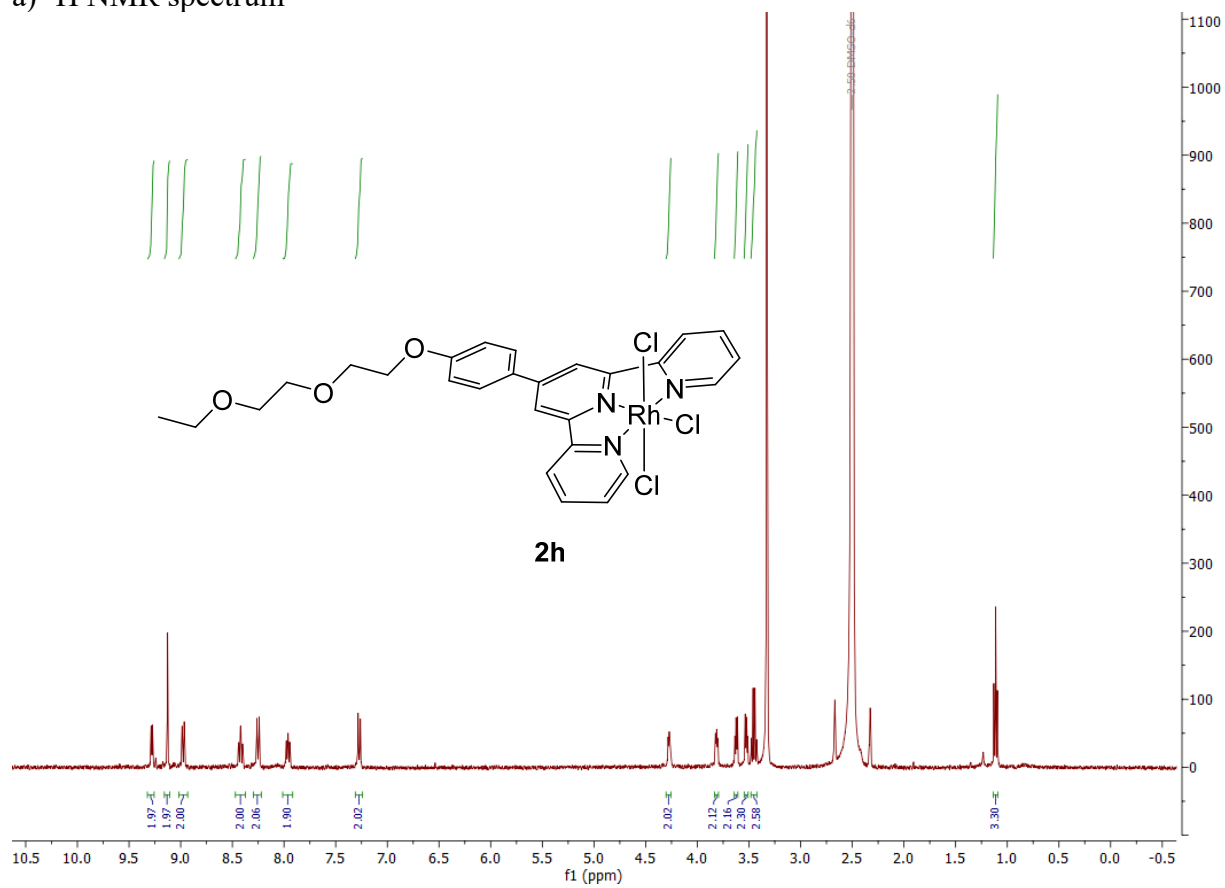
b) ^{13}C NMR spectrum



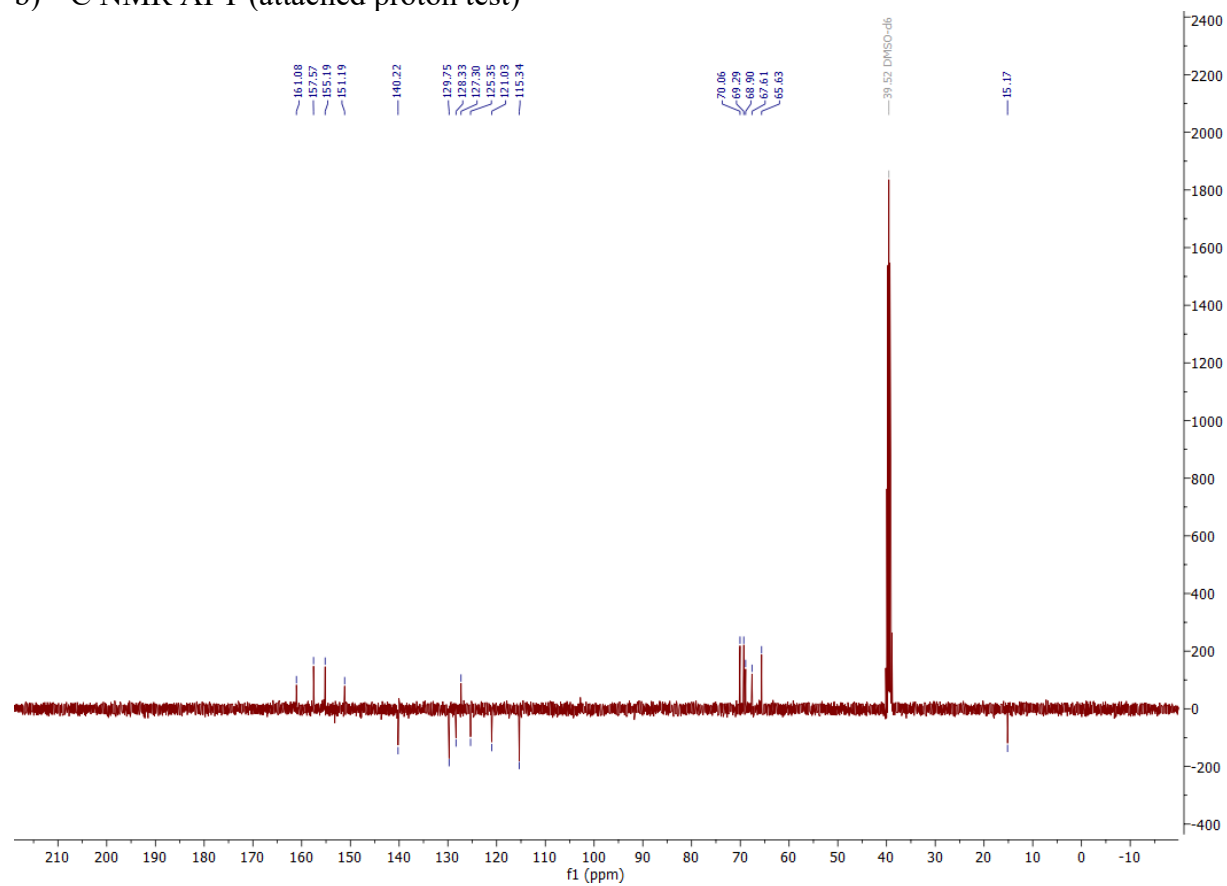
Rh-terpyridine **2g**
a) ^1H NMR spectrum



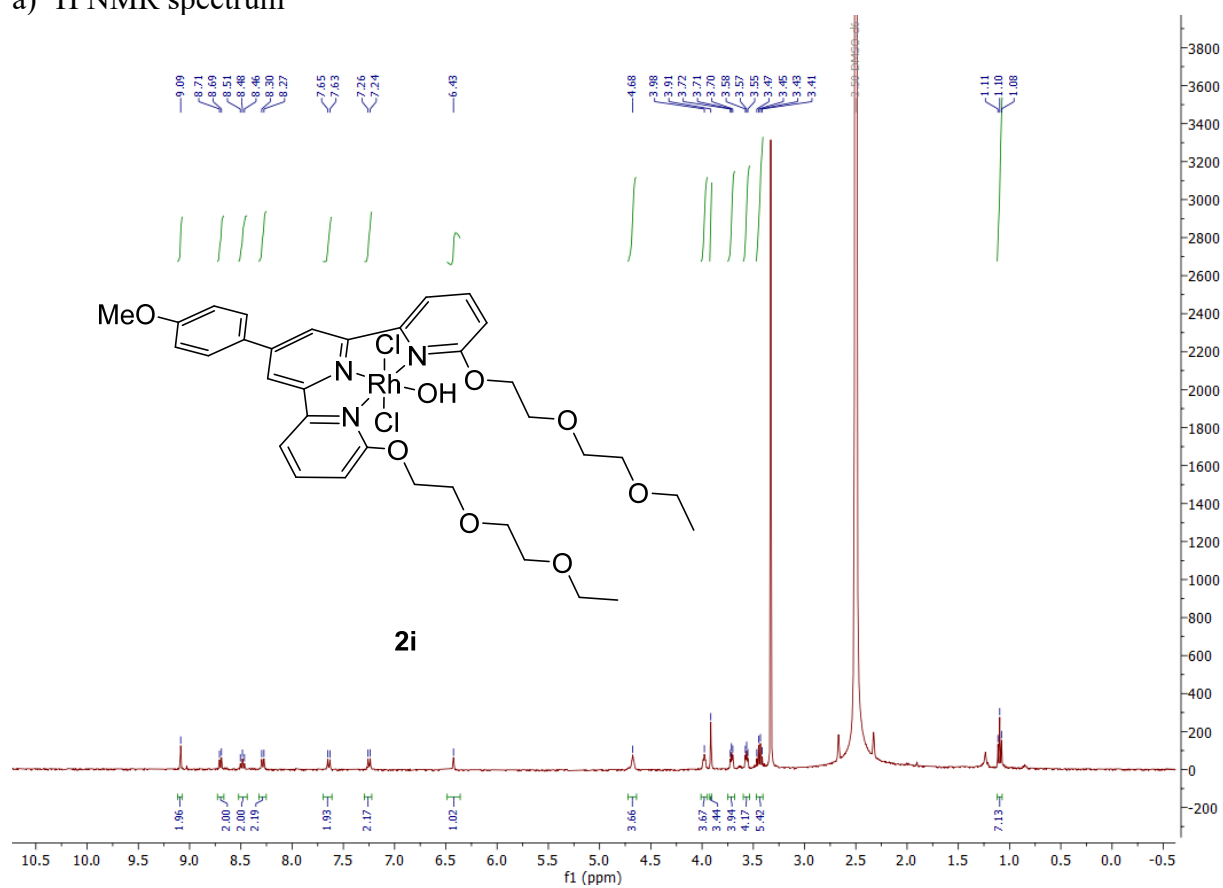
Rh-terpyridine **2h**
a) ^1H NMR spectrum



b) ^{13}C NMR APT (attached proton test)



Rh-terpyridine **2i**
a) ^1H NMR spectrum

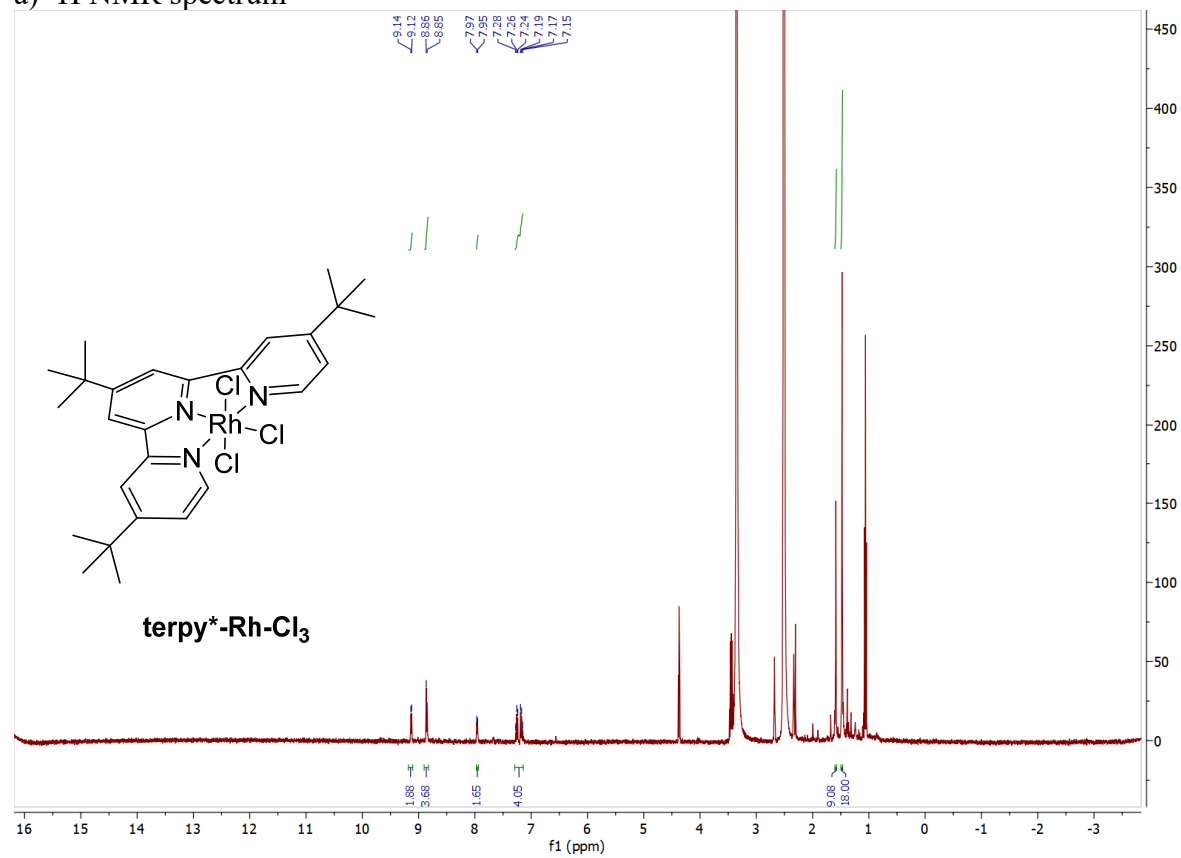


a) ^1H NMR spectrum



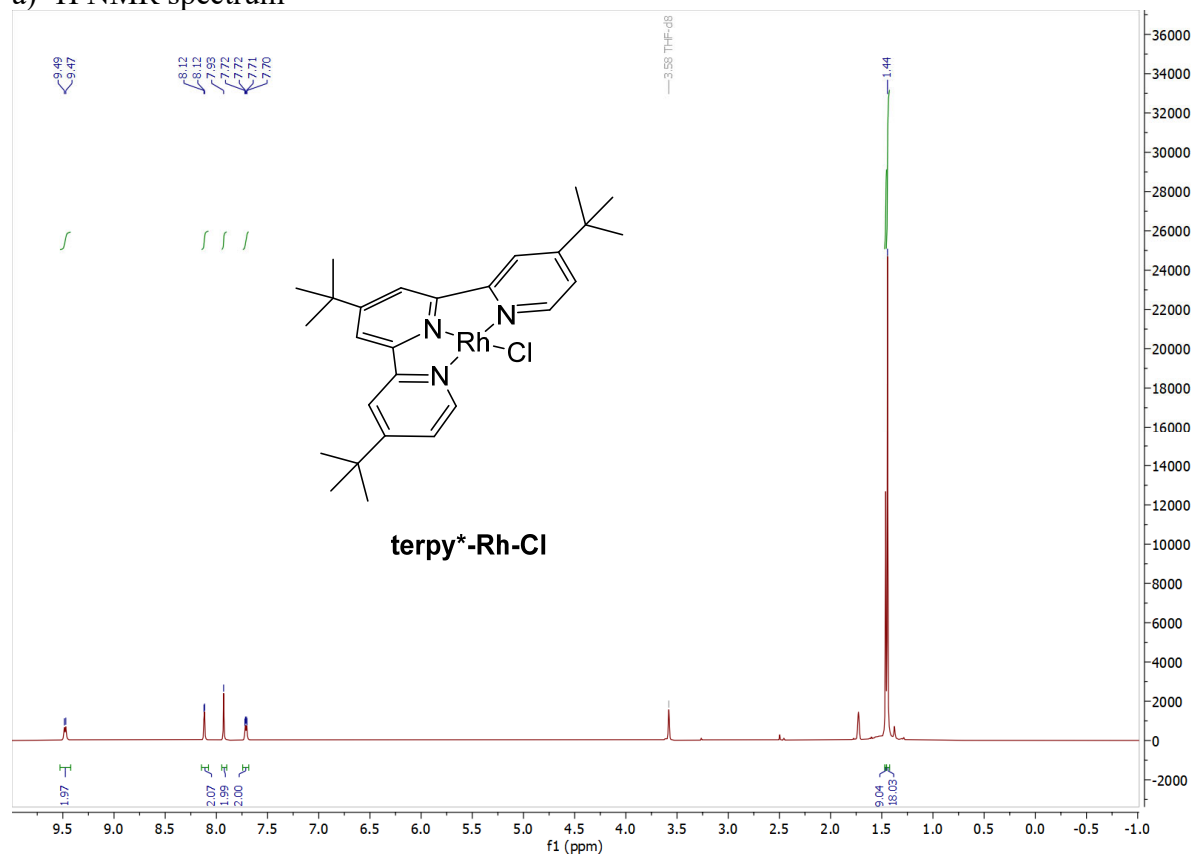
Rh-terpyridine **terpy*-Rh-Cl₃**

a) ¹H NMR spectrum

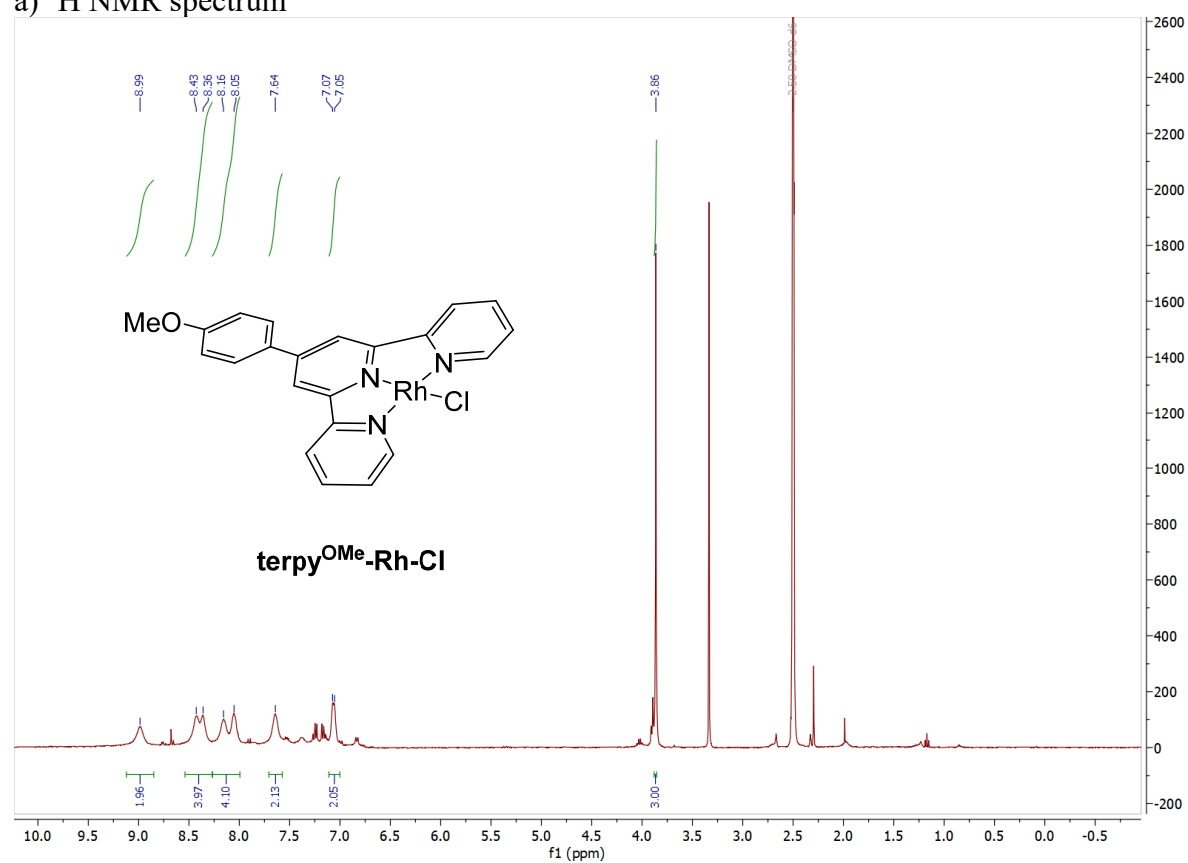


Rh-terpyridine **terpy*-Rh-Cl**

a) ^1H NMR spectrum



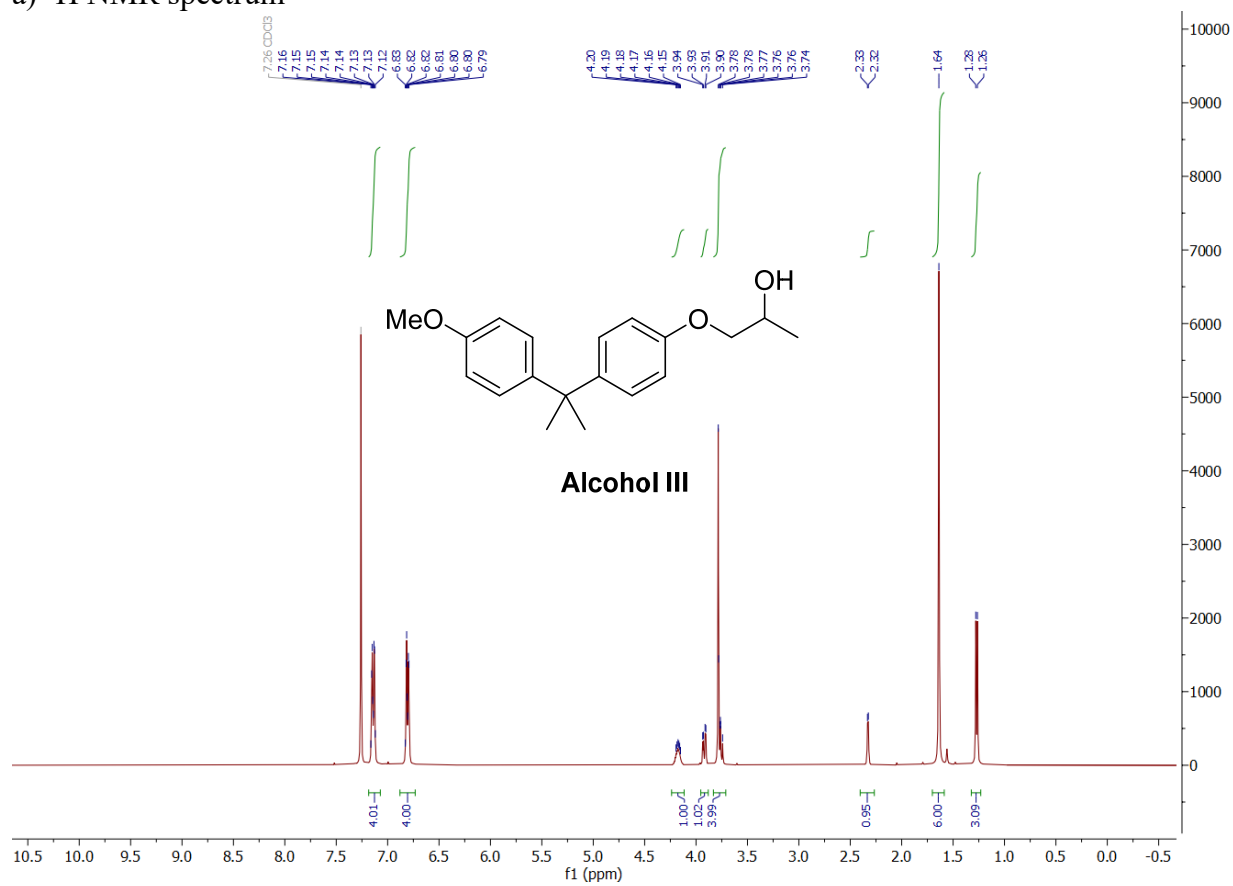
Rh-terpyridine **terpy^{OMe}-Rh-Cl**
a) ¹H NMR spectrum



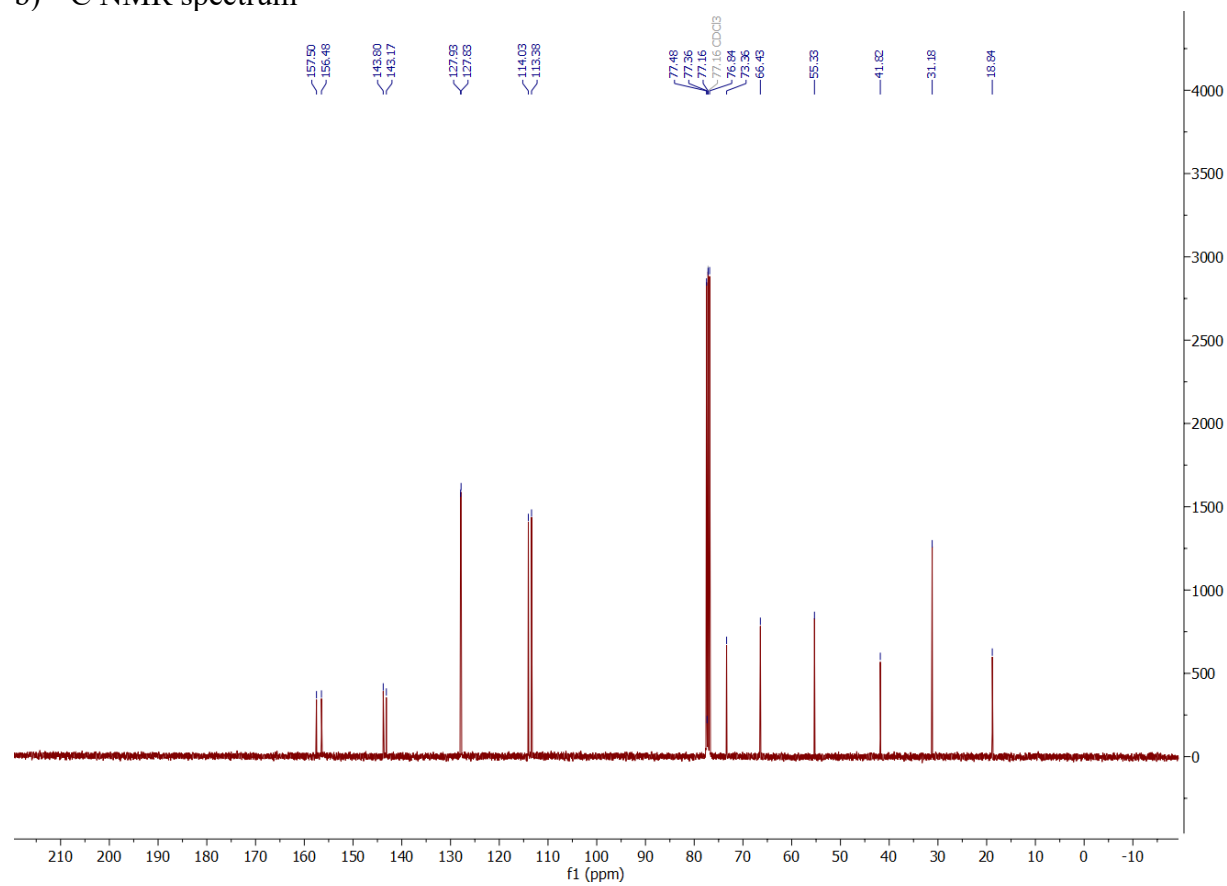
Model substrates

Alcohol III

a) ^1H NMR spectrum

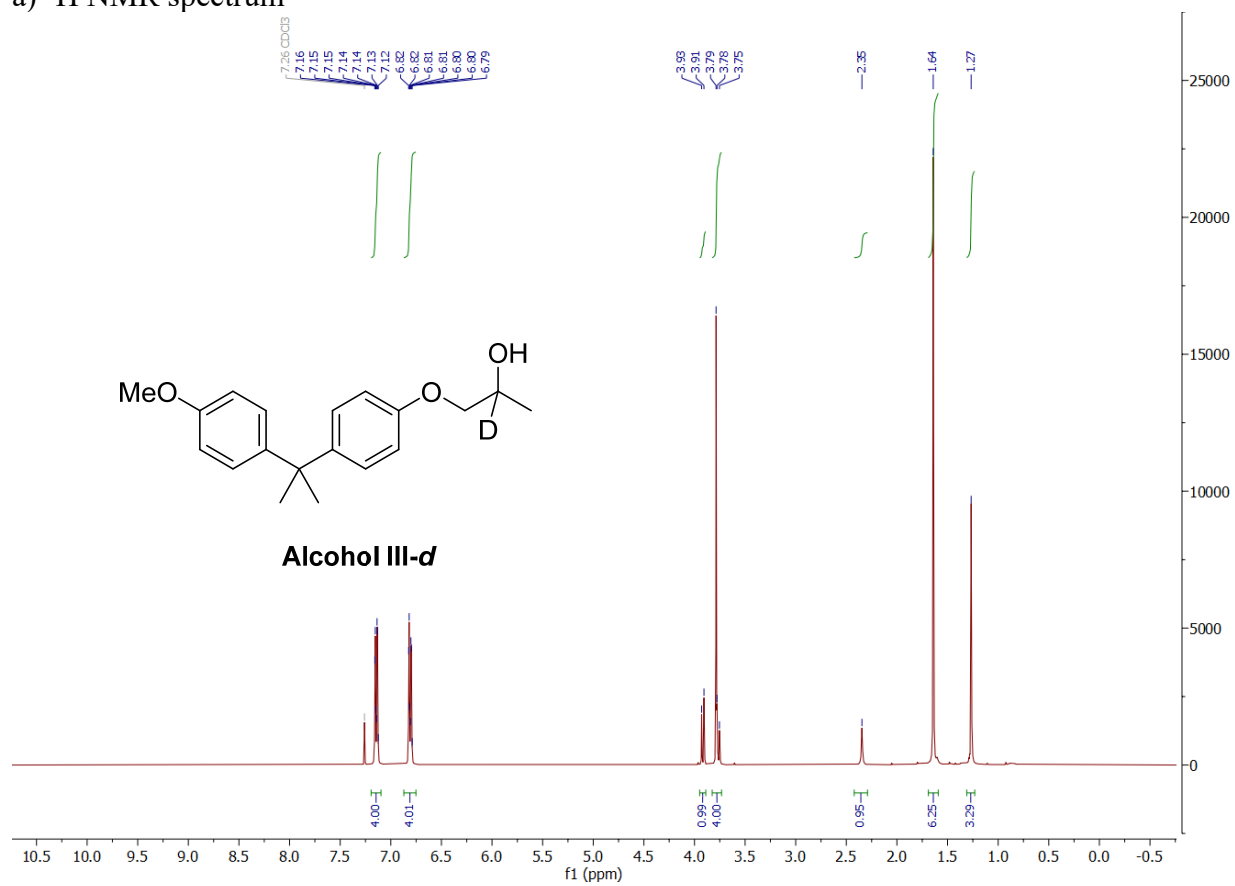


b) ^{13}C NMR spectrum

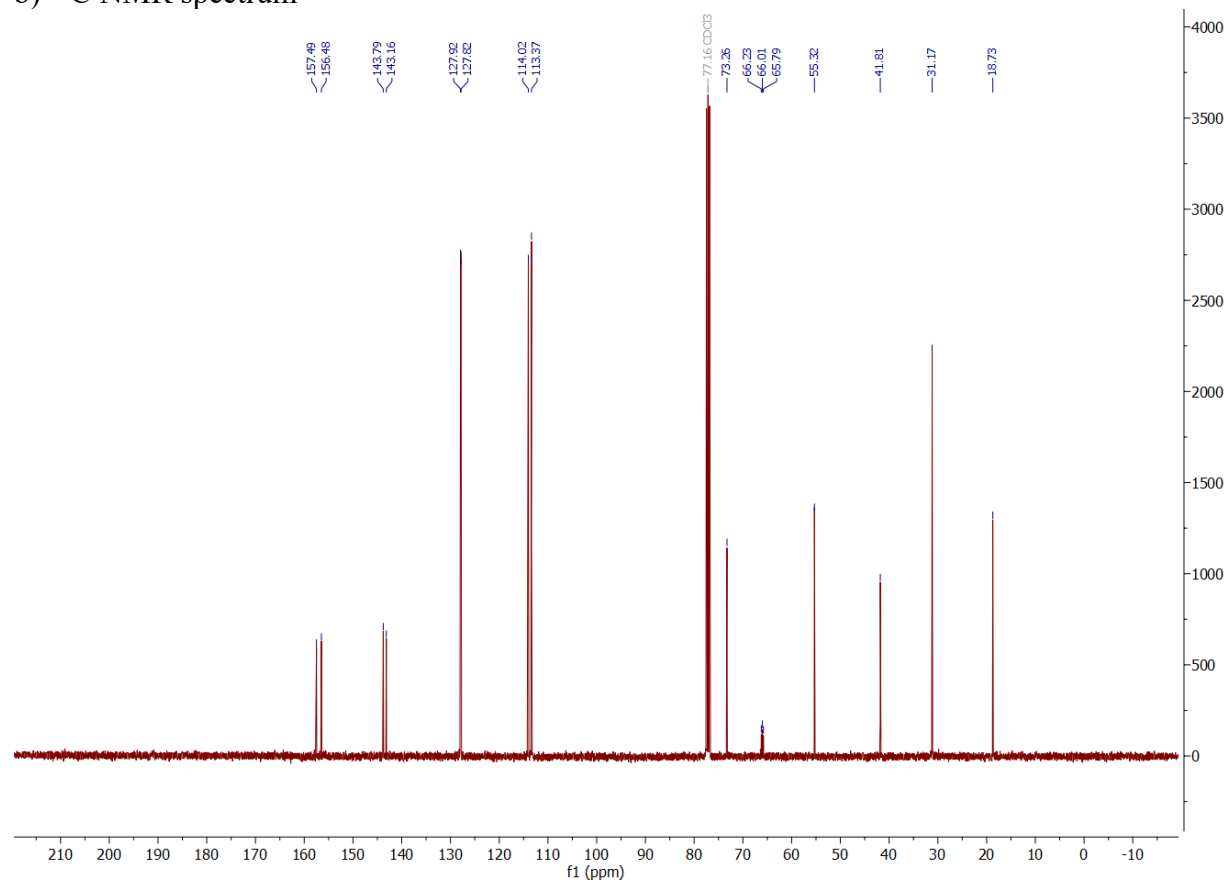


Alcohol III-d

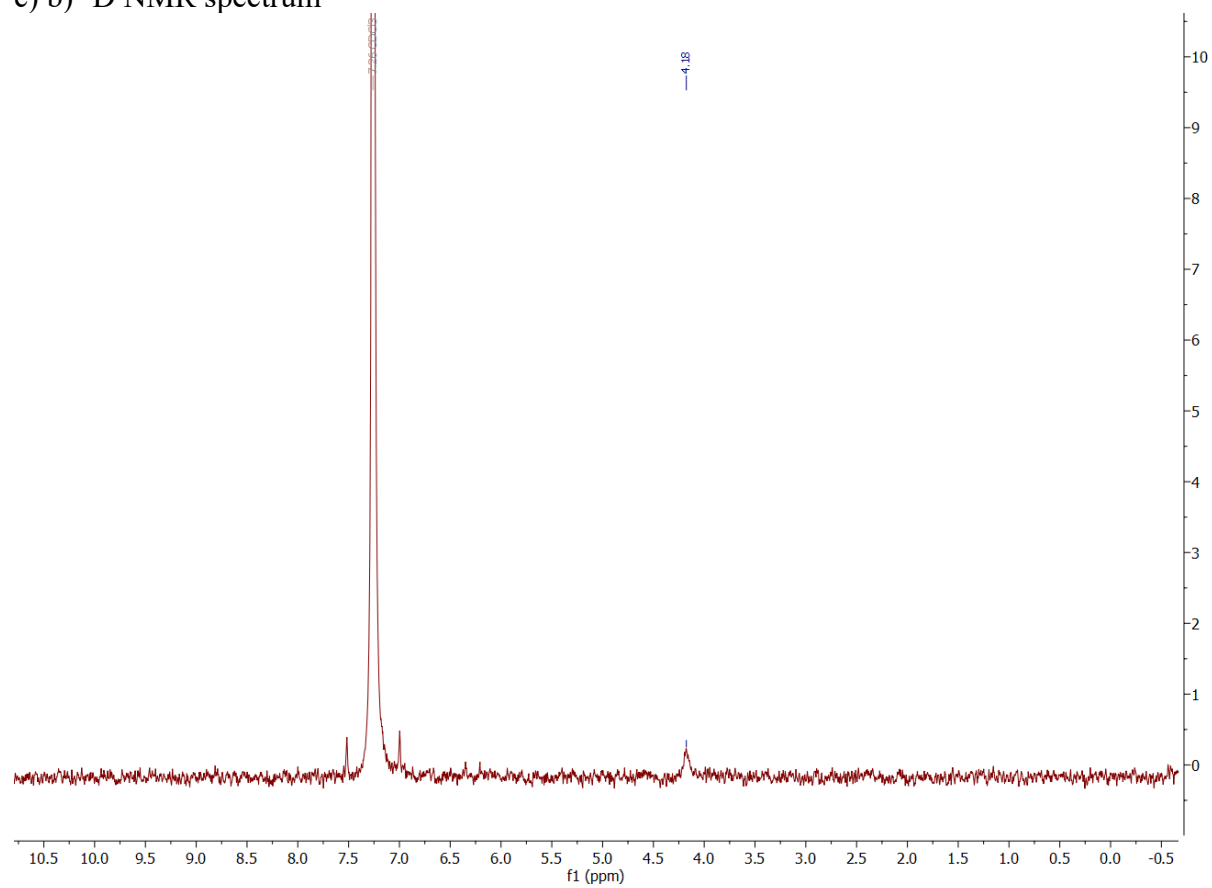
a) ^1H NMR spectrum



b) ^{13}C NMR spectrum



c) b) ^2D NMR spectrum



S8.2 Microscopic Images of Recovered Fibers (SEM)

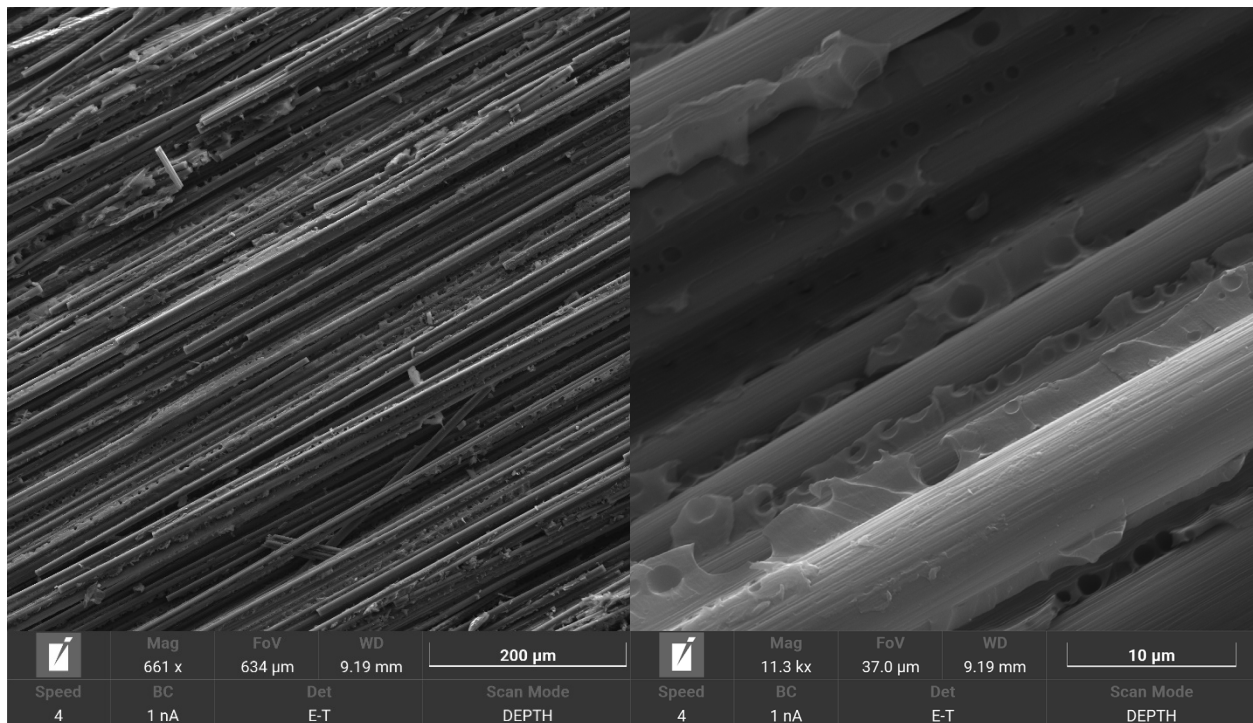


Fig. S50. Microscopic images of carbon fiber-based pultrusion composite from the core piece of a wind turbine blade provided by Vestas.

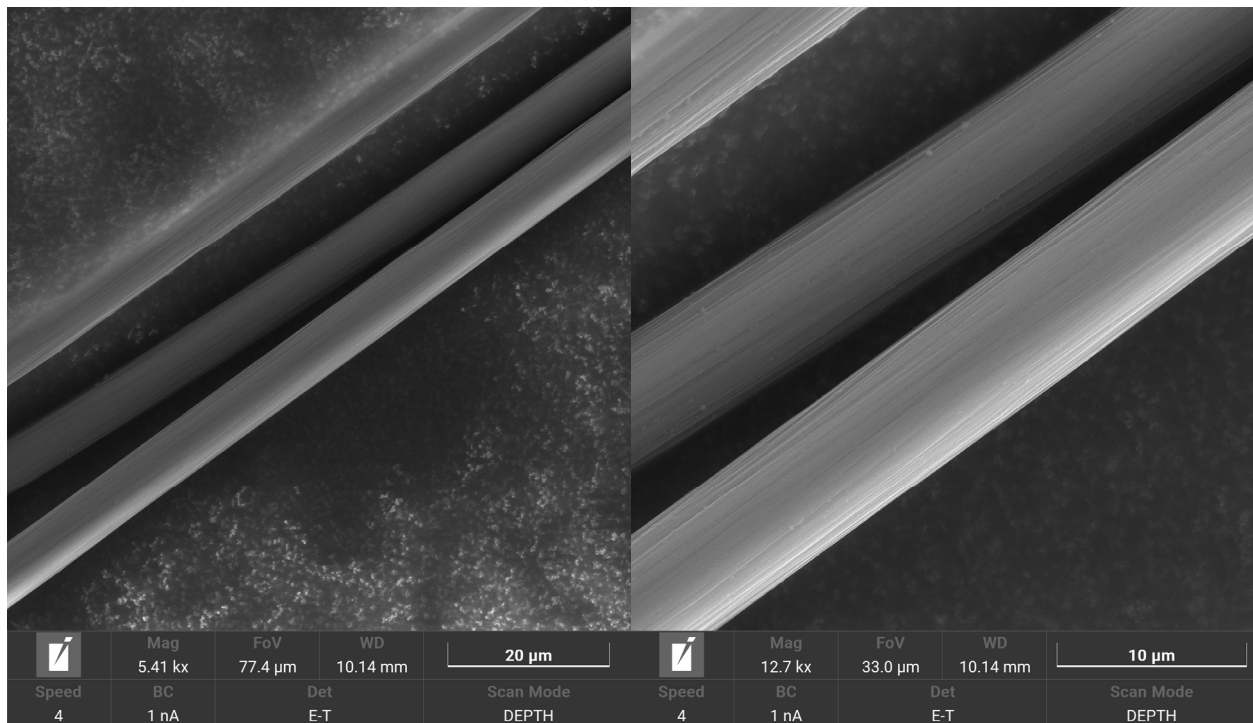


Fig. S51. Microscopic images of carbon fibers recovered from carbon fiber-based pultrusion composite from the core piece of a wind turbine blade provided by Vestas.

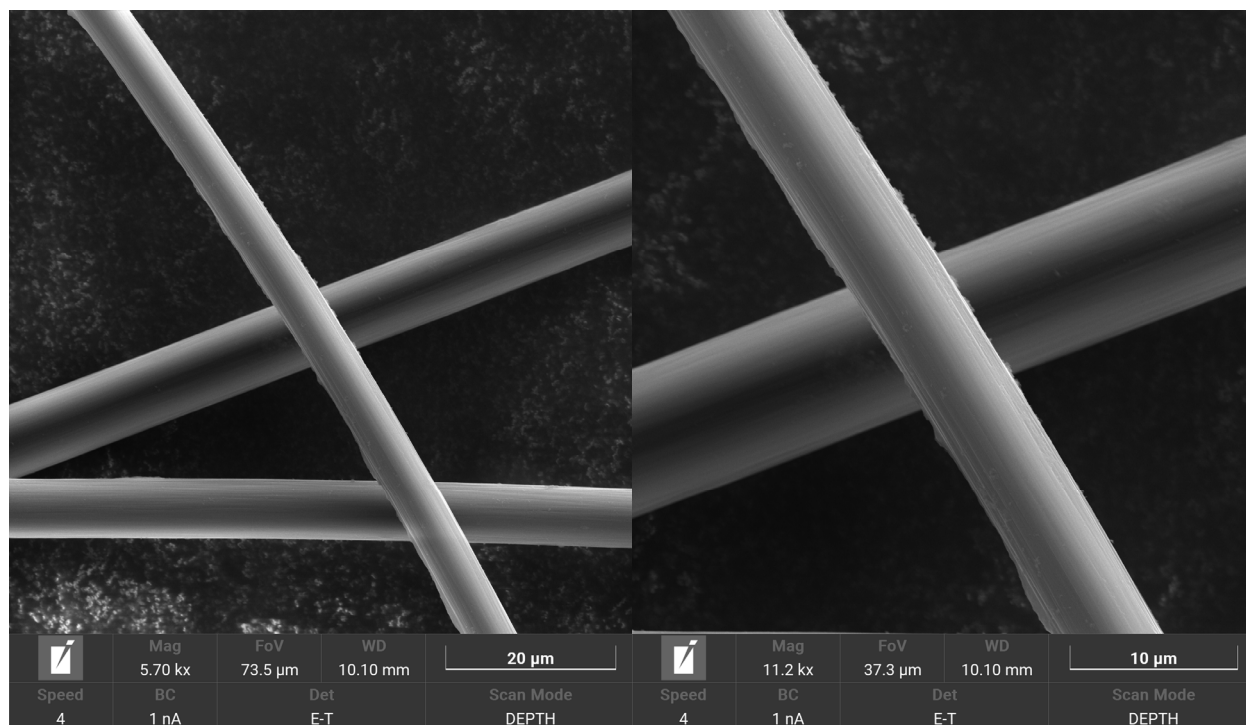


Fig. S52. Microscopic images of carbon fibers recovered from a carbon fiber-based pultrusion composite provided by Olin.

S8.3 X-Ray Micro Computed Tomography (μ -CT)

Due to insufficient grey-level variation and presumably similar material densities of the black epoxy matrix and the embedded carbon fibers in the composite, μ -CT imaging of the composite pieces could not be performed successfully. The neat carbon fiber sample, and the composite samples, were donated by different collaborators, respectively. Hence, μ -CT results cannot be interpreted as absolute and quantitative results regarding fiber diameter, or shape, but rather as an indication complementary to the SEM images that the fibers are not degraded when subjected to the reaction conditions.

The carbon fibers were bundled and packed inside a 1.5 mm glass capillary. The X-ray energy and power were adjusted to 40 kV and 3 W, with little to no attenuation to obtain optimal imaging conditions for these types of materials. The high-resolution measurements were performed employing a 20 \times objective, 1601 projections/360 $^\circ$ to result in isotropic voxel sizes of 0.5 μ m. The data were analyzed using Dragonfly Version 2021.3 (Object Research Systems Inc, Montreal, Canada).

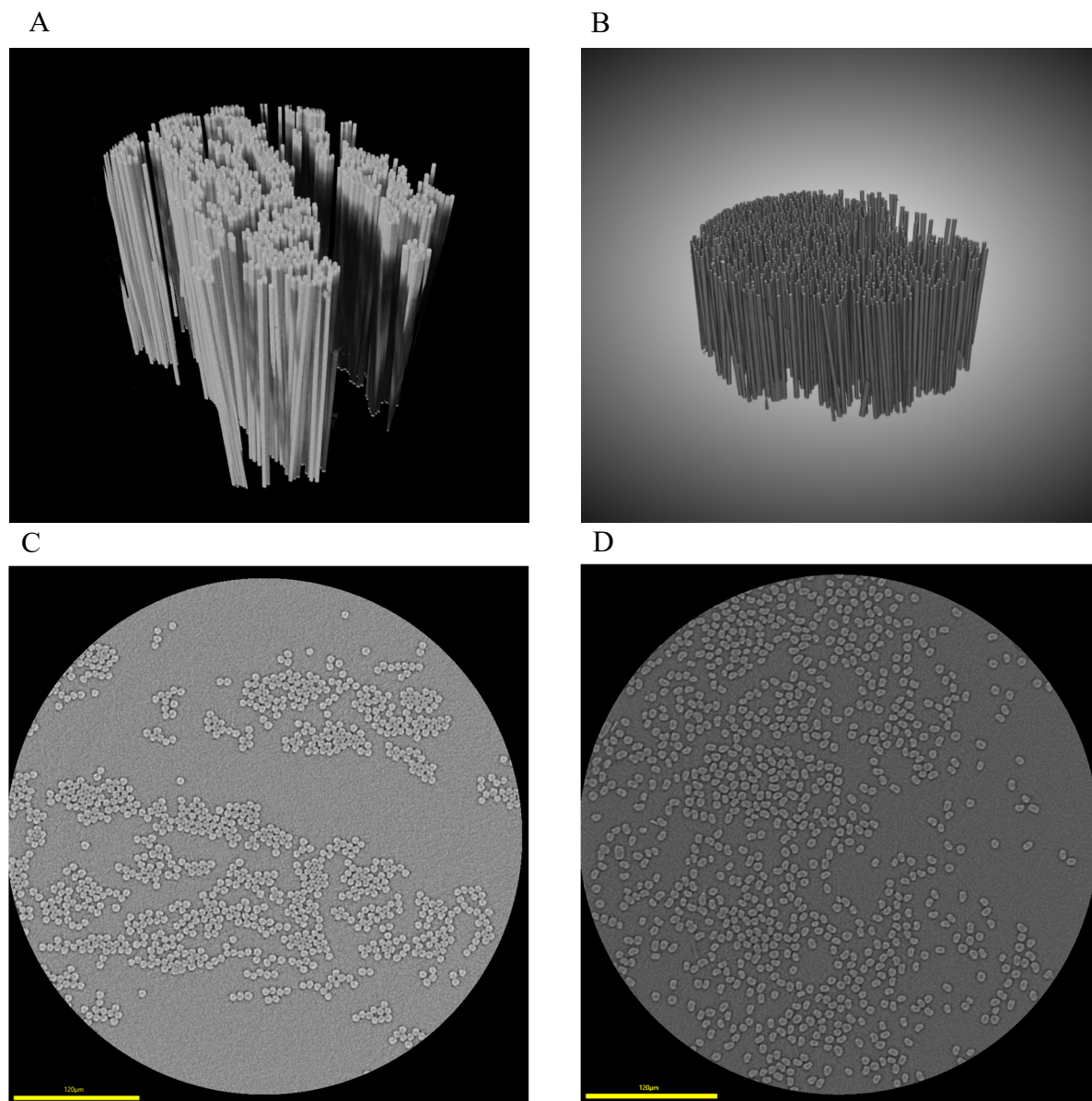


Fig. S53. (A) Bundle view of neat carbon fibers, (B) Bundle view of carbon fibers from Olin composite after the catalysis, (C) Slice view of neat carbon fibers, (D) Slice view of carbon fibers from Olin composite after the catalysis. (A), (B) Grey levels corresponding to air have been rendered transparent, (C), (D) Scale bar 120 μm .

Using Dragonfly Version 2021.3, the carbon fibers were transformed into a Multi ROI (region of interest) using a watershed transform. The isolated fibers were then converted into a thickness mesh, and the diameters were obtained as scalar values using spheres. As shown below in **Fig. S54**, neat and recovered fibers have a similar diameter distribution around 7-8 μm .

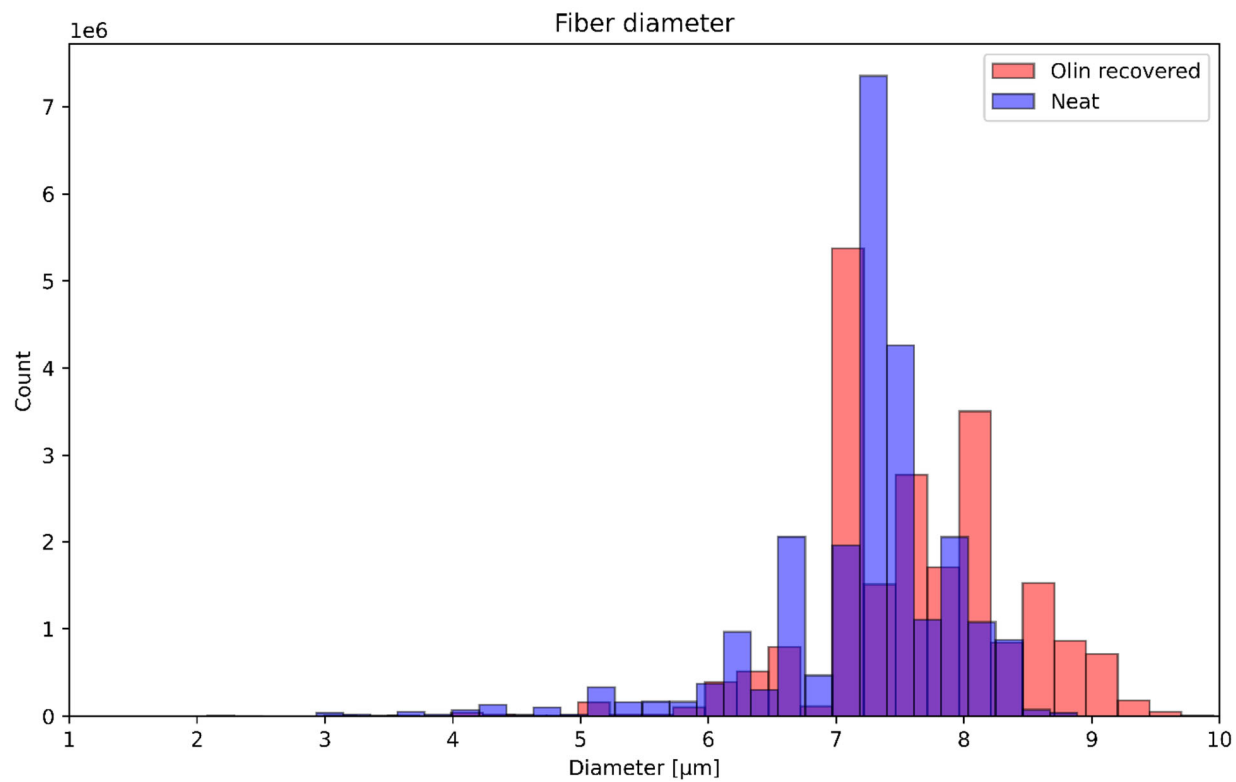


Fig. S54. Counts of computed fiber diameters for neat (blue) and recovered (red) carbon fibers.

References

- 1 Fulmer, G. R. *et al.* NMR Chemical Shifts of Trace Impurities: Common Laboratory Solvents, Organics, and Gases in Deuterated Solvents Relevant to the Organometallic Chemist. *Organometallics* **29**, 2176–2179 (2010). <https://doi.org/10.1021/om100106e>
- 2 Ahrens, A. *et al.* Catalytic disconnection of C–O bonds in epoxy resins and composites. *Nature* **617**, 730–737 (2023). <https://doi.org/10.1038/s41586-023-05944-6>
- 3 Sun, H. *et al.* Solvent–base mismatch enables the deconstruction of epoxy polymers and bisphenol A recovery. *Green Chem.* **26**, 815–824 (2024). <https://doi.org/10.1039/D3GC03707J>
- 4 Liu, Y. *et al.* Mild Redox-Neutral Depolymerization of Lignin with a Binuclear Rh Complex in Water. *ACS Catal.* **9**, 4441–4447 (2019). <https://doi.org/10.1021/acscatal.9b00669>
- 5 Liu, Y. *et al.* Rhodium-terpyridine catalyzed redox-neutral depolymerization of lignin in water. *Green Chem.* **22**, 33–38 (2020). <https://doi.org/10.1039/C9GC03057C>
- 6 Zhang, Y., Luo, Y., Hu, C., Tang, D. & Su, Z. Redox-neutral depolymerization of lignin-derived aryl ethers catalyzed by Rh(iii)-complexes: a mechanistic insight. *Phys. Chem. Chem. Phys.* **26**, 23710–23721 (2024). <https://doi.org/10.1039/D4CP02660H>
- 7 Stropp, J., Wili, N., Nielsen, N. C. & Klose, D. Increased sensitivity in electron–nuclear double resonance spectroscopy with chirped radiofrequency pulses. *Magn. Reson.* **6**, 33–42 (2025). <https://doi.org/10.5194/mr-6-33-2025>
- 8 Neese, F. Software update: The ORCA program system—Version 5.0. *Comput. Mol. Sci.* **12** (2022). <https://doi.org/10.1002/wcms.1606>
- 9 Neese, F. An improvement of the resolution of the identity approximation for the formation of the Coulomb matrix. *J. Comput. Chem.* **24**, 1740–1747 (2003). <https://doi.org/https://doi.org/10.1002/jcc.10318>
- 10 Neese, F., Wennmohs, F., Hansen, A. & Becker, U. Efficient, approximate and parallel Hartree–Fock and hybrid DFT calculations. A ‘chain-of-spheres’ algorithm for the Hartree–Fock exchange. *Chem. Phys.* **356**, 98–109 (2009). <https://doi.org/https://doi.org/10.1016/j.chemphys.2008.10.036>
- 11 Helmich-Paris, B., de Souza, B., Neese, F. & Izsák, R. An improved chain of spheres for exchange algorithm. *J Chem Phys* **155**, 104109 (2021). <https://doi.org/10.1063/5.0058766>
- 12 Becke, A. D. Density-functional thermochemistry. III. The role of exact exchange. *J. Chem. Phys.* **98**, 5648–5652 (1993). <https://doi.org/10.1063/1.464913>
- 13 Adamo, C. & Barone, V. Toward reliable density functional methods without adjustable parameters: The PBE0 model. *J. Chem. Phys.* **110**, 6158–6170 (1999). <https://doi.org/10.1063/1.478522>
- 14 Lenthe, E. v., Baerends, E. J. & Snijders, J. G. Relativistic regular two-component Hamiltonians. *J. Chem. Phys.* **99**, 4597–4610 (1993). <https://doi.org/10.1063/1.466059>
- 15 Canal Neto, A., Ferreira, I. B., Jorge, F. E. & de Oliveira, A. Z. All-electron triple zeta basis sets for ZORA calculations: Application in studies of atoms and molecules. *Chem. Phys. Lett.* **771**, 138548 (2021). <https://doi.org/https://doi.org/10.1016/j.cplett.2021.138548>
- 16 Stoychev, G. L., Auer, A. A. & Neese, F. Automatic Generation of Auxiliary Basis Sets. *J. Chem. Theory Comput.* **13**, 554–562 (2017). <https://doi.org/10.1021/acs.jctc.6b01041>

- 17 Neese, F. Metal and ligand hyperfine couplings in transition metal complexes: The effect of spin–orbit coupling as studied by coupled perturbed Kohn–Sham theory. *J. Chem. Phys.* **118**, 3939–3948 (2003). <https://doi.org/10.1063/1.1540619>
- 18 Stoll, S. & Schweiger, A. EasySpin, a comprehensive software package for spectral simulation and analysis in EPR. *J. Magn. Reson.* **178**, 42–55 (2006). <https://doi.org/10.1016/j.jmr.2005.08.013>
- 19 Munzarová, M. & Kaupp, M. A Critical Validation of Density Functional and Coupled-Cluster Approaches for the Calculation of EPR Hyperfine Coupling Constants in Transition Metal Complexes. *J. Phys. Chem. A* **103**, 9966–9983 (1999). <https://doi.org/10.1021/jp992303p>
- 20 Arbuznikov, A. V., Vaara, J. & Kaupp, M. Relativistic spin-orbit effects on hyperfine coupling tensors by density-functional theory. *J. Chem. Phys.* **120**, 2127–2139 (2004). <https://doi.org/10.1063/1.1636720>
- 21 Schotten, C. *et al.* Making electrochemistry easily accessible to the synthetic chemist. *Green Chem.* **22**, 3358–3375 (2020). <https://doi.org/10.1039/D0GC01247E>
- 22 Elgrishi, N. *et al.* A Practical Beginner’s Guide to Cyclic Voltammetry. *J. Chem. Educ.* **95**, 197–206 (2018). <https://doi.org/10.1021/acs.jchemed.7b00361>
- 23 Paul, J., Spey, S., Adams, H. & Thomas, J. A. Synthesis and structure of rhodium complexes containing extended terpyridyl ligands. *Inorg. Chim. Acta.* **357**, 2827–2832 (2004). <https://doi.org/10.1016/j.ica.2003.12.023>
- 24 Castillo, C. E. *et al.* Visible Light-Driven Electron Transfer from a Dye-Sensitized p-Type NiO Photocathode to a Molecular Catalyst in Solution: Toward NiO-Based Photoelectrochemical Devices for Solar Hydrogen Production. *J. Phys. Chem. B* **119**, 5806–5818 (2015). <https://doi.org/10.1021/jp511469f>
- 25 Castillo, C. E. *et al.* Electrochemical Generation and Spectroscopic Characterization of the Key Rhodium(III) Hydride Intermediates of Rhodium Poly(bipyridyl) H₂-Evolving Catalysts. *Inorg. Chem.* **57**, 11225–11239 (2018). <https://doi.org/10.1021/acs.inorgchem.8b01811>
- 26 Stoll, T. *et al.* An Efficient RuII–RhIII–RuII Polypyridyl Photocatalyst for Visible-Light-Driven Hydrogen Production in Aqueous Solution. *Angew. Chem. Int. Ed.* **53**, 1654–1658 (2014). <https://doi.org/10.1002/anie.201308132>
- 27 Kayanuma, M. *et al.* A computational mechanistic investigation of hydrogen production in water using the [RhIII(dmbpy)₂Cl₂]⁺/[RuII(bpy)₃]₂⁺/ascorbic acid photocatalytic system. *Phys. Chem. Chem. Phys.* **17**, 10497–10509 (2015). <https://doi.org/10.1039/C4CP04949G>
- 28 Camara, F. *et al.* Electrochemical Properties of a Rhodium(III) Mono-Terpyridyl Complex and Use as a Catalyst for Light-Driven Hydrogen Evolution in Water. *Molecules* **27**, 6614–6614 (2022). <https://doi.org/10.3390/molecules27196614>
- 29 Frisch, M. J. *et al.* (Gaussian, Inc., Wallingford CT, 2016).
- 30 Weigend, F. & Ahlrichs, R. Balanced basis sets of split valence, triple zeta valence and quadruple zeta valence quality for H to Rn: Design and assessment of accuracy. *Phys. Chem. Chem. Phys.* **7**, 3297–3297 (2005). <https://doi.org/10.1039/b508541a>
- 31 Grimme, S., Antony, J., Ehrlich, S. & Krieg, H. A consistent and accurate ab initio parametrization of density functional dispersion correction (DFT-D) for the 94 elements H–Pu. *J. Chem. Phys.* **132**, 154104–154104 (2010). <https://doi.org/10.1063/1.3382344>

- 32 Zhao, Y. & Truhlar, D. G. The M06 suite of density functionals for main group thermochemistry, thermochemical kinetics, noncovalent interactions, excited states, and transition elements: two new functionals and systematic testing of four M06-class functionals and 12 other function. *Theor. Chem. Acc.* **120**, 215–241 (2008).
<https://doi.org/10.1007/s00214-007-0310-x>
- 33 Marenich, A. V., Cramer, C. J. & Truhlar, D. G. Universal Solvation Model Based on Solute Electron Density and on a Continuum Model of the Solvent Defined by the Bulk Dielectric Constant and Atomic Surface Tensions. *J. Phys. Chem. B* **113**, 6378–6396 (2009). <https://doi.org/10.1021/jp810292n>
- 34 Pracht, P., Bohle, F. & Grimme, S. Automated exploration of the low-energy chemical space with fast quantum chemical methods. *Phys. Chem. Chem. Phys.* **22**, 7169–7192 (2020). <https://doi.org/10.1039/C9CP06869D>
- 35 Neese, F. The ORCA program system. *Comput. Mol. Sci.* **2**, 73–78 (2012).
<https://doi.org/10.1002/wcms.81>
- 36 Neese, F., Wennmohs, F., Becker, U. & Riplinger, C. The ORCA quantum chemistry program package. *J. Chem. Phys.* **152** (2020). <https://doi.org/10.1063/5.0004608>
- 37 Grimme, S. & Hansen, A. A Practicable Real-Space Measure and Visualization of Static Electron-Correlation Effects. *Angew. Chem. Int. Ed.* **54**, 12308–12313 (2015).
<https://doi.org/10.1002/anie.201501887>
- 38 Ahrens, A. *et al.* Unveiling the mechanism of triphos-Ru catalysed C–O bond disconnections in polymers. *Nat. Comm.* **15**, 5656–5656 (2024).
<https://doi.org/10.1038/s41467-024-50083-9>
- 39 Min, H.-Y. *et al.* Theoretical Mechanism of Rh-Containing Species Catalyzing the Hydrogenolysis of Lignin Model Compounds Using $-\text{C}\alpha\text{O}-\text{H}$ and $-\text{C}\alpha-\text{H}$ Groups as Superior H-Sources. *J. Phys. Chem. B* **128**, 12540–12548 (2024).
<https://doi.org/10.1021/acs.jpcc.4c06298>
- 40 Riplinger, C., Sandhoefer, B., Hansen, A. & Neese, F. Natural triple excitations in local coupled cluster calculations with pair natural orbitals. *J. Chem. Phys.* **139** (2013).
<https://doi.org/10.1063/1.4821834>
- 41 Riplinger, C. & Neese, F. An efficient and near linear scaling pair natural orbital based local coupled cluster method. *J. Chem. Phys.* **138** (2013).
<https://doi.org/10.1063/1.4773581>
- 42 Saitow, M., Becker, U., Riplinger, C., Valeev, E. F. & Neese, F. A new near-linear scaling, efficient and accurate, open-shell domain-based local pair natural orbital coupled cluster singles and doubles theory. *J. Chem. Phys.* **146** (2017).
<https://doi.org/10.1063/1.4981521>
- 43 Riplinger, C., Pinski, P., Becker, U., Valeev, E. F. & Neese, F. Sparse maps—A systematic infrastructure for reduced-scaling electronic structure methods. II. Linear scaling domain based pair natural orbital coupled cluster theory. *J. Chem. Phys.* **144** (2016). <https://doi.org/10.1063/1.4939030>
- 44 Guo, Y. *et al.* Communication: An improved linear scaling perturbative triples correction for the domain based local pair-natural orbital based singles and doubles coupled cluster method [DLPNO-CCSD(T)]. *J. Chem. Phys.* **148** (2018).
<https://doi.org/10.1063/1.5011798>

- 45 Delaney, C. P. *et al.* Cross-coupling by a noncanonical mechanism involving the addition of aryl halide to Cu(II). *Science* **381**, 1079–1085 (2023).
<https://doi.org/10.1126/science.adi9226>
- 46 Inoki, D., Matsumoto, T., Nakai, H. & Ogo, S. Experimental Study of Reductive Elimination of H₂ from Rhodium Hydride Species. *Organometallics* **31**, 2996–3001 (2012). <https://doi.org/10.1021/om2009759>
- 47 Inoki, D. *et al.* Establishing the mechanism of Rh-catalysed activation of O₂ by H₂. *Dalton Trans.* **41**, 4328–4334 (2012). <https://doi.org/10.1039/C1DT11599E>
- 48 Ghosh, B. K. & Chakravorty, A. Electrochemical studies of ruthenium compounds part I. Ligand oxidation levels. *Coord. Chem. Rev.* **95**, 239–294 (1989).
[https://doi.org/10.1016/0010-8545\(89\)80027-X](https://doi.org/10.1016/0010-8545(89)80027-X)
- 49 Shaffer, D. W., Xie, Y. & Concepcion, J. J. O–O bond formation in ruthenium-catalyzed water oxidation: single-site nucleophilic attack vs. O–O radical coupling. *Chem. Soc. Rev.* **46**, 6170–6193 (2017). <https://doi.org/10.1039/C7CS00542C>
- 50 Concepcion, J. J., Jurss, J. W., Templeton, J. L. & Meyer, T. J. One Site is Enough. Catalytic Water Oxidation by [Ru(tpy)(bpm)(OH₂)]²⁺ and [Ru(tpy)(bpz)(OH₂)]²⁺. *J. Chem. Soc.* **130**, 16462–16463 (2008). <https://doi.org/10.1021/ja8059649>
- 51 Chen, Z. *et al.* Concerted O atom-proton transfer in the O–O bond forming step in water oxidation. *Proc. Natl. Acad. Sci.* **107**, 7225–7229 (2010).
<https://doi.org/10.1073/pnas.1001132107>
- 52 Tao, J., Perdew, J. P., Staroverov, V. N. & Scuseria, G. E. Climbing the Density Functional Ladder: Nonempirical Meta-Generalized Gradient Approximation Designed for Molecules and Solids. *Phys. Rev. Lett.* **91**, 146401–146401 (2003).
<https://doi.org/10.1103/PhysRevLett.91.146401>
- 53 Lee, C., Yang, W. & Parr, R. G. Development of the Colle-Salvetti correlation-energy formula into a functional of the electron density. *Phys. Rev. B* **37**, 785–789 (1988).
<https://doi.org/10.1103/PhysRevB.37.785>
- 54 Stephens, P. J., Devlin, F. J., Chabalowski, C. F. & Frisch, M. J. Ab Initio Calculation of Vibrational Absorption and Circular Dichroism Spectra Using Density Functional Force Fields. *J. Phys. Chem.* **98**, 11623–11627 (1994). <https://doi.org/10.1021/j100096a001>
- 55 Vosko, S. H., Wilk, L. & Nusair, M. Accurate spin-dependent electron liquid correlation energies for local spin density calculations: a critical analysis. *Can. J. Phys.* **58**, 1200–1211 (1980). <https://doi.org/10.1139/p80-159>
- 56 Perdew, J. P., Burke, K. & Ernzerhof, M. Generalized Gradient Approximation Made Simple [Phys. Rev. Lett. 77, 3865 (1996)]. *Phys. Rev. Lett.* **78**, 1396–1396 (1997).
<https://doi.org/10.1103/PhysRevLett.78.1396>
- 57 Perdew, J. P., Burke, K. & Ernzerhof, M. Generalized Gradient Approximation Made Simple. *Phys. Rev. Lett.* **77**, 3865–3868 (1996).
<https://doi.org/10.1103/PhysRevLett.77.3865>
- 58 Adamo, C., Cossi, M. & Barone, V. An accurate density functional method for the study of magnetic properties: the PBE0 model. *J. Mol. Struct. THEOCHEM* **493**, 145–157 (1999). [https://doi.org/10.1016/S0166-1280\(99\)00235-3](https://doi.org/10.1016/S0166-1280(99)00235-3)
- 59 Batista, G. M. F. *et al.* Efficient palladium-catalyzed electrocarboxylation enables late-stage carbon isotope labelling. *Nat. Comm.* **15**, 2592–2592 (2024).
<https://doi.org/10.1038/s41467-024-46820-9>

- 60 Pedersen, S. S. *et al.* Lignocellulose Conversion via Catalytic Transformations Yields Methoxyterephthalic Acid Directly from Sawdust. *JACS Au* **3**, 1221–1229 (2023). <https://doi.org/10.1021/jacsau.3c00092>
- 61 Mühlfenzl, K. S. *et al.* Nickel Catalyzed Carbonylative Cross Coupling for Direct Access to Isotopically Labeled Alkyl Aryl Ketones. *Angew. Chem.* **136** (2024). <https://doi.org/10.1002/ange.202412247>
- 62 Davies, J. *et al.* Kinetically-Controlled Ni-Catalyzed Direct Carboxylation of Unactivated Secondary Alkyl Bromides without Chain Walking. *J. Chem. Soc.* **146**, 1753–1759 (2024). <https://doi.org/10.1021/jacs.3c11205>
- 63 Wang, J. & Hanan, G. S. A Facile Route to Sterically Hindered and Non-Hindered 4'-Aryl-2,2':6',2''-Terpyridines. *Synlett* **2005**, 1251–1254 (2005). <https://doi.org/10.1055/s-2005-868481>
- 64 Mutai, T., Cheon, J.-D., Arita, S. & Araki, K. Phenyl-substituted 2,2':6',2''-terpyridine as a new series of fluorescent compounds—their photophysical properties and fluorescence tuning. *J. Chem. Soc., Perkin trans. II*, 1045–1050 (2001). <https://doi.org/10.1039/B102685M>
- 65 Dumur, F., Mayer, C. R., Dumas, E., Marrot, J. & Sécheresse, F. Synthesis of valuable terpyridine building blocks to generate a variety of metallodendrons by the convergent approach. *Tetrahedron Lett.* **48**, 4143–4146 (2007). <https://doi.org/10.1016/j.tetlet.2007.03.160>
- 66 Hampson, E. *et al.* Asymmetric Hybrid Polyoxometalates: A Platform for Multifunctional Redox-Active Nanomaterials. *Angew. Chem. Int. Ed.* **58**, 18281–18285 (2019). <https://doi.org/https://doi.org/10.1002/anie.201912046>
- 67 Yoo, D.-W., Yoo, S.-K., Kim, C. & Lee, J.-K. A novel mononuclear Fe(iii) mono(terpyridine) complex having labile solvent ligands and its catalytic activity. *J. Chem. Soc., Dalton Trans.*, 3931–3932 (2002). <https://doi.org/10.1039/B208413A>
- 68 Constable, E. C. *et al.* Metal-Directed Synthesis and Photophysical Studies of Trinuclear V-Shaped and Pentanuclear X-Shaped Ruthenium and Osmium Metallorods and Metallostars Based upon 4'-(3,5-Dihydroxyphenyl)-2,2':6',2''-terpyridine Divergent Units. *Chem. Eur. J.* **11**, 4024–4034 (2005). <https://doi.org/https://doi.org/10.1002/chem.200500119>
- 69 Liu, Y., Park, S. K., Xiao, Y. & Chae, J. Copper(ii)-catalyzed C–O coupling of aryl bromides with aliphatic diols: synthesis of ethers, phenols, and benzo-fused cyclic ethers. *Org. Biomol. Chem.* **12**, 4747–4753 (2014). <https://doi.org/10.1039/C4OB00649F>
- 70 He, Y.-J. *et al.* Facile Construction of Metallo-supramolecular Poly(3-hexylthiophene)-block-Poly(ethylene oxide) Diblock Copolymers via Complementary Coordination and Their Self-Assembled Nanostructures. *J. Chem. Soc.* **139**, 4218–4224 (2017). <https://doi.org/10.1021/jacs.7b01010>
- 71 Yu, F. *et al.* Iminopyridyl ligands bearing polyethylene glycol unit for nickel catalyzed ethylene polymerization. *Polymer* **229**, 124023 (2021). <https://doi.org/https://doi.org/10.1016/j.polymer.2021.124023>
- 72 Wang, E. *et al.* Porous polymeric ligand promoted copper-catalyzed C–N coupling of (hetero)aryl chlorides under visible-light irradiation. *Sci. China Chem.* **64**, 17–21 (2021). <https://doi.org/10.1007/s11426-020-9859-9>
- 73 Chen, C.-T. & Huang, W.-P. A Highly Selective Fluorescent Chemosensor for Lead Ions. *J. Chem. Soc.* **124**, 6246–6247 (2002). <https://doi.org/10.1021/ja025710e>

- 74 Pruchnik, F. P., Robert, F., Jeannin, Y. & Jeannin, S. New Rhodium(II) Complexes with 2,2':6',2''-Terpyridine. *Inorg. Chem.* **35**, 4261–4263 (1996).
<https://doi.org/10.1021/ic950529a>
- 75 Paul, P. *et al.* Synthesis and Characterization of Rhodium Complexes Containing 2,4,6-Tris(2-pyridyl)-1,3,5-triazine and Its Metal-Promoted Hydrolytic Products: Potential Uses of the New Complexes in Electrocatalytic Reduction of Carbon Dioxide. *Inorg. Chem.* **37**, 5733–5742 (1998). <https://doi.org/10.1021/ic9709739>
- 76 O'Reilly, M. E. *et al.* Reductive functionalization of a rhodium(iii)–methyl bond by electronic modification of the supporting ligand. *Dalton Trans.* **43**, 8273–8281 (2014).
<https://doi.org/10.1039/C4DT00234B>
- 77 de Pater, Boke C. *et al.* Strongly Nucleophilic RhI Centre in Square-Planar Complexes with Terdentate ($\kappa 3$) 2,2':6',2''-Terpyridine Ligands: Crystallographic, Electrochemical and Density Functional Theoretical Studies. *Eur. J. Inorg. Chem.* **2004**, 1675–1686 (2004). <https://doi.org/https://doi.org/10.1002/ejic.200300699>
- 78 Leal-Duaso, A., Pérez, P., Mayoral, J. A., García, J. I. & Pires, E. Glycerol-Derived Solvents: Synthesis and Properties of Symmetric Glyceryl Diethers. *ACS Sustain. Chem. Eng.* **7**, 13004–13014 (2019). <https://doi.org/10.1021/acssuschemeng.9b02105>
- 79 Hanada, S., Yuasa, A., Kuroiwa, H., Motoyama, Y. & Nagashima, H. Hydrosilanes Are Not Always Reducing Agents for Carbonyl Compounds, II: Ruthenium-Catalyzed Deprotection of tert-Butyl Groups in Carbamates, Carbonates, Esters, and Ethers. *Eur. J. Org. Chem.* **2010**, 1021–1025 (2010).
<https://doi.org/https://doi.org/10.1002/ejoc.200901279>
- 80 Pan, W. *et al.* A mild and practical method for deprotection of aryl methyl/benzyl/allyl ethers with HPPH₂ and tBuOK. *Org. Biomol. Chem.* **19**, 7633–7640 (2021).
<https://doi.org/10.1039/D1OB01286J>